Astrophysical plasma modeling of the hot Universe

Advances and challenges
in high-resolution X-ray spectroscopy

Astrophysical plasma modeling of the hot Universe

Advances and challenges
in high-resolution X-ray spectroscopy

Proefschrift

ter verkrijging van
de graad van Doctor aan de Universiteit Leiden,
op gezag van de Rector Magnificus prof. mr. C. J. J. M. Stolker,
volgens besluit van het College voor Promoties
te verdedigen op donderdag 7 juni 2018
klokke 10:00 uur

door

Junjie Mao

geboren te Ningbo, China
in 1988

Promotiecommissie:

Promotor:
Prof. dr. J. S. Kaastra

Co-promotor:
Dr. J. de Plaa (SRON)

Overige leden:
Prof. dr. H. Röttgering
Prof. dr. J. Schaye
Prof. dr. W. R. Jaffe
Prof. dr. G. Branduardi-Raymont (University College London)
Prof. dr. F. B. S. Paerels (Columbia University)

To Lilan
our active family nucleus
with her inflows
and outflows

Cover design by Junjie Mao
Image credit: Adobe Spark

Contents

1

Introduction

1

1.1. Hot astrophysical plasmas in X-rays

Hot astrophysical plasmas pervade the Universe: about half of the baryonic content in the Universe is expected to have a temperature of $T > 10^5$ K, which is largely undetectable by observational facilities at wavelength longer than X-rays (0.1–100 Å). The X-ray band therefore provides unique opportunities to find clues to answer major astrophysical questions like "How does AGN feedback influence the host galaxies and beyond?" and "What is the chemical composition of the Universe and what are the origins of these elements?".

X-ray spectroscopy enables us to constrain physical properties (temperature, density, abundance, microscopic turbulence, line of sight velocity, etc.) of these hot plasmas. Thanks to the grating spectrometers aboard *XMM-Newton* (den Herder et al. 2001; Mason et al. 2001; Strüder et al. 2001) and *Chandra* (Brinkman et al. 2000; Canizares et al. 2005), our knowledge of the hot and energetic Universe has advanced in the past two decades. We are also looking forward to new missions like *Arcus* (Smith et al. 2016), *Astro-H* (also known as *Hitomi*, Takahashi et al. 2014), and *Athena* (Nandra et al. 2013), which are built on new technologies. Compared to the current generation of spectrometers, the next generation improves the spectral resolution by one or two orders of magnitude so that blended spectral features can be clearly resolved.

High quality spectra from both current and future generations of X-ray spectrometers challenge plasma models that are widely used in the community. More accurate and complete atomic data are required to build better plasma models. Otherwise, the interpretation of the physical properties of the plasmas might be incorrect.

When I started my PhD project in 2014, the *Hitomi* satellite was scheduled to be launched in 2016. There was and still is an urgent need for improvements on the SPEX code. SPEX is a software package, including atomic data and various plasma models, designed for the analysis and interpretation of high-resolution cosmic X-ray spectra. My first project was to update the radiative recombination data in the SPEX code. Radiative recombination is a fundamental atomic process, therefore, almost all plasma models are affected by the accuracy and completeness of the radiative recombination data. We aimed to test the updated SPEX code by measuring the chemical abundances in the CHEERS sample (de Plaa et al. 2017) of clusters observed with *XMM-Newton* at that time and apply to *Hitomi* data when they are available.

While I made progresses on updating the radiative recombination data in SPEX

and commenced on studying the nitrogen enrichment of the CHEERS sample in my second year as a PhD student, *Hitomi* spun out of control about forty days after its successful launch. Although I did not work directly on the Perseus spectra observed with the Soft X-ray Spectrometer aboard *Hitomi*, the updated collisional ionization plasma model in the SPEX code has been applied to the Perseus spectra which lead to several high profile publications (e.g., Hitomi Collaboration et al. 2017a,b). I decided to shift my focus to Active Galactic Nuclei (AGN) since there are still many interesting questions to be answered with photoionization modeling of high-resolution X-ray spectra of AGN obtained with the current generation of spectrometers aboard *Chandra* and *XMM-Newton*. For instance, it was recently discovered that some Seyfert 1 galaxies have a special type of photoionized outflow, which heavily obscures the soft X-ray continuum and causes simultaneous deep, broad UV absorption troughs (e.g., Kaastra et al. 2014; Mehdipour et al. 2017). As a result, X-ray narrow emission lines stand out above the diminished continuum. Such a special state of the AGN offers a unique opportunity to study relatively weak narrow emission lines in the soft X-ray band that are previously hidden by the unobscured continuum.

1.2. Active Galactic Nuclei and circumnuclear media

The center of almost every galaxy, except for the smallest ones, contains a supermassive black hole (SMBH) with $M_{\rm BH} > 10^5$ $\rm M_\odot$. The growth of the supermassive black hole is realized via accretion of matter. When the accretion rate is above a certain limit ($\gtrsim 10^{-5}$ Eddington ratio), the central region of this active galaxy is called an active galactic nucleus (AGN). The rich phenomenology of AGN, covering the entire electromagnetic spectrum, is intriguing yet puzzling. This is evident because even the number of acronyms or classes related to AGN has exceeded a dozen and each reveals certain aspects of the nature of AGN.

Seyfert galaxies (Seyfert 1943) are one of the two largest groups of AGN, along with quasars (Schmidt 1963). Seyferts, accounting for about 10% of all galaxies (Maiolino & Rieke 1995), are thought to be powered by the same mechanism that occurs in quasars, but Seyferts are closer (thus brighter) and less luminous than quasars. Quasars are also known as quasi-stellar objects (QSOs). The former term originally requires radio detection (no longer required now, Padovani et al. 2017), while the latter refers to a quasar-like, non-radio source. If its ratios of radio (5 GHz)

to optical (B-band) flux $F_5/F_B \gtrsim 10$ (Kellermann et al. 1989), the AGN is radio-loud (RL). Otherwise, it is radio quiet (RQ). Nevertheless, Padovani et al. (2017) made a convincing plea to abandon the RL and RQ terms, replacing them with "jetted" and "non-jetted" since the two classes are intrinsically different.

In terms of optical spectral features, Seyfert galaxies are first divided into two subgroups (Weedman 1973). Seyfert 1 galaxies possess broad permitted emission lines with a velocity broadening of a few 10^3 km s^{-1} and narrow forbidden emission lines with a velocity broadening of a few 10^2 km s^{-1}, while Seyfert 2 galaxies only have narrow permitted and forbidden emission lines. Later, Osterbrock (1981) introduced the notations Seyfert 1.5, 1.8 and 1.9, where the subclasses are again based on the optical appearance of the spectrum, with the numerically larger subclasses having weaker broad lines relative to the narrow lines. The commonly used term Type I/II applies to both Seyferts and quasars, based on their optical spectra features described above.

It is also possible that the optical spectrum is relatively featureless. Blazars are a type of AGN that show rapid variability, high polarization and a relatively featureless spectrum.

It is important to emphasize that the aforementioned acronyms or (sub)classes cover merely the most frequently used ones, a more complete list can be found in a recent review by Padovani et al. (2017). Regardless of the variety of naming, most AGN include several of the following components (Figure 1.1):

1. Accretion disk: a rotation-dominated accretion flow, typically at a sub-parsec scale. A corona of hot plasma might sit above the centre of the accretion disk and produces photons at hard X-ray energies via inverse-Compton scattering (Haardt & Maraschi 1991, 1993).

2. Broad-line region (BLR): a high-density, high-velocity ($v \gtrsim 10^3$ km s^{-1}) and dust-free plasma. The BLR is about a few light-days to light-weeks away from the black hole (Peterson et al. 2004).

3. Torus: an axisymmetric dusty structure with its inner boundary about 0.01–1 pc, which is about four times the Blamer line BLR (Koshida et al. 2014).

4. Narrow-line region (NLR): a low-density and low-velocity ($v \lesssim 10^3$ km s^{-1}) plasma. The NLR extends from the outer edge of the torus to at least a few parsec away (Bennert et al. 2006a,b), along the ionization cone.

5. Outflows: feedback in the radiative mode (wind) or radio mode (jet).

It is important to understand the physics of inflows and outflows associated with AGN, thus, the evolution of SMBHs, the regulated evolution of the host galaxies and the origin of the circumnuclear media (for recent reviews see Fabian 2012; Kormendy & Ho 2013; Netzer 2015).

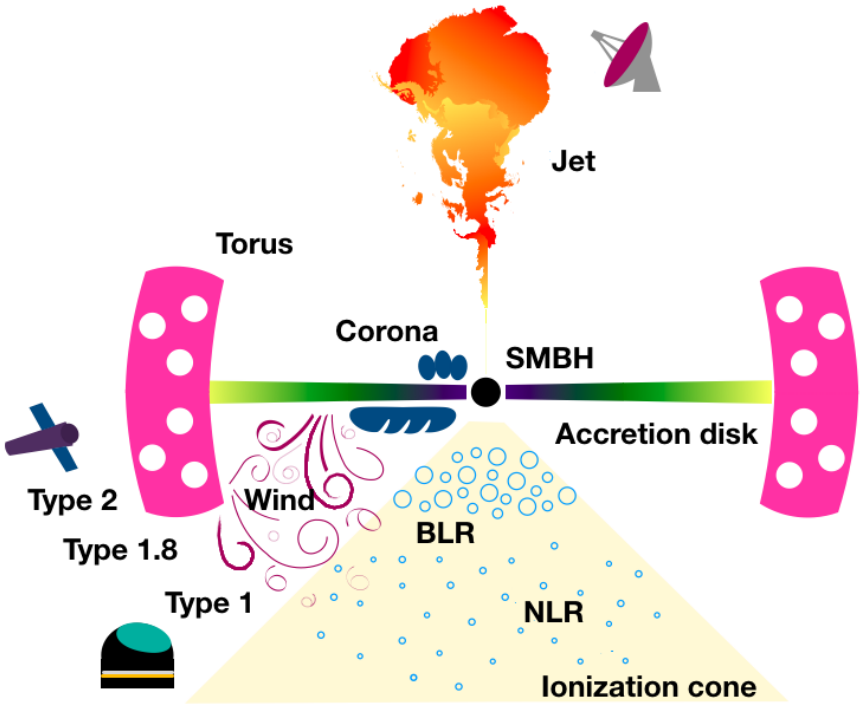

Figure 1.1: A sketch of the main components in active galactic nuclei, including the supermassive black hole (SMBH), accretion disk, corona, broad-line region (BLR), dusty torus, narrow-line region (NLR), outflows (jet and wind).

The radiative mode of the AGN outflow (wind) is of particular interest here since there are significant gaps in our understanding of this outflow phenomenon. Whether the outflow plays an important role in the cosmic feedback is determined by the mass outflow rate and kinetic power carried by the outflow

$$\dot{M}_{\rm out} \propto n_{\rm H}\, v_{\rm out}\, r^2,\ L^{\rm KE}_{\rm out} = \frac{1}{2}\,\dot{M}_{\rm out}\, v^2_{\rm out}, \tag{1.1}$$

where $n_{\rm H}$ is the hydrogen number density of the outflow, $v_{\rm out}$ the outflow velocity and r the distance to the central engine (e.g., King & Pounds 2003). An accurate measurement of the distance of the outflow is the prerequisite of estimating $\dot{M}_{\rm out}$

and $L_{\rm out}^{\rm KE}$ (Equation 1.1). Unfortunately, circumnuclear media are often not spatially resolved with direct imaging. Distance can be indirectly measured via density:

$$\xi = \frac{L}{n_{\rm H}\, r^2} \tag{1.2}$$

where ξ is the ionization parameter of the outflow, L is the 1–1000 Ryd ionizing luminosity (Krolik et al. 1981; Tarter et al. 1969). Both the ionization parameter and ionizing luminosity are observable. Nevertheless, it is not trivial to determine the density of the photoionized outflow.

Three different approaches have been used to measure the density of AGN outflows. The first approach is a spectral analysis of density sensitive emission lines. It is well known that the ratio of intercombination to forbidden emission lines in the He-like triplets varies for plasmas with different density values (e.g., Porquet et al. 2010). This density probe, observed in the X-ray wavelength range, has been applied to a few AGNs, e.g., NGC 4051 (Collinge et al. 2001), NGC 4593 (McKernan et al. 2003), and NGC 4151 (Schurch et al. 2004), where the upper limits of the plasma density are derived. The density of circumnuclear media is orders of magnitude lower for the triplet line ratios to be effective, thus, only upper limits are obtained.

A second approach is a timing analysis where the response of the changing ionizing continuum is monitored. A high-density plasma recombines more rapidly, thus yields a shorter recombination timescale. This approach has been used to constrain the density in, for instance, Mrk 509 (Kaastra et al. 2012), NGC 5548 (Ebrero et al. 2016), and NGC 4051 (Silva et al. 2016). The timing analysis is challenging in general because it requires frequent (if not continuous) monitoring with adequately high-quality spectra to verify the response. Note that even if perfect observations were available for an ideal variable target, the maximum continuous observational window for some sources is typically less than 100 days due to the sky positions of the targets and the pointing constraints of the space observatories. This maximum continuous observational window determines the lowest density (10^{4-5} cm^{-3}) that can be probed via the timing analysis(Figure 1.2). In addition, if the plasma density is so low that the recombination timescale ($\tau_{\rm rec}$) is orders of magnitude higher than the variability timescale $\tau_{\rm var}$ of the ionizing continuum, the plasma is in a quasi-steady state (Nicastro et al. 1999). In other words, the ionization balance of the plasma varies slightly around the mean value corresponding to the mean ionizing flux level over time (Kaastra et al. 2012; Silva et al. 2016).

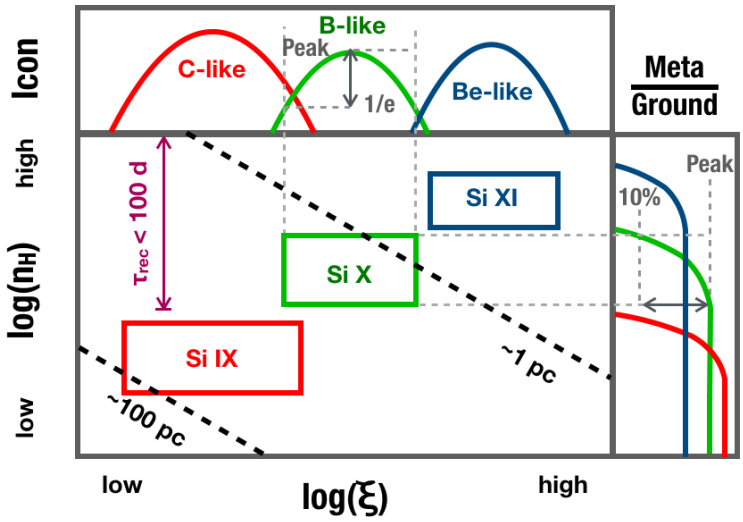

Figure 1.2: A sketch of the domain of density and ionization parameter where metastable absorption lines can be used for diagnostics in a photoionized plasma. Each box in the main plot corresponds to a certain ion. Within each box, plasma density and ionization parameter can be well constrained. Outside the box, only an upper or lower limit can be obtained. This is because the ion concentration ("Icon" in the upper plot) and the metastable to ground level population ratio (in the right plot) are too low. Dashed lines indicate the distance of the photoionized plasma with respect to the central engine. The limit of the timing analysis for the density measurement is also shown here.

The third approach is a spectral analysis where density sensitive metastable absorption lines are identified. A metastable level has a longer lifetime than ordinary excited levels and a shorter lifetime than the ground level. The line ratio of the metastable to ground absorption lines is determined by the level population ratio of the metastable to ground level, which, in turn, depend on the density of the plasma as the metastable level can be populated via collisional excitation from the ground level (Figures 1.3 and 1.4). This method has been successfully used for absorption lines observed in the UV band (e.g., Arav et al. 2015). In the X-ray band, either upper or lower limits have been obtained for a few AGNs, including Mrk 279 (Kaastra et al. 2004), NGC 4051 (King et al. 2012) and NGC 5548 (Mao et al. 2017b). This approach requires less observational time compared to the timing analysis. But current grating spectrometers on board *XMM-Newton* and *Chandra* lack spectral resolution and effective area to put tight constraints on the density. Future missions like *Arcus* (Smith et al. 2016) are required for such kind of analysis. Note that even if perfect instruments were available, for each ion, its ground and metastable lines can only be detected when the ionization parameter of the plasma falls in a

certain range and when the line ratio of the metastable to ground absorption lines is sensitive to a certain range of plasma densities (Figure 1.2). When all the ions are considered, there are still some uncovered regions in the density and ionization parameter space (Figure 7 in Mao et al. 2017b). Therefore, a timing analysis would be needed as a complementary approach.

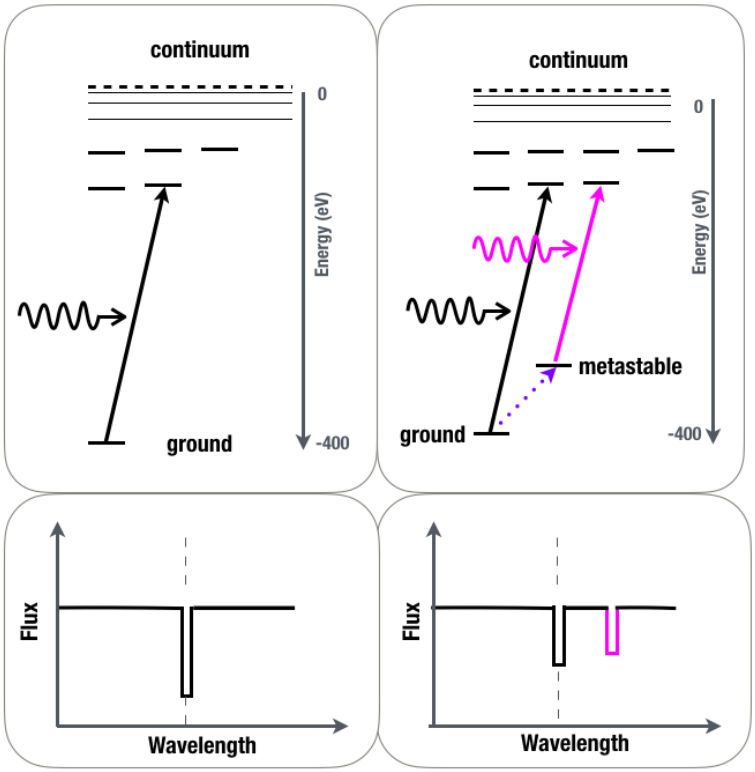

Figure 1.3: A sketch of ground and metastable absorption lines. The metastable level can be populated via collisional excitation from the ground level, thus the line ratio of the metastable to ground absorption lines is sensitive to the density of the plasma. The metastable level can also be populated via cascades from higher levels, but collisional excitation is the dominant process.

Apart from the density/distance of the outflow, there are more open questions concerning the circumnuclear media in active galactic nuclei. For instance, broad and narrow emission lines are observed in optical, UV and sometimes in X-rays, what are the physical properties and geometry of these emission line regions? More importantly, what is the origin of these emission line regions? And do these emission line regions relate to AGN outflows?

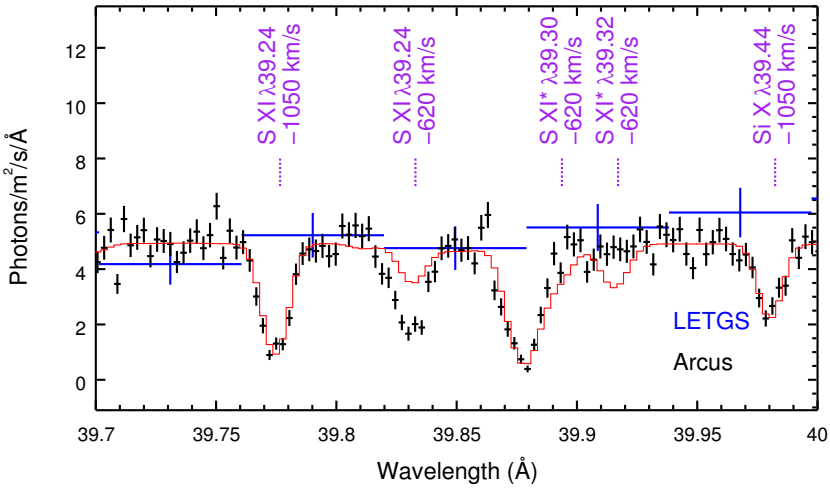

Figure 1.4: Observed *Chandra*/LETGS (in blue, with 345 ks exposure) spectrum of NGC 5548 in the neighbourhood of S XI (39.24 Å in the observed frame) and a 300 ks simulation of the same spectrum with *Arcus*. Two outflow components with different velocities are present here. The red solid line is a model with high density, while the simulated data (in black) corresponds to a lower density scenario. The metastable absorption lines are labelled with $\star$. More details can be found in Kaastra et al. (2017).

1.3. Intracluster media and chemical enrichment

Clusters of galaxies, also known as galaxy clusters, are the largest gravitational bound structures in the Universe. Galaxy clusters usually consist of hundreds to thousands member galaxies[1], with a total mass of 10^{14-15} $M_\odot$. A large fraction ($\sim 15-20$ %) of the total mass forms the hot ($kT \sim 10^{7-8}$ K) and X-ray emitting intracluster medium (ICM), while the visible member galaxies contribute merely $\sim 3-5$ %. The rest is dark matter (Schindler & Diaferio 2008).

Based on the radial temperature profile, galaxy clusters can be divided into two subclasses (Böhringer & Werner 2010): those with temperature profiles decreasing towards the center are called cool core clusters (e.g. NGC 5846 in Figure 1.5); and clusters with no central drop of temperature are called non-cool core clusters. In this thesis, I focus on cool core clusters since their chemical abundances can be relatively well constrained. Their centrally peaked surface brightness profiles are suitable for grating spectrometers like RGS. Due to the deep gravitational potential well, within some sufficient large radius, a relaxed massive cluster can be considered as a "closed-box", namely all the baryons are conserved. This conservation also

[1]Smaller aggregates of galaxies are referred to as groups of galaxies or galaxy groups.

applies to metals in the ICM that are directly observed in X-rays.

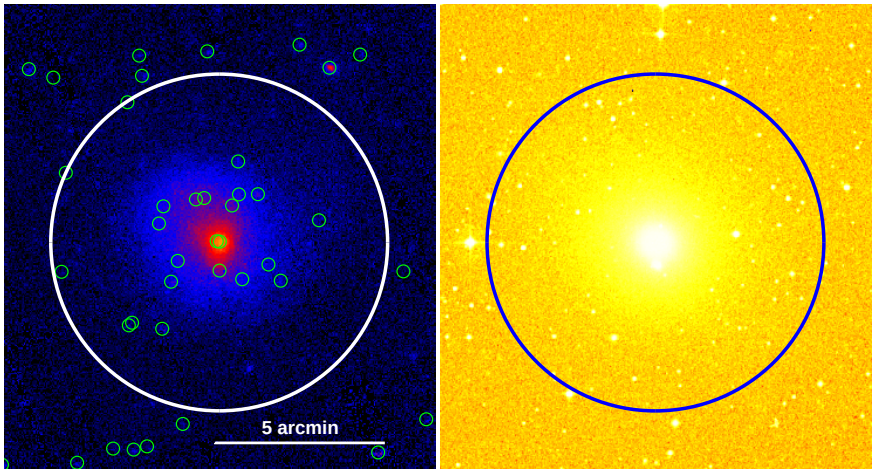

Figure 1.5: *Left*: X-ray image of NGC 5846 from *XMM-Newton*. The small green circles indicate X-ray point sources in the field of view. The white circle has a radius of 5 arcmin. The corresponding physical scale is 36 kpc or $0.1\ r_{500}$, where r_{500} is the radius within which the plasma mass density is 500 times the critical density of the Universe at the redshift of the source. *Right*: Optical image from the Digital Sky Survey (DSS).

Metals in the ICM are originally synthesized by different stellar populations in the member galaxies. Throughout the evolution of the galaxy cluster, different metal transportation mechanisms working on different size-scales and time-scales redistribute these metals from the interstellar medium (ISM) into the ICM (for a review, see Schindler & Diaferio 2008).

Almost every star, except for the least massive ones, contributes to the chemical enrichment of the ICM. Asymptotic giant branch (AGB) stars are low- and intermediate mass stars with $M_* \in (0.9,\ 7)\ \mathrm{M}_\odot$ undergoing the last nuclear burning phase. In this phase, a complex interplay of nucleosynthesis and mixing alters the chemical composition of the stellar atmosphere Karakas (2010). The stellar envelope is enriched with products of hydrogen and helium burning, and heavy elements produced by the slow neutron capture process (i.e., the s process). Metals, especially C and N, are eventually expelled into the ISM via a slow stellar wind.

Massive stars in the mass range of $M_* \in (11,\ 140)\ \mathrm{M}_\odot$ undergo Fe core collapse at the end of their evolution and become Type II and Ib/c supernovae unless the entire star collapses into a black hole with no mass ejection (Nomoto et al. 2013). Hence, core-collapse supernovae (SNcc) products, especially α elements from O to Mg (Figure 1.6), are released into the ISM.

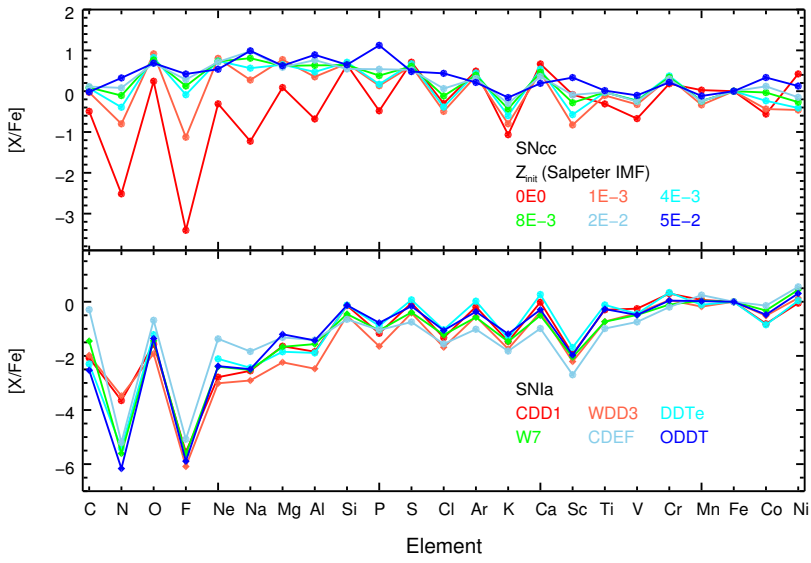

Figure 1.6: *Upper*: IMF weighted yields of core-collapse supernovae (SNcc) with the Salpeter IMF assumed for the progenitor stars. Odd-Z elements like N, Na, and Al are very sensitive to the initial metallicity ($Z_{\rm init}$) of the progenitor stars. *Lower*: Yields of Type Ia supernovae (SNIa) for selective explosion models. Compared to SNcc, elements lighter than Si are significantly less produced by SNIa.

If very massive stars with mass between 140 $\mathrm{M}_\odot$ and 300 $\mathrm{M}_\odot$ do not lose much mass, they undergo thermonuclear explosions triggered by pair-creation instability (PISNe, Barkat et al. 1967). Such events disrupt the progenitors thoroughly without forming a black hole and thus eject a large amount of heavy elements, especially ^{56}Ni (e.g. Heger & Woosley 2002; Umeda & Nomoto 2002) (see also the upper panel of Figure 1.6 with $Z_{\rm init} = 0$).

Degenerate stars in a binary system also contribute to the metal content of the ICM via Type Ia supernovae (SNIa). It is possible that SNIa from different channels (i.e. single- or double-degenerate, super- or sub-Chandrasekhar limit, and deflagration or detonation, Iwamoto et al. 1999; Livio 2000; Maeda et al. 2010) all play a role in the chemical enrichment. SNIa are the main metal factory of Fe-peak elements such as Cr, Mn, Fe and Ni (Figure 1.6).

In many cases, merely the iron abundance in the ICM can be well constrained via the prominent Fe XXVI Lyα and/or Fe XXV He-like triplets. Nonetheless, for bright nearby cool-core clusters, elemental abundances of α elements and Fe-peak elements can be relatively well constrained, especially in terms of abundance ratios

with respect to Fe. These time-integrated abundance ratios are footprints of different enrichment channels (AGBs, SNcc, SNIa).

Assuming that the observed elemental abundances in the ICM are consistent ($\lesssim 20$ %) with the proto-solar abundance (Lodders & Palme 2009), Figure 1.7 illustrates a possible scenario of the chemical enrichment of the ICM. Under a standard Salpeter (Salpeter 1955) initial mass function (IMF, $\xi(M_\star) \propto M_\star^{-2.35}$), progenitor stars with initial metallicity $Z_{\rm init} = 0.008$ enrich C and N mainly via the AGB channel, with a minor contribution from the core-collapse supernovae (SNcc) channel. On the contrary, the enrichment of O to Al is dominated by SNcc. The number of low- and intermediate massive stars (progenitors of AGBs) that contribute to the enrichment with respect to the total number of AGBs and SNcc progenitors is large, $r^{\rm li} = 87 \pm 18$. For elements heavier than Al, Type Ia supernovae start to play a role. In this exercise, we assume the WDD3[2] model (Iwamoto et al. 1999) for SNIa. The number fraction of SNIa ($f^{\rm Ia}$) with respect to the total number of SNIa and SNcc that contributes to the enrichment is (22.3 ± 2.1) %.

From the observational point of view, it is not trivial to interpret the chemical enrichment of the ICM. First, imperfect instruments can also lead to biased abundances. For instance, the European Photon Imaging Camera on board *XMM-Newton* has two sets of CCD (charge-coupled device) arrays: pn and mos. The Ni abundance in the ICM measured by pn and mos can differ up to 60 % (e.g. Figure 6 in Mernier et al. 2016a). The next generation of instruments, like the Soft X-ray Spectrometer (SXS), a calorimeter type of spectrometer, on the *Hitomi* satellite can certainly improve the accuracy of the abundance measurement (Hitomi Collaboration et al. 2017a).

Second, imperfect plasma models can also lead to an incorrect abundance determination. For instance, as shown in de Plaa et al. (2017), inaccurate radiative recombination data implemented in the plasma model can lead to biased O/Fe ratio up to 50 %. Even the state-of-the-art atomic codes can lead to different abundance measurements (Hitomi Collaboration et al. 2017b). More accurate atomic data and plasma models are definitely required.

Third, stellar yields of AGBs, SNcc and SNIa are also not perfect. Current stellar yields are more accurate for elements (e.g. C, N, O, Mg, Si and Fe) observed in optical in galactic chemical evolution studies (e.g., Romano et al. 2010). The accuracy on the yields table of other elements like Ne, P, Ar, and K needs to be

[2] A delayed-detonation explosion scenario with the deflagration to detonation density of 3×10^7 g cm^{-3}, readers are refer to Iwamoto et al. (1999) for more details.

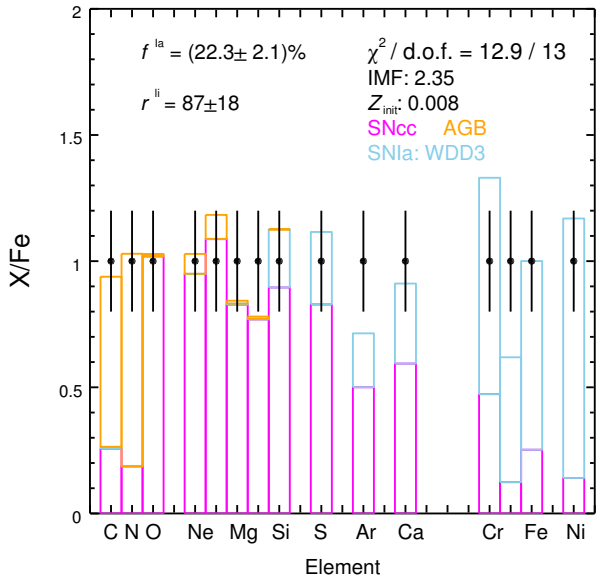

Figure 1.7: Illustration of chemical enrichment. The data points correspond to solar abundance with artificial 20% measurement uncertainties. Metals are enriched via AGBs, SNcc and SNIa. The initial mass function (IMF) of the stellar progenitors is assumed to be follow a power law $\propto M_\star^{-\alpha}$ with $\alpha = 2.35$ (Salpeter 1955). The initial metallicity ($Z_{\rm init}$) of the stellar population is 0.008. The number of low- and intermediate massive stars (progenitors of AGBs) that contributes to the enrichment with respect to the total number of AGBs and SNcc progenitors $r^{\rm li} = 87 \pm 18$. The WDD3 model (Iwamoto et al. 1999) is assumed here for the enrichment by SNIa. The number of SNIa that contribute to the enrichment with respect to the total number of SNIa and SNcc $f^{\rm Ia} = (22.3 \pm 2.1)\%$.

checked with observations in X-ray and/or optical.

There are more questions to be addressed for future studies: (1) Whether the IMF and/or initial metallicity is universal? (2) What is the role of hypernova in chemical enrichment? (3) What is the role of pre-enrichment by fast rotating very massive stars via stellar winds? (4) How does chemical enrichment evolve over cosmic time?

1.4. Plasma code and atomic data

Evidently, a suitable plasma code is the prerequisite of interpreting the observed high-resolution X-ray spectra with physical models. Only a handful of plasma codes are available (see also Kaastra et al. 2008, for a review):

1. The SPEX spectral fitting package[3] (Kaastra et al. 1996) has evolved from work by Mewe et al. in 1970s, including the MEKAL (named after MEwe, KAastra & Liedahl) code. The latest version is v3.04. Readers are referred to Section 1 of the SPEX manual[4] for a detailed timeline from MEKAL to the latest version of SPEX. Plasma models provided by SPEX cover various astrophysical scenarios, such as collisional ionization equilibrium in stellar coronae and intracluster media, photoionization equilibrium around black holes, non-equilibrium ionization in supernova remnant and charge exchange recombination at the interface between hot and cold plasmas.

2. AtomDB (Atomic DataBase)[5] is an atomic database useful for X-ray plasma spectral modeling. It includes APEC (Astrophysical Plasma Emission Code Smith et al. 2001), which has evolved originally from the work by Raymond & Smith (1977) for collisional ionization equilibrium, as well as NEI for non-equilibrium ionization. The latest version is v3.0.9. Note that APEC and NEI codes are used through spectral fitting packages like XSPEC (Arnaud 1996).

3. XSTAR[6] is a code for calculating the physical conditions and emission spectra of photoionized plasmas. It has evolved from the early work by Kallman & McCray (1982) and the latest version is v2.39.

4. Cloudy[7] is a code for simulating conditions in interstellar matter under a broad range of conditions, including photoionization equilibrium and collisional ionization equilibrium. The latest version (v17.00) was released in 2017 (Ferland et al. 2017).

5. CHIANTI[8] (named after the wine region near Firenze Landi et al. 2006) has evolved from early work by Landini & Monsignori Fossi (1970), focusing on solar spectral analysis. The package performs collisional ionization equilibrium calculation and the latest version is v8.0 (Del Zanna et al. 2015).

All these codes require an extensive atomic database covering relevant atomic processes such as collisional ionization, photoionization, radiative recombination, dielectronic recombination, charge exchange recombination, collisional (de-)excitation,

[3] https://www.sron.nl/astrophysics-spex
[4] http://var.sron.nl/SPEX-doc/manualv3.04.00.pdf
[5] http://www.atomdb.org/
[6] https://heasarc.gsfc.nasa.gov/lheasoft/xstar/xstar.html
[7] http://www.nublado.org/
[8] http://www.chiantidatabase.org/

and bremsstrahlung, etc. The leading concern is that incomplete and imperfect atomic data/code can lead to inaccurate plasma diagnostics, thus influencing our understanding of the Universe. Another issue is that code developers need to find the balance among evergrowing atomic data (tens of gigabytes at the moment) and computation time.

Over the past few years, the SPEX development team has made significant updates to atomic data and code for all built-in plasma models. Gu et al. (2016) introduced the new charge exchange model (CX). Mehdipour et al. (2016) described the updated the photoionization model (PION) and compared it to other population photoionization codes. Mao & Kaastra (2016, i.e., **Chapter 2**) and Mao et al. (2017a, i.e., **Chapter 3**) updated the radiative recombination related data, Urdampilleta et al. (2017) updated the inner-shell ionization data and revised accordingly the charge stage distribution of the collisional ionization equilibrium (CIE). Mao et al. (2017b, i.e., **Chapter 4**) demonstrated how the updated photoionization model (PION) allows density diagnostics with metastable absorption lines in Be-like to C-like isoelectronic sequences. Kaastra et al. (2017) highlighted the astrophysical applications of the updated plasma code in the context of the current and future generation of X-ray spectroscopy observatories.

Nonetheless, there are unresolved issues. Spectra that contain Fe XVII emission features, for instance, are poorly fitted even with the best collisional ionization plasma models (Bernitt et al. 2012). A significant portion of atomic data of many-electron ions (e.g. O-like isoelectronic sequence) are still lacking in the updated atomic database of the SPEX code.

1.5. This thesis

This thesis includes publications where I did the majority of the work and writing. All the coauthors have reviewed, discussed and commented on the manuscripts. In particular, prof. dr. N. R. Badnell made important contribution on publishing his AUTOSTRUCTURE and ADASRR codes and providing some insights to his code in Chapter 3. In Chapters 4 to 6, prof. dr. J. S. Kaastra and dr. M. Mehdipour made important contributions on leading the multi-wavelength observational proposals as primary investigators and reducing the data. In Chapter 7, dr. J. de Plaa is the primary investigator of *XMM-Newton* proposal and dr. F. Mernier contributed on the EPIC abundance measurements of NGC 5044. A full list of publications is available as the penultimate part of this thesis.

This thesis starts with updates of radiative recombination data in the spectral

analysis package SPEX, where various plasma models are built on a single atomic database. The updated plasma models are then used to better understand the physics of circumnuclear media and the nitrogen enrichment in the intracluster media.

Radiative recombination (RR) is a fundamental atomic process where a positively charged ion captures a free electron to one of its bound orbits. A photon is emitted during the process with its energy equal to the kinetic energy of the free electron plus the binding energy of the newly-recombined electron. Since the kinetic energy is not quantized, this forms a continuous emission. Furthermore, the newly-recombined electron can lead to line emission via cascades to the ground level.

Previously, the RR rate coefficients (i.e., the electron capture rates per ion) in SPEX were approximated with a power law. In **Chapter 2**, I propose a slightly more complicated math function, which matches much better ($\lesssim 5\%$) the state-of-the-art RR rate coefficients (Badnell 2006). While the RR rate coefficients are available, the associated electron energy loss rates are lacking, except for H-like ions and He I. The total electron energy loss rates due to RR are required to solve the thermal equilibrium in photoionized plasma modeling. Therefore, in **Chapter 3**, I update the AUTOSTRUCTURE and ADASRR codes (Badnell 2006) to calculate detailed electron energy loss rates systematically. This is the first time the electron energy loss rates due to RR of He-like to Ne-like ions have been calculated.

For photoionized plasmas, these electron energy loss rates due to radiative recombination are essential for thermal equilibrium calculations, which assume a local balance between the energy gain and loss. A systematic study of density diagnostics using absorption lines from metastable levels is also lacking for photoionized plasmas. Therefore, I carry out such kind of study in **Chapter 4**.

With the self-consistent PhotoIONization (PION) model in the SPEX code, we are able to calculate detailed level populations, including the ground and metastable levels. This enables us to determine under what physical conditions the metastable levels are significantly populated. Observationally, due to the lack of sufficient spectral resolution and limited photon collecting area, density diagnostics of the spectra obtained with the current generation of X-ray spectrometers are not very effective. For instance, I reanalyze the high-resolution grating spectra of NGC 5548 observed with Chandra in January 2002 using a set of PION components to account for the ionized outflow. I derive lower (or upper) limits of plasma density in five out of six PION components based on the presence (or absence) of the metastable

absorption lines. For NGC 5548, it is the first time plasma density of the ionized outflows in X-ray has been constrained using metastable absorption lines. Future missions like *Arcus* (Smith et al. 2016) will allow us to better constrain the density thus the distance and kinetic power of AGN outflows (Kaastra et al. 2017).

Photoionized plasmas in AGN are manifest not only in absorption features but also in emission features, such as the X-ray broad and narrow emission features observed in Seyfert galaxies. It is easier to study the soft X-ray emission features in Seyfert 2 galaxies (e.g., Kinkhabwala et al. 2002, for NGC 1068) because the AGN continuum is blocked by the dusty torus. But there is a growing number of studies of the soft X-ray emission features in Seyfert 1 galaxies, either because the source was caught in a low flux state (e.g., Nucita et al. 2010, for NGC 4051), or due to the newly discovered heavy obscuration of the soft X-ray continuum (Kaastra et al. 2014; Mehdipour et al. 2017).

In **Chapter 5**, the X-ray narrow emission features in the archetypal Seyfert 1 galaxy NGC 5548 are studied. I find that the X-ray narrow emission features in NGC 5548 can be described by a two-phase photoionized plasma with different ionization parameters and kinematics, and no further absorption by the warm absorber components. The X-ray and optical narrow emission line region are most likely the same multi-phase photoionized plasma. The X-ray narrow emission line region is not the counterpart of the UV/X-ray absorber outside the line of sight because their distances and kinematics are not consistent. In short, our understanding of the relations among different circumnuclear media components has been advanced.

Similar to NGC 5548, our *Swift* monitoring programme triggered two joint *XMM-Newton*, *NuSTAR* and HST observations on 11 and 21 December 2016 targeting NGC 3783, as its soft X-ray continuum was also heavily obscured. Consequently, emission features, including the O VII radiative recombination continuum, stand out above the diminished continuum. In **Chapter 6**, I focus on the photoionized emission features in the December 2016 RGS spectra, and compare them to the time-averaged RGS spectrum obtained in 2000–2001 when the continuum was unobscured. Two distinct photoionized components are required to account for the narrow emission features. The narrow emission features are weakly varying between 2000–2001 and December 2016. We also find a statistically significant broad emission component in the time-averaged RGS spectrum in 2000–2001. This broad emission component is significantly less prominent in December 2016. I demonstrate that the weakening might be due to the extra screening by the obscurer, indicating that the obscurer is beyond the X-ray broad-line region.

1

While previous chapters are about photoionized plasma modeling, the last chapter focuses on collisional ionized plasma modeling. The chemical abundance measurement of collisionally ionized plasmas in clusters and groups of galaxies depends on the line emissivity predicted by the plasma model. Therefore, more accurate radiative recombination data lead to more accurate abundance measurement (de Plaa et al. 2017; Mernier et al. 2016a) and thus their origins.

Previous studies (e.g., Mernier et al. 2016b) have established that α elements (e.g., O, Ne, and Mg) are mainly produced in massive stars as they explode as core-collapse supernovae, while the Fe-peak elements (e.g., Cr, Mn, Fe, and Ni) are produced in single- and/or double-degenerate stars as they explode as Type Ia supernovae. In **Chapter 7**, I investigate the nitrogen enrichment in the CHEmical Evolution Rgs Sample of ellipticals, groups and clusters of galaxies. Under a standard initial mass function, low- and intermediate-mass stars are the main metal factory of nitrogen in the hot X-ray halos of groups and clusters of galaxies. In addition, I point out that the initial metallicity of stellar populations is more sensitive to abundances of odd-Z elements (N, Na, and Al). Future missions like the X-ray Astronomy Recovery mission (*XARM*) are required to have accurate abundances of these elements.

References

Arav, N., Chamberlain, C., Kriss, G. A., et al. 2015, A&A, 577, A37
Arnaud, K. A. 1996, in Astronomical Society of the Pacific Conference Series, Vol. 101, Astronomical Data Analysis Software and Systems V, ed. G. H. Jacoby & J. Barnes, 17
Badnell, N. R. 2006, ApJS, 167, 334
Barkat, Z., Rakavy, G., & Sack, N. 1967, Physical Review Letters, 18, 379
Bennert, N., Jungwiert, B., Komossa, S., Haas, M., & Chini, R. 2006a, A&A, 459, 55
Bennert, N., Jungwiert, B., Komossa, S., Haas, M., & Chini, R. 2006b, A&A, 456, 953
Bernitt, S., Brown, G. V., Rudolph, J. K., et al. 2012, Nature, 492, 225
Böhringer, H. & Werner, N. 2010, A&A Rev., 18, 127
Brinkman, A. C., Gunsing, C. J. T., Kaastra, J. S., et al. 2000, ApJ, 530, L111
Canizares, C. R., Davis, J. E., Dewey, D., et al. 2005, PASP, 117, 1144
Collinge, M. J., Brandt, W. N., Kaspi, S., et al. 2001, ApJ, 557, 2
de Plaa, J., Kaastra, J. S., Werner, N., et al. 2017, A&A, 607, A98
Del Zanna, G., Dere, K. P., Young, P. R., Landi, E., & Mason, H. E. 2015, A&A, 582, A56
den Herder, J. W., Brinkman, A. C., Kahn, S. M., et al. 2001, A&A, 365, L7
Ebrero, J., Kaastra, J. S., Kriss, G. A., et al. 2016, A&A, 587, A129
Fabian, A. C. 2012, ARA&A, 50, 455
Ferland, G. J., Chatzikos, M., Guzmán, F., et al. 2017, , 53, 385
Gu, L., Kaastra, J., & Raassen, A. J. J. 2016, A&A, 588, A52

Haardt, F. & Maraschi, L. 1991, ApJ, 380, L51
Haardt, F. & Maraschi, L. 1993, ApJ, 413, 507
Heger, A. & Woosley, S. E. 2002, ApJ, 567, 532
Hitomi Collaboration, Aharonian, F., Akamatsu, H., et al. 2017a, Nature, 551, 478
Hitomi Collaboration, Aharonian, F., Akamatsu, H., et al. 2017b, ArXiv e-prints
Iwamoto, K., Brachwitz, F., Nomoto, K., et al. 1999, ApJS, 125, 439
Kaastra, J. S., Detmers, R. G., Mehdipour, M., et al. 2012, A&A, 539, A117
Kaastra, J. S., Gu, L., Mao, J., et al. 2017, Journal of Instrumentation, 12, C08008
Kaastra, J. S., Kriss, G. A., Cappi, M., et al. 2014, Science, 345, 64
Kaastra, J. S., Mewe, R., & Nieuwenhuijzen, H. 1996, in UV and X-ray Spectroscopy of Astrophysical and Laboratory Plasmas, ed. K. Yamashita & T. Watanabe, 411–414
Kaastra, J. S., Paerels, F. B. S., Durret, F., Schindler, S., & Richter, P. 2008, Space Sci. Rev., 134, 155
Kaastra, J. S., Raassen, A. J. J., Mewe, R., et al. 2004, A&A, 428, 57
Kallman, T. R. & McCray, R. 1982, ApJS, 50, 263
Karakas, A. I. 2010, MNRAS, 403, 1413
Kellermann, K. I., Sramek, R., Schmidt, M., Shaffer, D. B., & Green, R. 1989, AJ, 98, 1195
King, A. L., Miller, J. M., & Raymond, J. 2012, ApJ, 746, 2
King, A. R. & Pounds, K. A. 2003, MNRAS, 345, 657
Kinkhabwala, A., Sako, M., Behar, E., et al. 2002, ApJ, 575, 732
Kormendy, J. & Ho, L. C. 2013, ARA&A, 51, 511
Koshida, S., Minezaki, T., Yoshii, Y., et al. 2014, ApJ, 788, 159
Krolik, J. H., McKee, C. F., & Tarter, C. B. 1981, ApJ, 249, 422
Landi, E., Del Zanna, G., Young, P. R., et al. 2006, ApJS, 162, 261
Landini, M. & Monsignori Fossi, B. C. 1970, A&A, 6, 468
Livio, M. 2000, in Type Ia Supernovae, Theory and Cosmology, ed. J. C. Niemeyer & J. W. Truran, 33
Lodders, K. & Palme, H. 2009, Meteoritics and Planetary Science Supplement, 72, 5154
Maeda, K., Röpke, F. K., Fink, M., et al. 2010, ApJ, 712, 624
Maiolino, R. & Rieke, G. H. 1995, ApJ, 454, 95
Mao, J. & Kaastra, J. 2016, A&A, 587, A84
Mao, J., Kaastra, J., & Badnell, N. R. 2017a, A&A, 599, A10
Mao, J., Kaastra, J. S., Mehdipour, M., et al. 2017b, A&A, 607, A100
Mason, K. O., Breeveld, A., Much, R., et al. 2001, A&A, 365, L36
McKernan, B., Yaqoob, T., George, I. M., & Turner, T. J. 2003, ApJ, 593, 142
Mehdipour, M., Kaastra, J. S., Kriss, G. A., et al. 2017, A&A, 607, A28
Mehdipour, M., Kaastra, J. S., Kriss, G. A., et al. 2016, A&A, 588, A139
Mernier, F., de Plaa, J., Pinto, C., et al. 2016a, A&A, 592, A157
Mernier, F., de Plaa, J., Pinto, C., et al. 2016b, A&A, 595, A126
Nandra, K., Barret, D., Barcons, X., et al. 2013, ArXiv e-prints
Netzer, H. 2015, ARA&A, 53, 365
Nicastro, F., Fiore, F., Perola, G. C., & Elvis, M. 1999, ApJ, 512, 184
Nomoto, K., Kobayashi, C., & Tominaga, N. 2013, ARA&A, 51, 457
Nucita, A. A., Guainazzi, M., Longinotti, A. L., et al. 2010, A&A, 515, A47
Osterbrock, D. E. 1981, ApJ, 249, 462
Padovani, P., Alexander, D. M., Assef, R. J., et al. 2017, A&A Rev., 25, 2

Peterson, B. M., Ferrarese, L., Gilbert, K. M., et al. 2004, ApJ, 613, 682
Porquet, D., Dubau, J., & Grosso, N. 2010, Space Sci. Rev., 157, 103
Raymond, J. C. & Smith, B. W. 1977, ApJS, 35, 419
Romano, D., Karakas, A. I., Tosi, M., & Matteucci, F. 2010, A&A, 522, A32
Salpeter, E. E. 1955, ApJ, 121, 161
Schindler, S. & Diaferio, A. 2008, Space Sci. Rev., 134, 363
Schmidt, M. 1963, Nature, 197, 1040
Schurch, N. J., Warwick, R. S., Griffiths, R. E., & Kahn, S. M. 2004, MNRAS, 350, 1
Seyfert, C. K. 1943, ApJ, 97, 28
Silva, C. V., Uttley, P., & Costantini, E. 2016, A&A, 596, A79
Smith, R. K., Abraham, M. H., Allured, R., et al. 2016, in Proc. SPIE, Vol. 9905, Space Telescopes and Instrumentation 2016: Ultraviolet to Gamma Ray, 99054M
Smith, R. K., Brickhouse, N. S., Liedahl, D. A., & Raymond, J. C. 2001, ApJ, 556, L91
Strüder, L., Briel, U., Dennerl, K., et al. 2001, A&A, 365, L18
Takahashi, T., Mitsuda, K., Kelley, R., et al. 2014, in Proc. SPIE, Vol. 9144, Space Telescopes and Instrumentation 2014: Ultraviolet to Gamma Ray, 914425
Tarter, C. B., Tucker, W. H., & Salpeter, E. E. 1969, ApJ, 156, 943
Umeda, H. & Nomoto, K. 2002, ApJ, 565, 385
Urdampilleta, I., Kaastra, J. S., & Mehdipour, M. 2017, A&A, 601, A85
Weedman, D. W. 1973, ApJ, 183, 29

2

Parameterization of the level-resolved radiative recombination rate coefficients for the SPEX code

Junjie Mao & J. S. Kaastra

The level-resolved radiative recombination (RR) rate coefficients for H-like to Na-like ions from H ($Z = 1$) up to and including Zn ($Z = 30$) are studied here. For H-like ions, the quantum-mechanical exact photoionization cross sections for nonrelativistic hydrogenic systems are used to calculate the RR rate coefficients under the principle of detailed balance, while for He-like to Na-like ions, the archival data on ADAS are adopted. Parameterizations are made for the direct capture rates in a wide temperature range. The fitting accuracy is better than 5% for about 99% of the $\sim 3 \times 10^4$ levels considered here. The $\sim 1\%$ exceptions include levels from low-charged many-electron ions, and/or high-shell ($n \gtrsim 4$) levels, which are less important in terms of interpreting X-ray emitting astrophysical plasmas. The RR data are incorporated into the X-ray spectral analysis package SPEX.

This chapter has been published in Astronomy & Astrophysics, 2016, 587, A84.

2.1. Introduction

Some astrophysical plasmas, for instance, the intracluster medium (ICM), are generally not in local temperature equilibrium (LTE). To determine the ionization state of these plasmas, the individual collisional and radiative ionization and recombination processes need to be considered in great detail. The recombination processes can be divided into three subclasses: (resonant) dielectronic recombination (DR), (nonresonant) radiative recombination (RR), and charge-exchange recombination (CXR). Generally speaking, DR is the dominant recombination process for hot plasmas compared with RR for most ions (Bryans et al. 2009). On the other hand, when the temperature of the plasma is low enough for neutral atoms, molecules, and ions to co-exist, CXR can be a process that competes with DR (Arnaud & Rothenflug 1985). Nevertheless, RR cannot be ignored at least in some temperature ranges in terms of the total recombination rate. In addition, knowledge of the level-resolved RR rate coefficient is required to calculate the emission line spectrum of astrophysical plasmas, for instance, the collisional ionization equilibrium (CIE) spectrum and the radiative recombination spectrum (Tucker & Gould 1966).

In Sect. 2.2 we briefly summarize the main points of the previous studies on RR data, focusing on the parameterizations for the total RR rates. In Sect. 2.3 we show the details of the numerical approaches to derive the RR rate coefficients for H-like ions. Subsequently, in Sect. 2.4, we describe to which extent the archival data on ADAS are analyzed for He-like to Na-like ions. Details of the fitting strategy are shown in Sect. 2.5. Results of the parameterizations, available in CDS, are discussed in Sect. 2.6.

2.2. Historical background

Key issues for atomic data are always how precisely the analytical and/or numerical calculations can be made, and how to parameterize the data for a full description, yet in a quick and accurate way.

The SPEX (Kaastra et al. 1996) code, aiming at interpreting high-energy resolution X-ray spectra, allows users to make fast (all the calculations are run on the fly) yet adequately accurate analyses, including spectral fitting, plotting, and diagnostic output of the astrophysical plasma. Driven by the practical user experience, the number of mathematical operations used and atomic data storage for the complete description of the basic atomic processes need to be minimized. The SPEX code makes great efforts to parameterize the detailed atomic data as best possible. The

parameterization of the level-resolved RR rate coefficients is one of them.

Previously, only the total RR rates were parameterized, and we briefly summarize them here. To begin with, pioneering work was done by Seaton (1959). With the asymptotic expansion of the Gaunt factor, the photoionization cross sections (PICSs) of the hydrogenic ions were derived. And then the total RR rates are fitted with

$$\begin{aligned} \alpha_{\rm ttl}^{\rm RR}(T) &= 5.197\times10^{-14}\ Z\ \lambda^{-1/2}\ (0.4288+0.5\ \ln\lambda \\ &\quad +0.469\ \lambda^{-1/3})\ {\rm cm}^3\ {\rm s}^{-1}\ , \end{aligned} \tag{2.1}$$

where $\lambda = Z^2\frac{E_{\rm H}}{kT}$, Z is the atomic number, and $E_{\rm H}$ is the Rydberg unit of energy.

Aldrovandi & Pequignot (1973) calculated the radiative recombination data for the non-hydrogenic ions of He, C, N, O, Ne, Mg, Si, and S by using the ground-state PICSs from literature and extrapolating along the isoelectronic sequences. Furthermore, a power-law (PL) fitting function for the total RR rates was proposed,

$$\alpha_{\rm ttl}^{\rm RR}(T) = A\ T_4^{-\eta}\ , \tag{2.2}$$

where A and η are the fitting parameters, and T_4 is the electron temperature in units of 10^4 K. The PL model was subsequently also favored by Shull & van Steenberg (1982), Arnaud & Rothenflug (1985), Landini & Monsignori Fossi (1990) and Landini & Fossi (1991).

Pequignot et al. (1991) took advantage of the latest references available at that time for the ground states and part of the excited states ($n = 2$ or 3) of PICSs, as well as the proper extrapolation and scaling law (analogy with the hydrogenic ions). RR data for H, He, C, N, O, and Ne ions were obtained. The total RR rates were fitted with the following expression:

$$\alpha_{\rm ttl}^{\rm RR}(T) = 10^{-13}\ Z\ \frac{a\ t^b}{1+c\ t^d}\ {\rm cm}^3\ {\rm s}^{-1}\ , \tag{2.3}$$

where $t = T_4/Z^2$ and Z is the ionic charge ($Z = 1$ for recombination toward the neutral state).

Using the Hartree-Fock wave functions, the standard partial PICSs for subshells (nl) up to $5g$ of He-like through Al-like ions were provided by Clark et al. (1986). Based on this important progress, Arnaud & Raymond (1992) calculated the RR data of $\rm Fe^{+14}$ through $\rm Fe^{+25}$. The total RR rates of these iron ions in the temperature range of $10^5 - 10^8$ K were described (with a fitting accuracy better than 5%) by a log parabola function

$$\alpha_{\rm ttl}^{\rm RR}(T) = A\ T_4^{-\alpha-\beta\ \log T_4}\ , \tag{2.4}$$

where A, α and β are the fitting parameters. Additionally, Mazzotta et al. (1998) summarized the RR data mentioned above, and more importantly, updated the ionization balance for optically thin plasmas by collecting all the available ionization and recombination (RR + DR) data.

Verner et al. (1996) extended the calculation of RR data for recombination toward H-like, He-like, Li-like, and Na-like ions for all the elements from H up to and including Zn. For the PICSs of the ground states of He-like, Li-like, and Na-like ions, the latest results provided by Verner & Ferland (1996) were adopted. For those of the excited states with $n \leq 5$ of the highly ionized (at least five times) species, the partial PICSs of Clark et al. (1986) were used. To calculate excited states with $n \leq 10$ of the first four ionization states, correction for incomplete shielding (Gould 1978) was required. The hydrogenic approximation was used for the remaining states. We note that a comparison with the Opacity Project (OP) calculations (Seaton et al. 1992) were made, and the conclusion was that the accuracy is better than 10%. The fitting model used for the total RR rates in the temperature range from 3 K to 10^{10} K is

$$\alpha_{\rm ttl}^{\rm RR}(T) = a\left[\sqrt{\frac{T}{T_0}}\left(1+\sqrt{\frac{T}{T_0}}\right)^{1-b}\left(1+\sqrt{\frac{T}{T_1}}\right)^{1+b}\right]^{-1}, \tag{2.5}$$

where a, b, T_0, and T_1 are the fitting parameters.

Gu (2003) used a distorted-wave approximation, similar to the Dirac-Hartree-Slater model used in Verner et al. (1993), to calculate the detailed PICSs with $n \leq 10$ for bare through F-like isoelectronic sequences of Mg, Si, S, Ar, Ca, Fe, and Ni. For $n > 10$ shells the semiclassical Kramers formula was used. The computational procedure of the flexible atomic code (FAC, Gu 2003), which provides not only RR data but also other important atomic data, is similar to the fully relativistic distorted-wave method of Zhang (1998). Based on the fitting model given by Verner et al. (1996), Gu (2003) used a modified expression to fit the total RR rates in the temperature range from 10^{-4} to 10^{4} eV, that is, 10 K to 10^{8} K. Compared to Eq. (2.5), one necessary modification is that for some elements (e.g., F-like Mg, O-like Mg, F-like Si) parameter b is replaced by $b + b_1 \exp(T_2/T)$, which means that two more parameters b_1 and T_2 are required. The fitting accuracy is within 5% throughout the entire temperature range.

? used the AUTOSTRUCTURE code (Badnell 1986; Badnell & Seaton 2003) to calculate PICSs, thus the RR data, for all the elements up to and including Zn, plus Kr, Mo, and Xe, for all the isoelectronic sequences up to Na-like forming Mg-like in

the temperature range of $Z^2(10^1 - 10^7)$ K, where Z is the atomic number. Similar to Gu (2003), Badnell (2006) adopted Eq. (2.5) to fit the total RR rates. Likewise, the additional fitting parameters $b_1$and T_2 are also required for some of the low-charge ions because of the highly nonhydrogenic screening of the wave functions for the low–nl states in low-charged many-electron ions. The fits are accurate to within 5% for singly and doubly ionized ions, and better than 1% for multiply charged ions.

In addition, Nahar and coworkers, for example, Nahar (1999), obtained the total (unified DR + RR) rate coefficients for various ions with their *R*-matrix calculations. Meanwhile, adopting most recent RR and DR calculations, Bryans et al. (2006) updated the collisional ionization equilibrium for optically thin plasmas.

Throughout the entire analysis, we refer to the recombined ion when we speak of the radiative recombination of a certain ion.

2.3. RR rate coefficients for H-like ions

2.3.1. Photoionization cross sections

For the hydrogen sequence, the archival data on ADAS are ready to use, with fully $nLSJ$ resolved RR rate coefficients complete up to n = 8. With the calculation details described below, we completed the rate coefficients for all the levels up to n=16.

The time-reversed process of (dielectronic and radiative) recombination is (resonant and non-resonant) photoionization (PI). Therefore, in turn, radiative recombination cross sections (RRCSs) can be obtained through the Milne relation under the principle of detailed balance (or microscopic reversibility) for PICSs. The exact PICS for nonrelativistic hydrogenic systems can be obtained with the quantum mechanical treatment provided by Storey & Hummer (1991, SH91). Their FORTRAN code, based on recursion techniques, yields accurate, stable, and fast numerical evaluations of bound-free PICSs (and bound-bound electron dipole transition probability) for nonrelativistic hydrogenic systems with n up to 500. Apparently, PICSs of hydrogenic systems can also be precisely calculated with the AUTOSTRUCTURE (Badnell 1986) code.

When PICSs ($\sigma^{\rm PI}_{n(l)}$) are available, RRCSs ($\sigma^{\rm RR}_{n(l)}$, which refers to recombination to the nth shell or to the subshell nl, respectively) can be obtained through the Milne relation under the principle of detailed balance.

Alternatively, if only the total RR rates ($\alpha^{\rm RR}_{\rm ttl}$) are needed, since the numerical Maxwellian convolution of the RR rates to $n \geq 100$ shells are computationally ex-

pensive, the semiclassical Kramers formula of the RRCS can be used instead to save computational time, similar to the approach presented by Gu (2003).

2.3.2. Radiative recombination data

The $n(l)$-resolved radiative recombination rate coefficients $R_{n(l)}$ can then be calculated by

$$R_{n(l)} = \int_0^\infty v_e f(v_e) \sigma^{\rm RR}_{n(l)}(v_e) dv_e \ {\rm cm^3\ s^{-1}}\ , \tag{2.6}$$

where $f(v_e)$ is the probability density distribution of the velocity of the free electrons, and the Maxwell-Boltzmann distribution for the free electrons is adopted in the following calculation. Accordingly, the total radiative recombination rate

$$\alpha^{\rm RR}_{\rm ttl} = \sum_n R_n\ . \tag{2.7}$$

We note that the level-resolved RR rate coefficients can be obtained through the term-resolved RR rate coefficients

$$R_{\rm lev} = \frac{(2J+1)}{(2S+1)(2L+1)} R_{nl}\ , \tag{2.8}$$

where L is the angular momentum quantum number, S is the spin quantum number, and for H-like ions $S = 1/2$, and J is the total angular momentum quantum number. This distribution (Eq. 2.8) agrees with the ADAS term-resolved (LS coupling) and level-resolved (intermediate coupling) RR rate coefficients of the hydrogenic systems with $n <= 8$.

2.4. RR rate coefficients for He-like to Na-like ions

For RR rate coefficients of He-like to Na-like ions, the archival RR data of ADAS were used. We note that there are two sets of RR data for each ion: the one calculated with LS coupling is term-resolved (or nLS resolved), while the other, calculated with intermediate coupling, is level-resolved (or $nLSJ$ resolved). Only the level-resolved data are analyzed here. Moreover, the ADAS RR data (both LS and intermediate coupling) cover not only radiative recombinations from the ground state of the recombining ion but also from meta-stable states. Even more complicated, the ground state is not necessarily identical to the ground level. For C-like to F-like ions, there are fine-structure levels within the ground term of the recombining ion. For F-like ions, for example, the ground term is ($1s^2 2s^2 2p^4,\ ^3P$), and accordingly, the fine-structure levels are $^3P_2$ (the ground level), $^3P_0$ and $^3P_1$. The RR rate coefficients from the excited fine-structure levels are lower than those from the ground level

as a result of the additional auto-ionization pathways (Badnell 2006). We here only carried out the parameterization for RR from the ground level of the recombining ion.

Additionally, all the levels were coded according to intrinsic level indices of SPEX. The advantage is that a set of group numbers are included to distinguish (by different group numbers) those levels with the exact same $nLSJ$ quantum numbers and slightly different configuration for many-electron ions. For instance, for O-like ions, the electron configuration of $1s^2 2s^2 2p^3 (^2P)\ np$ (where $n \geq 3$) has a ^1P term, where ^2P in the parenthesis denotes the coupling of the $2p^3$ electron configuration, but also the electron configuration of $1s^2 2s^2 2p^3 (^2D) np$.

2.5. Fitting strategy

For the hydrogenic systems, the RR data are calculated (following SH91) in a wide temperature grid ranging from 10^1 to 10^8 K, with ten steps per decade on a $\log_{10}$-scale. At even higher temperature $T > 10^8$ K, in principle, relativistic effects for the large-Z elements should be taken into account. However, differences that are due to relativistic effects may not play an important role because the RR rate coefficients at high temperature are lower than those at low temperature, and more importantly, lower than the rate coefficients of other processes at high temperature. Therefore, when the RR data for $T > 10^8$ K are not calculated, extrapolation to $T > 10^8$ K should be feasible. For the He-like to Na-like ions, the temperature sets in $z^2(10^1 - 10^7)$ K on ADAS were used, where z is the nuclear charge of the recombining ion.

Sherpa[1] was used for the fitting procedure, with its Simplex (i.e., Neldermead) optimization method. We propose the following model function for the fitting:

$$R(T) = 10^{-10}\ \mathrm{cm^3\ s^{-1}}\ a_0\ T^{-b_0 - c_0 \ln T} \left(\frac{1 + a_2 T^{-b2}}{1 + a_1 T^{-b1}} \right), \tag{2.9}$$

where the electron temperature T is in units of eV, $a_{0,\,1}$ and $b_{0,\,1}$ are primary fitting parameters, c_0 and $(a_2,\ b_2)$ are additional fitting parameters. The additional parameters were frozen to zero if they were not used. Furthermore, we constrained b_{0-2} to between -10.0 and 10.0 and c_0 to between 0.0 and 1.0. The initial values of the four primary fitting parameters $a_{0,\,1}$ and $b_{0,\,1}$ were set to unity together with the two additional fitting parameters a_2 and b_2 when these were thawed. Conversely, the initial value of c_0, if it was thawed, was set to either side of its boundary, that is, $c_0 = 0.0$ or $c_0 = 1.0$ (both were performed).

[1] http://cxc.harvard.edu/sherpa/index.html

To estimate the goodness of fit, the fits were performed with a set of artificial relative errors (r). We started with $r = 1.25\%$, followed by increasing r by a factor of two, up to and including 5.0%. The chi-squared statistics adopted here were

$$\chi^2 = \sum_{i=1}^{N} \left(\frac{n_i - m_i}{r\, n_i} \right)^2 , \tag{2.10}$$

where n_i is the ith numerical calculation result and m_i is the ith model prediction (Eq. 2.9).

On the other hand, for the model comparison, the RR data were first fitted with the simplest model (i.e., the three additional parameters were frozen to zero), followed by attempted fits with free c_0 and/or free $(a_2,\ b_2)$. We used the chi-squared distribution for all the fitting statistics, and thawing one additional parameter decreases the degrees of freedom by one; therefore, only if the final statistic (χ^2) improves by at least 2.71, 4.61, or 6.25 for one, two, or three additional free parameter(s) (at a 90% confidence level) is the more complicated model favored. From these attempted fits and considering both the fitting accuracy and simplicity of the model, we determined the best-fit model.

2.6. Results and discussion

2.6.1. Total RR rates

The total RR rates, adding up contributions from $n = 1$ up to $n = 10^4$, for all the H-like ions considered here can be parameterized with Eq. (2.9). This also holds for the total RR rates for He-like to Na-like ions, but no significant improvement can be achieved compared to previous results from Badnell (2006).

2.6.2. Level-resolved RR rate coefficients

The fitting results, available at the CDS, contain the following information: Column 1 lists the isoelectronic sequence number of the recombined ion, Col. 2 gives the atomic number, Cols. 3-9 list the fitting parameters, Cols. 10-12 are the degree of freedom (d.o.f.), the final statistics (χ^2), and the maximum deviation $(\delta_{\max})$. Columns 13-16 indicate the $nLSJ$ quantum numbers, and Col. 17 lists the electron configuration. The fitting accuracy is generally better than 5% with the exceptions described below.

The most inaccurate fitting result $(\delta_{\max} = 5.8\%)$ for the helium sequence captures the free electron to the $(1s\ 6p,\ ^3P_0)$ level to form He-like copper (Cu XXVIII). As for the lithium sequence, the poorest fitting $(\delta_{\max} = 7.2\%)$ is achieved for the

$(1s^2 6s,\ ^2S_{1/2})$ level of Li-like chromium (Cr XXII). In the beryllium sequence, the $(1s^2 2s\ 8s,\ ^1S_0)$ level of the beryllium atom (Be I) deviates most strongly with 7.8%. From the beryllium sequence, the characteristic high-temperature bump for the low-charged many-electron ions is present. In the boron sequence, the poorest fitting is the $(1s^2 2s^2 8s,\ ^2S_{1/2})$ level of the boron atom (B I), with $\delta_{\max} = 12.2\%$. However, the RR to this level is overwhelmingly dominated by other channels within the same $n = 8$ shell, except for the high-temperature end. Nevertheless, at the high-temperature end, the high shell RR rate coefficients are merely a few percent lower than those of the low shell. In this case, for instance, at $T = 1$ keV (or 10^7 K), the rate coefficient to the $n = 8$ shell is lower by a few percent than that of the $n = 2$ shell. Similarly, in the carbon and nitrogen sequences, all the poorly fitted ($\delta_{\max} \gtrsim 10\%$) levels of the carbon atom (C I) and nitrogen atom (N I) are also dominated by other channels within their corresponding shells. Again, similar arguments hold for the oxygen sequence, not only for the poorly fitted high shell levels of the oxygen atom (O I), but also for the poorly fitted high shell ($n \gtrsim 4$) levels from the low-charged many-electron ions of O-like fluorine (F II) and O-like neon (Ne III). As expected, similar results are found in the fluorine sequence for the fluorine atom (F I) and F-like neon (Ne II), in the neon sequence, the neon atom (Ne I) and Ne-like soldium (Na II), in the sodium sequence, the soldium atom (Na I) and Na-like magnesium (Mg II).

The relative ion fractions of all the neutral atoms are negligible ($\lesssim 0.005$) for a CIE plasma with a plasma temperature as low as 5 eV and assuming the ionization balance of Bryans et al. (2009); we highlighted the $\sim 1\%$ poor fits above. While the ion fraction of the low-charged many-electron ions can be ~ 0.6 in this extreme case, only a few tens of the high shell levels (in total for F II, Ne II, Na II, Mg II, Ne III, etc.) are poorly fitted. In general, a CIE plasma, such as the intracluster medium (ICM) with a temperature of ~ 1 keV, does not suffer from the poor fits at all. The situation can be difficult for a non-equilibrium ionization (NEI) plasma or a photoionizied plasma, while emission coming from these poorly fitted levels is either too weak or entirely absent in the X-ray wavelength range. Introducing more parameters might improve the fitting results, but for simplicity, we did not add more parameters. Alternatively, if emission from the full wavelength range is needed or very high accuracy is required, interpolation with the original ADAS data should be adopted.

2.7. Summary

We parameterized for the first time the level-resolved radiative recombination rate coefficients for H-like to Na-like ions from hydrogen up to and including zinc ($Z = 30$) in a wide temperature range. For the the hydrogen sequence, we calculated the RR data with the photoionization cross sections for nonrelativistic hydrogenic systems provided by Storey & Hummer (1991). The fully $nLSJ$-resolved levels are complete up to $n = 16$ for H-like ions. For helium to sodium sequences, the archival data from ADAS (**?**) were adopted, with levels complete up to $n = 8$. The bulk ($\sim 99\%$) of the 3×10^4 levels are fitted with accuracy better than 5%. The $\sim 1\%$ exceptions that yield relative poor fitting accuracy from 5% to 40% is less important in terms of interpreting X-ray emitting astrophysical plasmas.

Together with updated inner shell ionization data (Urdampilleta et al. 2017), a charge-exchange model (Gu et al. 2016) and other atomic data will be included in the upcoming version (3.0) of the X-ray spectral modeling and fitting code SPEX (Kaastra et al. 1996), which will be highly useful once Astro-H/SXS data become available.

References

Aldrovandi, S. M. V. & Pequignot, D. 1973, A&A, 25, 137
Arnaud, M. & Raymond, J. 1992, ApJ, 398, 394
Arnaud, M. & Rothenflug, R. 1985, A&AS, 60, 425
Badnell, N. R. 1986, Journal of Physics B Atomic Molecular Physics, 19, 3827
Badnell, N. R. 2006, ApJS, 167, 334
Badnell, N. R. & Seaton, M. J. 2003, Journal of Physics B Atomic Molecular Physics, 36, 4367
Bryans, P., Badnell, N. R., Gorczyca, T. W., et al. 2006, ApJS, 167, 343
Bryans, P., Landi, E., & Savin, D. W. 2009, ApJ, 691, 1540
Clark, R. E. H., Cowan, R. D., & Bobrowicz, F. W. 1986, Atomic Data and Nuclear Data Tables, 34, 415
Gould, R. J. 1978, ApJ, 219, 250
Gu, L., Kaastra, J., & Raassen, A. J. J. 2016, A&A, 588, A52
Gu, M. F. 2003, ApJ, 589, 1085
Kaastra, J. S., Mewe, R., & Nieuwenhuijzen, H. 1996, in UV and X-ray Spectroscopy of Astrophysical and Laboratory Plasmas, ed. K. Yamashita & T. Watanabe, 411–414
Landini, M. & Fossi, B. C. M. 1991, A&AS, 91, 183
Landini, M. & Monsignori Fossi, B. C. 1990, A&AS, 82, 229
Mazzotta, P., Mazzitelli, G., Colafrancesco, S., & Vittorio, N. 1998, A&AS, 133, 403
Nahar, S. N. 1999, ApJS, 120, 131
Pequignot, D., Petitjean, P., & Boisson, C. 1991, A&A, 251, 680
Seaton, M. J. 1959, MNRAS, 119, 81
Seaton, M. J., Zeippen, C. J., Tully, J. A., et al. 1992, , 23

Shull, J. M. & van Steenberg, M. 1982, ApJS, 48, 95
Storey, P. J. & Hummer, D. G. 1991, Computer Physics Communications, 66, 129
Tucker, W. H. & Gould, R. J. 1966, ApJ, 144, 244
Urdampilleta, I., Kaastra, J. S., & Mehdipour, M. 2017, A&A, 601, A85
Verner, D. A. & Ferland, G. J. 1996, ApJS, 103, 467
Verner, D. A., Ferland, G. J., Korista, K. T., & Yakovlev, D. G. 1996, ApJ, 465, 487
Verner, D. A., Yakovlev, D. G., Band, I. M., & Trzhaskovskaya, M. B. 1993, Atomic Data and Nuclear Data Tables, 55, 233
Zhang, H. L. 1998, Phys. Rev. A, 57, 2640

3

The electron energy loss rate due to radiative recombination

Junjie Mao, J. S. Kaastra, N. R. Badnell

For photoionized plasmas, electron energy loss rates due to radiative recombination (RR) are required for thermal equilibrium calculations, which assume a local balance between the energy gain and loss. While many calculations of total and/or partial RR rates are available from the literature, specific calculations of associated RR electron energy loss rates are lacking. Here we focus on electron energy loss rates due to radiative recombination of H-like to Ne-like ions for all the elements up to and including zinc ($Z = 30$), over a wide temperature range. We used the AUTOSTRUCTURE code to calculate the level-resolved photoionization cross section and modify the ADASRR code so that we can simultaneously obtain level-resolved RR rate coefficients and associated RR electron energy loss rate coefficients. We compared the total RR rates and electron energy loss rates of H I and He I with those found in the literature. Furthermore, we utilized and parameterized the weighted electron energy loss factors (dimensionless) to characterize total electron energy loss rates due to RR. The RR electron energy loss data are archived according to the Atomic Data

This chapter has been published in Astronomy & Astrophysics, 2017, 599, A10.

and Analysis Structure (ADAS) data class *adf48*. The RR electron energy loss data are also incorporated into the SPEX code for detailed modeling of photoionized plamsas.

3.1. Introduction

Astrophysical plasmas observed in the X-ray band can roughly be divided into two subclasses: collisional ionized plasmas and photoionized plasmas. Typical collisional ionized plasmas include stellar coronae (in coronal/collisional ionization equilibrium), supernova remnants (SNRs, in nonequilibrium ionization) and the intracluster medium (ICM). In low-density, high-temperature collisional ionized plasma, for example, ICM, collisional processes play an important role (for a review see e.g., Kaastra et al. 2008). In contrast, in a photoionized plasma, photoionization, recombination and fluorescence processes are important in addition to collisional processes. Both the equations for the ionization balance (also required for a collisional ionized plasma) and the equations of the thermal equilibrium are used to determine the temperature of the photoionized plasma. Typical photoionized plasmas in the X-ray band can be found in X-ray binaries (XRBs) and active galactic nuclei (AGN).

For collisional ionized plasmas, various calculations of total radiative cooling rates are available in the literature, such as Cox & Daltabuit (1971), Raymond et al. (1976), Sutherland & Dopita (1993), Schure et al. (2009), Foster et al. (2012), and Lykins et al. (2013). These calculations take advantage of full plasma codes, such as SPEX (Kaastra et al. 1996) and APEC (Smith et al. 2001), and do not treat individual energy loss (cooling) processes separately. Total radiative cooling rates include the energy loss of both the line emission and continuum emission. The latter includes the energy loss due to radiative recombination (RR). Even more specifically, the energy loss due to RR can be separated into the electron energy loss and ion energy loss.

On the other hand, for photoionized plasmas, the electron energy loss rate due to RR is one of the fundamental parameters for thermal equilibrium calculations, which assume a local balance between the energy gain and loss. Energy can be gained via photoionization, Auger effect, Compton scattering, collisional ionization, collisional de-excitation and so forth. Energy loss can be due to, for example, radiative recombination, dielectronic recombination, three-body recombination, inverse Compton scattering, collisional excitation, and bremsstrahlung, as well as the line/continuum emission following these atomic processes. In fact, the energy loss and gain of all these individual processes need to be known. The calculations of electron energy loss rates due to RR in the Cloudy code (Ferland et al. 1998, 2013) are based on hydrogenic results (Ferland et al. 1992; LaMothe & Ferland 2001). In this manuscript, we focus on improved calculations of the electron energy loss

due to radiative recombination, especially providing results for He-like to Ne-like isoelectronic sequences.

While several calculations of RR rates, including total rates and/or detailed rate coefficients, for different isoelectronic sequences are available, for example, Gu (2003) and Badnell (2006), specific calculations of the associated electron energy loss rate due to RR are limited. The pioneering work was carried out by Seaton (1959) for hydrogenic ions using the asymptotic expansion of the Gaunt factor for photoionization cross sections (PICSs).

By using a modified semiclassical Kramers formula for radiative recombination cross sections (RRCSs), Kim & Pratt (1983) calculated the total RR electron energy loss rate for a few ions in a relatively narrow temperature range.

Ferland et al. (1992) used the nl-resolved hydrogenic PICSs provided by Storey & Hummer (1991) to calculate both n-resolved RR rates ($\alpha_{\rm i}^{\rm RR}$) and electron energy loss rates ($L_{\rm i}^{\rm RR}$). Contributions up to and including $n = 1000$ are taken into account.

Using the same nl-resolved hydrogenic PICSs provided by Storey & Hummer (1991), Hummer (1994) calculated the RR electron energy loss rates for hydrogenic ions in a wide temperature range. In addition, Hummer & Storey (1998) calculated PICSs of He I (photoionizing ion) for $n \leq 25$ with their close-coupling ***R***-matrix calculations. Together with hydrogenic (Storey & Hummer 1991) PICSs for $n > 25$ (up to $n = 800$ for low temperatures), the RR electronic energy loss rate coefficient of He I (recombined ion) was obtained.

Later, **?** used the exact PICSs from the Opacity Project (Seaton et al. 1992) for $n < 30$ and PICSs of **?** for $n \geq 30$ to obtain n-resolved RR electron energy loss rates for hydrogenic ions in a wide temperature range. The authors introduced the ratio of β/α (dimensionless), where $\beta = L/kT$ and L is the RR electron energy loss rate. The authors also pointed out that β/α changes merely by 1 dex in a wide temperature range; meanwhile α and β change more than 12 dex.

In the past two decades, more detailed and accurate calculations of PICSs of many isoelectronic sequences have been carried out (e.g., **?**), which can be used specifically to calculate the electron energy loss rates due to RR.

Currently, in the SPEX code (Kaastra et al. 1996), the assumption that the mean kinetic energy of a recombining electron is $3kT/4$ (Kallman & McCray 1982) is applied for calculating the electron energy loss rate due to RR. Based on the level-resolved PICSs provided by the AUTOSTRUCTURE[1] code (v24.24.3; Badnell 1986), the electron energy loss rates due to RR are calculated in a wide temperature range

[1] http://amdpp.phys.strath.ac.uk/autos/

for the H-like to Ne-like isoelectronic sequences for elements up to and including Zn ($Z = 30$). Subsequently, the electron energy loss rate coefficients ($\beta = L/kT$) are weighted with respect to the total RR rates (α_t), yielding the weighted electron energy loss factors ($f = \beta/\alpha_\mathrm{t}$, dimensionless). The weighted electron energy loss factors can be used, together with the total RR rates, to update the description of the electron energy loss due to RR in the SPEX code or other codes.

In Sect. 4.2, we describe the details of the numerical calculation from PICSs to the electron energy loss rate due to RR. Typical results are shown graphically in Sect. 6.4. Parameterization of the weighted electron energy loss factors is also illustrated in Sect. 3.3.1. The detailed RR electron energy loss data are archived according to the Atomic Data and Analysis Structure (ADAS) data class *adf48*. Full tabulated (unparameterized and parameterized) weighted electron energy loss factors are available in CDS. Comparison of the results for H I and He I can be found in Section 3.4.1. The scaling of the weighted electron energy loss factors with respect to the square of the ionic charge of the recombined ion can be found in Section 3.4.2. We also discuss the electron and ion energy loss due to RR (Section 3.4.3) and the total RR rates (Section 3.4.4).

Throughout this paper, we refer to the recombined ion when we speak of the radiative recombination of a certain ion, since the line emission following the radiative recombination comes from the recombined ion. Furthermore, only RR from the ground level of the recombining ion is discussed here.

3.2. Methods

3.2.1. Cross sections

The AUTOSTRUCTURE code is used for calculating level-resolved nonresonant PICSs under the intermediate coupling ("IC") scheme (Badnell & Seaton 2003). The atomic and numerical details can be found in Badnell (2006); we briefly state the main points here. We use the Slater-type-orbital model potential to determine the radial functions. We calculated PICSs first at zero kinetic energy of the escaping electron. Subsequently, we calculated them on a z-scaled logarithmic energy grid with three points per decade, ranging from $\sim z^2 10^{-6}$ to $z^2 10^2$ ryd, where z is the ionic charge of the photoionizing ion/atom. PICSs at even higher energies are at least several orders of magnitude smaller compared to PICSs at zero kinetic energy of the escaping electron. Nonetheless, it still can be important, especially for the s- and p-orbit, to derive the RR data at the high tem-

perature end. We take advantage of the analytical hydrogenic PICSs (calculated via the dipole radial integral; Burgess 1965) and scale them to the PICS with the highest energy calculated by AUTOSTRUCTURE to obtain PICSs at very high energies. Fully $nLSJ$-resolved PICSs for those levels with $n \leq 15$ and $l \leq 3$ are calculated specifically. For the rest of the levels, we use the fast, accurate and recurrence hydrogenic approximation (Burgess 1965). Meanwhile, bundled-n PICSs for n = 16, 20, 25, 35, 45, 55, 70, 100, 140, 200, 300, 450, 700, and 999 are also calculated specifically to derive the total RR and electron energy loss rates (interpolation and quadrature required as well).

The inverse process of dielectronic and radiative recombination is resonant and nonresonant photoionization, respectively. Therefore, radiative recombination cross sections (RRCSs) are obtained through the Milne relation under the principle of detailed balance (or microscopic reversibility) from nonresonant PICSs.

3.2.2. Rate coefficients

The RR rate coefficient is obtained by

$$\alpha_i(T) = \int_0^\infty v\ \sigma_i(v)\ f(v,\ T)\ dv\ , \tag{3.1}$$

where v is the velocity of the recombining electron, σ_i is the individual detailed (level/term/shell-resolved) RRCS, $f(v,\ T)$ is the probability density distribution of the velocity of the recombining electrons for the electron temperature T. The Maxwell-Boltzmann distribution for the free electrons is adopted throughout the calculation, with the same quadrature approach as described in Badnell (2006). Accordingly, the total RR rate per ion/atom is

$$\alpha_{\rm t}(T) = \sum_i \alpha_i(T)\ . \tag{3.2}$$

Total RR rates for all the isoelectronic sequences, taking contributions up to $n = 10^3$ into account (see its necessity in Section 6.4).

The RR electron energy loss rate coefficient is defined as (e.g., Osterbrock 1989)

$$\beta_i(T) = \frac{1}{kT} \int_0^\infty \frac{1}{2}\ m\ v^3\ \sigma_i(v)\ f(v,\ T)\ dv\ , \tag{3.3}$$

The total electron energy loss rate due to RR is obtained simply by adding all the contributions from individual captures,

$$L_{\rm t}(T) = \sum_i L_i = kT \sum_i \beta_i\ , \tag{3.4}$$

which can be identically derived via

$$L_{\rm t}(T) = kT\ \alpha_{\rm t}(T)\ f_{\rm t}(T)\ , \tag{3.5}$$

where

$$f_{\rm t}(T) = \frac{\sum_i\ \beta_i(T)}{\alpha_{\rm t}(T)}\ , \tag{3.6}$$

is defined as the weighted electron energy loss factor (dimensionless) hereafter.

The above calculation of the electron energy loss rates is realized by adding Equation (3.3) into the archival post-processor FORTRAN code ADASRR[2] (v1.11). Both the level-resolved and bundled-n/nl RR data and the RR electron energy loss data are obtained. The output files have the same format of *adf48* with RR rates and electron energy loss rates in the units of $\rm cm^3\ s^{-1}$ and $\rm ryd\ cm^3\ s^{-1}$, respectively. Ionization potentials of the ground level of the recombined ions from NIST[3] (v5.3) are adopted to correct the conversion from PICSs to RRCSs at low kinetic energy for low-charge ions. We should point out that the level-resolved and bundled-nl/n RR data are, in fact, available on OPEN ADAS[4], given the fact that we use the latest version of the AUTOSTRUCTURE code and a modified version of the ADASRR code, here we recalculate the RR data, which are used together with the RR electron energy loss data to derive the weighted electron energy loss factor $f_{\rm t}$ for consistency. In general, our re-calculate RR data are almost identical to those on OPEN ADAS, except for a few many-electron ions at the the high temperature end, where our recalculated data differ by a few percent. Whereas, both RR data and electron energy loss data are a few orders of magnitude smaller compared to those at the lower temperature end, thus, the above-mentioned difference has negligible impact on the accuracy of the weighted electron energy loss factor (see also in Section 3.4.4).

For all the isoelectronic sequences discussed here, the conventional ADAS 19-point temperature grid $z^2(10-10^7)$ K is used.

3.3. Results

For each individual capture due to radiative recombination, when $kT \ll I$, where I is the ionization potential, the RR electron energy loss rate L_i is nearly identical to $kT\ \alpha_i$, since the Maxwellian distribution drops exponentially for $E_{\rm k} \gtrsim kT$, where $E_{\rm k}$ is the kinetic energy of the free electron before recombination. On the other hand,

[2] http://amdpp.phys.strath.ac.uk/autos/ver/misc/adasrr.f
[3] http://physics.nist.gov/PhysRefData/ASD/ionEnergy.html
[4] http://open.adas.ac.uk/adf48

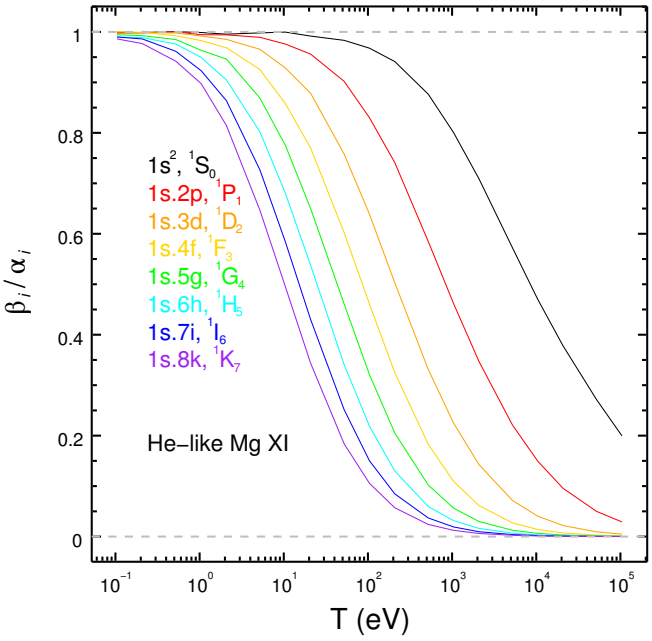

Figure 3.1: For He-like Mg XI, the ratio between level-resolved electron energy loss rates L_i and the corresponding radiative recombination rates times the temperature of the plasma, i.e. β_i/α_i (not be confused with β_i/α_t), where i refers to the $nLSJ$-resolved levels with $n \leq 8$ (shown selectively in the plot).

when $kT \gg I$, the RR electron energy loss rate is negligible compared with $kT\ \alpha_i$. As in an electron-ion collision, when the total energy in the incident channel nearly equals that of a closed-channel discrete state, the channel interaction may cause the incident electron to be captured in this state (Fano & Cooper 1968). That is to say, those electrons with $E_\mathrm{k} \simeq I$ are preferred to be captured, thus, $L_i \sim I\ \alpha_i$. Figure 3.1 shows the ratio of $\beta_i/\alpha_i = L_i/(kT\alpha_i)$ for representative $nLSJ$-resolved levels (with $n \leq 8$) of He-like Mg XI .

In terms of capturing free electrons into individual shells (bundled-n), owing to the rapid decline of the ionization potentials for those very high-n shells, the ionization potentials can be comparable to kT, if not significantly less than kT, at the low temperature end. Therefore we see the significant difference between the top panel (low-n shells) and middle panel (high-n shells) of Figure 3.2. In order to achieve adequate accuracy, contributions from high-n shells (up to $n \leq 10^3$) ought

to be included. The middle panel of Figure 3.2 shows clearly that even for $n = 999$ (the line at the bottom), at the low temperature end, the ratio between $\beta_{n=999}$ and $\alpha_{n=999}$ does not drop to zero. Nevertheless, the bottom panel of Figure 3.2 illustrates the advantage of weighting the electron energy loss rate coefficients with respect to the total RR rates, i.e. $\beta_i/\alpha_{\rm t}$, which approaches zero more quickly. At least, for the next few hundred shells following $n = 999$, their weighted electron energy loss factors should be no more than 10^{-5}, thus, their contribution to the total electron energy loss rate should be less than 1%.

The bottom panels of Figure 3.3 and 3.4 illustrate the weighted electron energy loss factors for He-like isoelectronic sequences (He, Si and Fe) and Fe isonuclear sequence (H-, He-, Be- and N-like), respectively. The deviation from (slightly below) unity at the lower temperature end is simply because the weighted electron energy loss factors of the very high-n shells are no longer close to unity (Figure 3.2, middle panel). The deviation from (slightly above) zero at the high temperature end occurs because the ionization potentials of the first few low-n shells can still be comparable to kT, while sum of these n-resolved RR rates are more or less a few tens of percent of the total RR rates.

Because of the nonhydrogenic screening of the wave function for low-nl states in low-charge many-electron ions, the characteristic high-temperature bump is present in not only the RR rates (see Figure 4 in Badnell 2006, for an example) but also in the electron energy loss rates. The feature is even enhanced in the weighted electron energy loss factor.

3.3.1. Parameterization

We parameterize the ion/atom-resolved radiative recombination electron energy loss factors using the same fitting strategy described in Mao & Kaastra (2016) with the model function of

$$f_{\rm t}(T) = a_0\, T^{-b_0 - c_0 \log T} \left(\frac{1 + a_2 T^{-b2}}{1 + a_1 T^{-b1}}\right), \tag{3.7}$$

where the electron temperature T is in units of eV, a_0 and b_0 are primary fitting parameters, and c_0, $a_{1,\,2}$, and $b_{1,\,2}$ are additional fitting parameters. The additional parameters are frozen to zero if they are not used. Furthermore, we constrain b_{0-2} to be within -10.0 to 10.0 and c_0 between 0.0 and 1.0. The initial values of the two primary fitting parameters a_0 and b_0 are set to unity together with the four additional fitting parameters $a_{1,\,2}$ and $b_{1,\,2}$ if they are thawed. Conversely, the initial value of c_0, if it is thawed, is set to either side of its boundary, i.e., $c_0 = 0.0$

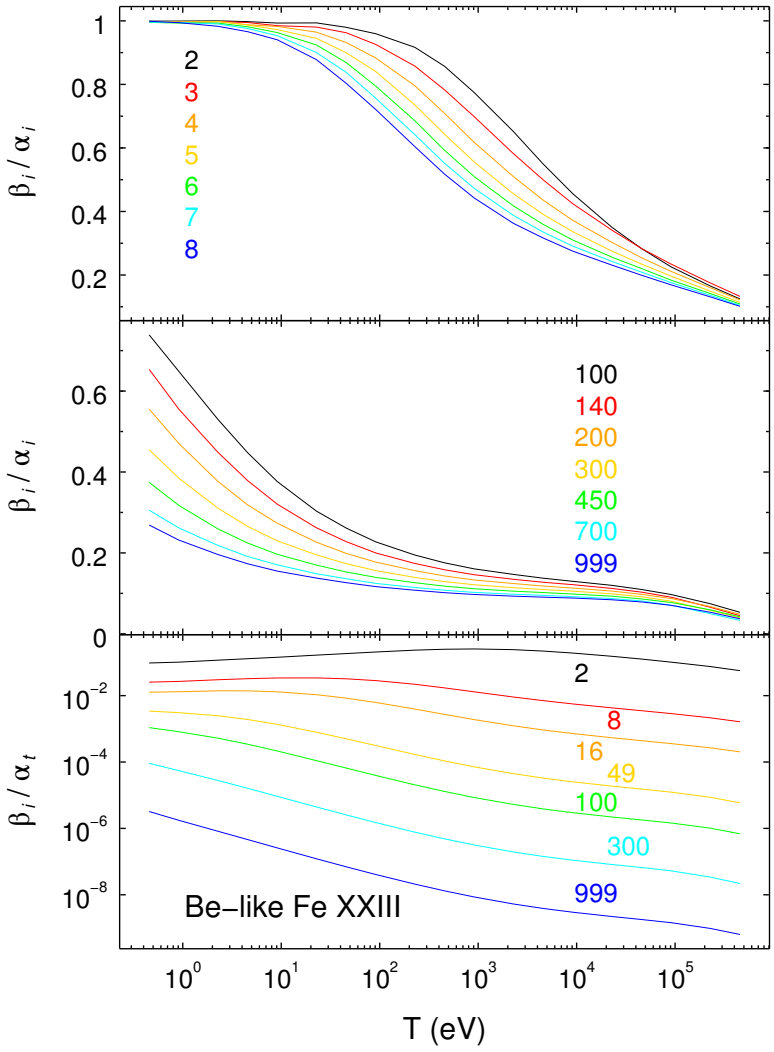

Figure 3.2: Ratios of β_i/α_i for Be-like Fe XXIII (upper and middle panel) and ratios of β_i/α_t (bottom panel), where i refers to the shell number. Low- and high-n shell results are shown selectively in the plot. The upper panel shows all the shells with $n \leq 8$. The middle panel shows shells with n =100, 140, 200, 300, 450, 700, and 999. In the lower panel the shells are n =2, 8, 16, 49, 100, 300, and 999.

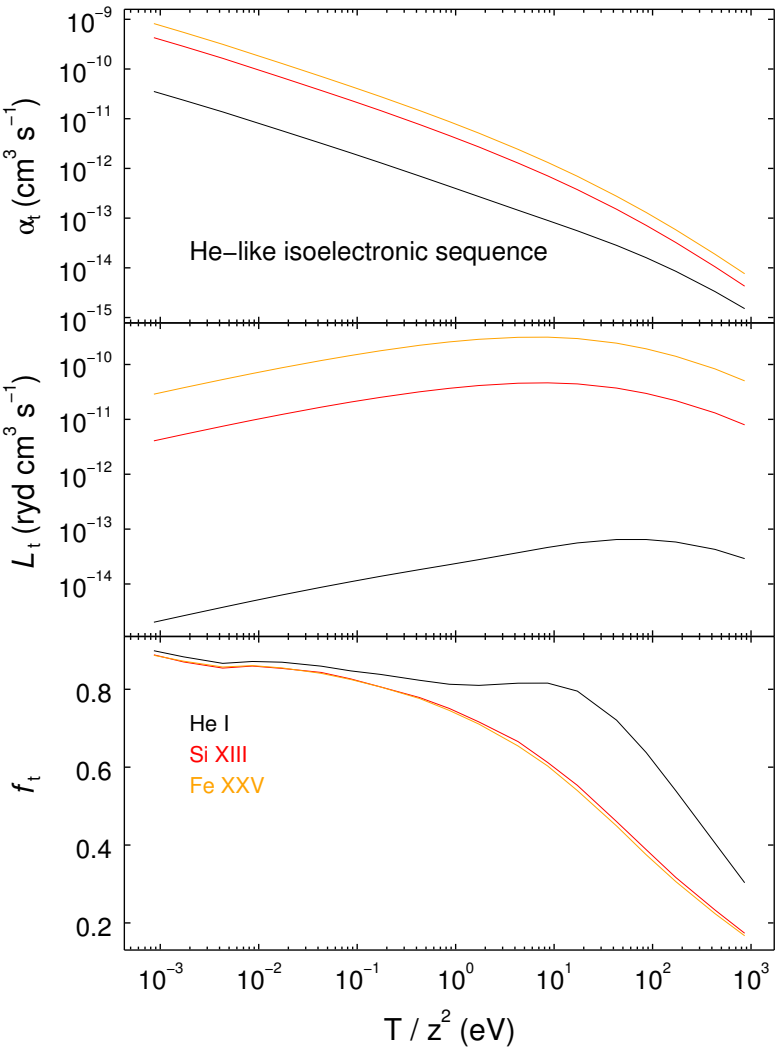

Figure 3.3: Total RR rates α_t (top), electron energy loss rates L_t (middle) and weighted electron energy loss factors f_t (bottom) of He-like isoelectronic sequences for ions, including He I (black), Si XIII (red) and Fe XXV (orange). The temperature is downscaled by z^2, where z is the ionic charge of the recombined ion, to highlight the discrepancy between hydrogenic and nonhydrogenic. The captures to form the He I shows nonhydrogenic feature in the bottom panel.

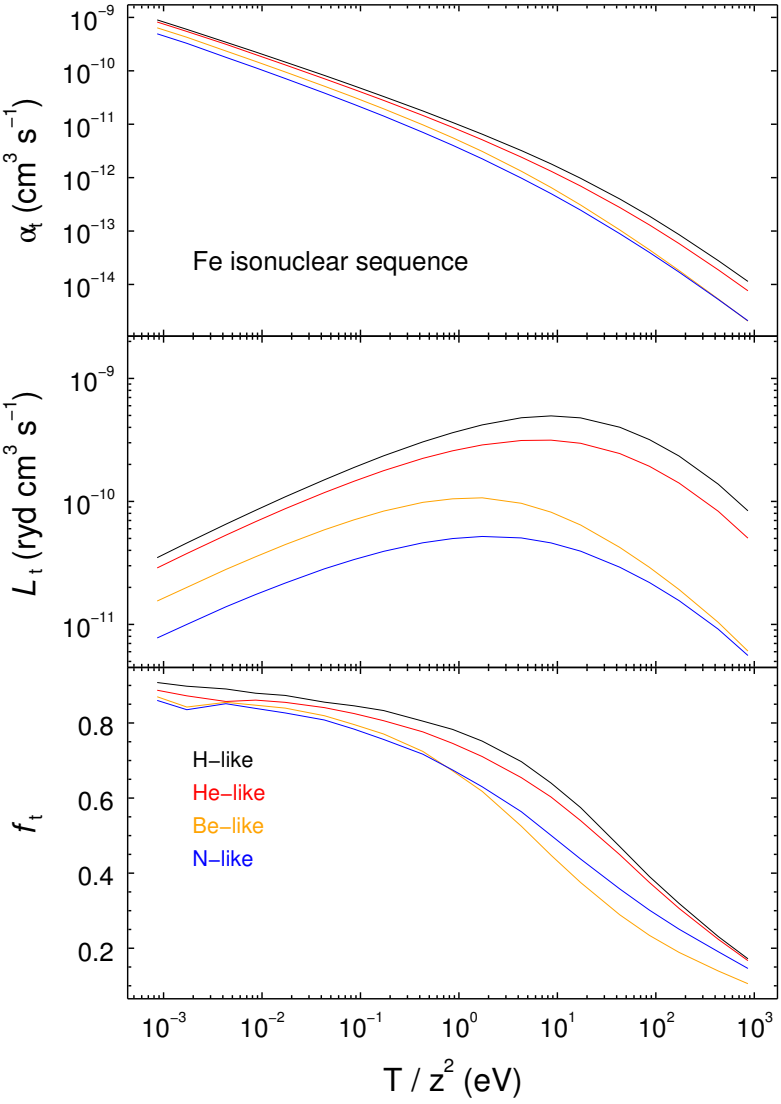

Figure 3.4: Top panel is total RR rates α_t of the Fe isonuclear sequence, including H- (black), He- (red), Be- (orange) and N-like (blue); middle panel is the RR electron energy loss rates L_t; and the bottom panel is the weighted electron energy loss factors f_t. The temperature of the plasma is downscaled by z^2, as in Figure 3.3.

or $c_0 = 1.0$ (both fits are performed).

In order to estimate the goodness of fit, the fits are performed with a set of artificial relative errors (r). We started with $r = 0.625\%$, following with increasing the artificial relative error by a factor of two, up to and including 2.5%. The chi-squared statistics adopted here are

$$\chi^2 = \sum_{i=1}^{N} \left(\frac{n_i - m_i}{r\ n_i} \right)^2 , \tag{3.8}$$

where n_i is the ith numerical calculation result and m_i is the ith model prediction (Equation 3.7).

For the model selection, we first fit the data with the simplest model (i.e. all the five additional parameters are frozen to zero), following with fits with free additional parameters step by step. Thawing one additional parameter decreases the degrees of freedom by one. Thus, the more complicated model is only favored (at a 90% nominal confidence level) if the obtained statistics (χ^2) of this model improves by at least 2.71, 4.61, 6.26, 7.79, and 9.24 for one to five additional free parameter(s), respectively.

Parameterizations of the ion/atom-resolved RR weighted electron energy loss factors for individual ions/atoms in H-like to Ne-like isoelectronic sequences were performed. A typical fit for nonhydrogenic systems is shown in Figure 3.5 for N-like iron (Fe XX). The fitting parameters can be found in Table 3.2. Again, the weighted energy loss factor per ion/atom is close to unity at low temperature end and drops toward zero rapidly at the high temperature end.

In Figure 3.6 we show the histogram of maximum deviation $\delta_{\max}$ (in percent) between the fitted model and original calculation for all the ions considered here. In short, our fitting accuracy is within 4%, and is even accurate ($\lesssim 2.5\%$) for the more important H-like, He-like and Ne-like isoelectronic sequences.

In addition, we also specifically fit for Case A ($f_{\rm A} = \beta_{\rm t}/\alpha_{\rm t}$) and Case B (Baker & Menzel 1938, $f_{\rm B} = \beta_{n\geq 2}/\alpha_{n\geq 2}$) the RR weighted electron energy loss factors of H I (Figure 3.7) and He I (Figure 3.8). Typical unparameterized factors ($f_{\rm A}$ and $f_{\rm B}$) and fitting parameters can be found in Table 3.1 and 3.2, respectively.

3.4. Discussions

3.4.1. Comparison with previous results

Figure 3.9 shows a comparison of RR rates ($\alpha_t^{\rm RR}$), electron energy loss rates ($L_t^{\rm RR}$), weighted electron energy loss factors ($f_t^{\rm RR}$) from this work, Seaton (1959, blue),

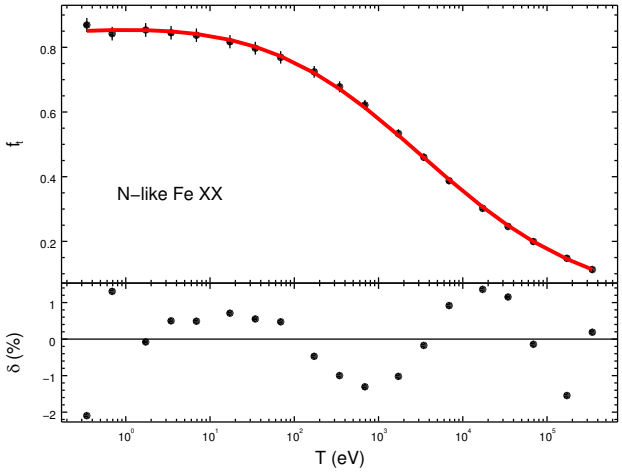

Figure 3.5: Radiative recombination weighted electron energy loss factor for N-like iron (Fe XX). The black dots in both panels (associated with artificial error bars of 2.5% in the upper panel) are the calculated weighted electron energy loss factor. The red solid line is the best fit. The lower panel shows the deviation (in percent) between the best fit and the original calculation.

Table 3.1: Unparameterized of RR weighted electron energy loss factors for H I, He I and Fe XX. For the former two, both Case A and Case B results are treated separately.

T/z^2 K	H I Case A	H I Case B	He I Case A	He I Case B	Fe XX Case A
10^1	0.911	0.895	0.899	0.882	0.869
10^2	0.879	0.851	0.871	0.844	0.845
10^3	0.841	0.786	0.847	0.797	0.797
10^4	0.780	0.668	0.813	0.701	0.678
10^5	0.642	0.470	0.816	0.578	0.460
10^6	0.392	0.268	0.637	0.486	0.246
10^7	0.172	0.123	0.303	0.265	0.113

Notes. Machine readable unparameterized Case A factors for all the ions considered here are available on CDS.

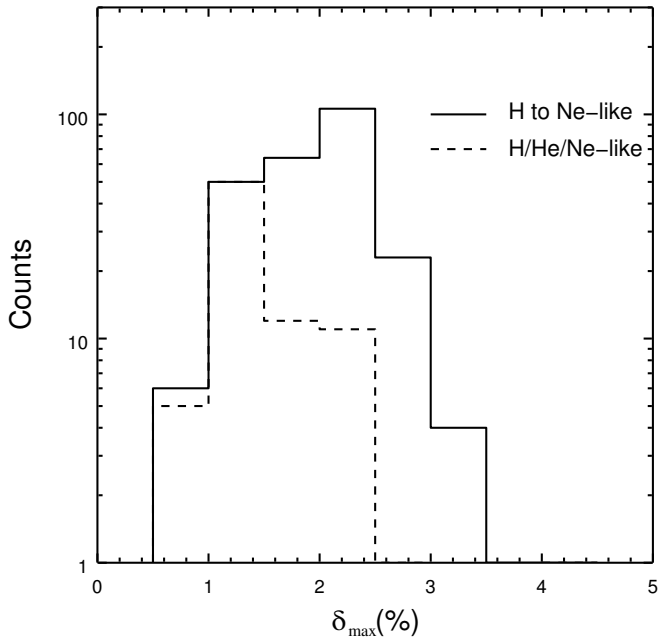

Figure 3.6: Histogram of maximum deviation in percent ($\delta_{\max}$) for all the ions considered here, which reflects the overall goodness of our parameterization. The dashed histogram is the statistics of the more important H-like, He-like and Ne-like isoelectronic sequences, while the solid histogram is the statistics of all the isoelectronic sequences.

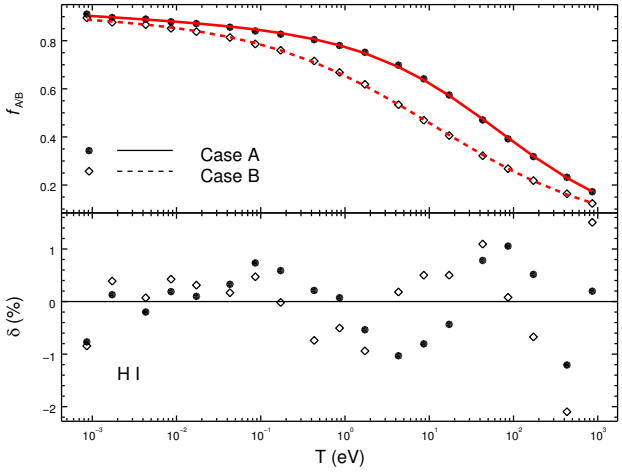

Figure 3.7: Case A (solid line, filled circles) and Case B (dashed line, empty diamonds) RR weighted electron energy loss factor ($f_{\mathrm{A/B}}$) for H I. The black dots in both panels (associated with artificial error bars in the upper one) are the calculated weighted electron energy loss factor. The red solid line is the best fit. The lower panel shows the deviation (in percent) between the best fit and the original calculation.

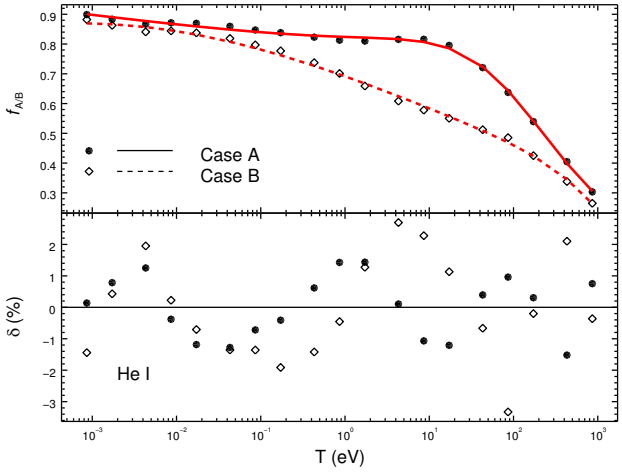

Figure 3.8: Similar to Figure 3.7 but for He I.

Table 3.2: Fitting parameters of RR weighted electron energy loss factors for H I, He I and Fe XX. For the former two, both Case A and Case B results are included.

Ion	H I	H I	He I	He I	Fe XX
Case	A	B	A	B	A
a_0	8.655E+00	2.560E+00	2.354E+00	1.011E+04	2.466E+01
b_0	5.432E-01	4.230E-01	3.367E-01	1.348E+00	4.135E-01
c_0	0.000E+00	0.000E+00	0.000E+00	4.330E-03	0.000E+00
a_1	1.018E+01	2.914E+00	6.280E+01	1.462E+04	2.788E+01
b_1	5.342E-01	4.191E-01	8.875E-01	1.285E+00	4.286E-01
a_2	0.000E+00	0.000E+00	2.133E+01	0.000E+00	0.000E+00
b_2	0.000E+00	0.000E+00	5.675E-01	0.000E+00	0.000E+00
$\delta_{\max}$	1.2%	2.1%	1.5%	3.5%	2.1%

Notes. s is the isoelectronic sequence number of the recombined ion, Z is the atomic number of the ion, a_{0-2}, b_{0-2} and c_0 are the fitting parameters and $\delta_{\max}$ is the maximum deviation (in percent) between the "best-fit" and original calculation. Case A and Case B refers to $\beta_{\rm t}/\alpha_{\rm t}$ and $\beta_{n\geq 2}/\alpha_{n\geq 2}$ RR weighted electron energy loss factors, respectively. Machine readable fitting parameters and maximum deviation (in percent) for the total weighted electron energy loss factors for all the ions considered here are available on CDS.

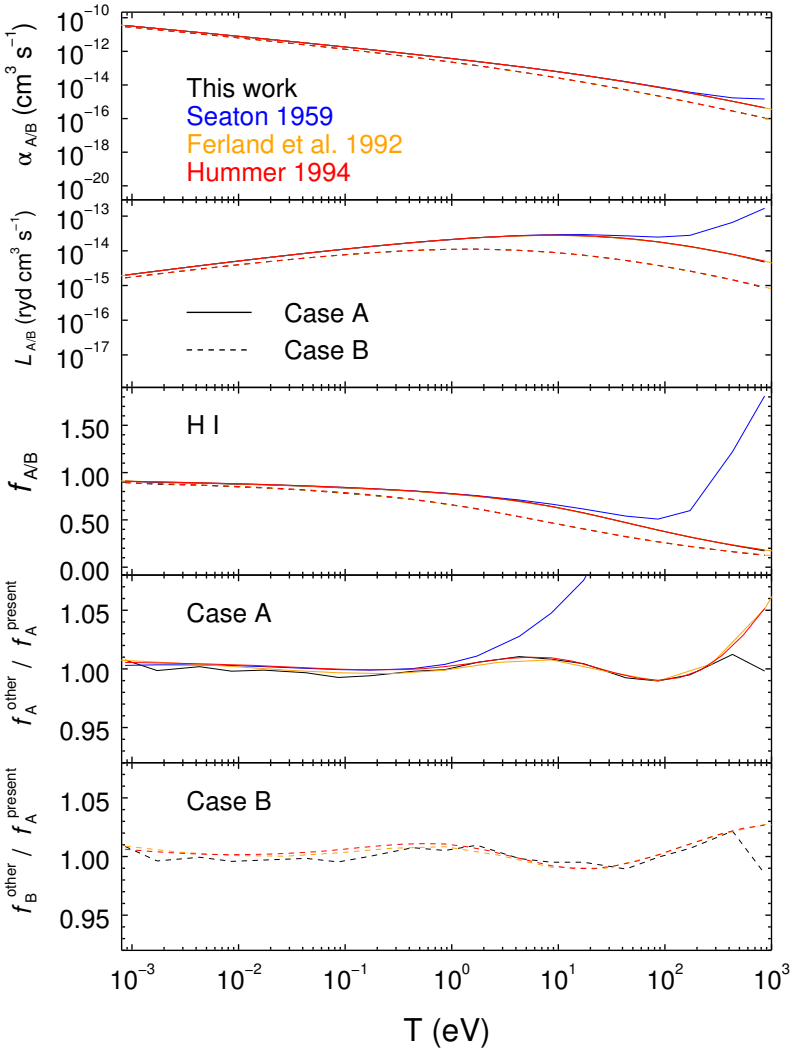

Figure 3.9: Comparison of the RR data for H I among results from this work (black), Seaton (1959, blue), Ferland et al. (1992, orange), and Hummer (1994, red). Both results of case A (solid lines) and case B (dashed lines) are shown. The total RR rates ($\alpha_{\mathrm{A/B}}^{\mathrm{RR}}$) and electron energy loss rates ($L_{\mathrm{A/B}}^{\mathrm{RR}}$) are shown in the top two panels. The RR weighted electron energy loss factors ($f_{\mathrm{A/B}}$) are shown in the middle panel. The ratios of $f_{\mathrm{A/B}}$ from this work and previous works with respect to the fitting results (Equation 3.7 and Table 3.2) of this work, i.e., $f_{\mathrm{A/B}}^{\mathrm{other}}/f_{\mathrm{A/B}}^{\mathrm{present}}$, are shown in the bottom two panels.

Ferland et al. (1992, orange) and Hummer (1994, red). Since both Ferland et al. (1992) and Hummer (1994) use the same PICSs (Storey & Hummer 1991), as expected the two results are highly consistent. The Case A and Case B results of this work are also consistent within 1% at the low temperature end and increase to ~5% (underestimation). For the high temperature end ($T \gtrsim 0.1$ keV), since the ion fraction of H I is rather low (almost completely ionized), the present calculation is still acceptable. A similar issue at the high temperature end is also found in Case A results of Seaton (1959) with a relatively significant overestimation ($\gtrsim 5\%$) from the other three calculations.

Likewise, the comparison for He I between this work and Hummer & Storey (1998) is presented in Figure 3.10. The Case A and Case B results from both calculations agree well (within 2%) at the low temperature end ($T \lesssim 2.0$ eV). At higher temperatures with $T \gtrsim 2$ eV, the RR rate and electron energy loss rate for He I are not available in Hummer & Storey (1998).

3.4.2. Scaling with z^2

In previous studies of hydrogenic systems, Seaton (1959), Ferland et al. (1992), and Hummer & Storey (1998), all use z^2 scaling for $\alpha_{\rm t}^{\rm RR}$. That is to say, $\alpha_{\rm t}^{X} = z^2\ \alpha_{\rm t}^{\rm H}$, where z is the ionic charge of the recombined ion X.The same z^2 scaling also applies for $\beta_{\rm t}^{\rm RR}$ (or $L_{\rm t}^{\rm RR}$). LaMothe & Ferland (2001) also pointed out that the shell-resolved ratio of f_n^{RR} (=$\beta_n^{\rm RR}/\alpha_n^{\rm RR}$) can also be scaled with z^2/n^2, i.e., $f_n^X = \frac{z^2}{n^2}\ f_n^{\rm H}$ where n refers to the principle quantum number.

In the following, we merely focus on the scaling for the ion/atom-resolved data set. In the top panel of Figure 3.11 we show the ratios of f_t/z^2 for H-like ions. Apparently, from the bottom panel of Figure 3.11, the z^2 scaling for the H-like isoelectronic sequence is accurate within 2%. For the rest of the isoelectronic sequences, for instance, the He-like isoelectronic sequence shown in Figure 3.12, the z^2 scaling applies at the low temperature end, whereas, the accuracies are poorer toward the high temperature end. We also show the z^2 scaling for the Fe isonuclear sequence in Figure 3.13.

3.4.3. Radiative recombination continua

We restrict the discussion above to the RR energy loss of the electrons in the plasma. The ion energy loss of the ions due to RR can be estimated as $P^{\rm RR} \sim I_i\ \alpha_i$, where I_i is the ionization potential of the level/term into which the free electron is captured, and α_i is the corresponding RR rate coefficient. Whether to include the ionization

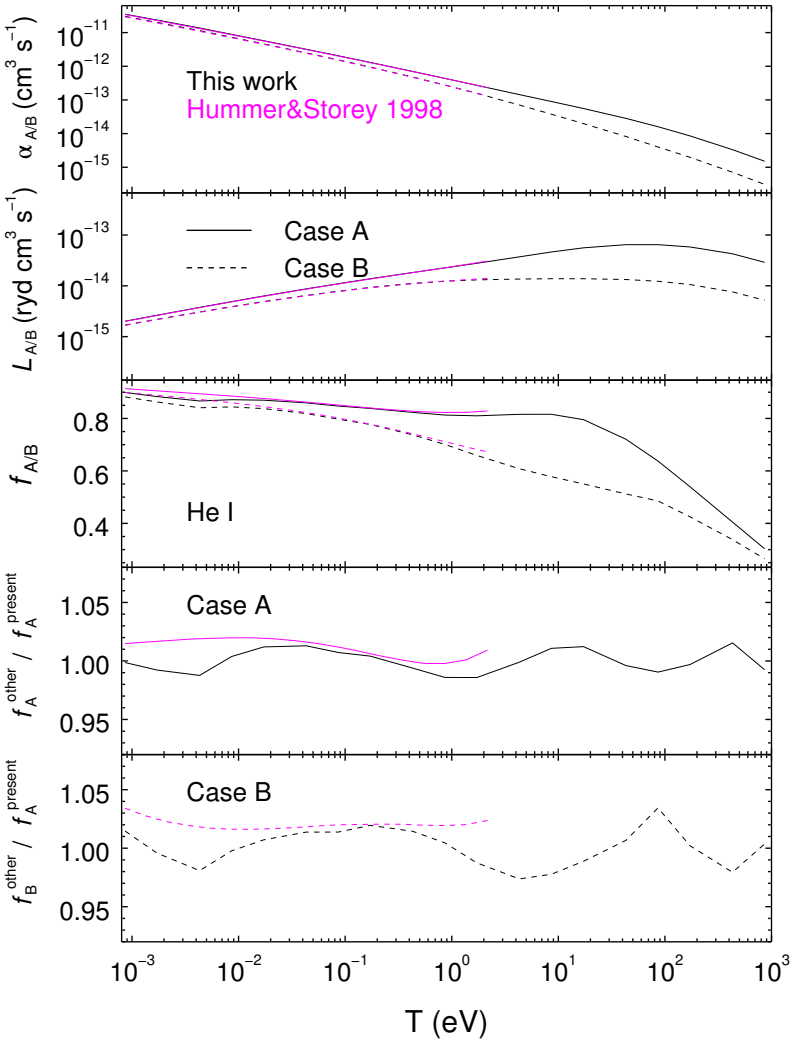

Figure 3.10: Similar to Figure 3.10 but for He I between this work (black) and Hummer & Storey (magenta 1998). The latter only provides data with $T \leq 10^{4.4}$ K.

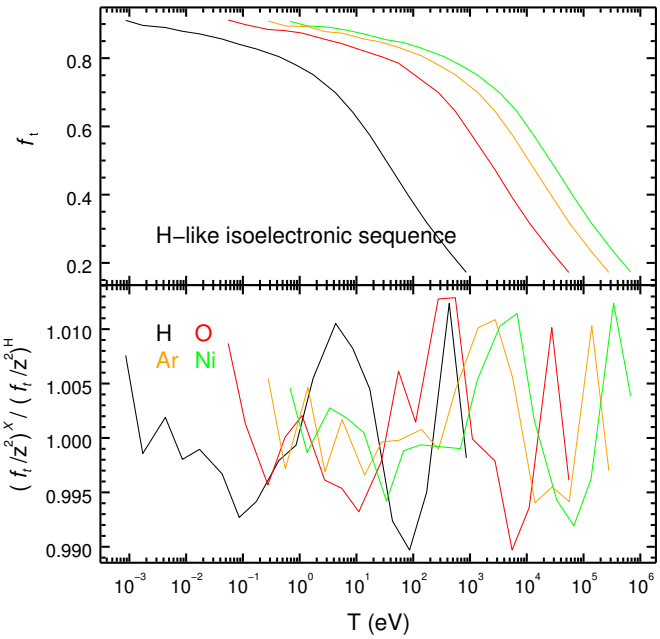

Figure 3.11: z^2 scaling for the H-like isoelectronic sequence (Case A), including H I (black), O VIII (red), Ar XVIII (orange) and Ni XXVIII (green). The top panel shows the ratios of f_t/z^2 as a function of electron temperature (T). The bottom panel is the ratio of $(f_t/z^2)^X$ for ion X with respect to the ratio of $(f_t/z^2)^H$ for H.

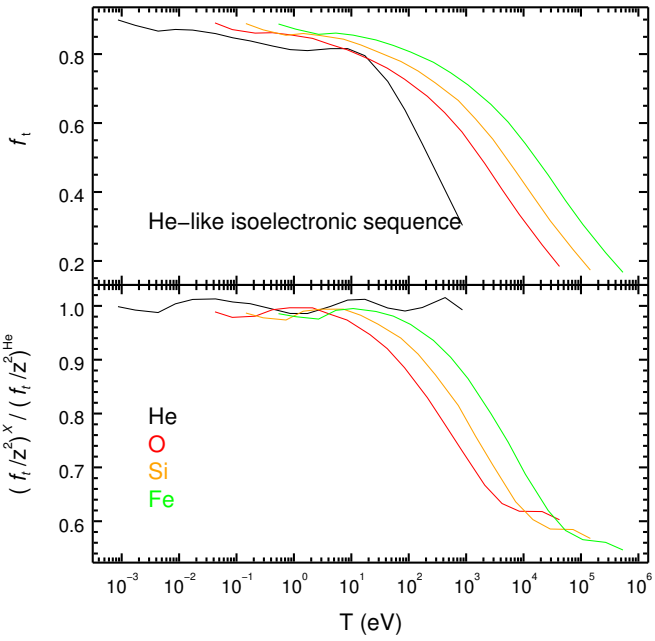

Figure 3.12: Similar to Figure 3.11 but for the z^2 scaling for the He-like isoelectronic sequences.

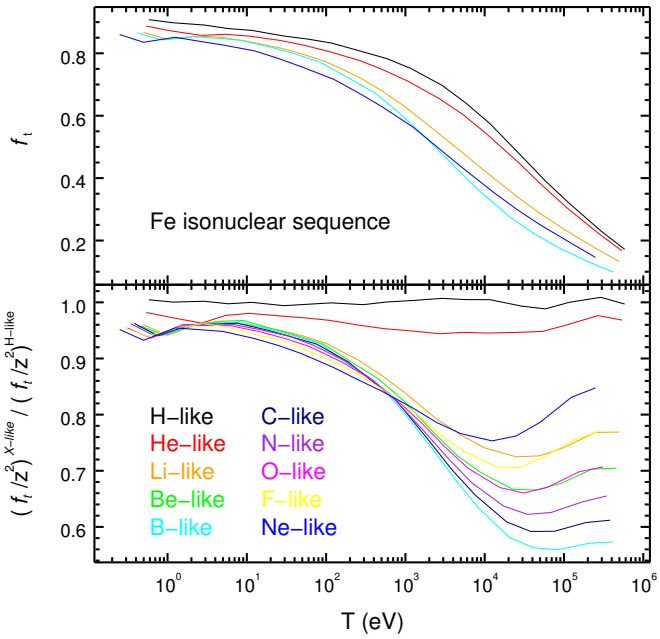

Figure 3.13: z^2 scaling for the Fe isonuclear sequence. The top panel shows the ratios of f_t/z^2 as a function of electron temperature (T). The bottom panel is the ratio of $(f_t/z^2)^{X-\mathrm{like}}$ for X-like Fe with respect to the ratio of $(f_t/z^2)^{\mathrm{H-like}}$ for H-like Fe XXVI.

potential energies as part of the total internal energy of the plasma is not critical as long as the entire computation of the net energy gain/loss is self-consistent (see a discussion in Gnat & Ferland 2012). On the other hand, when interpreting the emergent spectrum due to RR, such as the radiative recombination continua (RRC) for a low-density plasma, the ion energy loss of the ion is essentially required. The RRC emissivity (Tucker & Gould 1966) can be obtained via

$$\begin{aligned} \frac{dE^{\rm RRC}}{dt\ dV} &= \int_0^\infty n_{\rm e}\ n_{\rm i} \left(I + \frac{1}{2}mv^2\right) v\ \sigma(v)\ f(v,\ kT) dv \\ &= n_{\rm e}\ n_{\rm i} I\ (1 + f_{\rm t}\ kT/I)\ \alpha_{\rm t}\ , \end{aligned} \tag{3.9}$$

where $n_{\rm e}$ and $n_{\rm i}$ are the electron and (recombining) ion number density, respectively. Generally speaking, the ion energy loss of the ion dominates the electron energy loss of the electrons, since $f_{\rm t}$ is on the order of unity while $kT \lesssim I$ holds for those X-ray photoionizing plasmas in XRBs (Liedahl & Paerels 1996), AGN (Kinkhabwala et al. 2002) and recombining plasmas in SNRs (Ozawa et al. 2009). Figure 3.14 shows the threshold temperature above which the electron energy loss via RR cannot be neglected compared to the ion energy loss. For hot plasmas with $kT \gtrsim 2$ keV, the electron energy loss is comparable to the ion energy loss for $Z > 5$. We emphasize that we refer to the electron temperature T of the plasma here, which is not necessarily identical to the ion temperature of the plasma, in particular, in the nonequilibrium ionization scenario.

3.4.4. Total radiative recombination rate

Various calculations of (total or shell/term/level-resolved) RR data are available from the literature. Historically, different approaches have been used for calculating the total RR rates, including the Dirac-Hartree-Slater method (Verner et al. 1993) and the distorted-wave approximation (Badnell 2006; Gu 2003). Additionally, Nahar and coworkers (e.g., Nahar 1999) obtained the total (unified DR + RR) recombination rate for various ions with their ***R***-matrix calculations. Different approaches can lead to different total RR rates (see a discussion in Badnell 2006) as well as the individual term/level-resolved RR rate coefficients, even among the most advanced ***R***-matrix calculations. Nevertheless, the bulk of the total RR rates for various ions agrees well among each other. As for the detailed RR rate coefficients, and consequently, the detailed RR electron energy loss rate, the final difference in the total weighted electron energy loss factors $f_{\rm t}$ are still within 1%, as long as the difference among different methods are within a few percent and given the fact that each individual RR is $\lesssim 10\%$ of the total RR rate for a certain ion/atom. In other words, although we

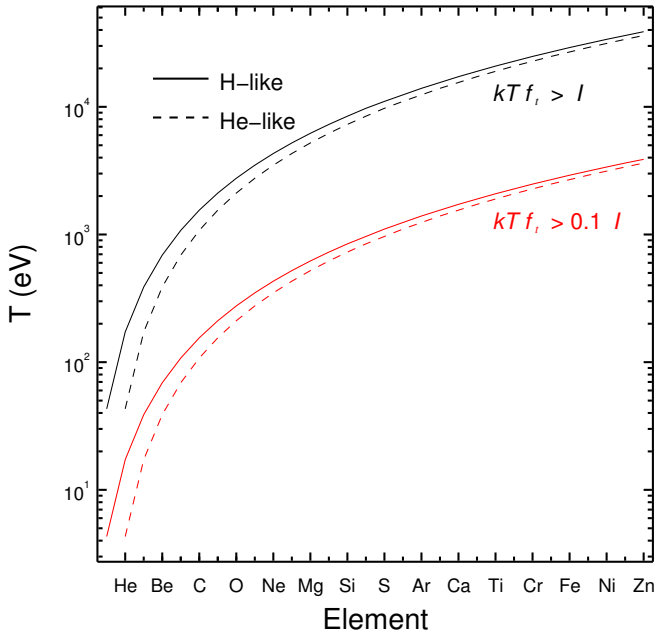

Figure 3.14: Threshold temperature above which the electron energy loss via RR cannot be neglected, compared to the ion energy loss, for H-like (solid lines) and He-like ions (dashed lines).

used the recalculated total RR rate (Section 3.2.2) to derive the weighted electron energy loss factors, we assume these factors can still be applied to other total RR rates.

References

Badnell, N. R. 1986, Journal of Physics B Atomic Molecular Physics, 19, 3827
Badnell, N. R. 2006, ApJS, 167, 334
Badnell, N. R. & Seaton, M. J. 2003, Journal of Physics B Atomic Molecular Physics, 36, 4367
Baker, J. G. & Menzel, D. H. 1938, ApJ, 88, 52
Burgess, A. 1965, MmRAS, 69, 1
Cox, D. P. & Daltabuit, E. 1971, ApJ, 167, 113
Fano, U. & Cooper, J. W. 1968, Reviews of Modern Physics, 40, 441
Ferland, G. J., Korista, K. T., Verner, D. A., et al. 1998, PASP, 110, 761
Ferland, G. J., Peterson, B. M., Horne, K., Welsh, W. F., & Nahar, S. N. 1992, ApJ, 387, 95
Ferland, G. J., Porter, R. L., van Hoof, P. A. M., et al. 2013, , 49, 137
Foster, A. R., Ji, L., Smith, R. K., & Brickhouse, N. S. 2012, ApJ, 756, 128

Gnat, O. & Ferland, G. J. 2012, ApJS, 199, 20
Gu, M. F. 2003, ApJ, 589, 1085
Hummer, D. G. 1994, MNRAS, 268, 109
Hummer, D. G. & Storey, P. J. 1998, MNRAS, 297, 1073
Kaastra, J. S., Mewe, R., & Nieuwenhuijzen, H. 1996, in UV and X-ray Spectroscopy of Astrophysical and Laboratory Plasmas, ed. K. Yamashita & T. Watanabe, 411–414
Kaastra, J. S., Paerels, F. B. S., Durret, F., Schindler, S., & Richter, P. 2008, Space Sci. Rev., 134, 155
Kallman, T. R. & McCray, R. 1982, ApJS, 50, 263
Kim, Y. S. & Pratt, R. H. 1983, Phys. Rev. A, 27, 2913
Kinkhabwala, A., Sako, M., Behar, E., et al. 2002, ApJ, 575, 732
LaMothe, J. & Ferland, G. J. 2001, PASP, 113, 165
Liedahl, D. A. & Paerels, F. 1996, ApJ, 468, L33
Lykins, M. L., Ferland, G. J., Porter, R. L., et al. 2013, MNRAS, 429, 3133
Mao, J. & Kaastra, J. 2016, A&A, 587, A84
Nahar, S. N. 1999, ApJS, 120, 131
Osterbrock, D. E. 1989, Astrophysics of gaseous nebulae and active galactic nuclei
Ozawa, M., Koyama, K., Yamaguchi, H., Masai, K., & Tamagawa, T. 2009, ApJ, 706, L71
Raymond, J. C., Cox, D. P., & Smith, B. W. 1976, ApJ, 204, 290
Schure, K. M., Kosenko, D., Kaastra, J. S., Keppens, R., & Vink, J. 2009, A&A, 508, 751
Seaton, M. J. 1959, MNRAS, 119, 81
Seaton, M. J., Zeippen, C. J., Tully, J. A., et al. 1992, , 23
Smith, R. K., Brickhouse, N. S., Liedahl, D. A., & Raymond, J. C. 2001, ApJ, 556, L91
Storey, P. J. & Hummer, D. G. 1991, Computer Physics Communications, 66, 129
Sutherland, R. S. & Dopita, M. A. 1993, ApJS, 88, 253
Tucker, W. H. & Gould, R. J. 1966, ApJ, 144, 244
Verner, D. A., Yakovlev, D. G., Band, I. M., & Trzhaskovskaya, M. B. 1993, Atomic Data and Nuclear Data Tables, 55, 233

4

Density diagnostics of ionized outflows in active galactic nuclei: X-ray and UV absorption lines from metastable levels in Be-like to C-like ions

Junjie Mao, J. S. Kaastra, M. Mehdipour,
A. J. J. Raassen, Liyi Gu, J. M. Miller

Ionized outflows in active galactic nuclei (AGNs) are thought to influence their nuclear and local galactic environment. However, the distance of the outflows with respect to the central engine is poorly constrained, which limits our understanding of their kinetic power as a cosmic feedback channel. Therefore, the impact of AGN outflows on their host galaxies is uncertain. However, when the density of the outflows is known, their distance can be immediately obtained from their modeled ionization parameters. We perform a theoretical study of density diagnostics of ionized outflows using absorption lines from metastable levels in Be-like to C-like cosmic abundant ions. With the new self-consistent PhotoIONization (PION)

This chapter has been published in Astronomy & Astrophysics, 2017, 607, A100.

model in the SPEX code, we are able to calculate detailed level populations, including the ground and metastable levels. This enables us to determine under what physical conditions the metastable levels are significantly populated. We then identify characteristic lines from these metastable levels in the $1 - 2000$ Å wavelength range.In the broad density range of $n_{\rm H} \in (10^6,\ 10^{20})$ m^{-3}, the metastable levels $2s2p$ ($^3P_{0-2}$) in Be-like ions can be significantly populated. For B-like ions, merely the first excited level $2s^2 2p$ ($^2P_{3/2}$) can be used as a density probe. For C-like ions, the first two excited levels $2s^2 2p^2$ ($^3P_1$ and $^3P_2$) are better density probes than the next two excited levels $2s^2 2p^2$ ($^1S_0$ and $^1D_2$). Different ions in the same isoelectronic sequence cover not only a wide range of ionization parameters, but also a wide range of density values. On the other hand, within the same isonuclear sequence, those less ionized ions probe lower density and smaller ionization parameters. Finally, we reanalyzed the high-resolution grating spectra of NGC 5548 observed with *Chandra* in January 2002 using a set of PION components to account for the ionized outflow. We derive lower (or upper) limits of plasma density in five out of six PION components based on the presence (or absence) of the metastable absorption lines. Once atomic data from N-like to F-like ions are available, combined with the next generation of spectrometers that cover both X-ray and UV wavelength ranges with higher spectral resolution and larger effective areas, tight constraints on the density and thus the location and kinetic power of AGN outflows can be obtained.

4.1. Introduction

Active galactic nucleus outflows may play an important role in cosmic feedback (see, e.g., Fabian 2012, for a review). For an outflow in a thin spherical shell geometry moving constantly with a radial velocity v, the mass outflow rate can be estimated via

$$\dot{M}_{\rm out} = 1.43\ m_{\rm p}\ N_{\rm H}\ v\ \Omega\ \left(\frac{r^2}{\Delta r}\right), \tag{4.1}$$

where $m_{\rm p}$ is the proton mass, $N_{\rm H}$ the hydrogen column density along the line of sight, r the distance between the outflow and the central engine, Δr the radial size of the outflow, and Ω the solid angle subtended by the outflow. The kinetic power carried by the outflow is $L_{\rm KE} = \frac{1}{2}\dot{M}_{\rm out}v^2$. Thus, distant and/or high-velocity outflow leads to higher mass outflow rate ($\dot{M}_{\rm out}$) and kinetic power ($L_{\rm KE}$).

While the line-of-sight hydrogen column density ($N_{\rm H}$) and velocity (v) of the outflow can be well constrained via spectral analysis, its solid angle (Ω) and location (r) are the main source of uncertainties in estimating the kinetic power that impacts the host galaxy. The solid angle highly depends on the exact geometry, which is not investigated here. On the other hand, the location can be immediately obtained via the definition of the ionization parameter[1] (Krolik et al. 1981; Tarter et al. 1969) if the density of the outflow is known,

$$\xi = \frac{L}{n_{\rm H}\ r^2}, \tag{4.2}$$

where L is the 1–1000 Ryd (or 13.6 eV–13.6 keV) band luminosity of the ionizing source, $n_{\rm H}$ the hydrogen number density of the ionized plasma, and r the distance of the plasma with respect to the ionizing source.

However, it is not trivial to determine the density of a photoionized plasma. Three different approaches have been used to measure the density of AGN outflows. The first approach is a timing analysis where the response of the ionized outflow to changes in the ionizing continuum is monitored. A high-density plasma recombines more rapidly, thus yields a shorter recombination timescale. This approach has been used to constrain density in Mrk 509 (Kaastra et al. 2012), NGC 5548 (Ebrero et al. 2016), and NGC 4051 (Silva et al. 2016), etc. The timing analysis is in general challenging because the observations of a given object are often sparse, washing out the possible effects of variability, and lack the signal-to-noise ratio required to significantly measure the expected changes (Ebrero et al. 2016).

[1] Throughout this paper, ξ is in units of 10^{-9} W m (i.e., erg s^{-1} cm).

The second approach is a spectral analysis of density sensitive emission lines. It is well known that the ratio of intercombination to forbidden emission lines in the He-like triplets (e.g., Porquet et al. 2010) varies for plasmas with different density values. This density probe, observed in the X-ray wavelength range, has been applied to a few AGNs, e.g., NGC 4051 (Collinge et al. 2001), NGC 4593 (McKernan et al. 2003), and NGC 4151 (Schurch et al. 2004), where the upper limits of the plasma density are derived. Meanwhile, as shown in Mehdipour et al. (2015a), line absorption of He-like ion triplet lines by Li-like ions make density diagnostics complicated. In addition, for solar corona studies, metastable emission lines observed in the EUV wavelength range from Be-like (Landi & Miralles 2014), B-like (Ciaravella et al. 2001; Gallagher et al. 1999; Keenan et al. 1998; Warren & Brooks 2009), C-like (Keenan et al. 1993; Landi & Landini 1998), and N-like (Keenan et al. 2004) ions are widely used to determine the density.

The third approach is a spectral analysis where density sensitive metastable absorption lines are identified. This method has been successfully used for absorption lines observed in the UV band (e.g., Arav et al. 2015). In the X-ray band, Kaastra et al. (2004) obtain an upper limit of the outflow density in Mrk 279, with the density sensitive metastable absorption transitions $2s^2$–$1s2s^22p$ in O V (Be-like) ~22.4 Å. Later, King et al. (2012) reported an upper limit of the outflow density in NGC 4051 by using the ground (11.77 Å) and metastable (11.92 Å) transitions in Fe XXII (B-like). The same transitions in Fe XXII were in fact previously used by Miller et al. (2008) in the stellar mass black hole GRO J1655–40, yielding a tight constraint on the density of a disk wind.

In this work, we carry out a systematic study of density diagnostics with ions in different isoelectronic sequences in photoionized equilibrium. A detailed calculation is made with our new photoionized plasma model PION[2] in the SPEX code (Kaastra et al. 1996). Given cosmic abundances (the proto-solar abundance table in Lodders & Palme 2009), we consider elements including C, N, O, Ne, Mg, Si, S, Ar, Ca, and Fe. Throughout this paper we consider plasma densities in the range between 10^6 m^{-3} (or 1 cm^{-3}) and 10^{20} m^{-3} (or 10^{14} cm^{-3}). At $n_{\rm H} = 10^{20}$ m^{-3}, metastable levels in Be-like to F-like ions can be significantly populated compared to the population of the ground level, while for Li-like, Ne-like, and Na-like ions, no metastable levels are significantly populated. Therefore, we focus on Be-like to C-like ions in Section 4.3.1 to 4.3.3. Due to the lack of atomic data, for N-like to F-like ions, we merely discuss

[2]An introduction of PION and a comparison to other photoionization codes can be found in Mehdipour et al. (2016a)

Fe XX, Fe XIX, and Fe XVIII in Appendix 4.A.

4.2. Methods

Unless specified otherwise, we use the spectral energy distribution (SED) of NGC 5548 in our photoionization modeling, i.e., the AGN1 SED shown in Fig. 1 of Mehdipour et al. (2016b). The photoionized outflow is assumed to be optically thin with a slab geometry. The line-of-sight hydrogen column density ($N_{\rm H}$) is 10^{24} m^{-2}. The covering factor is unity. No velocity shift with respect to the central engine is assumed here, and the turbulent velocity is set to 100 km s^{-1} in the calculation.

When modeling a photoionized plasma with our new PION model in the SPEX code, its thermal equilibrium, ionization balance, and level population are calculated self-consistently with detailed atomic data of relevant collisional and radiative processes, such as collisional excitation and de-excitation (FAC calculation, Gu 2008), radiative recombination (Badnell 2006; Mao & Kaastra 2016), inner shell ionization (Urdampilleta et al. 2017), etc. The thermal balance and instability curve are shown in Figs. 3–5 of Mehdipour et al. (2016a). Ion concentrations are derived accordingly, and we show in Figure 4.1 the ion concentrations of Si XIV (H-like) to Si V (Ne-like) as a function of the ionization parameter. The level population is also calculated simultaneously.

4.3. Results

In Section 4.3.1 (for Be-like ions) to Section 4.3.3 (for C-like ions), we first show which metastable levels (Table 4.1) can be significantly populated in a broad density range of $n_{\rm H} \in (10^6,\ 10^{20})$ m^{-3}. We note that different ionization parameters are used to maximize the ion concentration of different ions, e.g., $\log_{10}(\xi) = 1.90$ for Si XI (Be-like), $\log_{10}(\xi) = 2.0$ for S XII (B-like), and $\log_{10}(\xi) = 2.1$ for Ar XIII (C-like). Second, we list the characteristic absorption lines from these metastable levels. Absorption lines from the ground level are listed together with density sensitive lines from the metastable levels, so that it is possible to tell whether the spectral resolution of a certain instrument is fine enough to distinguish these lines. If so, these lines can be used for density diagnostics.

4.3.1. Be-like

Figure 4.2 shows the ratios of metastable to ground level populations as a function of plasma density. The lifetime of the first excited level $1s^2 2s2p\ (^3P_0)$ is rather

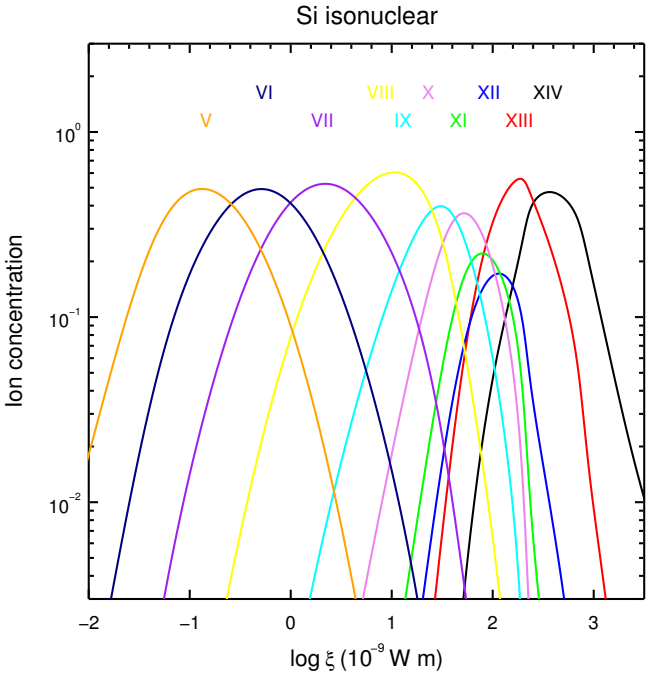

Figure 4.1: Ion concentration of the Si isonuclear sequence (H-like to Ne-like) as a function of the ionization parameter (in units of 10^{-9} W m, i.e., erg s^{-1} cm).

Table 4.1: Level indices for the ground level (Level 1) and density sensitive metastable levels (Levels 2-5) from the Be-like to F-like isoelectronic sequences.

Index	1		2		3		4		5	
Sequence	Conf.	$^{2S+1}L_J$	Conf.	$^{2S+1}L_J$	Conf.	$^{2S+1}L_J$	Conf.	$^{2S+1}L_J$	Conf.	$^{2S+1}L_J$
Be-like	$2s^2$	$^1S_0$	$2s2p$	$^3P_0$	$2s2p$	$^3P_1$	$2s2p$	$^3P_2$	– –	– –
B-like	$2s^2 2p$	$^2P_{1/2}$	$2s^2 2p$	$^2P_{3/2}$	– –	– –	– –	– –	– –	– –
C-like	$2s^2 2p^2$	$^3P_0$	$2s^2 2p^2$	$^3P_1$	$2s^2 2p^2$	$^3P_2$	$2s^2 2p^2$	$^1D_2$	$2s^2 2p^2$	$^1S_0$
N-like (Fe)	$2s^2 2p^3$	$^4S_{3/2}$	$2s^2 2p^3$	$^2D_{3/2}$	$2s^2 2p^3$	$^2D_{5/2}$	$2s^2 2p^3$	$^2P_{1/2}$	$2s^2 2p^3$	$^2P_{3/2}$
O-like (Fe)	$2s^2 2p^4$	$^3P_2$	$2s^2 2p^4$	$^3P_0$	$2s^2 2p^4$	$^3P_1$	$2s^2 2p^4$	$^1D_2$	$2s^2 2p^4$	$^1S_0$
F-like (Fe)	$2s^2 2p^5$	$^2P_{3/2}$	$2s^2 2p^5$	$^2P_{1/2}$	– –	– –	– –	– –	– –	– –

Notes. "Conf." is short for electron configuration. $^{2S+1}L_J$ refers to the spectroscopic notations, where S is the total spin quantum number ($2S + 1$ is the spin multiplicity), L is the total orbital quantum number, and J is the total angular momentum quantum number.

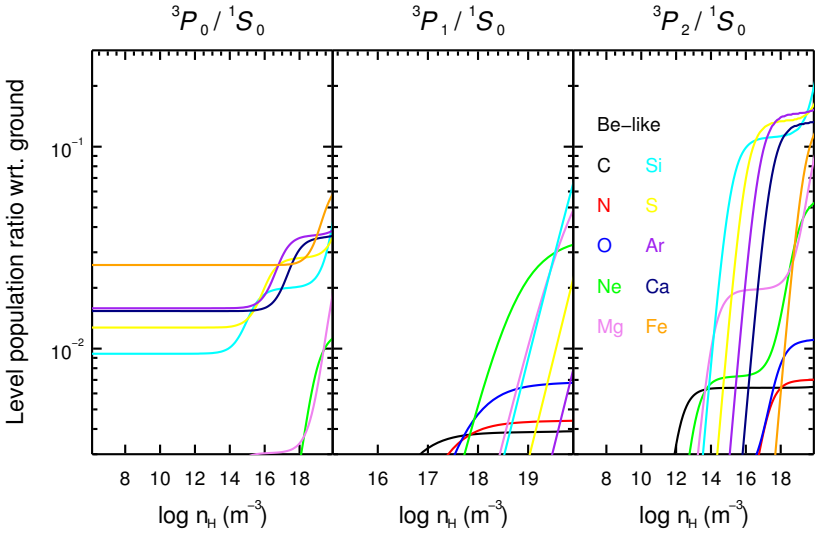

Figure 4.2: Level population ratios as a function of plasma density (in the range of $10^{6-20}\mathrm{m}^{-3}$ or $10^{0-14}\mathrm{cm}^{-3}$) at ionization parameter of maximum ion concentration in the ionization balance. The configuration of the ground ($^1S_0$) and metastable levels ($^3P_{0-2}$) are listed in Table 4.1.

long, so that even if the plasma density is rather low, the metastable level can still be populated up to a small percent of the ground level population. Accordingly, a plateau can be found in the $^3P_0/^3S_0$ level population ratio (left panel of Figure 4.2). The third excited level $1s^2 2s2p\ (^3P_2)$ can be more easily populated at lower density than the second excited level $1s^2 2s2p\ (^3P_1)$. The rest of the excited levels in Be-like ions are not significantly populated ($< 0.01\%$ of the ground level population) in a photoionized plasma with density $n_{\rm H} \lesssim 10^{20}\ \mathrm{m}^{-3}$.

Given that the metastable levels (Level 2-4) can be populated up to 20% of the ground level (Level 1) population, we list in Table 4.2 three sets of characteristic transitions ($n_j = 2-2,\ 2-3,\ \mathrm{and}\ 1-2$) for each level. The corresponding wavelengths (λ) and oscillator strengths (f) of these absorption features in the X-ray ($1-100$ Å) and UV ($100-2000$ Å) wavelength ranges are listed as well.

Among the three transitions of each level in the same ion, the inner shell $1s-2p$ transition (denoted as $n_j = 1-2$) always yields the shortest wavelength, while the $2s-2p$ transition ($n_j = 2-2$) yields the longest wavelength. There are of course more transitions than we listed in Table 4.2. For instance, there are in total six $1s^2 2s2p\ (^3P) - 1s^2 2p^2\ (^3P)$ metastable transitions around $\lambda \sim 1175$ Å for C III that have been successfully used for density diagnostics in AGN ionized outflows (e.g., Arav et al. 2015). Transitions with higher f-values are listed in Table 4.2 for

Table 4.2: Characteristic absorption lines from the ground and the metastable levels in Be-like ions.

Index	1		2		3		4	
n_j	Lower	Upper	Lower	Upper	Lower	Upper	Lower	Upper
$2-2$	$2s^2$ $(^1S_0)$	$2s2p$ $(^1P_1)$	$2s2p$ $(^3P_0)$	$2p^2$ $(^3P_1)$	$2s2p$ $(^3P_1)$	$2p^2$ $(^3P_2)$	$2s2p$ $(^3P_2)$	$2p^2$ $(^3P_2)$
Ion	λ (Å)	f	λ (Å)	f	λ (Å)	f	λ (Å)	f
C III	977.012	0.76	1175.254	0.27	1174.923	0.11	1175.702	0.20
N IV	765.141	0.61	922.511	0.22	921.986	0.09	923.212	0.17
O V	629.727	0.50	759.436	0.19	758.671	0.08	760.440	0.14
Ne VII	465.216	0.41	559.944	0.16	558.605	0.07	561.724	0.12
Mg IX	368.068	0.31	441.196	0.12	439.173	0.05	443.969	0.09
Si XI	303.323	0.27	361.410	0.10	358.650	0.04	365.431	0.08
S XIII	256.683	0.24	303.382	0.09	299.954	0.04	308.950	0.07
Ar XV	221.133	0.21	258.764	0.08	254.827	0.04	266.239	0.06
Ca XVII	192.818	0.19	223.018	0.08	218.821	0.03	232.827	0.05
Fe XXIII	132.906	0.15	147.270	0.06	144.389	0.03	166.689	0.03
n_j	Lower	Upper	Lower	Upper	Lower	Upper	Lower	Upper
$2-3$	$2s^2$ $(^1S_0)$	$2s3p$ $(^1P_1)$	$2s2p$ $(^3P_0)$	$2s3d$ $(^3D_1)$	$2s2p$ $(^3P_1)$	$2s3d$ $(^3D_2)$	$2s2p$ $(^3P_2)$	$2s3d$ $(^3D_3)$
Ion	λ (Å)	f	λ (Å)	f	λ (Å)	f	λ (Å)	f
C III	386.200	0.23	459.463	0.56	459.510	0.42	459.624	0.47
N IV	247.203	0.33	283.415	0.61	283.463	0.46	283.572	0.51
O V	172.168	0.38	192.749	0.63	192.795	0.47	192.902	0.53
Ne VII	97.495	0.47	106.040	0.68	106.085	0.51	106.189	0.57
Mg IX	62.751	0.53	67.089	0.72	67.134	0.54	67.239	0.61
Si XI	43.763	0.46	46.362	0.73	46.298	0.54	46.399	0.61

(Table 4.2 continued)

S XIII	32.242	0.38	33.806	0.74	33.852	0.55	33.951	0.61
Ar XV	24.759	0.32	25.808	0.75	25.850	0.56	25.953	0.62
Ca XVII	19.558	0.36	20.310	0.78	20.339	0.56	20.437	0.62
Fe XXIII	10.980	0.41	11.298	0.74	11.325	0.54	11.441	0.61
n_j	Lower	Upper	Lower	Upper (†)	Lower	Upper (†)	Lower	Upper (†)
$1-2$	$2s^2$ $(^1S_0)$	$1s2s^22p$ $(^1P_1)$	$2s2p$ $(^3P_0)$	$1s2s2p^2$ $(^3P_1)$	$2s2p$ $(^3P_1)$	$1s2s2p^2$ $(^3P_2)$	$2s2p$ $(^3P_2)$	$1s2s2p^2$ $(^3P_2)$
Ion	λ (Å)	f	λ (Å)	f	λ (Å)	f	λ (Å)	f
C III	42.165	0.62	42.385	0.31	42.384	0.13	42.385	0.23
N IV	29.941	0.65	30.088	0.33	30.086	0.14	30.088	0.24
O V	22.360	0.61	22.474	0.30	22.472	0.13	22.474	0.22
Ne VII	13.820	0.66	13.878	0.35	13.877	0.16	13.879	0.22
Mg IX	9.378	0.68	9.410	0.44	9.413	0.26 $(^3D_2)$	9.415	0.15 $(^3D_3)$
Si XI	6.776	0.70	6.798	0.52 $(^3D_1)$	6.799	0.27 $(^3D_2)$	6.797	0.27
S XIII	5.123	0.71	5.137	0.56 $(^3D_1)$	5.138	0.27 $(^3D_2)$	5.136	0.28
Ar XV	4.007	0.72	4.017	0.57 $(^3D_1)$	4.018	0.27 $(^3D_2)$	4.016	0.29
Ca XVII	3.222	0.72	3.228	0.59 $(^3D_1)$	3.228	0.28 $(^3D_2)$	3.228	0.29
Fe XXIII	1.870	0.69	1.873	0.61	1.874	0.29 $(^3D_2)$	1.874	0.26

Notes. For the $1s-2p$ transitions (denoted $n_j = 1-2$) from the metastable (lower) levels, the upper levels (marked †) vary ($^3P_{1-2}$ or $^3D_{1-3}$) for different elements (exceptions are marked following the f-values).

simplicity. For the six C III $\lambda \sim 1175$ Å lines, the three tabulated lines have $f > 0.1$, while the other three lines have slightly lower oscillator strength values.

For all three sets of transitions, the metastable to ground separation ($\Delta\lambda = |\lambda_{2,3,4} - \lambda_1|$) increases with increasing wavelength of the lines. For the inner shell transitions, the separations are rather small with $\Delta\lambda(n_j = 1 - 2) \lesssim 0.14$ Å. For the other two sets of transitions, the separations are relatively large, ranging from ~ 0.3 Å (for $\lambda \sim 10$ Å) to ~ 200 Å (for $\lambda \sim 1000$ Å), which are larger than the spectral resolution of current X-ray grating spectrometers. The metastable lines themselves, on the other hand, are closer to each other ($\lesssim 0.2$ Å for lines in the X-ray band and $\lesssim 3$ Å for lines in the UV band). This is simply due to the fact that the three metastable levels are the fine structure splitting of the same ^3P term.

4.3.2. B-like

For B-like ions, only the first excited level $2s^2\ 2p\ (^2P_{3/2})$ can be significantly populated up to a factor of two above the ground level population, as shown in Figure 4.3. None of the rest of the excited levels is significantly populated ($< 0.01\%$ of the ground level population) in a photoionized plasma with density $n_{\rm H} \lesssim 10^{20}$ m^{-3}. At a sufficiently high density, the ratio of metastable to ground level population follows the Boltzmann distribution (meanwhile the plasma is partially in local temperature equilibrium).

Characteristic absorption lines from the ground (Level 1) and metastable level (Level 2) in B-like ions are listed in Table 4.3. Similar to the Be-like isoelectronic sequence (Section 4.3.1), among the three transitions for the same ion, the inner shell transition ($n_j = 1-2$) has the shortest wavelength and the $n_j = 2-2$ transition has the longest wavelength. The metastable to ground separation ($\Delta\lambda$) is negligible for the inner shell transition ($n_j = 1 - 2$). For the other two sets of transitions, the separations between the ground and metastable lines are $\Delta\lambda(n_j = 2 - 3) \sim 0.15 - 0.30$ Å and $\Delta\lambda(n_j = 2 - 2) \sim 0.2 - 2.7$ Å, respectively, which are larger than the spectral resolution of current X-ray grating spectrometers (see, e.g., Table 1 in **?**).

4.3.3. C-like

For C-like ions, the first two excited levels $2s^2\ 2p^2\ (^3P_1 \text{ and } ^3P_2)$ can be significantly populated up to a factor of a few of the ground level population, as shown in Figure 4.4. The next two excited levels $2s^2\ 2p^2\ (^1D_2 \text{ and } ^1\mathrm{S}_0)$ can also be populated up to tens of percent of the ground level population. The rest of the excited lev-

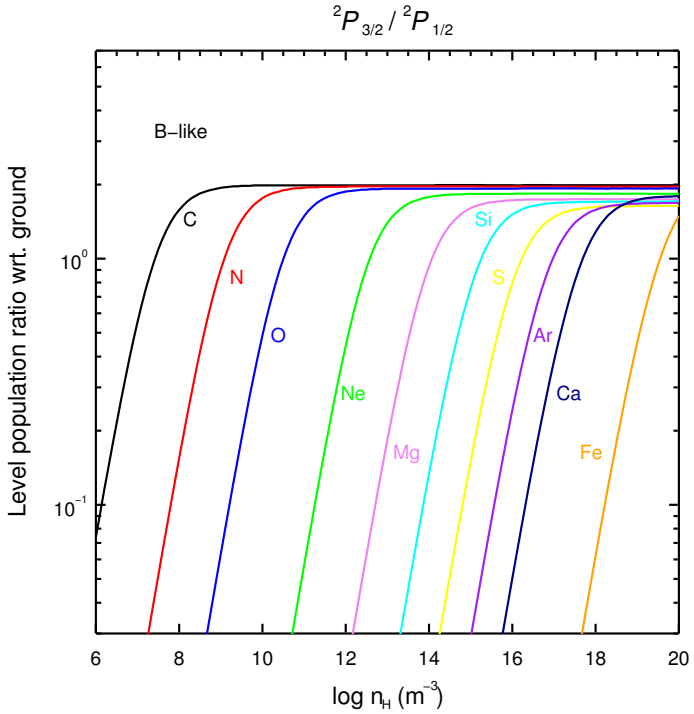

Figure 4.3: Similar to Figure 4.2, but for B-like ions.

Table 4.3: Characteristic absorption lines from the ground and metastable level in B-like ions.

Index	1		2	
n_j	Lower	Upper (†)	Lower	Upper
$2-2$	$2s^2 2p\ (^2P_{1/2})$	$2s2p^2\ (^2P_{1/2})$	$2s^2 2p\ (^2P_{3/2})$	$2s2p^2\ (^2P_{3/2})$
Ion	λ (Å)	f	λ (Å)	f
C II	903.962	0.33	904.142	0.42
N III	685.515	0.28	685.818	0.36
O IV	554.076	0.23	554.514	0.29
Ne VI	401.146	0.17	401.941	0.22
Mg VIII	313.754	0.13	315.039	0.18
Si X	256.384	0.09	258.372	0.15
S XII	227.490	0.07 ($^2S_{1/2}$)	218.200	0.13
Ar XIV	194.401	0.08 ($^2S_{1/2}$)	187.962	0.12
Ca XVI	168.868	0.08 ($^2S_{1/2}$)	164.165	0.11
Fe XXII	117.144	0.08	114.409	0.09
n_j	Lower	Upper (†)	Lower	Upper
$2-3$	$2s^2 2p\ (^2P_{1/2})$	$2s^2 3d\ (^2D_{3/2})$	$2s^2 2p\ (^2P_{3/2})$	$2s^2 3d\ (^2D_{5/2})$
Ion	λ (Å)	f	λ (Å)	f
C II	687.053	0.33	687.346	0.30
N III	374.198	0.44	374.434	0.39
O IV	238.360	0.50	238.570	0.45
Ne VI	122.516	0.56	122.701	0.50
Mg VIII	74.858	0.60	75.034	0.54
Si X	50.524	0.62	50.691	0.56
S XII	36.399	0.63	36.564	0.57
Ar XIV	27.469	0.64	27.631	0.58

(Table 4.3 continued)

Ca XVI	21.451	0.65	21.609	0.58
Fe XXII	11.767	0.67	11.921	0.59
n_j	Lower	Upper (†)	Lower	Upper
$1-2$	$2s^2 2p\ (^2P_{1/2})$	$1s2s^2 2p^2\ (^2P_{3/2})$	$2s^2 2p\ (^2P_{3/2})$	$1s2s^2 2p^2\ (^2P_{3/2})$
Ion	λ (Å)	f	λ (Å)	f
C II	43.050	0.13	43.049	0.17
N III	30.533	0.16	30.532	0.20
O IV	22.762	0.18	22.761	0.22
Ne VI	14.030	0.20	14.030	0.25
Mg VIII	9.500	0.22	9.500	0.28
Si X	6.853	0.23	6.853	0.29
S XII	5.179	0.25 ($^2D_{3/2}$)	5.174	0.30
Ar XIV	4.048	0.27 ($^2D_{3/2}$)	4.046	0.31
Ca XVI	3.249	0.29 ($^2D_{3/2}$)	3.247	0.31
Fe XXII	1.882	0.32 ($^2D_{3/2}$)	1.882	0.30

Notes. For the $2s-2p$ ($n_j = 2-2$) and $1s-2p$ ($n_j = 1-2$) transitions from the ground (lower) level, the upper level (denoted as †) vary for different elements (exceptions are marked following the f-values).

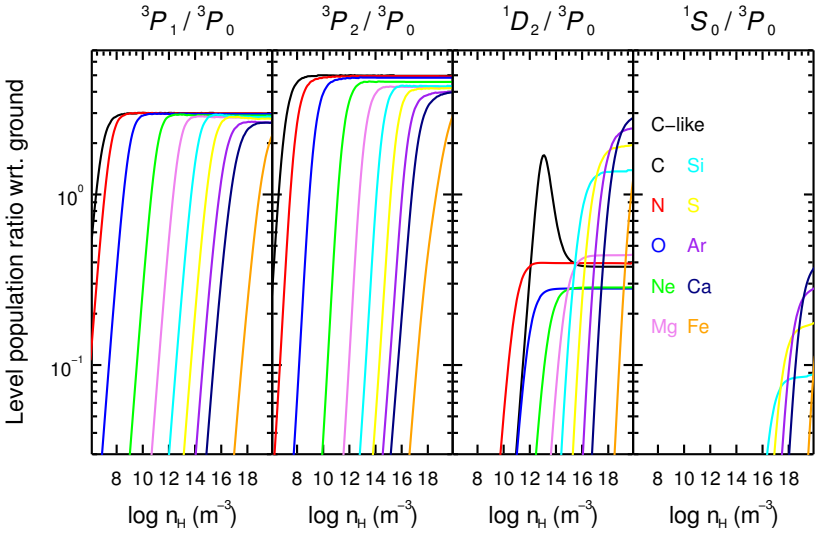

Figure 4.4: Similar to Figure 4.2, but for C-like ions..

els are not significantly populated ($< 0.01\%$ of the ground level population) in a photoionized plasma with density $n_{\rm H} \lesssim 10^{20}$ m^{-3}.

Since the metastable level $2s^2 2p^2$ ($^1S_0$) is only significantly populated at rather high density (the right panel in Figure 4.4), for simplicity only transitions from the ground (Level 1) and the first three metastable levels (Level $2-4$) are listed in Table 4.4. Again, the inner shell transition ($n_j = 1-2$) corresponds to the line with the shortest wavelength and the $n_j = 2-2$ transition corresponds to the line with the longest wavelength. For the inner shell transition, the ground to metastable separation ($\Delta\lambda$) is negligible. For the other two transitions ($n_j = 2-2$ and $2-3$) that we listed here, it is easier (with $\Delta\lambda \gtrsim 0.1$ Å) to distinguish lines from the ground $2s^2\ 2p^2$ ($^3P_0$) and lines from the third excited level $2s^2\ 2p^2$ ($^1D_2$). Lines from the ground and the first two excited levels are close to each other since the lower levels are the fine structure splitting of the same term ^3P. Between the $n_j = 2-3$ and $n_j = 2-2$ transitions, it is more difficult to distinguish lines from the ground and the first two excited levels for the former, e.g., C I lines around $\lambda \sim 1277$ Å, N II lines around $\lambda \sim 533$ Å.

4.3.4. Summary

For Be-like ions, the first three excited levels $2s2p$ ($^3P_{0-2}$) can be significantly populated ($\gtrsim 1\%$ of the ground level population) when $n_{\rm H} \gtrsim 10^{14}$ m^{-3}. Moreover, the

Table 4.4: Characteristic absorption lines from the ground and the metastable levels in C-like ions.

Index	1		2		3		4	
n_j	Lower	Upper	Lower	Upper	Lower	Upper	Lower	Upper
$2-2$	$2s^2 2p^2$ $(^3P_0)$	$2s2p^3$ $(^3S_1)$	$2s^2 2p^2$ $(^3P_1)$	$2s2p^3$ $(^3S_1)$	$2s^2 2p^2$ $(^3P_2)$	$2s2p^3$ $(^3S_1)$	$2s^2 2p^2$ $(^1D_2)$	$2s2p^3$ $(^1D_2)$
Ion	λ (Å)	f	λ (Å)	f	λ (Å)	f	λ (Å)	f
C I	1560.310	0.18 $(^3D_1)$	1560.683	0.14 $(^3D_2)$	1561.439	0.15 $(^3D_3)$	1021.853	0.61
N II	644.634	0.25	644.837	0.25	645.179	0.25	775.966	0.36
O III	507.389	0.20	507.680	0.20	508.178	0.20	599.590	0.34
Ne V	357.947	0.15	358.475	0.15	359.374	0.15	416.212	0.27
Mg VII	276.154	0.12	277.001	0.12	278.402	0.12	319.027	0.22
Si IX	223.743	0.10	225.024	0.10	227.000	0.10	258.080	0.19
S XI	186.839	0.08	188.675	0.08	191.266	0.09	215.968	0.16
Ar XIII	236.268	0.08 $(^3D_1)$	161.610	0.07	164.802	0.08	184.899	0.14
Ca XV	200.976	0.08 $(^3D_1)$	140.583	0.06	144.309	0.07	161.018	0.12
Fe XXI	128.752	0.09 $(^3D_1)$	142.149	0.05 $(^3D_2)$	102.216	0.06	113.292	0.09
n_j	Lower	Upper	Lower	Upper	Lower	Upper	Lower	Upper
$2-3$	$2s^2 2p^2$ $(^3P_0)$	$2s^2 2p3d$ $(^3D_1)$	$2s^2 2p^2$ $(^3P_1)$	$2s^2 2p3d$ $(^3D_2)$	$2s^2 2p^2$ $(^3P_2)$	$2s^2 2p3d$ $(^3D_3)$	$2s^2 2p^2$ $(^1D_2)$	$2s^2 2p3d$ $(^1F_3)$
Ion	λ (Å)	f	λ (Å)	f	λ (Å)	f	λ (Å)	f
C I	1277.246	0.11	1277.283	0.08	1277.550	0.10	1463.337	0.10
N II	533.511	0.33	533.582	0.25	533.729	0.27	574.650	0.29
O III	305.596	0.54	305.656	0.37	305.768	0.41	320.978	0.46
Ne V	143.220	0.76	143.265	0.57	143.345	0.58	147.137	0.69
Mg VII	83.910	0.93	83.959	0.68	84.025	0.66	85.407	0.83

(Table 4.4 continued)

Si IX	55.305	1.05	55.356	0.74	55.401	0.71	56.027	0.91
S XI	39.240	1.13	39.300	0.74	39.323	0.73	39.648	0.97
Ar XIII	29.318	1.19	29.252	0.68	29.348	0.73	29.549	1.00
Ca XV	22.730	1.23	22.758	0.57	22.777	0.72	22.902	1.00
Fe XXI	12.292	1.24	12.433	0.43	12.331	0.59	12.411	0.94
n_j	Lower	Upper (†)	Lower	Upper (†)	Lower	Upper (†)	Lower	Upper (†)
$1-2$	$2s^2 2p^2$ $(^3P_0)$	$1s2s^2 2p^3$ $(^3D_1)$	$2s^2 2p^2$ $(^3P_1)$	$1s2s^2 2p^3$ $(^3P_1)$	$2s^2 2p^2$ $(^3P_2)$	$1s2s^2 2p^3$ $(^3D_3)$	$2s^2 2p^2$ $(^1D_2)$	$1s2s^2 2p^3$ $(^1D_2)$
Ion	λ (Å)	f	λ (Å)	f	λ (Å)	f	λ (Å)	f
C I	43.567	0.09	43.568	0.08 $(^3D_1)$	43.568	0.08 $(^3D_1)$	43.492	0.17
N II	30.963	0.11	30.944	0.10 $(^3S_1)$	30.945	0.10 $(^3S_1)$	30.914	0.21
O III	23.056	0.13 $(^3S_1)$	23.057	0.11 $(^3S_1)$	23.058	0.11 $(^3S_1)$	23.061	0.24
Ne V	14.234	0.16	14.205	0.14 $(^3S_1)$	14.237	0.12	14.211	0.28
Mg VII	9.604	0.19 $(^3S_1)$	9.605	0.16 $(^3S_1)$	9.628	0.14	9.611	0.30
Si IX	6.912	0.21 $(^3P_1)$	6.914	0.18	6.929	0.14	6.916	0.32
S XI	5.225	0.24	5.218	0.19	5.229	0.15	5.220	0.33
Ar XIII	4.086	0.27	4.081	0.20	4.088	0.15	4.081	0.33
Ca XV	3.277	0.32	3.274	0.22	3.280	0.15	3.275	0.32
Fe XXI	1.895	0.44	1.894	0.22 $(^3S_1)$	1.894	0.17 $(^1D_2)$	1.894	0.19 $(^3P_2)$

Notes. For the $2s-2p$ $(n_j = 2-2)$ and $1s-2p$ $(n_j = 1-2)$ transitions from the ground and metastable (lower) levels, the upper levels (marked †) vary for different element (exceptions are marked following the f-values).

third excited level $2s2p\ (^3P_2)$ can be populated more easily at such a high density. For B-like ions, merely the first excited level $2s^22p\ (^2P_{3/2})$ can be used as a density probe. For C-like ions, the metastable levels $2s^22p^2\ (^3P_1 \text{ and } ^3P_2)$ can be more easily populated than $2s^22p^2\ (^1D_2 \text{ and } ^1S_0)$. On the other hand, the transition from the $2s^22p^2\ (^1D_2)$ level can be more easily distinguished from the transition from the ground level $2s^22p^2\ (^3P_0)$.

The metastable levels in Be-like ions are less populated than B-like and C-like ions at the same density. For all three isoelectronic sequences, it is rather difficult to distinguish inner shell transitions from the ground and metastable levels.

The wavelengths and oscillator strengths can be obtained from the SPEX atomic code and table (SPEXACT) v3.04. We cross-checked the wavelengths of the lines in Tables 4.2 to 4.4 with those from NIST v5.3 (Kramida et al. 2015) when available.

4.4. Discussion

4.4.1. Ionization parameter dependence

In Section 4.3, for each ion, the level population is calculated given a certain ionization parameter. Here we discuss the level population dependence on both ionization parameter and density. Since the majority of the $n_j = 2 - 2$ and $n_j = 2 - 3$ transitions from ions in the same isoelectronic sequence share the same lower and upper levels (Table 4.2 to 4.4), we take these transitions from Be-like Si XI to C-like Si IX for this exercise. The ionization dependence can be applied to the rest of the ions in the same sequence. We note that inner shell transitions ($n_j = 1 - 2$) are excluded since it is difficult to distinguish lines from ground and metastable levels in any case (Section 6.4.5). We choose three different ionization parameters for each ion, corresponding to the maximum ion concentration and $\sim 90\%$ of the maximum ion concentration.

As shown in Figure 4.5, the optical depth at the line center ($\tau_0 \propto N_i\ f$) varies with ionization parameter and density. Similarly, the metastable to ground equivalent width ratios ($EW_{\text{meta}}/EW_{\text{ground}}$) involving the $2s2p\ (^3P_2)$ metastable level in Be-like ions and the $2s^22p^2\ (^1D_2)$ metastable level in C-like ions are sensitive to both ionization parameter and density of the plasma. Nonetheless, the ratios of metastable to ground equivalent width involving the $2s^22p\ (^2P_{3/2})$ metastable level in the B-like sequence and the $2s^22p^2\ (^3P_1 \text{ and } ^3P_2)$ metastable levels in the C-like sequence are only sensitive to the density of the plasma, which makes them ideal density probes.

Table 4.5: Values of $\log_{10}(\xi)$ where Be-like Si XI to C-like Si IX reach the maximum ion concentration in the ionization balance adopting different ionizing SED.

SED	AGN1	AGN2	PL
Si XI	1.90	2.03	1.90
Si X	1.72	1.94	1.71
Si IX	1.48	1.82	1.48

Notes. The three SEDs are adapted from Mehdipour et al. (2016b). AGN1 and AGN2 refer to the SEDs of an archetypal Seyfert 1 galaxy NGC 5548 in a normal and obscured state. PL refers to a SED that follows the power law with $\Gamma = 2$.

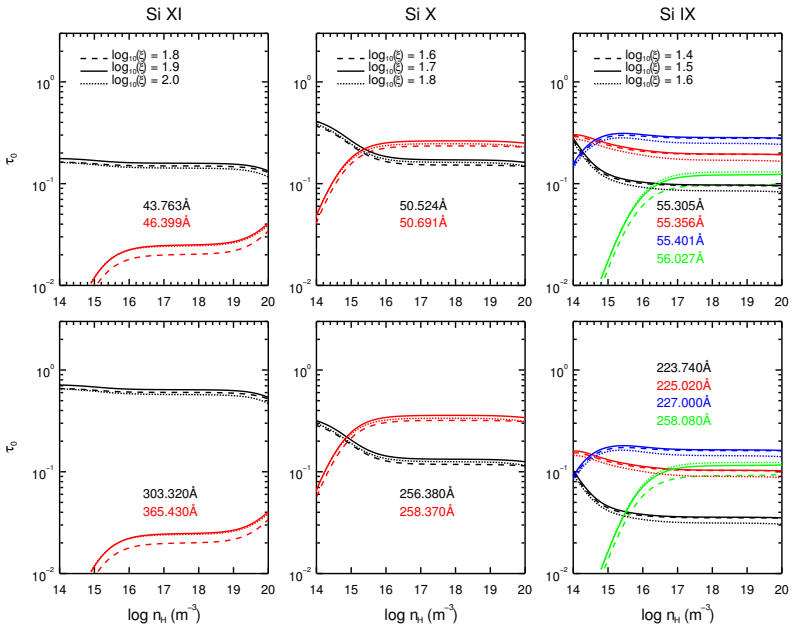

Figure 4.5: Optical depth at the line center (τ_0) for characteristic lines from ground and metastable levels in Be-like Si XI to C-like Si IX. The assumptions (SED, geometry, column density, turbulence, etc.) of the calculation are described in Section 4.2.

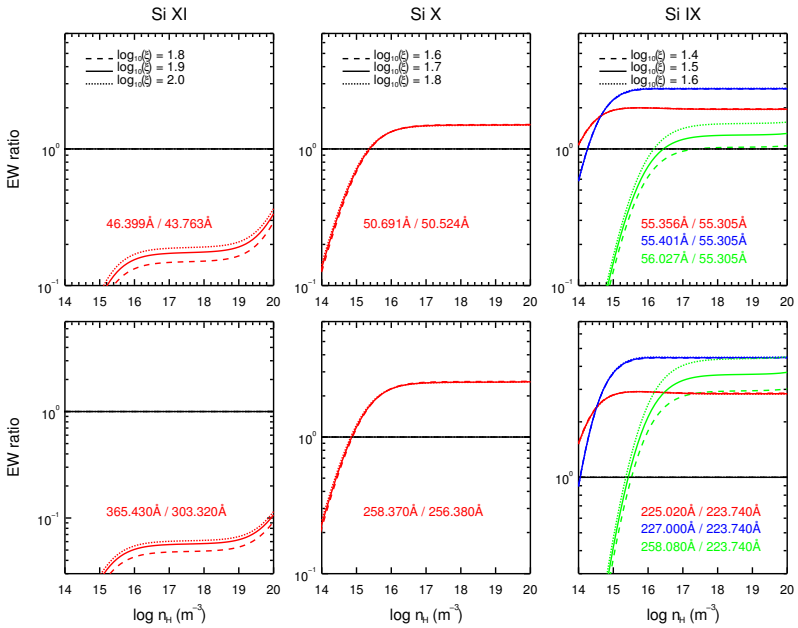

Figure 4.6: Equivalent width (EW) ratios for characteristic lines from ground and metastable levels in Be-like Si XI to C-like Si IX. The assumptions (SED, geometry, column density, turbulence, etc.) of the calculation are described in Section 4.2. For those lines with non-negligible optical depth ($\tau_0 \gtrsim 1$), the exact EWs depend on the line broadening profiles.

We caution that adopting a different ionizing SED yields a different ionization balance for the plasma. That is to say, the exact value of the ionization parameters where the ion concentration reaches a maximum or 90% of the maximum in Figure 4.6 differs for different SEDs (Table 4.5). The SED adopted here is representative of a typical Seyfert 1 galaxy. Of course, the exact values of τ_0 and EW also depend on the hydrogen column density ($N_{\rm H}$) and turbulence velocity ($v_{\rm b}$) of the ionized outflow.

4.4.2. Domain of density and ionization parameter diagnostics

Ions from different isoelectronic sequences cover an extensive area in the $n_{\rm H} - \xi$ two-dimensional parameter space. In Figure 4.7, each box corresponds to a certain ion. Within the box, the density of the plasma can be well constrained with lines from the metastable levels. Above (below) the box, only a lower (upper) limit can be obtained.

The box width gives the range of ionization parameters where lines from the ground and metastable levels are expected to be detected. The lower and upper boundaries correspond to $1/e$ of the maximum ion concentration using the AGN1 SED. Again we caution that a different ionizing SEDs yield different ionization parameters[3].

The box height corresponds to the density of the plasma. The lower and upper boundaries of the box corresponds to 10% and 99% of the maximum ratio of metastable to ground level population. Only the $2s^2 2p\ (^2P_{3/2})$ metastable level in B-like ions and the $2s^2 2p^2\ (^3P_1 \text{ and } ^3P_2)$ metastable levels in C-like ions are used for the calculation since their corresponding metastable-to-ground-EW ratios barely depend on the ionization parameter (Figure 4.6).

Be-like ions are not included in Figure 4.7 because the level population depends on both the ionization parameter (thus SED dependent) and density, and because the metastable levels are less populated than B-like and C-like ions at the same density (Section 6.4.5).

In addition, we also show the distance of the plasma inferred from the definition of ionization parameter (Equation 4.2). Within the same isoelectronic sequence, high-Z ions probe higher density, higher ionization parameters and smaller distances, while low-Z ions measure lower density, lower ionization parameters, and larger distances. For ions in the same isonuclear sequence (i.e., the same Z), less

[3] Additionally, with the same ionizing SED, different photoionization codes (e.g., SPEX, XSTAR and Cloudy) yield different ionization parameters (for further details, see Mehdipour et al. 2016a)

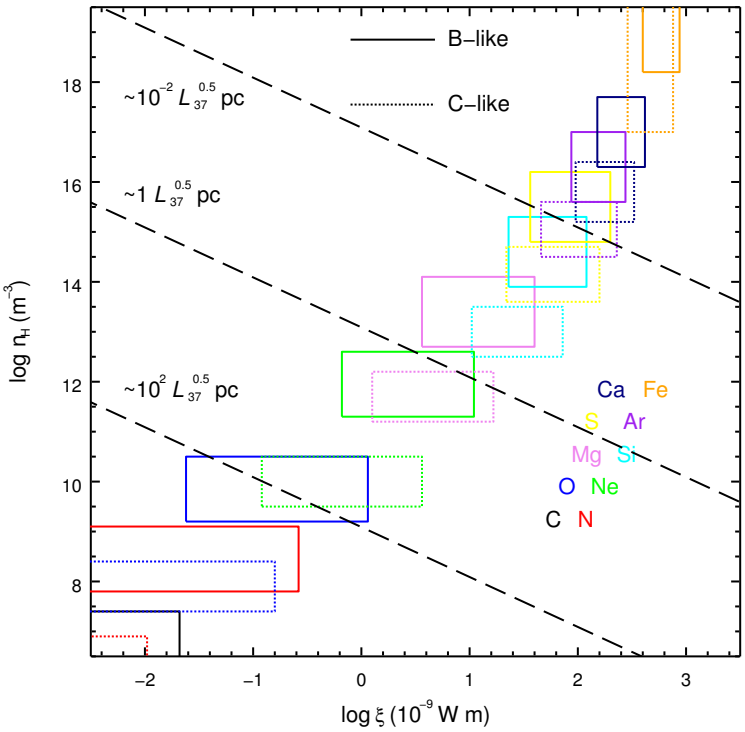

Figure 4.7: Domain of density and ionization parameter where metastable absorption line from B-like (solid) and C-like (dotted) ions can be used for diagnostics in the case of photoionized equilibrium (see Section 4.4.2 for a detailed description). Dashed lines indicate the distance of the photoionized plasma with respect to the central engine. L_{37} is the 1 to 1000 Ryd luminosity in units of 10^{37} W.

ionized ions can probe lower density, thus larger distances.

4.5. Density diagnostics for the ionized outflow in NGC 5548

NGC 5548 is the archetypal Seyfert 1 galaxy. As such, it exhibits all the typical spectral features seen in type 1 Seyfert galaxies. The broadband (from optical to hard X-ray) spectral energy distribution (SED) and various properties from the multiphase ionized outflow are well studied (e.g., Arav et al. 2015; Ebrero et al. 2016; Kaastra et al. 2014; Mehdipour et al. 2015b). NGC 5548 was observed with *Chandra*

Table 4.6: Parameters of the six absorption PION components in NGC 5548.

Component	$N_{\rm H}$	$\log_{10}(\xi)$	$v_m ic$ (km s^{-1})	$v_{\rm out}$ (km s^{-1})	$n_{\rm H}$ (m^{-3})
A	2.6 ± 0.8	0.51 ± 0.12	150 ± 29	-557 ± 37	$--$
B	2.6 ± 0.8	1.35 ± 0.06	49 ± 14	-547 ± 35	$\gtrsim 10^{13}$
C	6.9 ± 0.9	2.03 ± 0.04	40 ± 10	-1108 ± 31	$\lesssim 10^{19}$
D	10.8 ± 2.8	2.22 ± 0.03	67 ± 17	-271 ± 24	$\lesssim 10^{19}$
E	13.4 ± 2.1	2.47 ± 0.13	6 ± 5	-670 ± 14	$\lesssim 10^{20}$
F	52.0 ± 8.5	2.83 ± 0.03	115 ± 29	-1122 ± 34	$\lesssim 10^{19}$

Notes. The lower or upper limits of the density ($n_{\rm H}$) are at the confidence level of $\gtrsim 3\sigma$, while the statistical uncertainties of all the other parameters are at the confidence level of 1σ.

in January 2002 with both high- and low-energy transmission grating spectrometers (HETGS and LETGS), which allow us to study the X-ray absorption features in a wide wavelength range (~2-60 Å). Moreover, the 2002 spectra have the best signal-to-noise ratio of all the high-resolution grating spectra of NGC 5548.

Here we reanalyze these spectra to search for density diagnostic lines. The HETGS (ObsID: 3046, with ~ 150 ks exposure) and LETGS (ObsID: 3383 and 3045, with ~ 340 ks total exposure) spectra are optimally binned (Kaastra & Bleeker 2016) and fitted simultaneously. Fits to LEG, MEG, and HEG spectra are restricted to the 11–60 Å, 4–19 Å, and 1.8–10 Å wavelength range, respectively.

Six PION components are used to account for the six components in the ionized outflow (Ebrero et al. 2016; Kaastra et al. 2014). Assuming a low plasma density ($n_{\rm H} = 10^6$ m^{-3} or 1 cm^{-3}, kept frozen) for all six PION components, the best-fit C-statistics are 5146.0 (denoted as the baseline C-statistics in the following) with a degree of freedom of 4843. The hydrogen column density ($N_{\rm H}$), ionization parameter (ξ), turbulent velocity ($v_{\rm mic}$), and outflow velocity ($v_{\rm out}$) for the PION components (Table 4.6) are consistent with values found in previous studies by Kaastra et al. (2014) and Ebrero et al. (2016).

For each PION component, we then vary its density from $n_{\rm H} = 10^6$ m^{-3} to 10^{20} m^{-3}, with one step per decade. All the other parameters are kept frozen. The deviation of C-statistics (ΔC) from the baseline fit are demonstrated in Figure 4.8.

For the least ionized component A, the X-ray spectra with $\lambda \lesssim 60$ Å are insensitive to the density. The density sensitive lines that can be distinguished from the ground absorption lines of O IV (B-like) and Ne V (C-like) are at longer wavelength range ($\lambda \gtrsim 100$ Å, Table 4.3 and 4.4). That is to say, high-resolution UV spectra are

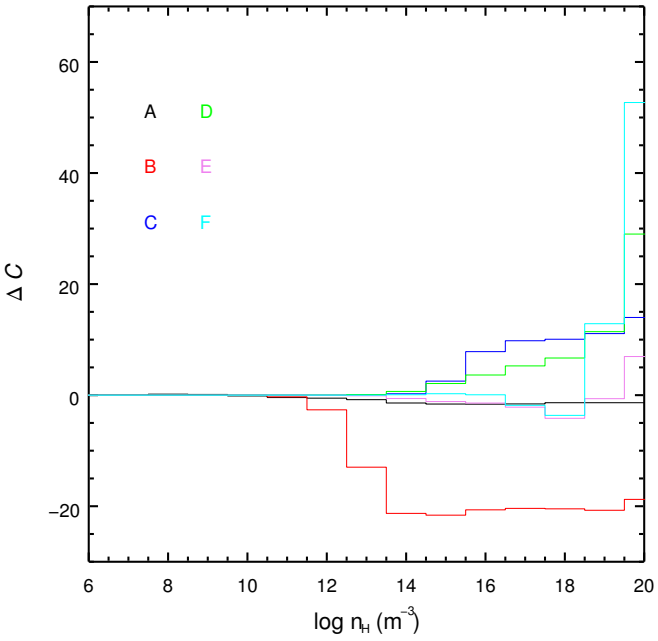

Figure 4.8: Deviation of C-statistics (ΔC) from the baseline fit (C-stat. = 5146.0 and d.o.f. = 4843) with varying plasma density ($n_{\rm H}$) for each photoionized absorber component (A–F). Component A refers to the least ionized photoionized absorber and F refers to the most ionized photoionized absorber (Table 4.6).

required to determine the density for this component.

Meanwhile, we find a lower limit (at the confidence level of 3σ) of $n_{\rm H} \gtrsim 10^{13}$ m^{-3} for component B. Figure 4.9 shows the LETGS spectrum in the neighborhood of Si IX absorption lines (~ 56 Å), where the C-statistics are improved at high density. When $n_{\rm H} \gtrsim 10^{13}$ m^{-3}, the population of the ground level $2s^2 2p^2$ ($^3P_0$) decreases, while the population of the metastable levels $2s^2 2p^2$ ($^3P_1$ and $^3P_2$) increases (Figure 4.4). Accordingly, the ground absorption line at 56.15 Å (in the observed frame) is shallower, while the metastable absorption lines at 56.20 Å and 56.25 Å are deeper. The 3σ upper limit of the distance of component B is accordingly 0.23 pc. The inferred density and distance disagree with the results reported in Ebrero et al. (2016), where a timing analysis (Section 7.1) is used. For the photoionized absorber component B, Ebrero et al. (2016) report $n_{\rm H} \in (2.9,\ 7.1) \times 10^{10}$ m^{-3} and $d \in (13,\ 20)$ pc, both at the confidence level of 1σ. The upper limits of density is based on the non-detection of variability on smaller timescales. The authors also

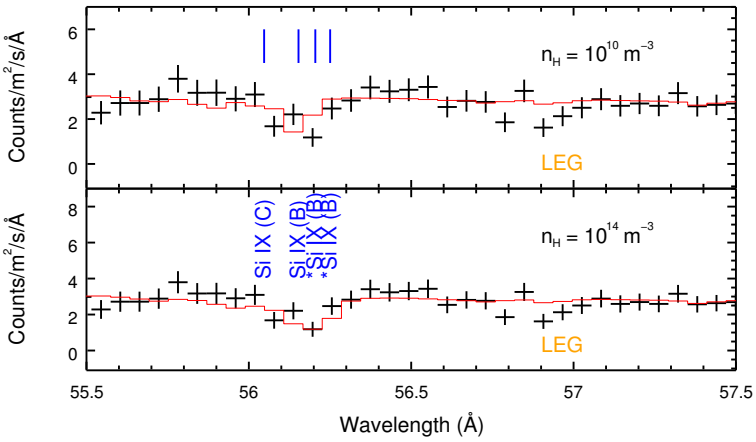

Figure 4.9: PION modeling of the LEG spectrum of NGC 5548 with $n_{\rm H} = 10^{10}$ m^{-3} (upper panel) and 10^{14} m^{-3} (lower panel). The spectral bin size is 0.025 Å. The overall C statistics is 5146.0 (d.o.f. = 4843) at low density and 5124.7 (d.o.f. = 4842) at high density. The two density sensitive metastable absorption lines of Si IX (C-like), from component B, at 55.20 Å and 56.25 Å (in the observed frame) are labeled with $*$.

note that there is a marginal hint of recombination timescale of ~ 4 and ~ 60 days, which would indicate a density lower limit (1σ) of $\sim 10^{10-11}$ m^{-3}, which would agree more with our results.

For components C – F, upper limits are obtained with $n_{\rm H} \lesssim 10^{19}$ m^{-3} (above 3σ for components C, E, and F) and $\lesssim 10^{20}$ m^{-3} (2.6σ for component D). We show in Figure 4.10 the spectra in the neighborhood of Fe XXII (B-like) and Fe XXI (C-like) with the density of component F set to $n_{\rm H} = 10^{10}$ m^{-3} (left panels) and 10^{19} m^{-3} (right panels). At high density the metastable absorption lines at 12.08 Å (Fe XXII), at 12.50 Å (Fe XXI), and at 12.60 Å (Fe XXI) are deeper. This overestimation of absorption lines contradicts the data and leads to poorer C-statistics. Of course, the spectra are crowded in this wavelength range, so that density diagnostics are challenging. The 3σ lower limits of the distance of components C – F are a few light-hours ($\sim 10^{12}$ m). The obtained density and distance for components C – F do not contradict the results ($n_{\rm H} \gtrsim 10^{10}$ m^{-3} and $d \lesssim 1$ pc) reported in Ebrero et al. (2016).

Due to the narrow wavelength coverage and rather limited effective area of current grating instruments, and the lack of atomic data for N-like to F-like ions, density diagnostics using absorption lines from the metastable levels are not very effective. Once the N-like to F-like atomic data are included, a significant portion

Table 4.7: Characteristic absorption lines from the ground and the metastable levels in N-like Fe XX to F-like Fe XVIII (SPEXACT v3.04).

Index		1		2		3	
Ion	n_j	λ (Å)	f	λ (Å)	f	λ (Å)	f
Fe XX	2-2	132.850	0.05	110.626	0.08	93.782	0.09
Fe XX	2-3	12.835	0.48	12.984	0.60	12.885	0.87
Fe XX	1-2	1.908	0.15	1.906	0.24	1.906	0.15
Fe XIX	2-2	108.355	0.06	109.952	0.08	119.983	0.03
Fe XIX	2-3	13.521	0.73	13.420	1.23	13.735	0.50
Fe XIX	1-2	1.918	0.15	1.918	0.23	1.921	0.10
Fe XVIII	2-2	93.923	0.06	103.937	0.05	– –	– –
Fe XVIII	2-3	14.203	0.88	14.121	0.86	– –	– –
Fe XVIII	2-1	1.928	0.11	1.931	0.11	– –	– –

of the $n_{\rm H} - \xi$ parameter space can be covered. This, combined with the next generation of spectrometers on board *Arcus* (Smith et al. 2016) and Athena (Nandra et al. 2013), will allow us to identify the presence/absence of these density-sensitive absorption lines (Kaastra et al. 2017), thus tightly constraining the location and the kinetic power of AGN outflows. We refer the readers to Fig. 6 of Kaastra et al. (2017) for a simulated *Arcus* spectrum of NGC 5548, compared with the observed 2002 LETGS spectrum.

4.A. N-like Fe XX to F-like Fe XVIII

Currently, in SPEXACT v3.04, the atomic data for the N-like to F-like isoelectronic sequences are lacking, except for Fe XX, Fe XIX, and Fe XVIII. Here we repeat the same analyses described above, but for N-like to F-like Fe. For both N-like Fe XX and O-like Fe XIX, the first two excited levels can be populated up to 50%, compared to the ground level population, while only the first excited level of F-like Fe XVIII can be populated significantly (Figure 4.11). Characteristic transitions from these ground and metastable levels are listed in Table 4.7.

Comparing the density-sensitive metastable levels for Be-like Fe XXIII to F-like Fe XVIII (Figure 4.11), we find that, in general, the metastable levels in C-like Fe XXI can be more easily populated when $n_{\rm H} \gtrsim 10^{16}$ m^{-3}. In addition, when $n_{\rm H} \lesssim 10^{16}$ m^{-3}, the first excited level $2s^2\ 2p^4\ (^3P_0)$ of O-like Fe XIX can be populated up to 10% of the ground level population, which has been pointed out in Kaspi et al. (2001). Nonetheless, the density-sensitive line (13.420 Å) of O-like Fe XIX is weaker than the ground level absorption lines (13.521 Å and 13.492 Å). Meanwhile,

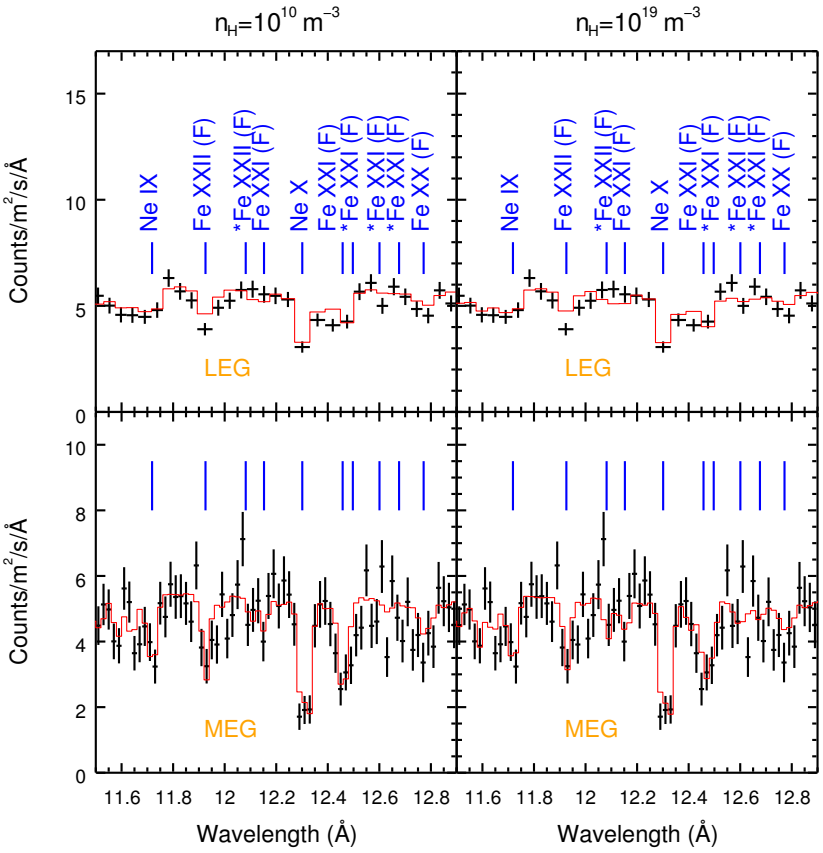

Figure 4.10: PION modeling of the spectra of NGC 5548 with $n_{\rm H} = 10^{10}$ m^{-3} (left panels) and 10^{19} m^{-3} (right panels). The spectral bin sizes are 0.025 Å (for LEG) and 0.01 Å (for MEG), respectively. The overall C statistics is 5146.0 (d.o.f. = 4843) at low density and 5158.9 (d.o.f. = 4842) at high density. The density sensitive metastable absorption lines of Fe XXII (B-like) and Fe XXI (C-like), from component F, are labeled with $*$.

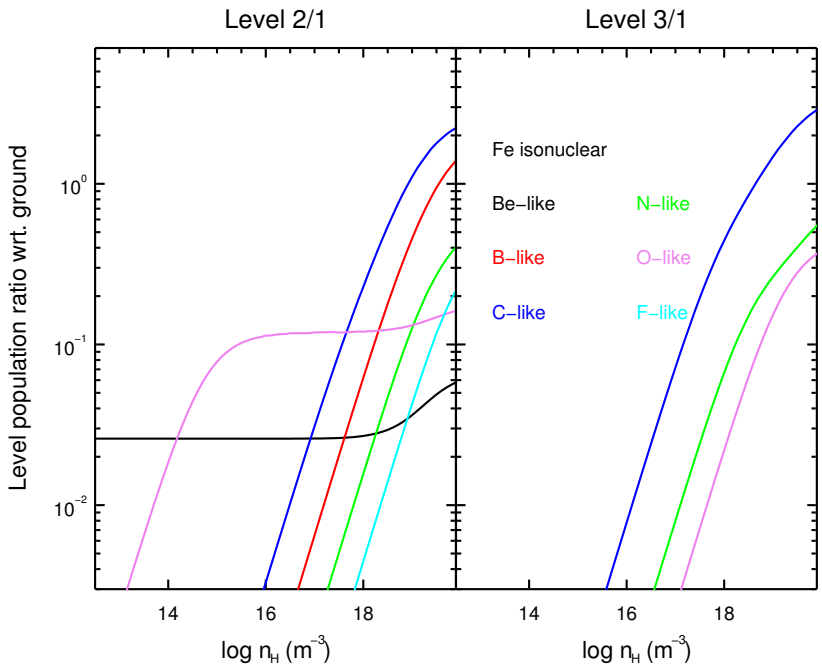

Figure 4.11: Ratio of metastable to ground level population as a function of density of the Fe isonuclear sequence (from Be-like to F-like) at the temperature of maximum ion concentration in ionization equilibria. The configuration and $^{2S+1}L_J$ notation of the ground (Level 1) and metastable levels (Level 2 and 3) are listed in Table 4.1.

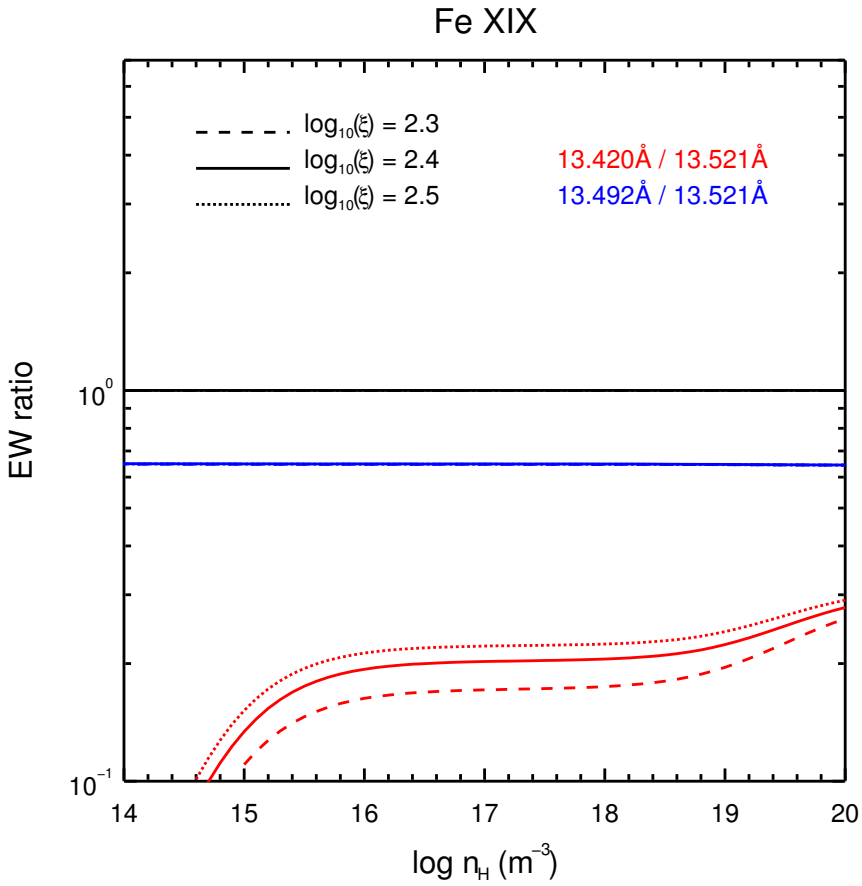

Figure 4.12: Equivalent width (EW) ratios for characteristic absorption lines of O-like Fe XIX. The two lines with λ =13.521 Å and 13.492 Å are from the ground level. The line with λ =13.420 Å is from the first excited level. Dashed (ξ = 2.3), solid (ξ = 2.4, where ion concentration reaches its maximum), and dotted (ξ = 2.5) lines indicate different ionization parameters of the photoionized plasma.

Table 4.8: Characteristic absorption lines from the ground and metastable levels in N-like to F-like iron ions.

	Index	1		2		3	
Sequence	n_j	Lower	Upper	Lower	Upper	Lower	Upper
Fe XX	2-2	$2s^2 2p^3$ ($^4S_{3/2}$)	$2s2p^4$ ($^4P_{5/2}$)	$2s^2 2p^3$ ($^2D_{3/2}$)	$2s2p^4$ ($^2D_{3/2}$)	$2s^2 2p^3$ ($^2D_{5/2}$)	$2s2p^4$ ($^2P_{3/2}$)
Fe XX	2-3	$2s^2 2p^3$ ($^4S_{3/2}$)	$2s^2 2p^2(^3P)3d$ ($^4P_{3/2}$)	$2s^2 2p^3$ ($^2D_{3/2}$)	$2s^2 2p^2(^3P)3d$ ($^2D_{5/2}$)	$2s^2 2p^3$ ($^2D_{5/2}$)	$2s^2 2p^2(^3P)3d$ ($^2F_{3.5}$)
Fe XX	1-2	$2s^2 2p^3$ ($^4S_{3/2}$)	$1s2s^2 2p^4$ ($^4P_{5/2}$)	$2s^2 2p^3$ ($^2D_{3/2}$)	$1s2s^2 2p^4$ ($^2D_{3/2}$)	$2s^2 2p^3$ ($^2D_{5/2}$)	$1s2s^2 2p^4$ ($^2D_{5/2}$)
Fe XIX	2-2	$2s^2 2p^4$ ($^3P_2$)	$2s2p^5$ ($^3P_2$)	$2s^2 2p^4$ ($^3P_0$)	$2s2p^5$ ($^3P_1$)	$2s^2 2p^4$ ($^3P_1$)	$2s2p^5$ ($^3P_2$)
Fe XIX	2-3	$2s^2 2p^4$ ($^3P_2$)	$2s^2 2p^3(^2D)3d$ ($^3D_3$)	$2s^2 2p^4$ ($^3P_0$)	$2s^2 2p^3(^2P)3d$ ($^3P_1$)	$2s^2 2p^4$ ($^3P_1$)	$2s^2 2p^3(^2D)3d$ ($^3D_2$)
Fe XIX	1-2	($^3P_2$) ($^3P_2$)	($^3P_2$) ($^3P_2$)	($^3P_0$) ($^3P_0$)	($^3P_1$) ($^3P_1$)	($^3P_1$) ($^3P_1$)	($^3P_2$) ($^3P_2$)
Fe XVIII	2-2	$2s^2 2p^5$ ($^2P_{3/2}$)	$2s2p^6$ ($^2S_{1/2}$)	$2s^2 2p^5$ ($^2P_{1/2}$)	$2s2p^6$ ($^2S_{1/2}$)	– – – –	– – – –
Fe XVIII	2-3	$2s^2 2p^5$ ($^2P_{3/2}$)	$2s^2 2p^4(^1D)3d$ ($^2D_{5/2}$)	$2s^2 2p^5$ ($^2P_{1/2}$)	$2s^2 2p^4(^1S)3d$ ($^2D_{3/2}$)	– – – –	– – – –
Fe XVIII	1-2	$2s^2 2p^5$ ($^2P_{3/2}$)	$1s2s^2 2p^6$ ($^2S_{1/2}$)	$2s^2 2p^5$ ($^2P_{1/2}$)	$1s2s^2 2p^6$ ($^2S_{1/2}$)	– –	– –

the density-sensitive line (13.420 Å) of O-like Fe XIX is sensitive to both ionization parameter and density (Figure 4.12). Additionally, from the observational point of view, we caution that the $n_j = 2 - 3$ transitions of Fe XVIII at 14.203 Å (ground) and 14.121 Å (metastable) might be blended with the O VIII absorption edge at 14.228 Å.

4.B. Comparison of the level population calculation with CHIANTI

CHIANTI (Del Zanna et al. 2015) is a widely used atomic code for analyzing emission line spectra from astrophysical sources. Similar to SPEX, CHIANTI also provides detailed calculations (e.g., level populations). Therefore, here we compare the level population calculations for collisional ionized equilibrium (CIE) plasmas, using the latest version of CHIANTI v8.0.8 (with atomic database v8.0.6[4]) and SPEX v3.04 (with SPEXACT v3.04) to show the effects of different atomic codes.

For simplicity, we only compare the population of the first five levels (i.e., the ground level and the first four excited levels) of the Fe isonuclear sequence from He-like Fe XXV to Ne-like Fe XVII. The level populations are calculated in both codes using the same abundance table (Lodders & Palme 2009), the same ionization balance (Bryans et al. 2009), and the same plasma temperature (where the ion concentration reaches its maximum). Figure 4.13 shows the level population ratio with respect to the ground as a function of plasma density ranging from 10^6 m^{-3} to 10^{20} m^{-3} (or 10^1 cm^{-3} to 10^{14} cm^{-3}).

For He-like Fe XXV and Li-like Fe XXIV, the level population ratios provided by the two codes are consistent with each other. For Be-like Fe XXIII to Ne-like Fe XVII, the level population ratios share the same increasing and/or flattening trend, whereas the two codes yield slightly different level population ratios (a factor of few). This is not totally unexpected, given the fact that the two codes do not use the same atomic data for individual atomic processes, and the two codes use different means of implementing the atomic data for the calculation (interpolation or parameterization). For instance, the CHIANTI atomic database includes various atomic data with $n \leq 5$ for almost all ions with $Z \leq 30$ in the He-like to Ne-like isoelectronic sequences, while the SPEXACT includes atomic data with $n \leq 8$ for He-like to C-like ions with $Z \leq 30$, and only Fe ions in the N-like to Ne-like isoelectronic sequences. The atomic data collected in both codes are state-of-the-art, yet still incomplete

[4] http://www.chiantidatabase.org/

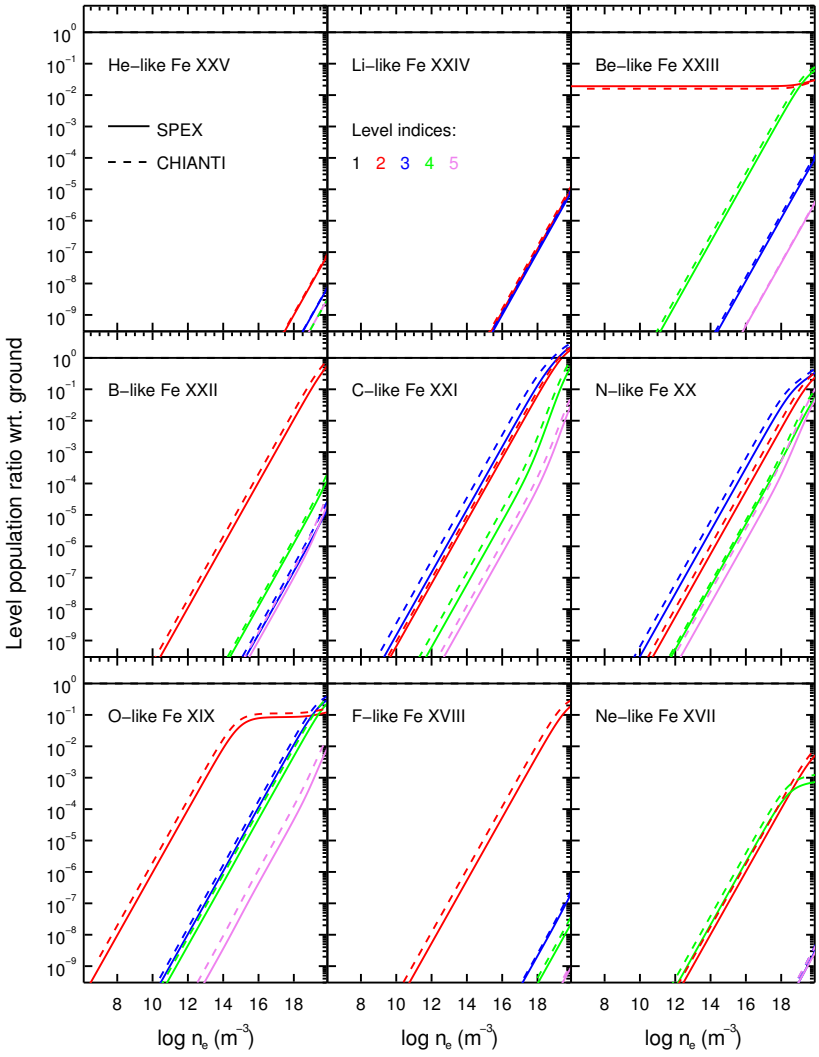

Figure 4.13: Level population ratio for the first four excited levels (level indices 2–5) of the Fe isonuclear sequence from He-like Fe XXV to Ne-like Fe XVII for collisional ionized equilibrium (CIE) plasma, using SPEXACT v3.04 (solid line) and CHIANTI v8.0.8 (dashed line). The CHIANTI atomic database v8.0.6 is used.

and not 100% accurate. Furthermore, the SPEX code parameterizes almost all the atomic data (e.g., Mao & Kaastra 2016; Urdampilleta et al. 2017), while CHIANTI uses interpolation instead.

In short, considering only the systematic uncertainties introduced by the different atomic data used in SPEX and CHIANTI, with the same density diagnostics in Be-like to Ne-like ions, the two codes are expected to estimate the plasma density to a similar order of magnitude. However, it is not clear which part(s) of the atomic data and/or code contribute to what percentage of the total "error" budget (i.e., the discrepancy between the codes) for the level population calculation of a specific level in a specific ion.

References

Arav, N., Chamberlain, C., Kriss, G. A., et al. 2015, A&A, 577, A37
Badnell, N. R. 2006, ApJS, 167, 334
Bryans, P., Landi, E., & Savin, D. W. 2009, ApJ, 691, 1540
Ciaravella, A., Raymond, J. C., Reale, F., Strachan, L., & Peres, G. 2001, ApJ, 557, 351
Collinge, M. J., Brandt, W. N., Kaspi, S., et al. 2001, ApJ, 557, 2
Del Zanna, G., Dere, K. P., Young, P. R., Landi, E., & Mason, H. E. 2015, A&A, 582, A56
Ebrero, J., Kaastra, J. S., Kriss, G. A., et al. 2016, A&A, 587, A129
Fabian, A. C. 2012, ARA&A, 50, 455
Gallagher, P. T., Mathioudakis, M., Keenan, F. P., Phillips, K. J. H., & Tsinganos, K. 1999, ApJ, 524, L133
Gu, M. F. 2008, Canadian Journal of Physics, 86, 675
Kaastra, J. S. & Bleeker, J. A. M. 2016, A&A, 587, A151
Kaastra, J. S., Detmers, R. G., Mehdipour, M., et al. 2012, A&A, 539, A117
Kaastra, J. S., Gu, L., Mao, J., et al. 2017, Journal of Instrumentation, 12, C08008
Kaastra, J. S., Kriss, G. A., Cappi, M., et al. 2014, Science, 345, 64
Kaastra, J. S., Mewe, R., & Nieuwenhuijzen, H. 1996, in UV and X-ray Spectroscopy of Astrophysical and Laboratory Plasmas, ed. K. Yamashita & T. Watanabe, 411–414
Kaastra, J. S., Raassen, A. J. J., Mewe, R., et al. 2004, A&A, 428, 57
Kaspi, S., Brandt, W. N., Netzer, H., et al. 2001, ApJ, 554, 216
Keenan, F. P., Conlon, E. S., Foster, V. J., Aggarwal, K. M., & Widing, K. G. 1993, Sol. Phys., 145, 291
Keenan, F. P., Katsiyannis, A. C., & Widing, K. G. 2004, ApJ, 601, 565
Keenan, F. P., Pinfield, D. J., Woods, V. J., et al. 1998, ApJ, 503, 953
King, A. L., Miller, J. M., & Raymond, J. 2012, ApJ, 746, 2
Kramida, A., Yu. Ralchenko, Reader, J., & and NIST ASD Team. 2015, NIST Atomic Spectra Database (ver. 5.3), [Online]. Available: https://physics.nist.gov/asd [2016, November 30]. National Institute of Standards and Technology, Gaithersburg, MD.
Krolik, J. H., McKee, C. F., & Tarter, C. B. 1981, ApJ, 249, 422
Landi, E. & Landini, M. 1998, A&A, 340, 265
Landi, E. & Miralles, M. P. 2014, ApJ, 780, L7
Lodders, K. & Palme, H. 2009, Meteoritics and Planetary Science Supplement, 72, 5154

Mao, J. & Kaastra, J. 2016, A&A, 587, A84
McKernan, B., Yaqoob, T., George, I. M., & Turner, T. J. 2003, ApJ, 593, 142
Mehdipour, M., Kaastra, J. S., & Kallman, T. 2016a, A&A, 596, A65
Mehdipour, M., Kaastra, J. S., Kriss, G. A., et al. 2016b, A&A, 588, A139
Mehdipour, M., Kaastra, J. S., Kriss, G. A., et al. 2015a, A&A, 575, A22
Mehdipour, M., Kaastra, J. S., & Raassen, A. J. J. 2015b, A&A, 579, A87
Miller, J. M., Raymond, J., Reynolds, C. S., et al. 2008, ApJ, 680, 1359
Nandra, K., Barret, D., Barcons, X., et al. 2013, ArXiv e-prints
Porquet, D., Dubau, J., & Grosso, N. 2010, Space Sci. Rev., 157, 103
Schurch, N. J., Warwick, R. S., Griffiths, R. E., & Kahn, S. M. 2004, MNRAS, 350, 1
Silva, C. V., Uttley, P., & Costantini, E. 2016, A&A, 596, A79
Smith, R. K., Abraham, M. H., Allured, R., et al. 2016, in Proc. SPIE, Vol. 9905, Space Telescopes and Instrumentation 2016: Ultraviolet to Gamma Ray, 99054M
Tarter, C. B., Tucker, W. H., & Salpeter, E. E. 1969, ApJ, 156, 943
Urdampilleta, I., Kaastra, J. S., & Mehdipour, M. 2017, A&A, 601, A85
Warren, H. P. & Brooks, D. H. 2009, ApJ, 700, 762

5

Anatomy of the AGN in NGC 5548: IX. Photoionized emission features in the soft X-ray spectra

Junjie Mao, J. S. Kaastra, M. Mehdipour, Liyi Gu, E. Costantini, G. A. Kriss, S. Bianchi, G. Branduardi-Raymont, E. Behar, L. Di Gesu, G. Ponti, P.-O. Petrucci, and J. Ebrero

The X-ray narrow emission line region (NELR) of the archetypal Seyfert 1 galaxy NGC 5548 has been interpreted as a single-phase photoionized plasma that is absorbed by some of the warm absorber components. This scenario requires these overlaying warm absorber components to be at a greater distance (from the central engine) than the X-ray NELR, which is not fully consistent with the distance estimates found in the literature. Therefore, we reanalyze the high-resolution spectra obtained in 2013–2014 with the Reflection Grating Spectrometer (RGS) on board *XMM*-Newton to provide an alternative interpretation of the X-ray narrow emission features. We find that the X-ray narrow emission features in NGC 5548 can be described by a two-phase photoionized plasma with different ionization parameters ($\log \xi = 1.3$ and 0.1) and kinematics ($v_{\rm out} = -50$ and -400 km s^{-1}),

This chapter has been published in Astronomy & Astrophysics, 2018, 612, A18.

but no further absorption by the warm absorber components. The X-ray and optical NELR might be the same multiphase photoionized plasma. The X-ray and the optical NELRs have comparable distances and asymmetric line profiles, and the underlying photoionized plasma is turbulent and compact in size. The X-ray NELR is not the counterpart of the UV/X-ray absorber outside the line of sight because their distances and kinematics are not consistent. In addition, X-ray broad emission features that we find in the spectrum can be accounted for by a third photoionized emission component. The RGS spectrum obtained in 2016 is analyzed as well, where the luminosity of most prominent emission lines (the O VII forbidden line and O VIII Lyα line) are the same (at a 1 σ confidence level) as in 2013–2014.

5.1. Introduction

Two types of emission lines are commonly observed in the optical spectra of active galactic nuclei (AGN): broad emission lines with a velocity broadening of a few 10^3 km s^{-1} and narrow emission lines with a velocity broadening of a few 10^2 km s^{-1}. The optical broad and narrow emission lines stem from the broad and narrow emission line regions (BELR and NELR, see Netzer 2015, for a recent review); the former are closer to the central engine (a few light days to weeks, Peterson et al. 2004) and the latter farther away (at least a few parsecs, Bennert et al. 2006a,b). In the X-ray band, broad and narrow emission lines are also observed (e.g., Costantini et al. 2007, 2016; Kaastra et al. 2000; Steenbrugge et al. 2005), often along with the characteristic narrow radiative recombination continua (RRC) of a photoionized plasma. The spatial extent and overall morphology of the optical and the X-ray NELRs are remarkably similar in a small sample of nearby Seyfert 2 galaxies (Bianchi et al. 2006). Nonetheless, there is no conclusive evidence that the optical and X-ray narrow emission features originate from the same photoionized plasma with a multiphase nature.

In terms of detailed spectral modeling of the narrow emission features in the X-ray band, a two-step approach is commonly used. First, a phenomenological local fit (e.g., Guainazzi & Bianchi 2007) is performed for individual emission lines and RRC. Typically, the (local) continuum is simply modeled as a (local) power law or spline function plus a model for RRC, and an emission line is modeled with a Gaussian or delta profile. The local fit is straightforward and useful, and provides primary information: whether a single line is shifted and/or broadened, the temperature of a photoionized plasma (via the width of the RRC), the temperature and density of the plasma (via the line ratios of the He-like triplets), etc.

With the knowledge obtained from the local fit, the entire spectrum is then modeled with a self-consistent plasma model or with a combination of plasma models (e.g., Guainazzi et al. 2009). The plasma model can be a photoionized plasma either with a single photoionized component (e.g., Whewell et al. 2015) or multiple photoionized components (e.g., Armentrout et al. 2007; Kallman et al. 2014; Kinkhabwala et al. 2002; Longinotti et al. 2008; Marinucci et al. 2011; Nucita et al. 2010), and sometimes a collisional ionized equilibrium (CIE) plasma, which is associated with star formation (Guainazzi et al. 2009) or jets (Bianchi et al. 2010).

For the photoionized plasma model, the widely used approach is to simulate a set of photoionized spectra with the Cloudy code (Ferland et al. 2017) for a fixed ionizing spectral energy distribution (SED) and for a grid of physical parameters, including

the ionization parameter, the line of sight column density, and sometimes the plasma number density and microscopic turbulence velocity as well. The number of free parameters and the size of the grid are limited; otherwise, it is computationally too expensive to simulate. Subsequently, the observed spectra are compared with these pre-calculated models, and the best-fit of the physical parameters is derived from the closest match. This last step is carried out in a separate spectral fitting package, e.g., XSPEC (Arnaud 1996).

A different approach for the photoionized plasma model is used here (see also Mao et al. 2017). We use SPEX (v3.03.02 Kaastra et al. 1996) to fit the entire observed spectra on the fly. The advantage of the SPEX code is that it includes an extensive atomic database and self-consistent plasma models, e.g., PION[1] for the photoionized plasma, which utilizes state-of-the-art atomic data (Kaastra 2017b). We refer to Mehdipour et al. (2016a) for a detailed comparison of the photoionization calculation between SPEX, Cloudy, and XSTAR (Bautista & Kallman 2001; Kallman & Bautista 2001). In each step of the photoionized plasma fitting the intrinsic SED, thermal equilibrium, ionization balance, level population, transmission, emissivity, and line broadening are calculated in real time to account for the absorption and emission features self-consistently. In short, the photoionization calculation is consistent with the instant ionizing SED and without pre-calculations using grid-defined parameters, thus more freedom and higher consistency can be achieved in SPEX.

NGC 5548 is the archetypal Seyfert 1 galaxy, with broad and narrow emission features across its optical to X-ray spectra (e.g., Chiang et al. 2000; Kaastra et al. 2002; Korista et al. 1995; Peterson et al. 2002; Steenbrugge et al. 2005). The extensive multiwavelength campaign of NGC 5548 in 2013–2014 (Kaastra et al. 2014; Mehdipour et al. 2015) unveiled a special state of the source, where the soft X-ray flux is highly obscured. Such a special state offers a unique opportunity to study the narrow emission lines and radiative recombination continua that were previously hidden by the unobscured continuum (Detmers et al. 2009; Kaastra et al. 2002; Steenbrugge et al. 2005). With a detailed study of the narrow emission features using both the local fit and Cloudy based photoionization modeling, Whewell et al. (2015) interpret the X-ray NELR as a single-phase photoionized plasma that is absorbed by the warm absorber components B+E or A+B+C (see Table S2 of Kaastra et al. 2014, for the nomenclature). That is to say, these warm absorber

[1]The model description and a list of parameters for the PION model can be found in the SPEX manual (Section 4.29).

components intervene along the line of sight from the X-ray narrow line emitter to the observer.

This scenario does not fully agree with the distance estimates of the X-ray NELR and warm absorber components in NGC 5548. Using the variability of the forbidden line of O VII, Detmers et al. (2009) derived a distance of 1–15 pc for the X-ray NELR, consistent with the optical NELR distance estimate of 1–3 pc (Peterson et al. 2013) and joint optical and X-ray NELR distance estimate of ~ 2.4 pc (Landt et al. 2015). According to the Cloudy-based photoionization model, Whewell et al. (2015) found that the X-ray narrow emission lines originate mainly from the illuminated face of the X-ray NELR with a distance of 14 pc. Ebrero et al. (2016) estimate the distance of the warm absorber components based on variability, with component A and B at least 10 pc away from the central engine and components C to F within 5 pc from the central engine. Nonetheless, based on a spectral analysis using the density sensitive metastable absorption lines, Mao et al. (2017) find that the warm absorber component B is even closer (< 0.23 pc, 3σ upper limit) than the optical NELR rather than farther away. Ebrero et al. (2016) constrain the lower limit of the distance of the warm absorber component B based on the non-detection of variability on a timescale of 500 days. However, the authors also point out that there are marginal hints of variability at 4 and 60 days. If the variability at a shorter timescale is true, the inferred distance of component B would be much smaller.

Therefore, we reanalyze the high-resolution spectra of NGC 5548 obtained with the Reflection Grating Spectrometer (RGS, den Herder et al. 2001) on board *XMM-Newton* (Jansen et al. 2001) to provide an alternative interpretation of the X-ray narrow emission features. To be more specific, we attempt to model the soft X-ray emission features with a multiphase photoionized plasma with no additional absorption by the warm absorber components. Whewell et al. (2015) did not consider this scenario in their study.

In Section 6.2, we present the observed RGS spectrum. We describe the detailed spectral analysis in Section 6.3, including the phenomenological local fit (Section 5.3.1) and the physical global fit (Section 5.3.2). The physical global fit is based on the self-consistent photoionization model PION in the SPEX code, with both the single-phase and multiphase scenarios studied. We discuss the relation between the X-ray and optical narrow emission line region in Section 5.4.1 and the relation between the X-ray emitter and absorber in Section 5.4.2, respectively. We justify our usage of the unobscured ionizing SED for the X-ray emitter in Section 5.4.3. We also point out the abnormally high Lyγ/Lyα ratio of N VII and discuss it in terms

Table 5.1: Observation log of NGC 5548 in 2016 (PI: G. Kriss) with *XMM*-Newton.

Start date	Exp. (ks)	ObsID
2016-01-14	37	0771000101
2016-01-16	34	0771000201

Notes. The observation log for 2013–2014 can be found in Table 1 in Mehdipour et al. (2015).

of a possible charge exchange component in Section 5.4.4. The summary can be found in Section 6.4.5.

5.2. Observations and data reduction

The RGS data used here were obtained in two epochs, June 2013 – February 2014 (PI: J. Kaastra) and January 2016 (PI: G. Kriss), respectively. Data for the first epoch (2013–2014) were taken as part of a large multiwavelength campaign of NGC 5548 (Kaastra et al. 2014). There are in total 14 XMM-*Newton* observations (∼50 ks exposure each), 12 taken between 22 June and 31 July 2013 and 2 more taken in December 2013 and February 2014. The observation log for 2013–2014 can be found in Mehdipour et al. (2015, their Table 1); our Table 6.1 lists the observation log for 2016.

Details of the RGS data reduction method are similar to those described in Kaastra et al. (2011). The first-order RGS1 and RGS2 spectra for all observations are stacked for each epoch, with a total exposure of ∼770 ks (for 2013–2014) and ∼70 ks (for 2016), respectively. The stacked RGS spectrum of 2013–2014 is the same as that used by Whewell et al. (2015) for the study of the narrow emission features.

5.3. Spectral analysis and results

SPEX v3.03.02 is used for the spectral analysis. We use the C-statistic throughout this work (Kaastra 2017a). Statistical errors are quoted at the 68% confidence level ($\Delta C = 1.0$), unless indicated otherwise. The spectral fit is performed in the 7–35 wavelength range. The stacked 2013–2014 and 2016 spectra are both optimally binned (Kaastra & Bleeker 2016) for the following spectral analysis (Sect. 6.3). The redshift of the AGN is fixed to $z = 0.017175$ (de Vaucouleurs et al. 1991), as given in the NASA/IPAC Extragalactic Database (NED).

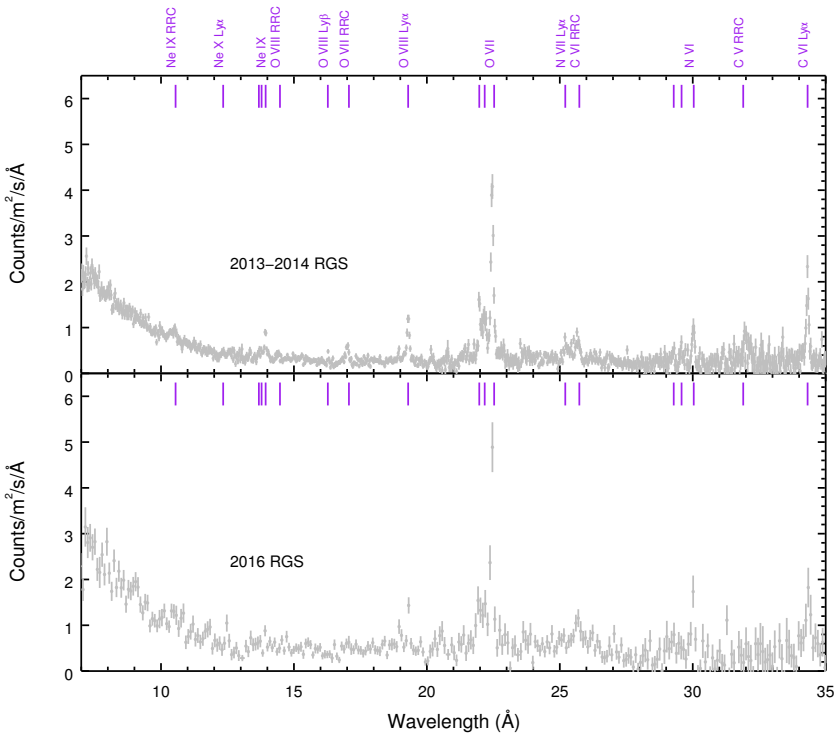

Figure 5.1: Stacked RGS spectra (in the observed frame) in 2013–2014 (upper panel) and 2016 (lower panel, rebinned for clarity).

5.3.1. Phenomenological local fit

In order to check the variability of the narrow emission features between 2013–2014 and 2016, we perform a simple local fit to spectra from the two epochs with a spline continuum model (SPLN in SPEX, see also Detmers et al. 2008), Gaussian line models (GAUS), and radiative recombination continua (RRC).

Even in the 770 ks 2013-2014 spectrum, the X-ray broad emission lines are difficult to fit due to their low significance (Whewell et al. 2015). Therefore, in this exercise, we do not include them in either spectra. In the 2016 spectrum, the Lyα line of O VIII and the forbidden line of O VII can be relatively well constrained, with statistical uncertainties $\lesssim 20\%$. The rest of the lines and RRC given in Table 5.2 have statistical uncertainties between 30% and 100% in the 2016 spectrum. In Table 5.2 we compare the intrinsic (unabsorbed) luminosity of these lines and RRC between the two epochs.

The most prominent narrow emission lines (the O VIII Lyα and O VII forbidden

Table 5.2: Intrinsic (unabsorbed) luminosity of the prominent narrow emission features for the 2013–2014 and 2016 RGS spectra of NGC 5548.

Ion	Line/RRC	λ_0 Å	$L_{2013-2014}$ 10^{32} W	L_{2016} 10^{32} W
Ne IX	$1s^2$	10.37	10.3 ± 5.6	23 ± 22
Ne IX	Heα (f)	13.70	6.7 ± 1.2	3.9 ± 2.2
O VII	$1s^2$	16.79	8.7 ± 1.6	6.4 ± 5.6
O VIII	Lyα	18.97	11.2 ± 0.7	11.2 ± 1.9
O VII	Heα (f)	22.10	35.7 ± 1.8	39.5 ± 5.4
C VI	$1s$	25.30	13.9 ± 6.6	8.9 ± 6.7
N VI	Heα (f)	29.53	6.4 ± 0.9	13.5 ± 4.3
C VI	Lyα	33.74	11.7 ± 1.2	8.3 ± 5.6

Notes. λ_0 is the rest-frame wavelength.

lines) have remained constant (at a 1σ confidence level) in the two epochs June 2013 – February 2014 and January 2016. This is not totally unexpected, as shown in Table 2 of Detmers et al. (2009); the O VII line flux is also consistent within 1σ for two epochs on a similar timescale, December 1999 – February 2000 and January 2002.

On the other hand, some weak features might have varied by a factor of 2 (the Ne IX RRC and N VI forbidden line), but still within a 2σ confidence level.

5.3.2. Physical global fit

For the physical global fit (Section 5.3.2), we first model the high-quality 2013–2014 spectrum with different models (Section 5.3.2.1). Then we simply apply the best-fit model to the low-quality 2016 spectrum (Section 5.3.2.2).

Our global fit includes the following components: (1) the intrinsic broadband spectral energy distribution (SED) of the AGN; (2) the Galactic absorption; (3) the continuum absorption caused by the obscurer; (4) the absorption features caused by the warm absorber; and (5) the narrow and/or broad emission features caused by the X-ray emitter.

The intrinsic SED consists of a Comptonized disk component (COMT in SPEX, for optical to soft X-ray), a power-law component (POW for X-ray), and a reflection component (REFL for the Fe K line and hard X-ray). For the 2013–2014 spectral analysis, all the relevant parameters are fixed to those values given in Mehdipour

et al. (2015), where the best constraints on these parameters have been obtained from multiwavelength data. For the 2016 spectral analysis, we fixed the parameters in the COMT component to values that corresponds to the average UVW2 flux in 2016 (the correlations can be found in Mehdipour et al. 2016b). The power-law and reflection components are allowed to vary in order to match the EPIC-pn data.

The Galactic absorption with $N_{\rm H} = 1.45 \times 10^{24}$ m^{-2} (Wakker et al. 2011) is modeled with the collisional ionization equilibrium absorption model (hereafter HOT) (de Plaa et al. 2004; Steenbrugge et al. 2005) in SPEX. The electron temperature of the HOT component is fixed to 0.5 eV to mimic the transmission of a neutral gas.

The continuum absorption caused by the obscurer is modeled with two XABS components (Kaastra et al. 2014; Mehdipour et al. 2017). The line of sight (LOS) hydrogen column densities ($N_{\rm H}$) and absorption covering factors ($f_{\rm cov}$) are allowed to vary in both 2013–2014 and 2016 spectra. The ionization parameters of the two XABS components are treated differently: the warmer one is allowed to vary ($\log \xi \sim -1$) and the cooler one is fixed to -4 (Di Gesu et al. 2015).

The absorption features caused by the warm absorber are accounted for using six PION components. In both the 2013–2014 and 2016 spectra the hydrogen column densities ($N_{\rm H}$), outflow velocities ($v_{\rm out}$), and microscopic turbulence velocities ($v_{\rm mic}$) of the PION components are fixed to the values given in Mao et al. (2017), which are obtained by fitting the high-quality 2002 *Chandra* grating spectra of NGC 5548. Nonetheless, the ionization parameters ($\log \xi$) can differ for these three epochs, due to the variability of the obscurer and to the changes in the intrinsic SED (Cappi et al. 2016). The ionization parameters are assumed to be proportional to the $1 - 10^3$ Ryd ionizing luminosity. That is to say, the number density times distance squared ($n_{\rm H} r^2$) in the two later epochs is assumed to be the same as in 2002.

The narrow and broad emission features caused by the X-ray emitter (sometimes called the warm mirror) are also modeled with PION. Six free parameters of each emission PION component are allowed to vary, including the hydrogen column densities ($N_{\rm H}$), ionization parameters ($\log \xi$), outflow velocities ($v_{\rm out}$), turbulence velocities ($v_{\rm mic}$), and the emission covering factors ($C_{\rm cov}$, see next paragraph). Additionally, each emission PION component is convolved with a Gaussian velocity broadening model (VGAU in SPEX), with the velocity parameter ($v_{\rm mac}$) free to vary, to account for macroscopic motion.

It should be noted that there are two covering factors in the PION model. The absorption covering factor $f_{\rm cov}$ is used to model any partial covering in the line

of sight (similar to that of the XABS component). The emission covering factor, $C_{\rm cov} = \Omega/4\pi$, corresponds to the normalized solid angle sustained by the emitting region as seen from the central engine. In our modeling, each absorption PION component has fixed $f_{\rm cov} = 1$ and $C_{\rm cov} = 0$, while each emission PION component has fixed $f_{\rm cov} = 0$ and free $C_{\rm cov} \in (0,\ 1)$. Furthermore, the ionizing SED for the absorption PION components is the obscured SED, as the obscurer locates between the warm absorber and the central engine (Kaastra et al. 2014). Nevertheless, the ionizing SED received by the emission PION components is assumed to be unobscured, and we will discuss this in detail in Section 5.4.3. Unless indicated otherwise, the proto-solar abundances of Lodders & Palme (2009) are used for all plasma models (HOT, XABS, and PION).

5.3.2.1. The 2013–2014 RGS spectrum

Five different models are used for the emission features in the RGS band. We start with a single-phase photoionized emitter (denoted Model S0), which can reproduce well some but not all of the observed narrow emission features. In particular, Model S0 fails to match the RRC of O VII (~17 Å) and C VI (~32 Å), the forbidden lines of N VI (~ 30 Å), etc. The fit residuals can be found in the top panels of Figures 5.2 and 5.3. The residuals indicate that either additional absorption is required or the X-ray emitter has at least two emission components.

Following Whewell et al. (2015), we apply absorption caused by the warm absorber components B+E (Model S1) or A+B+C (Model S2) to the single-phase photoionized emitter. As expected, the C-stat is significantly improved for both models (Table 5.3). Model S2 yields parameters that are more consistent with those of Whewell et al. (2015), i.e., a mildly ionized ($\log \xi \sim 1 - 1.5$), blueshifted ($v_{\rm out} \sim -300$ km s^{-1}), turbulent ($v_{\rm mic} \sim 200$ km s^{-1}) plasma with $N_{\rm H} \sim 10^{25-26}$ m^{-2}. The different values of the best-fit parameters and C-stat between the present work and Whewell et al. (2015) are not unexpected. We use here a narrower wavelength range (7–35 Å), ignoring the 5.7–7 Å and 35–38.2 Å wavelength ranges where the noise is relatively large and no strong lines or RRC are expected. Additionally, due to the different atomic database and calculation used by Cloudy and SPEX, fitting the same high-resolution spectra can lead to best-fit parameters that differ by 10–40% (Mehdipour et al. 2016a).

Alternatively, we also try a model with two emission components (Model D) to account for the narrow emission features. The hotter (~ 4.1 eV) component (EM 1) has a higher luminosity ($\sim 1.2 \times 10^{34}$ W in the 7–35 Å band) and a higher ratio of

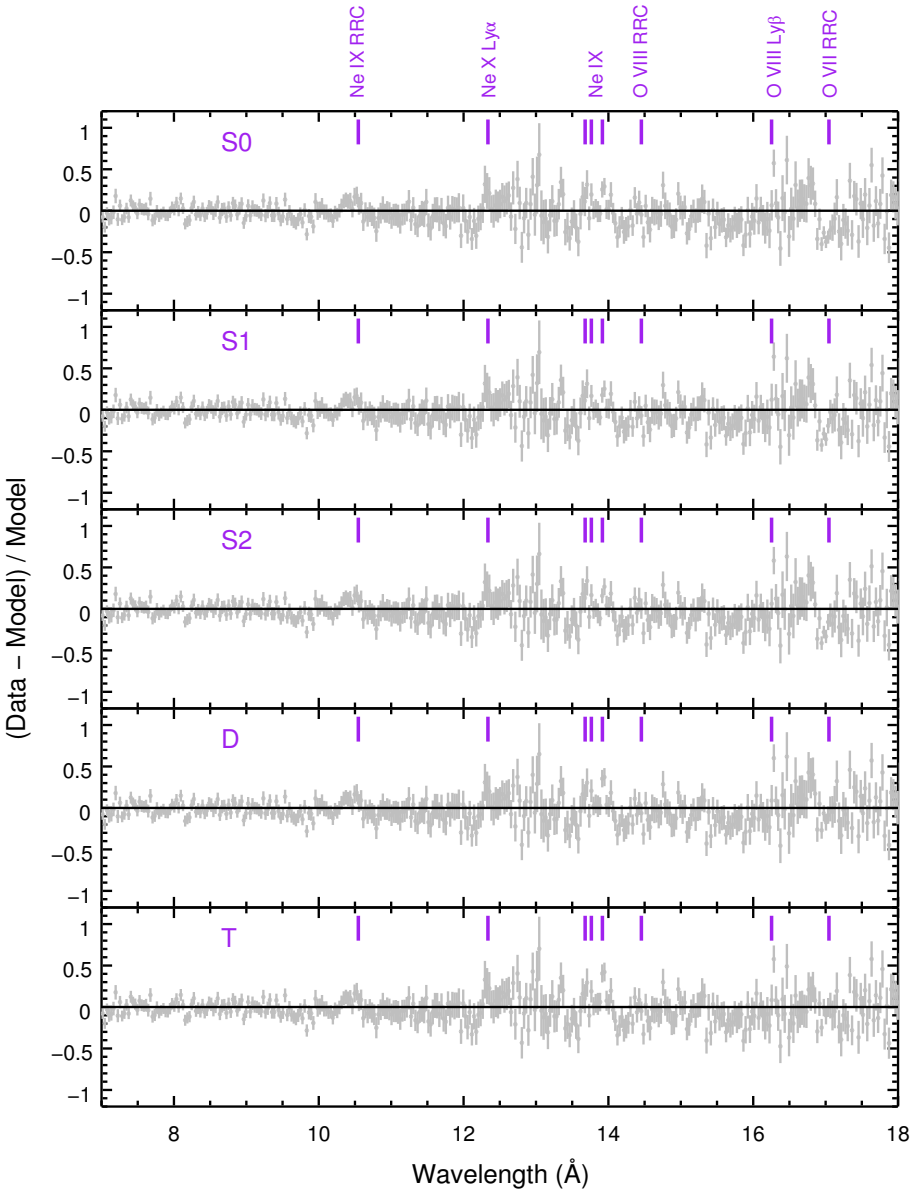

Figure 5.2: Fit residuals of the physical models in the 7–18 Å band.

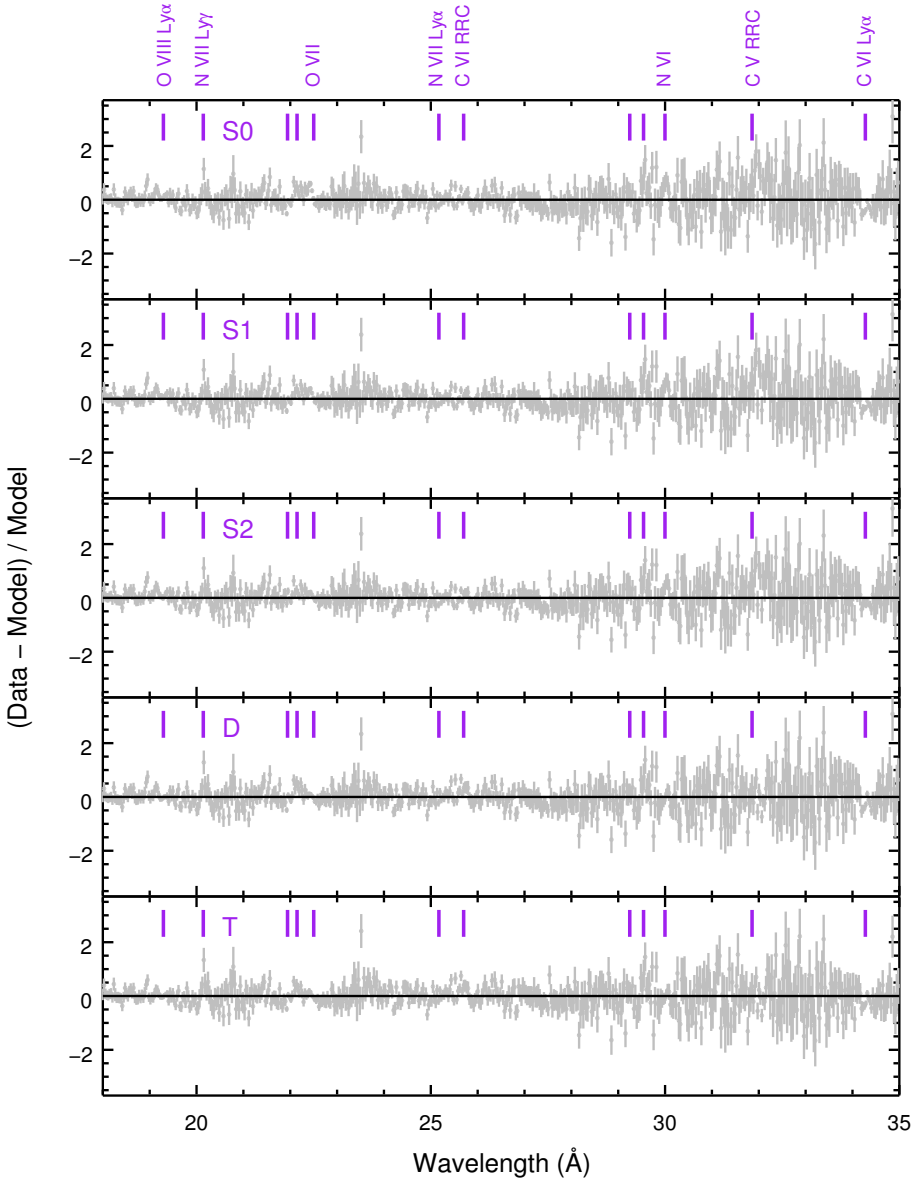

Figure 5.3: As Figure 5.2, but in the 18–35 Å band.

Table 5.3: Photoionized models of the emission features for NGC 5548.

Model	Comp.	$N_{\rm H}$ (10^{25} m^{-2})	log (ξ) (10^{-9} W m)	$v_{\rm mic}$ (km s^{-1})	$v_{\rm out}$ (km s^{-1})	$C_{\rm cov}$ (%)	$v_{\rm mac}$ (km s^{-1})	C-stat	d.o.f.
S0	EM 1	12.7 ± 1.9	1.18 ± 0.02	460 ± 30	-100 ± 20	2.4 ± 0.3	< 210	1774	920
S1	EM 1	12.4 ± 1.4	1.23 ± 0.02	420 ± 30	-190 ± 10	2.9 ± 0.3	< 250	1652	920
S2	EM 1	6.3 ± 1.2	1.20 ± 0.02	200 ± 50	-277 ± 4	6.3 ± 0.9	400 ± 40	1569	920
2*D	EM 1	14.7 ± 0.1	1.30 ± 0.02	520 ± 40	-49 ± 6	1.8 ± 0.6	< 160	2*1567	2*914
	EM 2	19.3 ± 1.3	0.14 ± 0.04	250 ± 60	-410 ± 50	0.60 ± 0.04	< 220		
3*T	EM 1	9.7 ± 1.3	1.31 ± 0.02	400 ± 30	-47 ± 4	2.2 ± 0.2	< 100	3*1525	3*910
	EM 2	30 ± 7	0.13 ± 0.05	< 280	-420 ± 30	0.41 ± 0.07	260 ± 80		
	EM 3	23 ± 6	1.24 ± 0.07	100 (f)	0 (f)	0.5 ± 0.3	7400 ± 1100		

Notes. The emission covering factor ($C_{\rm cov} = \Omega/4\pi$) refers to normalized the solid angle (Ω) subtended with respect to the central engine. The expected C-stat is 935 ± 43 for all the models. The degree of freedom (d.o.f.) is for the RGS band. For EM 3 in Model T, $v_{\rm mic}$ and $v_{\rm out}$ are frozen.

radiation to gas pressure[2] ($\Xi \sim 8$). The cooler (~ 1.6 eV) component (EM 2) has a lower luminosity ($\sim 3.4 \times 10^{33}$ W in the 7–35 Å band) and a lower ratio of radiation to gas pressure ($\Xi \sim 1.4$). The C-stat is improved significantly when comparing Model D to Model S0 ($\Delta C \sim -200$, compared with the root-mean-square deviation 43 of the expected C-stat), but it is negligible ($\Delta C = -2$) when compared to Model S2, as Model D fits the RRC of O VII better, yet the Lyα line of C VI slightly worse. Adding a third emission component (EM 3 in Model T) with a very broad line profile can further improve the C-stat ($\Delta C \sim -40$), but not significantly compared with the root-mean-square deviation 43 of the expected C-stat. The best-fit (Model T) to the 7–35 Å wavelength range RGS data is shown in Figure 5.5.

The narrow emission lines and RRC of Ne X (H-like) and Ne IX (He-like) are underestimated with all the models above. However, adding another emission component with a narrow line profile (including both the turbulent and Gaussian velocity broadening) does not improve the C-stat. An ad hoc solution is to use a super-solar Ne abundance (1.7 ± 0.2) for the highly ionized emission component (EM 1), which fits the Ne emission features well and improves the C-stat ($\Delta C \sim -30$).

In all the models above, the microscopic turbulence velocity ($v_{\rm mic}$) and the macroscopic motion ($v_{\rm mac}$) velocity are highly degenerate. That is to say, the 1σ uncertainties on $v_{\rm mic}$ and $v_{\rm mac}$ are underestimated ($\lesssim 30\%$) when considering either of the two parameters alone, as in Table 5.3. Figure 5.4 shows the confidence level contours of EM 1 and 2 in Model T. In this case, $v_{\rm mac}$ is less well constrained than $v_{\rm mic}$. The former is merely constrained by the velocity broadening of the line, while the latter puts an extra limit on the optical depth of the line. When $v_{\rm mac}$ is negligible, $v_{\rm mic}$ accounts for both the optical depth and velocity broadening. On the other hand, if $v_{\rm mic}$ is negligible (not the case for EM 1 in Model T), $v_{\rm mac}$ dominates the line broadening.

5.3.2.2. The 2016 RGS spectrum

In the global fit of the 2016 spectrum the power-law component, the reflection component, and the two XABS components (Section 5.3.2) are allowed to vary. Assuming the X-ray emitter remains unchanged between the two epochs (Section 5.3.1), with Model T for the narrow and broad emission features the ratio of best-fit C-stat to expected C-stat is 1443/1304 for the RGS band. Contrary to our simple assump-

[2]The ratio of radiation to gas pressure, also known as the pressure form of the ionization parameter, $\Xi = L/(4\pi r^2 n_{\rm H} ckT) = \xi/(4\pi ckT)$, where L is the 1–1000 Ryd ionizing luminosity, r the distance of the slab, $n_{\rm H}$ the hydrogen number density, k the Boltzmann constant, and T the electron temperature (Krolik et al. 1981).

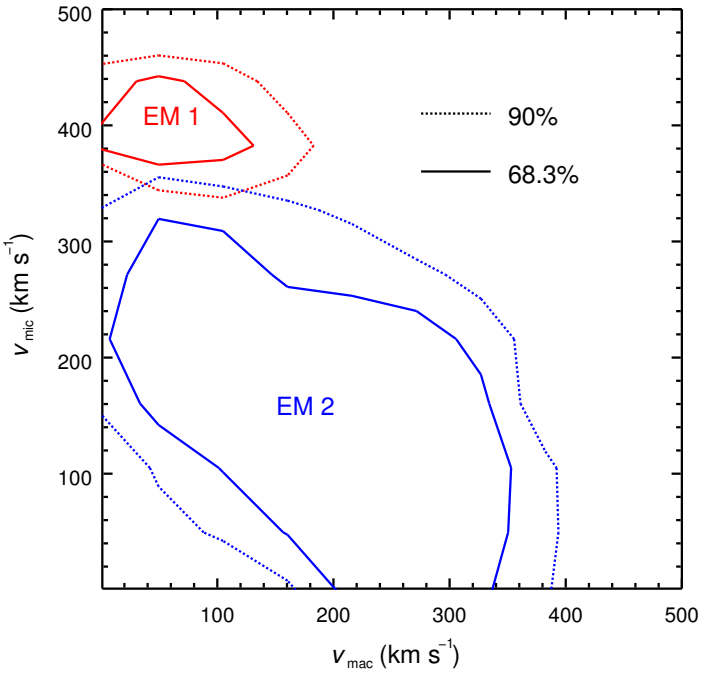

Figure 5.4: Confidence level contours for the microscopic turbulence velocities (v_{mic}) and macroscopic motion velocities (v_{mac}) of EM 1 (in red) and 2 (in blue) in Model T. The solid and dotted contours refer to 68.3% (or $\Delta C = 2.30$) and 90% (or $\Delta C = 4.61$), respectively.

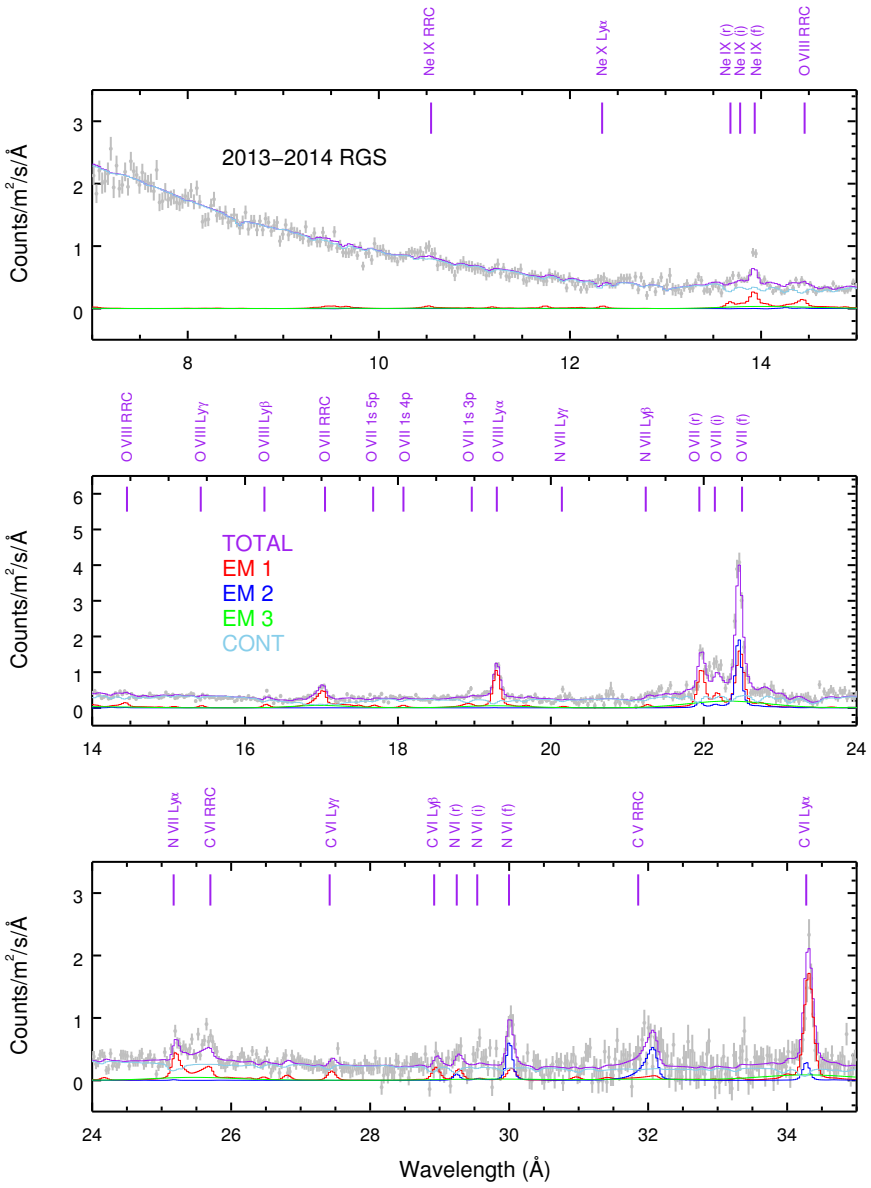

Figure 5.5: Best-fit to the 2013–2014 RGS spectrum with three emission components (Model T) for the narrow and broad emission features.

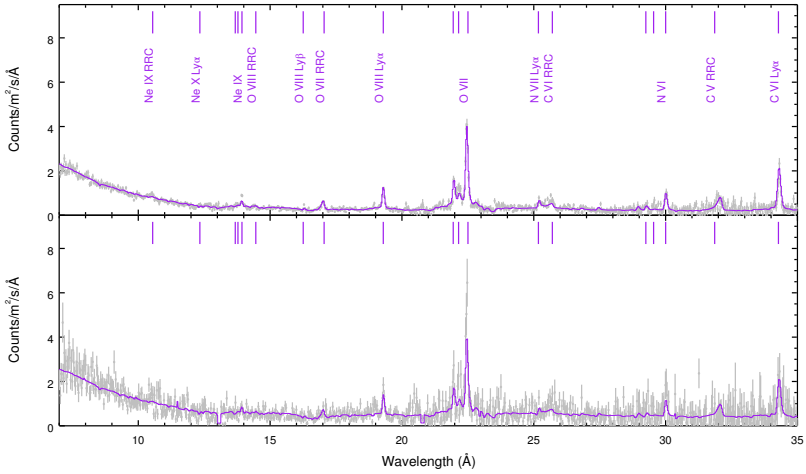

Figure 5.6: With the model of three emission components (Model T), the best-fit to the RGS spectra (in the observed frame) in 2013–2014 (upper panel) and 2016 (lower panel, rebinned for clarity).

tion that the narrow emission features are constant between the two epochs, we find that the forbidden lines of O VII and N VI are underestimated in our model when applied to the 2016 spectrum. These results are similar to what we found with the simple phenomenological fit (Section 5.3.1). Figure 5.6 shows the comparison of the best-fit model to both spectra in 2013–2014 and 2016.

5.4. Discussion

5.4.1. In relation to the optical NELR

From the variability of the optical narrow emission line [O III] 4959 Å and 5007 Å, Peterson et al. (2013) deduced that the optical narrow emission line region (NELR) has a radius of 1–3 pc with $n_{\rm e} \sim 10^{11}$ m^{-3}. A variability study of the X-ray narrow emission line [O VII] 22.10 Å yields an X-ray NELR distance of 1–15 pc (Detmers et al. 2009), which is consistent with the optical NELR. We cannot constrain the density and distance in the X-ray spectra. Although the He-like triplet of O VII is prominent, the associated density diagnostic is not effective since the forbidden-to-intercombination line ratio of O VII is strongly sensitive to the density only when $n_{\rm e} \sim 10^{15-18}$ m^{-3} (Porquet & Dubau 2000, their Fig. 10), which is too high for the NELR.

The asymmetric line profiles of the [O III] lines indicate that the NELR has an

outflowing component, with $\mathrm{HWHM_{blue}/HWHM_{red}} \simeq 2.12$ with an outflow velocity of ~ 460 km s^{-1} (Peterson et al. 2013). Similarly, the line profile of O VII observed in the X-ray band is also asymmetric (see Fig. 3 in Whewell et al. 2015). This can also be seen in our Models D and T, where two emission components with different outflow velocities are required. The emission component (EM 2) that dominates the forbidden lines of O VII and N VI (but not that of Ne IX, see Figure 5.5) is blueshifted (~ -400 km s^{-1}). The other emission component (EM 1), which dominates the Lyα lines of O VIII, N VII and C VI (Figure 5.5), has a negligible outflow velocity. Such divergent kinematic behavior can also be found in the phenomenological fit by Whewell et al. (2015, their Table 6).

We point out that Peterson et al. (2013) attribute the velocity broadening to the virial motion of the gas and no microscopic turbulence velocity broadening is taken into account. As noted by Kraemer et al. (2007), it is possible that microturbulence is present in the optical NELR of NGC 5548. Furthermore, if turbulence dissipates within the NELR, the plasma can be heated in excess of the temperature corresponding to photoionization. In our photoionization modeling of the X-ray narrow emission features, nondissipative microturbulence is taken into account. That is to say, the microscopic and macroscopic velocity broadening are both taken into account, but no extra heating is used to solve the thermal equilibrium.

In reality, it is possible that turbulence dissipates within the NELR; in practice, it is difficult to model the emergent spectrum. On the one hand, the extra heating can be included via the external heating option in the PION model[3] if we know the scale length over which the turbulence dissipates, the plasma mass density, and turbulence velocity of the photoionized plasma (Bottorff & Ferland 2002, their Eq. 1). The dissipation scale length and direction, as well as the mass density, can only be assumed in our analysis. On the other hand, the line broadening might appear to be different for the resonance and forbidden lines. Considering a slab with suitable ionization parameter for the resonance and forbidden lines, assuming that the turbulence dissipation direction is along the line of sight from the central engine toward the observer and that the dissipation length scale equals the size of the slab, the observed broadening of the forbidden lines is the integrated result of velocity broadening across the entire slab because they are optically thin. In contrast, due to the large optical depth, the observed resonance lines are only those escaping from the skin ($\tau \sim 1$) of the far side of the slab (with respect to

[3] In Kraemer et al. (2007), the dissipative heating is introduced via the additional heating terms in the Cloudy modeling.

the central engine); therefore, they are less broadened since turbulence converts to heating at the far side. In short, in order to model the emergent spectrum of a dissipative turbulent photoionized plasma, several assumptions are required, and the line broadening effects for resonance and forbidden lines are not trivial.

The bottom line is that the total velocity broadening of the narrow emission lines is $300 - 500$ km s^{-1} for individual emission components, well in excess of the thermal broadening. Both the microscopic turbulence and macroscopic motions can contribute to the total velocity broadening, but the two velocities are highly degenerate (Figure 5.4).

Furthermore, regardless of the number of emission components we used for the X-ray narrow emission features, the best-fit emission covering factor $C_{\rm cov} = \Omega/4\pi$ is rather small: $\sim 6\%$ for Model S2 and $2 - 3\%$ for the other models. This implies a compact geometry for the X-ray NELR. We caution that the photoionized plasma is assumed to be uniform with the PION model. If the NELR is clumpy, then the true covering factor can be larger. On the other hand, the optical NELR of NGC 5548 is also found to be compact ($C_{\rm cov} \sim 11\%$, Kraemer et al. 1998).

To summarize, in this work, the X-ray narrow emission features show asymmetric line profiles, and the underlying photoionized plasma is turbulent and compact in size. Similar results have been reported in previous optical studies of the NELR (Kraemer et al. 2007, 1998; Peterson et al. 2013). Moreover, distance estimates (from previous studies) of the X-ray and optical NELR indicate that the two regions might be co-located, i.e., a few parsec away from the central engine (Detmers et al. 2009; Landt et al. 2015; Peterson et al. 2013). These similarities further suggest that the X-ray and optical NELR might be the same multiphase photoionized plasma that manifests its emission in different energy bands. This interpretation has actually been established with the radiation pressure confinement (RPC) model (e.g., Stern et al. 2014). Of course, the RPC model is more sophisticated, where the multiphase photoionized plasma has a range of number densities and ionization parameters. We only have two uniform slabs for the X-ray narrow emission features, but we do notice that the ratio of radiation to gas pressure decreases from the highly ionized component EM 1 to the less ionized component EM 2 (Section 5.3.2.1), which agrees with the RPC model.

Interestingly, based on the measurement of the metastable absorption lines (C III 1175 Å and Si III 1298 Å) in the UV band, Arav et al. (2015) determined the number density ($\log n_{\rm e} = 10.8 \pm 0.1$ m^{-3}) and distance (~ 3.5 pc) of the UV absorption component 1, which are also similar to those of the optical NELR.

5.4.2. In relation to the X-ray warm absorber

As can be seen from Table 5.3, the single-phase emission component fully covered by the warm absorber components A+B+C (Whewell et al. 2015, i.e., Model S2 in this work) and the two-phase emission components with no overlying warm absorber components (Model D) yield comparable fit statistics. Nevertheless, the underlying geometries of the two scenarios are rather different.

In the first scenario (Model S2), the warm absorber components (A to C) are located between the X-ray emitter and the observer, with the warm absorber components fully covering the emission component. Given that the X-ray NELR is compact in size (Section 5.4.1), full covering by the warm absorber components is possible, as long as the warm absorber components are located farther away than the emission component. Ebrero et al. (2016) estimate the distances of the warm absorber components via a variability study. The warm absorber components A and B are at least 10 pc away from the central engine, while component C is between 1 and 5 pc (Figure 5.7).

Nevertheless, a distance estimation based on the density sensitive metastable absorption lines found a 3σ upper limit of 0.23 pc for the warm absorber component B (Mao et al. 2017). If this is the case, and assuming the X-ray NELR has a distance of 1–3 pc, the warm absorber component B cannot absorb the NELR. The second scenario (Model D), with no overlying absorption, does not suffer from the logical difficulty if the warm absorber component B is closer than the X-ray NELR.

Distance (and also density) estimation using either timing or spectral analysis is challenging. Timing analyses usually suffer from low cadence and sometimes the signal-to-noise ratio is not high enough to claim a significant change. On the other hand, spectral analyses (in the X-ray band) suffer from low spectral resolution and limited photon collecting area in the relevant energy band with current grating spectrometers. Future studies with either an intensive monitoring program or a spectral analysis with the next generation spectrometers (e.g., *Arcus,* Smith et al. 2016) are required to better constrain the number density and distance of the warm absorber (Kaastra 2017b).

We also compare the parameters of the emission and absorption components. We list the parameters for selected emission and absorption comparison in Table 5.4. The term $n_{\rm H}r^2$ of the X-ray emission component 1, (X-ray) warm absorber component B, and UV absorption component 1 are comparable ($\sim 10^{44}$ m^{-1}). The distances (thus number densities) of EM 1 are consistent with UV 1, but not with X-ray component B (Figure 5.7). The other parameters ($N_{\rm H}$, $v_{\rm out}$, and $v_{\rm mic}$) of

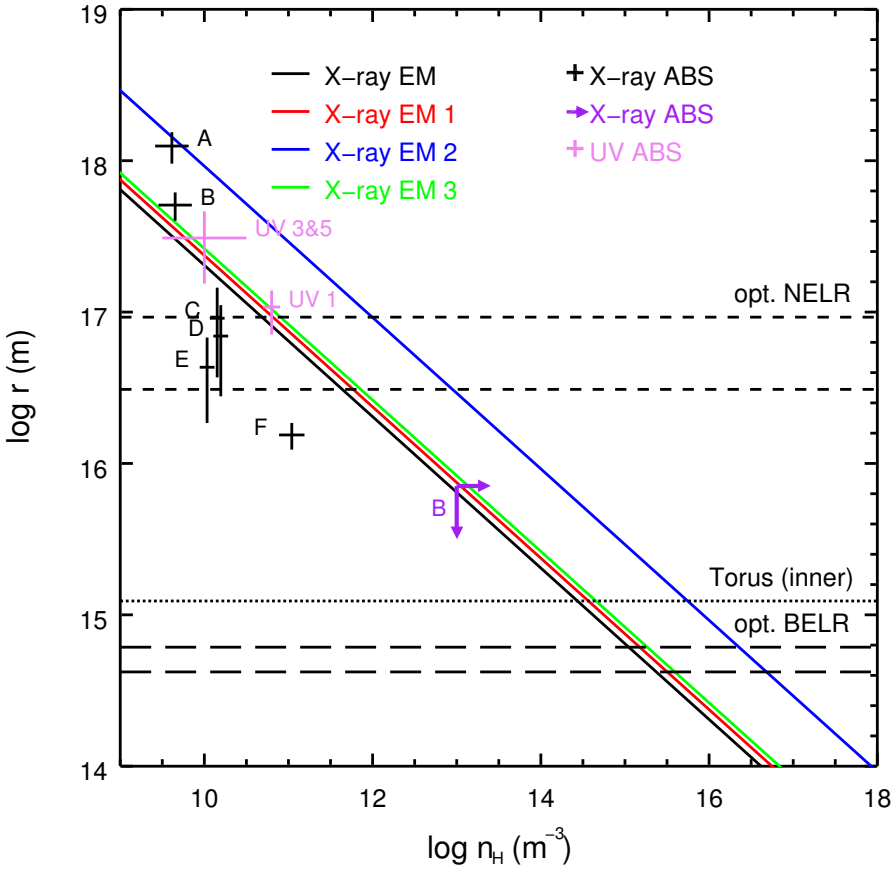

Figure 5.7: Distance and number density of optical, UV, and X-ray emission and/or absorption components in NGC 5548. The solid diagonal lines are the distance and density relations (i.e., $\log \xi = L/n_{\rm H} r^2$) of the X-ray emission components (EM for Whewell et al. 2015, and EM 1–3 for Model T). The black pluses (1σ uncertainties) refer to the six warm absorber components (via a timing analysis, Ebrero et al. 2016). The purple arrows are the 3σ upper (distance) and lower (density) limits of the warm absorber component B (via a spectral analysis, Mao et al. 2017). The pink pluses are for the UV absorption components (Arav et al. 2015). The horizontal short dashed lines refer to the optical narrow emission line region (Peterson et al. 2013). The horizontal long dashed lines refer to the optical broad emission line region (Bottorff et al. 2002; Kaspi et al. 2000). The horizontal dotted line indicates the inner edge of the torus (Suganuma et al. 2006).

these emission and absorption components do not agree with each other. For the X-ray absorption component A and X-ray emission component 2, three parameters ($n_{\rm H}r^2$, o$v_{\rm out}$, and $v_{\rm mic}$) are roughly of the same order of magnitude, but the hydrogen column density and distance (thus number density) are not consistent with each other.

The warm absorber components C to E have similar distances to the X-ray NELR (Figure 5.7), but the inferred number densities are lower by an order of magnitude, while component F has smaller distance and number density than the X-ray NELR (Ebrero et al. 2016). The UV absorption components 3 and 5 are slightly farther away (5–15 pc) than the X-ray NELR, while the distances of components 2, 4, and 6 are not well constrained (Arav et al. 2015).

In short, the emission components are not the counterparts of the UV/X-ray absorption components outside the line of sight.

5

5.4.3. Unobscured SED for the X-ray emitter

Although we have witnessed significant spectral changes since June 2011[4] (Kaastra et al. 2014), we argue that using the unobscured SED for the X-ray emitter (as in Whewell et al. 2015) is reasonable given the following effects.

First, there is a geometric effect. A possible geometry is shown in Fig. 4 of Kaastra et al. (2014) where the obscurer appears along our line of sight, yet only a small part is between the narrow line region and the black hole and the accretion disk.

Second, there is a time delay effect. It is also possible that the X-ray emitter has not yet responded to the changes in the ionizing SED, whether it is obscured or not. The delay timescale ($\tau_{\rm delay}$) is the sum of the light travel time ($\tau_{\rm lt}$) and the recombination time ($\tau_{\rm rec}$). The recombination timescale mainly depends on the number density ($n_{\rm H}$) of the plasma (Krolik & Kriss 1995; Nicastro et al. 1999): the higher the plasma density, the shorter the recombination time. In our photoionization modeling, the recombination timescale for O VII is roughly on the order of $10^{16}\ (n_{\rm H}/{\rm m}^{-3})^{-1}$ s. The light travel time is simply $3.26\ (r_{\rm X}/{\rm pc})$ yr, i.e., $10^8\ (r_{\rm X}/{\rm pc})$ s, where $r_{\rm X}$ is the distance of the X-ray NELR. As long as the number density of the photoionized plasma is $\gtrsim 10^{10}$ m^{-3} and the distance of the X-ray NELR $\gtrsim 1$ pc, the delay time ($\gtrsim$3.3 yr) is longer than the time separation ($\sim$2.6 yr) between our two epochs (2013–2014 and 2016).

[4]There were no observations of NGC 5548 between August 2007 and June 2012 with *XMM*–Newton, *Chandra*, *Suzaku*, or *Swift*.

Table 5.4: Comparing the parameters of selected emission and absorption components.

Comp.	$N_{\rm H}$ (10^{25} m^{-2})	$n_{\rm H} r^2$ (10^{44} m^{-1})	$v_{\rm mic}$ (km s^{-1})	$v_{\rm out}$ (km s^{-1})	E.M. (10^{70} m^{-3})	r (pc)
EM 1	9.7 ± 1.3	5.7 ± 0.3	400 ± 30	-47 ± 4	1.8 ± 0.6	1–3‡
B	0.69 ± 0.09	5.2 ± 0.8	49 ± 14	-550 ± 40	—	< 0.23 or 13–20†
UV 1	$3.2^{+4.7}_{-1.2}$	$7.4^{+4.3}_{-4.5}$	—	-1160	—	$3.5^{+1.0}_{-1.2}$
EM 2	30 ± 7	87 ± 11	< 280	-420 ± 30	16 ± 10	1–3‡
A	0.26 ± 0.08	36 ± 12	150 ± 30	-570 ± 40	—	31–50†

Notes. Results from this work and Peterson et al. (2013, ‡) are used for the narrow emission components (EM 1 and 2 in Model T). The warm absorber components (A and B) are from Mao et al. (2017) and Ebrero et al. (2016, †). The UV absorption component 1 is from Arav et al. (2015). We do not compare the ionization parameter because it can vary, due to the change in the ionizing luminosity. The emission measure (E.M.) is calculated via $n_{\rm e}\ n_{\rm H}\ 4\pi C_{\rm cov} r^2\ N_{\rm H}/n_{\rm H}$.

Third, there is a low-density effect. When the density of the photoionized plasma is sufficiently low, the recombination timescale ($\tau_{\rm rec}$) is orders of magnitude higher than the variability timescale ($\tau_{\rm var}$), and the plasma is in a quasi-steady state. In other words, the ionization balance of the plasma varies slightly around the mean value corresponding to the mean ionizing flux level over time (Kaastra et al. 2012; Nicastro et al. 1999; Silva et al. 2016).

5.4.4. Charge exchange component?

In our physical global fit (Section 5.3.2) to the stacked RGS spectrum in 2013–2014, we find that the N VII Lyγ[5] narrow emission line is abnormally high for a photoionized plasma (all panels in Figure 5.3). When we include a Gaussian profile for the N VII Lyγ narrow emission line, the C-stat is significantly improved with $\Delta C = -23$ at the price of two degrees of freedom. The best-fit line luminosity is $(1.9 \pm 0.5) \times 10^{32}$ W, and the N VII ratio of Lyγ to Lyα is $0.7^{+1.3}_{-0.3}$. Such a high Lyγ/Lyα cannot be explained by a photoionized plasma or a collisionally ionized plasma, but it can be obtained with a charge exchange plasma (e.g., Gu et al. 2015).

It is possible for charge exchange events to occur if a warm ($T \sim 10^{5-6}$ K) outflow runs into the cold ($T \lesssim 1800$ K) torus region. Assuming a constant radial velocity of ~ 300 km s^{-1}, if the outflow is short-lived ($\lesssim 10^{2-3}$ yr), only gas arising beyond the broad line region can reach the torus region (Blustin et al. 2005). If the outflow is long-lived, then outflows arising from the accretion disk can also reach the torus region (Proga 2000). In fact, putative charge exchange emission features at 1223.6 Å, 1242.4 Å, and 1244.0 Å (for Ne X and S XV) in the UV spectrum of NGC 1275 have been reported in Gu et al. (2017).

In our case, using a charge exchange component (the CX model in SPEX, Gu et al. 2016), we can reproduce a N VII Lyγ/Lyα of ~0.7, but the same CX plasma would also produce a high Lyγ/Lyα for C VI and Lyδ/Lyα for O VIII (~0.5), which are not found in the observed spectra. Therefore, we are not convinced that the N VII Lyγ/Lyα ratio alone can validate the presence of a charge exchange plasma in NGC 5548.

5.5. Summary

We reanalyze the high-resolution spectrum of the archetypal Seyfert 1 galaxy NGC 5548 obtained with the Reflection Grating Spectrometer on board *XMM*-Newton in 2013–

[5] 19.83 Å in the rest frame and 20.16 Å in the observed frame.

2014 (770 ks), and analyze the spectrum obtained in 2016 (70 ks). The main results are summarized as follows.

1. The most prominent emission lines (the O VII forbidden line and O VIII Lyα line) are consistent (at a 1 σ confidence level) between 2013–2014 and 2016. This is not totally unexpected, as the nonvariability at such a timescale has been reported previously.

2. The X-ray narrow emission line region (NELR) can be modeled as a two-phase photoionized plasma without further absorption by the warm absorber. This is an alternative to the previous interpretation of the NELR as a single-phase photoionized plasma absorbed by some of the warm absorber components.

3. The X-ray broad emission features can be modeled by a third photoionized component.

4. Our X-ray spectral analysis found that the line profiles of the narrow emission lines are asymmetric, the photoionized plasma is turbulent, and the emission region is compact in size. Similar results have been found in the optical studies. Furthermore, distance estimates from the literature of the X-ray and optical narrow emission line regions suggest that they might be co-located. Therefore, it is possible that the multiphase nature of the NELR manifests its emission in different energy bands.

5. Future missions like *Arcus* are needed in order to better constrain the distances of the warm absorber components. Hence, we can tell whether the warm absorber intervenes along the line of sight from the X-ray narrow line emitter to the observer.

6. The X-ray NELR is not the counterpart of the UV/X-ray absorber outside the line of sight.

7. The N VII Lyγ-to-Lyα ratio is abnormally high in the stacked RGS spectra in 2013–2014. We investigate the possibility that this line may be produced by charge exchange.

References

Arav, N., Chamberlain, C., Kriss, G. A., et al. 2015, A&A, 577, A37
Armentrout, B. K., Kraemer, S. B., & Turner, T. J. 2007, ApJ, 665, 237

Arnaud, K. A. 1996, in Astronomical Society of the Pacific Conference Series, Vol. 101, Astronomical Data Analysis Software and Systems V, ed. G. H. Jacoby & J. Barnes, 17
Bautista, M. A. & Kallman, T. R. 2001, ApJS, 134, 139
Bennert, N., Jungwiert, B., Komossa, S., Haas, M., & Chini, R. 2006a, A&A, 459, 55
Bennert, N., Jungwiert, B., Komossa, S., Haas, M., & Chini, R. 2006b, A&A, 456, 953
Bianchi, S., Chiaberge, M., Evans, D. A., et al. 2010, MNRAS, 405, 553
Bianchi, S., Guainazzi, M., & Chiaberge, M. 2006, A&A, 448, 499
Blustin, A. J., Page, M. J., Fuerst, S. V., Branduardi-Raymont, G., & Ashton, C. E. 2005, A&A, 431, 111
Bottorff, M. & Ferland, G. 2002, ApJ, 568, 581
Bottorff, M. C., Baldwin, J. A., Ferland, G. J., Ferguson, J. W., & Korista, K. T. 2002, ApJ, 581, 932
Cappi, M., De Marco, B., Ponti, G., et al. 2016, A&A, 592, A27
Chiang, J., Reynolds, C. S., Blaes, O. M., et al. 2000, ApJ, 528, 292
Costantini, E., Kaastra, J. S., Arav, N., et al. 2007, A&A, 461, 121
Costantini, E., Kriss, G., Kaastra, J. S., et al. 2016, A&A, 595, A106
de Plaa, J., Kaastra, J. S., Tamura, T., et al. 2004, A&A, 423, 49
de Vaucouleurs, G., de Vaucouleurs, A., Corwin, Jr., H. G., et al. 1991, Third Reference Catalogue of Bright Galaxies. Volume I: Explanations and references. Volume II: Data for galaxies between 0^h and 12^h. Volume III: Data for galaxies between 12^h and 24^h.
den Herder, J. W., Brinkman, A. C., Kahn, S. M., et al. 2001, A&A, 365, L7
Detmers, R. G., Kaastra, J. S., Costantini, E., McHardy, I. M., & Verbunt, F. 2008, A&A, 488, 67
Detmers, R. G., Kaastra, J. S., & McHardy, I. M. 2009, A&A, 504, 409
Di Gesu, L., Costantini, E., Ebrero, J., et al. 2015, A&A, 579, A42
Ebrero, J., Kaastra, J. S., Kriss, G. A., et al. 2016, A&A, 587, A129
Ferland, G. J., Chatzikos, M., Guzmán, F., et al. 2017, , 53, 385
Gu, L., Kaastra, J., & Raassen, A. J. J. 2016, A&A, 588, A52
Gu, L., Kaastra, J., Raassen, A. J. J., et al. 2015, A&A, 584, L11
Gu, L., Mao, J., O'Dea, C. P., et al. 2017, A&A, 601, A45
Guainazzi, M. & Bianchi, S. 2007, MNRAS, 374, 1290
Guainazzi, M., Risaliti, G., Nucita, A., et al. 2009, A&A, 505, 589
Jansen, F., Lumb, D., Altieri, B., et al. 2001, A&A, 365, L1
Kaastra, J. S. 2017a, Astronomische Nachrichten, 338, 146
Kaastra, J. S. 2017b, A&A, 605, A51
Kaastra, J. S. & Bleeker, J. A. M. 2016, A&A, 587, A151
Kaastra, J. S., de Vries, C. P., Steenbrugge, K. C., et al. 2011, A&A, 534, A37
Kaastra, J. S., Detmers, R. G., Mehdipour, M., et al. 2012, A&A, 539, A117
Kaastra, J. S., Kriss, G. A., Cappi, M., et al. 2014, Science, 345, 64
Kaastra, J. S., Mewe, R., Liedahl, D. A., Komossa, S., & Brinkman, A. C. 2000, A&A, 354, L83
Kaastra, J. S., Mewe, R., & Nieuwenhuijzen, H. 1996, in UV and X-ray Spectroscopy of Astrophysical and Laboratory Plasmas, ed. K. Yamashita & T. Watanabe, 411–414
Kaastra, J. S., Steenbrugge, K. C., Raassen, A. J. J., et al. 2002, A&A, 386, 427
Kallman, T. & Bautista, M. 2001, ApJS, 133, 221
Kallman, T., Evans, D. A., Marshall, H., et al. 2014, ApJ, 780, 121
Kaspi, S., Smith, P. S., Netzer, H., et al. 2000, ApJ, 533, 631
Kinkhabwala, A., Sako, M., Behar, E., et al. 2002, ApJ, 575, 732

Korista, K. T., Alloin, D., Barr, P., et al. 1995, ApJS, 97, 285
Kraemer, S. B., Bottorff, M. C., & Crenshaw, D. M. 2007, ApJ, 668, 730
Kraemer, S. B., Crenshaw, D. M., Filippenko, A. V., & Peterson, B. M. 1998, ApJ, 499, 719
Krolik, J. H. & Kriss, G. A. 1995, ApJ, 447, 512
Krolik, J. H., McKee, C. F., & Tarter, C. B. 1981, ApJ, 249, 422
Landt, H., Ward, M. J., Steenbrugge, K. C., & Ferland, G. J. 2015, MNRAS, 454, 3688
Lodders, K. & Palme, H. 2009, Meteoritics and Planetary Science Supplement, 72, 5154
Longinotti, A. L., Nucita, A., Santos-Lleo, M., & Guainazzi, M. 2008, A&A, 484, 311
Mao, J., Kaastra, J. S., Mehdipour, M., et al. 2017, A&A, 607, A100
Marinucci, A., Bianchi, S., Matt, G., et al. 2011, A&A, 526, A36
Mehdipour, M., Kaastra, J. S., & Kallman, T. 2016a, A&A, 596, A65
Mehdipour, M., Kaastra, J. S., Kriss, G. A., et al. 2017, A&A, 607, A28
Mehdipour, M., Kaastra, J. S., Kriss, G. A., et al. 2016b, A&A, 588, A139
Mehdipour, M., Kaastra, J. S., Kriss, G. A., et al. 2015, A&A, 575, A22
Netzer, H. 2015, ARA&A, 53, 365
Nicastro, F., Fiore, F., Perola, G. C., & Elvis, M. 1999, ApJ, 512, 184
Nucita, A. A., Guainazzi, M., Longinotti, A. L., et al. 2010, A&A, 515, A47
Peterson, B. M., Berlind, P., Bertram, R., et al. 2002, ApJ, 581, 197
Peterson, B. M., Denney, K. D., De Rosa, G., et al. 2013, ApJ, 779, 109
Peterson, B. M., Ferrarese, L., Gilbert, K. M., et al. 2004, ApJ, 613, 682
Porquet, D. & Dubau, J. 2000, A&AS, 143, 495
Proga, D. 2000, ApJ, 538, 684
Silva, C. V., Uttley, P., & Costantini, E. 2016, A&A, 596, A79
Smith, R. K., Abraham, M. H., Allured, R., et al. 2016, in Proc. SPIE, Vol. 9905, Space Telescopes and Instrumentation 2016: Ultraviolet to Gamma Ray, 99054M
Steenbrugge, K. C., Kaastra, J. S., Crenshaw, D. M., et al. 2005, A&A, 434, 569
Stern, J., Laor, A., & Baskin, A. 2014, MNRAS, 438, 901
Suganuma, M., Yoshii, Y., Kobayashi, Y., et al. 2006, ApJ, 639, 46
Wakker, B. P., Lockman, F. J., & Brown, J. M. 2011, ApJ, 728, 159
Whewell, M., Branduardi-Raymont, G., Kaastra, J. S., et al. 2015, A&A, 581, A79

6

Photoionized emission and absorption features in the high-resolution X-ray spectra of NGC 3783

Junjie Mao, M. Mehdipour, J. S. Kaastra, E. Costantini, C. Pinto, G. Branduardi-Raymont, E. Behar, U. Peretz, S. Bianchi, G. A. Kriss, G. Ponti, B. De Marco, P.-O. Petrucci, L. Di Gesu, R. Midde, J. Ebrero and N. Arav

Our *Swift* monitoring program triggered two joint *XMM-Newton*, *NuSTAR* and HST observations on 11 and 21 December 2016 targeting NGC 3783, as its soft X-ray continuum was heavily obscured. Consequently, emission features, including the O VII radiative recombination continuum, stand out above the diminished continuum. We focus on the photoionized emission features in the December 2016 RGS spectra, and compare them to the time-averaged RGS spectrum obtained in 2000–2001 when the continuum was unobscured. A two-phase photoionized plasma is required to account for the narrow emission features. These narrow emission

This chapter has been submitted to Astronomy & Astrophysics, 2018

features are weakly varying between 2000–2001 and December 2016. We also find a statistically significant broad emission component in the time-averaged RGS spectrum in 2000–2001. This broad emission component is significantly weaker in December 2016, suggesting that the obscurer is farther away than the X-ray broad-line region. In addition, by analyzing the archival high-resolution X-ray spectra, we find that nine photoionized absorption components with different ionization parameters and kinematics are required for the warm absorber in X-rays.

6.1. Introduction

The optical spectra of Seyfert 1 galaxies often show broad emission lines with a velocity broadening of a few 10^3 km s^{-1} and narrow emission lines with a velocity broadening about a few 10^2 km s^{-1} (e.g., Blandford et al. 1990). In the soft X-ray band of Seyfert 1 galaxies, broad and narrow emission lines are also observed (e.g., Costantini et al. 2007, 2016; Kaastra et al. 2000). Although in some Seyfert 2 galaxies the spatial extent of the optical and X-ray narrow emission line regions is remarkably similar (Bianchi et al. 2006), the relation of narrow emission lines in the optical and X-ray bands are not fully understood. Similarly, the connection of optical to X-ray broad emission lines is also poorly understood.

Optical broad emission lines are known to vary, as they are dependent on the luminosity of the nucleus (Bentz et al. 2013, and references therein). Optical narrow emission lines (e.g. [O III]) are historically thought to be constant in flux and used to calibrate spectroscopic monitoring data (Peterson et al. 2013). However, there is also a growing number of studies (Denney et al. 2014; Detmers et al. 2009; Landt et al. 2015; Peterson et al. 2013) suggesting that the optical and/or X-ray narrow emission lines in active galactic nuclei (AGN) are variable over long timescales (at least a few years). This is not totally unexpected considering the photoionization origin of these emission lines, the variable ionizing source and the distance of the narrow-line region (at least a few parsecs, Bennert et al. 2006a,b).

NGC 3783 is a nearby ($z = 0.009730$, Theureau et al. 1998) Seyfert 1 galaxy that has been extensively studied for the past few decades in the infrared, optical, UV and X-ray wavelength ranges (e.g., Chelouche & Netzer 2005; Fukumura et al. 2018; Goosmann et al. 2016; Hönig et al. 2013; Kaspi et al. 2000; Kraemer et al. 2001; Onken & Peterson 2002; Ramírez et al. 2005). NGC 3783 has a supermassive black hole with $M_{\rm BH} = (3.0 \pm 0.5) \times 10^7$ M$_\odot$ (Peterson et al. 2004). The radius of the optical broad-line region in NGC 3783 ranges from 0.0012 pc (or 1.4 light-days

for He II) to 0.0086 pc (or 10.2 light-days for Hβ, Peterson et al. 2004).

On 11 and 21 December 2016, our *Swift* monitoring program[1] triggered two joint *XMM-Newton*, *NuSTAR* and Hubble Space Telescope (HST) observations targeting NGC 3783 (Mehdipour et al. 2017). This is because the soft X-ray continuum of NGC 3783 was heavily obscured (See Fig. 2 in Mehdipour et al. 2017), similar to the obscuration events discovered in NGC 5548 (Kaastra et al. 2014) and NGC 985 (Ebrero et al. 2016). The obscurer in NGC 3783 is found to partially cover the central source with a column density on the order of 10^{27} m^{-2} (Mehdipour et al. 2017). The obscurer is outflowing with a range of velocities up to 6000 km s^{-1} and it is probably a disk wind at the outer broad-line region of the AGN (Mehdipour et al. 2017). Moreover, based on X-ray data accumulated in the past two decades, Kaastra et al. (2018) suggest that obscuration events with $N_{\rm H} \gtrsim 10^{26}$ m^{-2} are a frequent phenomenon in NGC 3783.

Here we present a study of photoionized emission features in the soft X-ray band of NGC 3783 from our recent observations in December 2016 and archival observations in 2000–2001. This paper is structured as follows: In Section 6.2, we list all the observations used. Then we detail the spectral analysis in Section 6.3, including the data treatment and the model description, which has been briefly mentioned in Mehdipour et al. (2017). We present the results of our spectral analysis in Section 6.4, as well as discussions of physical implications. Conclusions are available in Section 6.5.

6.2. Observations and data reduction

In 2000–2001 absorption features in NGC 3783 caused by the warm absorber were clearly detectable, as well as the O VIII and C VI Lyα emission lines and the He-like triplets of O VII (Blustin et al. 2002; Kaspi et al. 2000). However, in December 2016, the soft X-ray continuum was heavily absorbed by the obscurer so that narrow absorption features caused by the warm absorber were hardly visible. Due to this diminished continuum, narrow emission features are better visible in December 2016. This includes O VII narrow radiative recombination continuum (RRC), which is a characteristic emission feature of a photoionized plasma (Liedahl & Paerels 1996).

The spectral analysis of such complicated spectra depends crucially on disen-

[1]The X-ray hardness variability of eight type-I AGN was monitored with *Swift* in 2016 in order to find intense obscuration events and thereby study them with joint Hubble Space telescope, *XMM-Newton*, and *NuSTAR* observations (Mehdipour et al. 2017).

tangling the true continuum from the effects of the obscuration and absorption features, which may include many lines and edges that are unresolved and overlapping, as well as emission features. That is to say, this requires a model capable of fitting essentially the overall continuum as well as all the absorption and emission features, including those that cannot be clearly resolved.

Therefore, as described in Mehdipour et al. (2017), we construct a time-averaged spectrum in 2000 and 2001 to constrain the intrinsic spectral energy distribution (SED) and emission features in the unobscured state. Archival data from the optical monitor (OM, Mason et al. 2001), Reflection Grating Spectrometer (RGS, den Herder et al. 2001), and European Photon Imaging Camera-pn (EPIC-pn, Strüder et al. 2001) from *XMM-Newton* are used. We also use archival *Chandra* High-Energy Transmission Grating Spectrometer (HETGS, Canizares et al. 2005) data in 2000, 2001 and 2013 to better constrain the photoionized absorption features, which are rather stable over the 12-year period (Scott et al. 2014). The time-averaged spectrum has a total exposure of 1.37 Ms, with 1.05 Ms for *Chandra*/HETGS and 324 ks for *XMM-Newton*/RGS , respectively.

The optical to hard X-ray data in December 2016 are used for determining the intrinsic SED, obscuration effect, and photoionized emission features (present work) in the obscured state. The two data sets in December 2016 are fitted independently as the continua are different (e.g. Figure 2 in Mehdipour et al. 2017).

All the data used for the present work are listed in Table 6.1. The exposures of the obscured *XMM-Newton*/RGS spectra are 110 ks and 56 ks, respectively. A detailed description of the data reduction can be found in Appendix A of Mehdipour et al. (2015, for NGC 5548), which also applies to the NGC 3783 data used here.

6.3. Spectral analysis

The spectral analysis package SPEX (Kaastra et al. 1996) v3.04 is used, incorporating state-of-the-art atomic data, including radiative recombination (Badnell 2006; Mao & Kaastra 2016) and electron energy loss due to radiative recombination (Mao et al. 2017a). We use C-statistics following Kaastra (2017) throughout this work. Statistical errors are quoted at 68.3% (1σ) confidence level ($\Delta C = 1.0$) unless indicated otherwise. X-ray spectra are optimally binned according to Kaastra & Bleeker (2016). Spectra shown in this paper are background subtracted and displayed in the observed frame.

Table 6.1: List of NGC 3783 data used for the present spectral analysis.

Observatory	Inst.	ObsID	Start date	Length
Chandra	ACIS/HETG	373	2000-01-20	56 ks
XMM-Newton	OM, RGS, pn	0112210101	2000-12-28	40 ks
Chandra	ACIS/HETG	2090	2001-02-24	166 ks
Chandra	ACIS/HETG	2091	2001-02-27	169 ks
Chandra	ACIS/HETG	2092	2001-03-10	165 ks
Chandra	ACIS/HETG	2093	2001-03-31	166 ks
Chandra	ACIS/HETG	2094	2001-06-26	166 ks
XMM-Newton	OM, RGS, pn	0112210201/0401	2001-12-17	142 ks
XMM-Newton	OM, RGS, pn	0112210501/0601	2001-12-19	142 ks
Chandra	ACIS/HETG	14991	2013-03-25	59 ks
Chandra	ACIS/HETG	15626	2013-03-27	102 ks
HST	COS	LD3E03	2016-12-12	2 orbits
XMM-Newton	OM, RGS, pn	0780860901	2016-12-11	110 ks
NuSTAR	FPMA, FPMB	80202006002	2016-12-11	56 ks
HST	COS	LD3E04	2016-12-21	2 orbits
XMM-Newton	OM, RGS, pn	0780861001	2016-12-21	56 ks
NuSTAR	FPMA, FPMB	80202006004	2016-12-21	46 ks

6.3.1. Optical to X-ray spectra construction

The unobscured (2000–2001) and obscured (December 2016) spectra are constructed with all available data in each epoch as follows:

1. OM flux at V, B, U, UVW1, UVM2, and UVW2 bands;

2. Cosmic Origins Spectrograph (COS, Green et al. 2012) flux at 1139 Å, 1339 Å, 1477 Å, and 1794 Å, free from emission and absorption features;

3. first-order RGS data (RGS1 and RGS2 combined) in the $7-37$ Å wavelength range, in order to better constrain the emission and absorption features especially for $\lambda \gtrsim 25$ Å;

4. first-order MEG (Medium Energy Grating) data (positive and negative orders combined) in the $6-17$ Å wavelength range, which have better energy resolution compared to the RGS data at the same wavelength range. Note that MEG data are broken into several segments, with the local continuum of each segment re-scaled by $\lesssim \pm 15$ % to match the RGS continuum at the same wavelength range. The scaling factor of each segment is 1.158 for 6–7 Å, 1.120 for 7–8 Å, 1.003 for 8–9 Å, 1.029 for 9–11 Å, 0.889 for 11–14 Å, and 0.850 for 14–17 Å, respectively. This is to account for observations taken at different epochs, as well as the cross calibration between RGS and MEG;

5. first-order HEG (High Energy Grating) data (positive and negative orders combined) in the $1.7-3$ Å wavelength range, which has better energy resolution compared to the pn data in the same wavelength range. The HEG data are re-scaled by a factor of 1.218;

6. EPIC-pn data in the $1.5-10$ keV energy range (i.e. the 1.24–8 Å wavelength range). EPIC-pn data are re-scaled by 1.038 (2000–2001);

7. *NuSTAR* data in the $10-78$ keV energy range. *NuSTAR* data are re-scaled by 1.013 (11 December 2016) and 1.027 (21 December 2016), respectively.

The above optical to X-ray data are fitted simultaneously, which allows us to constrain the broadband (optical, UV and X-ray) continuum and the X-ray obscuration, absorption and emission features at the same time. Note that the COS grating spectra are analyzed in a separate paper (Kriss et al. in prep.).

6.3.2. Description of model components

In order to interpret the continuum, absorption and emission part of the spectrum at the same time, the following model components needs to be taken into account:

1. The intrinsic broadband spectral energy distribution (SED) of the AGN.
2. The obscuration effect caused by the obscurer and the high-ionization component in the obscured state.
3. Absorption features caused by the warm absorber.
4. Broad and narrow emission features caused by the X-ray photoionized emitter.
5. Broad and narrow emission lines in the optical/UV.
6. The host galaxy continuum emission in the optical/UV.
7. The Galactic extinction in the optical/UV and absorption in X-rays.

We refer readers to Mehdipour et al. (2017) for details of model components 2, 5, 6 and 7. The protosolar abundances of Lodders & Palme (2009) are used for all plasma models.

6.3.2.1. Intrinsic broadband SED of the AGN

A photoionization continuum is required for photoionization modeling of the obscurer, warm absorber, and X-ray photoionized emitter. Following previous analysis of NGC 5548 (Mehdipour et al. 2015), we fit the optical to X-ray data of NGC 3783 using a model consisting of a Comptonized disk component (COMT, Titarchuk 1994) for optical to soft X-rays, a power-law component (POW), and a neutral reflection component (REFL, Magdziarz & Zdziarski 1995; Zycki et al. 1999) for hard X-rays. An exponential cut-off is applied to the high- and low-energy end of the power-law component (Appendix 6.A). The intrinsic optical to X-ray continuum and all the obscuration, absorption, emission, and extinction effects are fitted simultaneously. Therefore, the fit iterates many times to get the best-fit intrinsic broadband SED of the AGN (results in Section 6.4.1).

6.3.2.2. Photoionization continuum

A photoionization continuum is required for the photoionization modeling and it can be different from the AGN SED mentioned above. The photoionization continuum received by the obscurer is indeed simply the contemporary AGN SED (Table 6.2).

For the warm absorber, in 2000–2001, when NGC 3783 is not obscured, its photoionization continuum is also the contemporary AGN SED. However in December 2016 the photoionization continuum for the warm absorber is the contemporary AGN SED with the obscuration effect taken into account.

The photoionization continuum received by the X-ray narrow-line region is assumed to be the 2000–2001 (time-averaged) AGN SED for all epochs (2000–2001 and December 2016). This is because if the photoionized plasma is too far away from the nucleus and/or the density of the plasma is too low, the plasma is in a quasi-steady state with its ionization balance varying slightly around the mean value corresponding to the mean ionizing flux level over time (Kaastra et al. 2012; Nicastro et al. 1999; Silva et al. 2016). Note that our assumption implies that the obscurer does not subtend a large solid angle so that it barely screens photons from the nucleus to the X-ray narrow emission component or the screened photons have not arrived the X-ray narrow emission component yet.

On the other hand, the photoionization continuum for the X-ray broad-line region is the intrinsic SED of NGC 3783. The density of the broad-line region is in general orders of magnitude higher than that of the narrow-line region, thus, the broad-line region responds much faster to changes in the photoionization continuum. No obscuration effect is taken into account for all epochs (2000–2001 and December 2016), since the obscurer is likely farther away than the broad-line region (Mehdipour et al. 2017). In Section 6.4.3, we show results of our independent check on this assumption.

6.3.2.3. Warm absorber

We use the photoionization plasma model PION in SPEX to account for the absorption features produced by the warm absorber. As described in Section 6.4.2, we require nine PION absorption components. For the time-averaged unobscured spectrum (2000–2013), we allow hydrogen column densities ($N_{\rm H}$), ionization parameters ($\log \xi$), and outflow velocities ($v_{\rm out}$) free to vary. After a few trials, microscopic turbulence velocities[2] ($v_{\rm mic}$) are coupled for components 1–2, 3–7, and 8–9 to reduce unnecessary free parameters. For the obscured spectra (December 2016), all the above parameters are fixed to values obtained in the unobscured spectrum, except the ionization parameters, which are assumed to be proportional to the $1 - 10^3$ Ryd ionizing luminosity. That is to say, the hydrogen number den-

[2]The Doppler parameter $b = (v_{\rm th}^2 + 2v_{\rm mic}^2)^{1/2}$, where $v_{\rm th} = \sqrt{2kT/m}$ is the thermal broadening velocity, T the temperature, and m the atomic mass. The full width at half maximum $\mathrm{FWHM} = 2\sqrt{\ln 2}\, b$. In the PION model in SPEX, $v_{\rm mic}$ is the "v" parameter.

sity times distance squared ($n_{\rm H}r^2$) of the warm absorber in the obscured state is assumed to be the same as in the unobscured state. In both unobscured and obscured states, for each PION absorption component, the absorption ($C_{\rm abs} = 1$) and emission ($C_{\rm em} = 0$) covering factors are fixed[3]. That is to say, we assume that the warm absorber fully covers the line of sight but has negligible extent with respect to the nucleus.

6.3.2.4. X-ray photoionized emitter

Similar to the previous analysis on NGC 5548 (Mao et al. 2018), the narrow emission features in NGC 3783 can be reasonably fitted with two PION components (details in Section 6.4.3). Whether the soft X-ray continuum is obscured or not, four free parameters of each PION emission component are allowed to vary, namely $N_{\rm H}$, $\log \xi$, $v_{\rm mic}$ and $C_{\rm em}$. Since the emission lines are consistent with not outflowing, as shown by previous studies (Behar et al. 2003; Kaspi et al. 2002), the outflow velocity ($v_{\rm out}$) is fixed to zero for each PION emission component. In addition, for each PION emission component, its absorption covering factor $C_{\rm abs}$ is fixed to zero.

Broad emission features are modeled with a third PION component. For the time-averaged unobscured spectrum (2000–2001), where the *XMM-Newton* and *Chandra* grating spectra are fitted simultaneously, four free parameters of this PION emission component are allowed to vary, including $N_{\rm H}$, $\log \xi$, $v_{\rm mic}$ and $C_{\rm em}$. For the obscured spectra (December 2016), these parameters are fixed to values obtained in the unobscured spectrum, except the ionization parameters, which are assumed to be proportional to the $1 - 10^3$ Ryd ionizing luminosity (Table 6.2).

For simplicity, all three emission components are assumed to be free of further absorption by the warm absorber (see discussion in Section 6.4.5).

6.4. Results and discussions

6.4.1. Intrinsic broadband SED of the AGN

The time-averaged intrinsic SED of NGC 3783 in 2000-2013 is shown in Figure 6.1. The intrinsic SED on 11 December 2016 is also shown for comparison, which is similar to that on 21 December 2016. Fig. 6 of Mehdipour et al. (2017) presents a version with the intrinsic SEDs overplotted with the observational data. The corresponding best-fit continuum parameters are listed in Table 6.2.

The two observations in December 2016 have similar intrinsic SEDs. However,

[3]In the PION model in SPEX, $C_{\rm abs}$ and $C_{\rm em}$ are the "fcov" and "omeg" parameters.

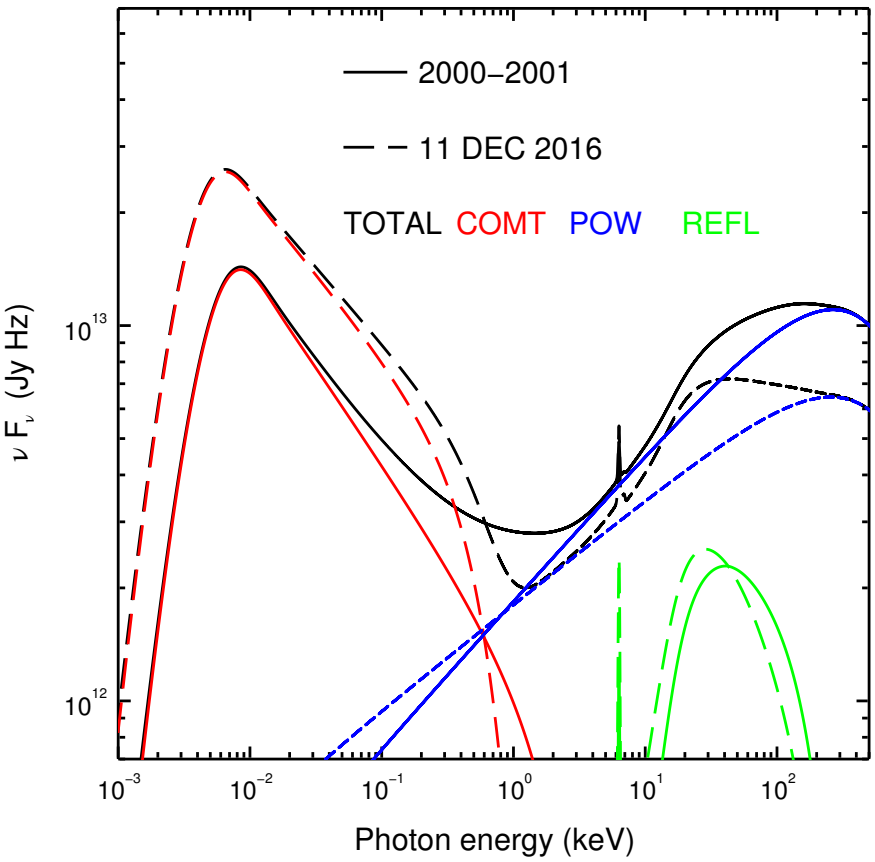

Figure 6.1: The intrinsic spectral energy distribution of NGC 3783 for the time-averaged data in 2000–2001 (solid lines) and 11 December 2016 data (dashed lines). Contributions from individual components are shown in red for the Comptonized disk component (COMT), blue for the power-law component (POW) and green for the reflection component (REFL).

Table 6.2: Best-fit parameters of the intrinsic broadband SED of NGC 3783 in 2000-2001 and December 2016.

Date	2000-2001	11 DEC 2016	21 DEC 2016
	COMT		
Norm	0.95 ± 0.05	9.7 ± 0.3	10.3 ± 0.4
$T_{\rm seed}$	1.47 ± 0.05	1.08 ± 0.03	1.08 ± 0.02
$T_{\rm c}$	0.54 ± 0.02	0.13 ± 0.02	0.14 ± 0.03
τ	9.9 ± 0.2	22.0 (f)	22.0 (f)
	POW		
Norm	2.40 ± 0.03	2.42 ± 0.16	3.03 ± 0.19
Γ	1.61 ± 0.01	1.73 ± 0.02	1.75 ± 0.02
C-stat / C-expt.	6092 / 2563	2335 / 1552	2340 / 1555
$L_{0.3-2\ \rm keV}$	1.20	1.28	1.52
$L_{2-10\ \rm keV}$	1.16	0.94	1.11
$L_{0.001-10\ \rm keV}$	10.6	18.8	21.1
$L_{1-1000\ \rm Ryd}$	7.01	10.2	11.9

Notes. Parameters followed by (f) are fixed in the fit. The temperature of seed photons is in units of eV, the warm corona temperature in keV, the normalization of the warm comptonization (COMT) component in 10^{55} ph s^{-1} keV^{-1}, and the normalization of the power-law (POW) component in 10^{51} ph s^{-1} keV^{-1} at 1 keV. The C-stat refer to the final best-fit, where all obscuration, absorption, emission and extinction effects are taken into account. The luminosities of COMT plus POW in different energy ranges are in units of 10^{36} W with uncertainties about $3-5\%$.

for the time-averaged SED in 2000–2013, both the Comptonized disk component and the power-law component differ significantly from December 2016.

We should emphasize that we apply a global SED model to fit the optical to hard X-ray data, thus, the continuum model in the present work differs from previous studies. Kaspi et al. (2001) and Scott et al. (2014) fitted the 1–26 Å continuum with "line-free zones" (LFZs). However, as pointed out by Scott et al. (2014), even when LFZs are entirely line-free, absorption edges still contribute to curvature in the spectrum. The 0.5–10 keV continuum of NGC 3783 has also been fitted by a power law with $\Gamma \in (1.5,\ 1.83)$ (Blustin et al. 2002; De Rosa et al. 2002), sometimes including an extra thermal component with $kT \sim 0.1$ keV (Krongold et al. 2003). Fu et al. (2017) constructed a SED with typical AGN SED (Elvis et al. 1994) but scaled with wavelength ($\propto \lambda^{-0.27}$) to match the intrinsic UV ($1135 - 1795$ Å) and X-ray ($2 - 11$ Å) continuum.

6.4.2. Warm absorber

The best-fit C-stat to expected C-stat ratio for the time-averaged spectrum in 2000–2013 is $6092/2563 \gtrsim 2$ (with 2505 degrees of freedom), which is not statistically acceptable. This is due to the very high photon statistics compared with systematic uncertainties in the instrumental response, the imperfect cross calibration of different instruments, and our model is still rather simple compared to the reality. But the result is still useful to assess whether the observed continuum and all absorption (and emission) features are reasonably accounted for. The best-fit time-averaged (2000, 2001 and 2013) MEG spectrum (6–15 Å) is shown in details in Figure 6.2. The best-fit time-averaged (2000–2001) RGS spectrum (8–35 Å) is fitted simultaneously but shown separately in Figure 6.3 for clarity.

There are in total nine PION absorption components for the warm absorber, with components 1–4 dominating highly ionized ions with large atomic number (e.g. Fe XXVI, Fe XVII, and Si XIV), components 5 and 6 mainly accounting for moderately ionized ions with intermediate atomic number (e.g. Mg IX, O VIII and O V), and components 7–9 for lowly ionized ions with intermediate atomic number (e.g. N IV and C IV). Contributions from individual warm absorber components (in percentage) to ions with column density $N_{\rm ion} \gtrsim 10^{20}$ m^{-2} are shown in Figure 6.4. Components 7–9 are required in our model because we include the RGS spectrum above 25 Å, while previous analyses simply focus on spectra at shorter wavelength range with $\lambda \lesssim 25$ (Behar et al. 2003; Krongold et al. 2003, for RGS and MEG, respectively). Admittedly, the signal-to-noise ratio decreases toward the longer wavelength, thus,

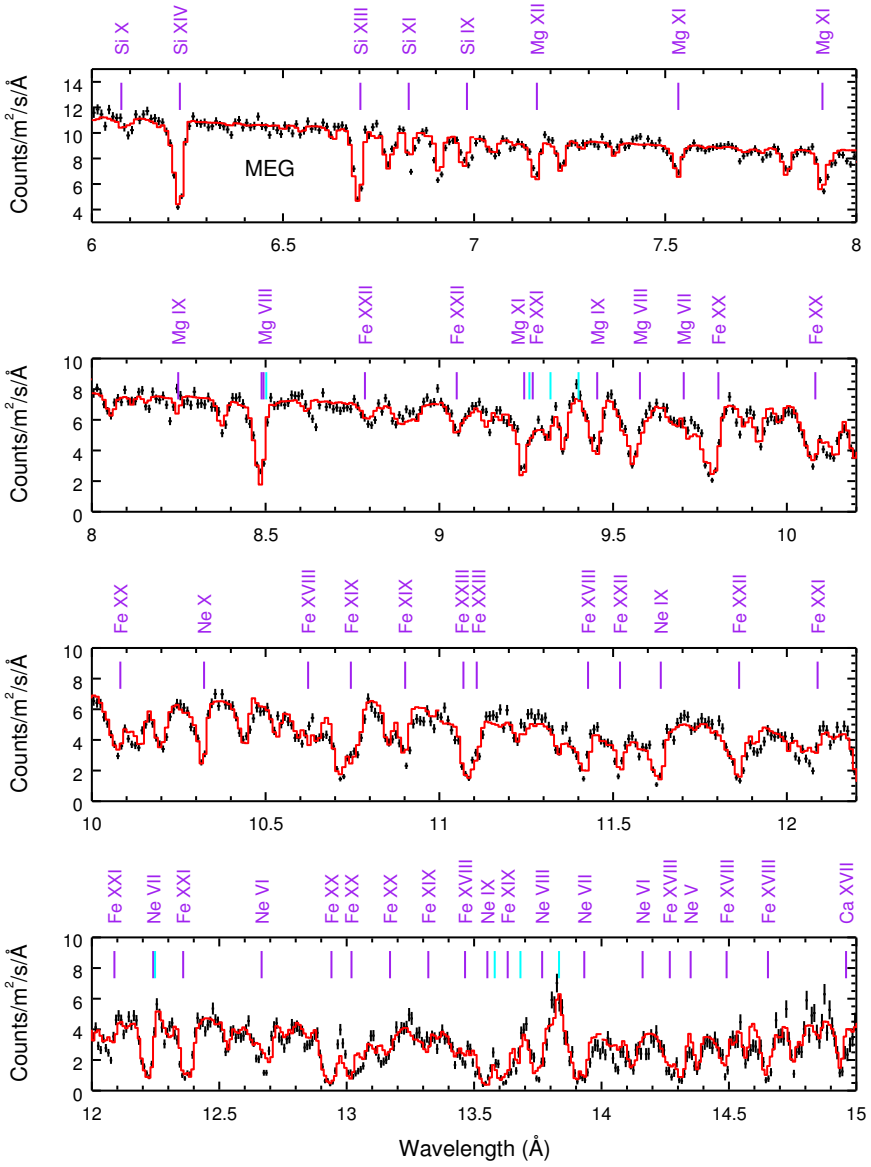

Figure 6.2: The best-fit to the time-averaged MEG spectrum (in the observed frame) of NGC 3783 observed in 2000, 2001 and 2013. Most prominent absorption and emission features are labeled. The solid vertical lines in purple (blue) indicate the photoionized absorption (emission) features.

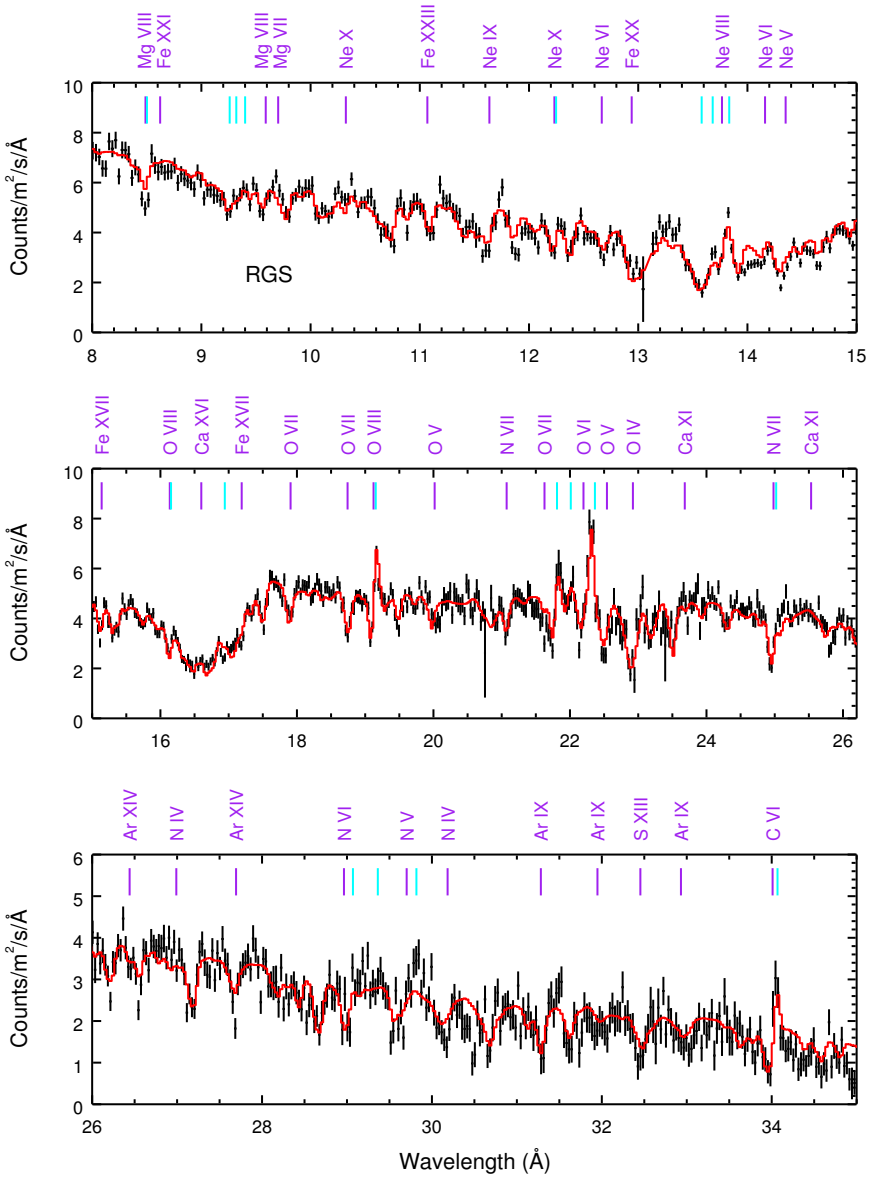

Figure 6.3: Similar to Figure 6.2 but for the time-averaged RGS spectrum (in the observed frame) of NGC 3783 observed in 2000 and 2001.

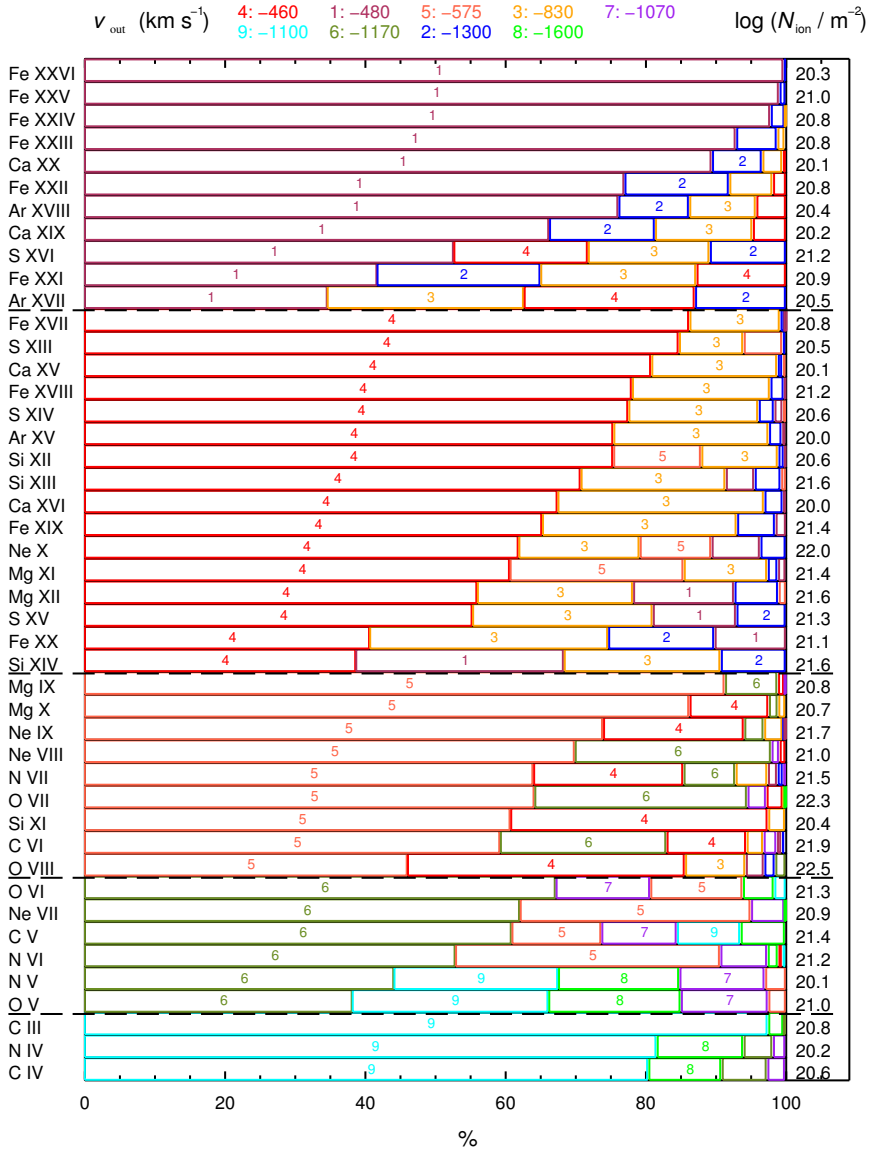

Figure 6.4: Ionic column density (units: m^{-2}, in log-scale listed to the right) with contributions from individual warm absorber components (in percentage). Ions with $N_{\mathrm{ion}} \gtrsim 10^{20}\ \mathrm{m}^{-2}$ are listed to the left. The warm absorber components are color coded with outflow velocities (v_{out}) listed to the top. The ionization parameters of the warm absorber components increase from component 9 to component 1.

Table 6.3: Best-fit parameters of the warm absorber components in the time-averaged spectra of NGC 3783 in 2000–2013.

Comp.	$N_{\rm H}$ 10^{25} m^{-2}	$\log_{10}(\xi)$ 10^{-9} W m	$v_{\rm mic}$ km s^{-1}	$v_{\rm out}$ km s^{-1}
1	11.1 ± 0.8	3.02 ± 0.01	120 ± 10	-480 ± 10
2	2.1 ± 0.2	2.74 ± 0.03	120 (c)	-1300 ± 25
3	6.1 ± 0.6	2.55 ± 0.02	46 ± 2	-830 ± 15
4	12.4 ± 0.5	2.40 ± 0.01	46 (c)	-460 ± 10
5	5.0 ± 0.2	1.65 ± 0.01	46 (c)	-575 ± 10
6	1.2 ± 0.2	0.92 ± 0.04	46 (c)	-1170 ± 30
7	$0.15^{+0.05}_{-0.14}$	$0.58^{+0.28}_{-0.17}$	46 (c)	-1070 ± 40
8	$0.07^{+0.15}_{-0.01}$	$-0.01^{+1.82}_{-0.05}$	790 ± 100	-1600 ± 800
9	0.44 ± 0.03	-0.65 ± 0.06	790 (c)	-1100 ± 140

Notes. Microscopic turbulence velocities ($v_{\rm mic}$) followed by (c) are coupled to $v_{\rm mic}$ of another component with the same value in the fit.

the best-fit parameters of components 7–9 are less well constrained. All the best-fit parameters for the warm absorber components of NGC 3783 in the 2000–2013 time-averaged spectra are tabulated in Table 6.3.

The hydrogen column density ($N_{\rm H}$) of the warm absorber is dominated by components 1–6 with $N_{\rm H}^{\rm total} \simeq 3.8 \times 10^{26}$ m^{-2}, similar to previous results by Netzer et al. (2003) with $N_{\rm H}^{\rm total} \sim 4 \times 10^{26}$ m^{-2}, which is higher than $N_{\rm H}^{\rm total} \sim 2 - 3 \times 10^{26}$ m^{-2} found by Kaspi et al. (2002) and Krongold et al. (2003).

Since the photoionization continuum, abundance table and number of absorption components used by different authors are different, we do not compare the ionization parameters with previous results (e.g., Kaspi et al. 2002; Krongold et al. 2003; Netzer et al. 2003).

In the present work, the microscopic turbulence velocities of the absorption components are 50 km s^{-1} for Components 3–7, 120 km s^{-1} for Components 1–2, and 800 km s^{-1} for Components 8 and 9, respectively (Table 6.3). The microscopic turbulence velocity found in the literature also cover a wide range of values, with $\sim$ 100 km s^{-1} for Kaspi et al. (2000) and Behar et al. (2003), $\sim$ 200 km s^{-1} for Krongold et al. (2003); Netzer et al. (2003), and up to $400 - 600$ km s^{-1} for a few ions in Table 3 of Kaspi et al. (2002).

Our best-fit outflow velocities vary for different absorption components, ranging from -450 km s^{-1} to -1300 km s^{-1}. A wide range of outflow velocities are also

reported in the literature, including -300 to -1000 km s^{-1} by Kaspi et al. (2002), -470 to -800 km s^{-1} by Behar et al. (2003), -750 km s^{-1} by Krongold et al. (2003), and -400 to -1300 km s^{-1} by Netzer et al. (2003).

We also note that the PION model in the SPEX code takes advantage of recently updated atomic data, which is more accurate and complete than previous models by Krongold et al. (K03, 2003) and Netzer et al. (N03, 2003). Previous models are able to fit some of the strong absorption lines but insufficient to fit the global spectrum. As pointed out by Netzer et al. (2003), the K03 model provides a better fit to the Fe UTA (unresolved transition array) yet fails to fit the Si X and Si XI lines around 6.8 Å. The N03 model has a better fit over the 5–7 Å wavelength range while the UTA features are poorly fitted. As for the PION model, we refer readers to Section 4.29 of the SPEX manual for a detailed model description, Mehdipour et al. (2016) for a comparison with other popular photoionization codes and Mao et al. (2017b) for a list of characteristic ground and metastable absorption lines.

6.4.3. X-ray photoionized emitter

In our PION modeling of the emission features (lines and RRCs), we find that a broad emission component is required in addition to two narrow emission components. For the time-averaged spectrum, the best-fit with only narrow emission components yields a C-stat of 6301 (d.o.f. = 2508), while the best-fit with both broad and narrow emission components yields a C-stat of 6092 (d.o.f. = 2505). The broad emission component improves the fit, at least significantly in statistics ($\Delta C \sim -200$). However, regardless of the presence of the broad emission component, there are still some structures in the residuals of the above two fits (Figure 6.5). Future missions (e.g., *Arcus*, Smith et al. 2016) with adequate spectral resolution and significantly larger photon collecting area are essential to verify the presence of such broad emission features in X-rays.

The broad emission component is obtained via convolving a narrow ($v_{\rm mic} = 100$ km s^{-1}) PION component with a velocity broadening model (VGAU in SPEX) with a fixed σ_v, so that the broadening effect applies to both emission lines and RRCs. Such kind of broadening is probably due to the macroscopic motion of the emitter. Unfortunately, the velocity broadening in X-rays is a difficult parameter to determine. It cannot be too narrow, otherwise there is no significant improvement on the C-stat. It cannot be too broad either, otherwise it is unclear whether we are fitting the broad emission line or a part of the complex continuum. At this stage, we tentatively fixed the value of σ_v ($= v_{\rm mac}$) to 9000 km s^{-1}. This value is within

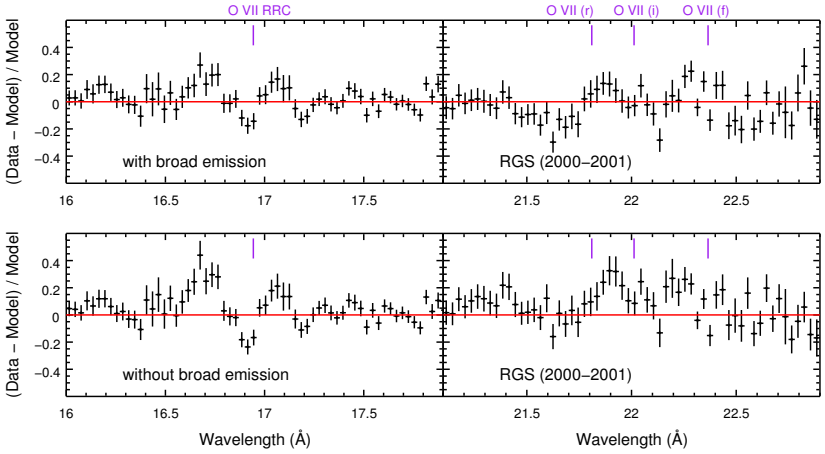

Figure 6.5: Residuals of the best-fit to the time-averaged RGS spectrum (in the observed frame) of NGC 3783 in 2000–2001 around the O VII RRC (left panels) and O VII He-like triplets (right panels). The upper and lower panels show residuals of the best-fit with and without the broad (FWHM~ 21000 km s^{-1}) PION emission component (the third component in Table 6.4), respectively.

6

the range of typical gas velocity $3000 - 10000$ km s^{-1} (Blandford et al. 1990) in the broad line region. For NGC 3783, the X-ray velocity broadening corresponds to a full width at half maximum (FWHM $= 2.355\ \sigma_v$) of about 21000 km s^{-1}, which is significantly larger than FWHM(Hβ) ~ 3000 km s^{-1} (Onken & Peterson 2002) in optical, but close to the width of the broadest component of Lyα in the UV, FWHM~18000km s^{-1} (Kriss et al., in prep.).

The broad and narrow emission model components derived from the 2000–2001 data do not match the data observed in December 2016 (the orange line in Figure 6.6). Narrow emission features might have varied slightly over the 15-year timescale (Section 6.4.4). The broad emission component seems to be much weaker in December 2016 (Figure 6.6). This apparent weakening can be accounted for by applying the obscuration to the broad emission component (the purple line in Figure 6.6). The parameters for the obscurer used here are the same as given in Table 1 of Mehdipour et al. (2017). The above interpretation supports the picture suggested by Mehdipour et al. (2017) that the obscurer is currently at the outer broad-line region of the AGN.

The best-fit to the RGS spectrum on 11 December 2016 is shown in Figure 6.7, which is similar to that on 21 December 2016. The best-fit parameters of the X-ray photoionized emitter in 2000–2001 and December 2016 are listed in Table 6.4. While the emission measures (E.M.$= n_e\ n_{\rm H}\ 4\pi\ C_{\rm em}\ r^2\ N_{\rm H}/n_{\rm H}$) of component 1 are

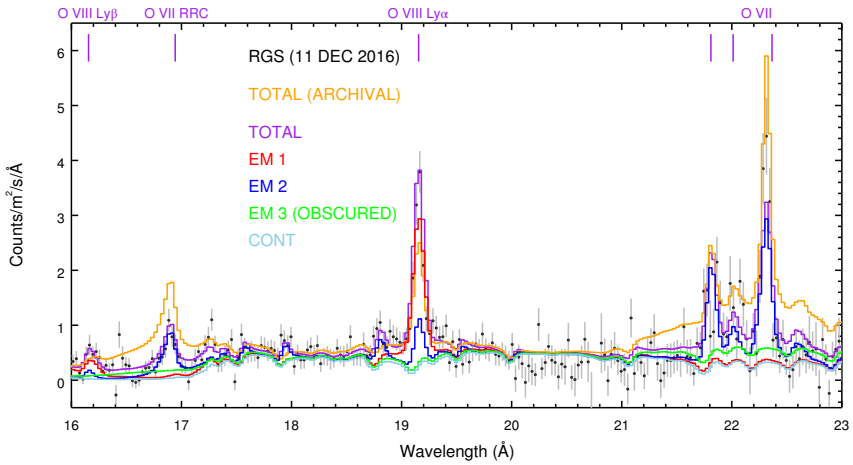

Figure 6.6: Best-fit to the $17 - 24$ Å RGS spectrum (in the observed frame) of NGC 3783 from 11 December 2016. The best-fit model with contributions from all emission components is shown in purple. Contributions from individual emission components are shown in different colors, with red and blue for narrow emission features and green for broad emission features. The orange solid line is a calculation using the best-fit parameters obtained from the time-averaged archival spectrum for all three emission components. Due to the obscuration effect, the broad emission component (EM 3) appears to be weaker in December 2016.

consistent (at 1σ confidence level) between epochs, the emission covering factor ($C_{\rm em}$), thus the emission measure of component 2 is an order of magnitude higher. If we fix $C_{\rm em}({\rm EM\ 2}) = 0.6$ when fitting the 11 December 2016 spectrum, the best-fit C-stat is 2406, which is a worse fit ($\Delta C \sim +70$) when compared to the best-fit C-stat in Table 6.2. This might suggest an increase of the physical size of the emitter over 15 years.

Different values of the best-fit parameters of the narrow emission components in different epochs (Table 6.4) need to be interpreted with caution. Due to lack of information, we assume the photoionization continuum to be the 2000–2001 AGN SED for all spectra in 2000-2001 and December 2016. Under this assumption, the ionization parameter $\xi = L/(n_{\rm H}\ r^2)$ should be the same, because the number density ($n_{\rm H}$) and distance (r) of the emission region are not expected to vary dramatically. The column density ($N_{\rm H}$), microscopic turbulence velocity ($v_{\rm mic}$) and emission covering fraction ($C_{\rm em}$) might not vary significantly as well. Deviation from the time-average photoionization continuum can be partly due to long-term variation in the intrinsic SED components and/or the obscuration events, which might be more frequent than previously thought for NGC 3783. Based on the hardness ratio

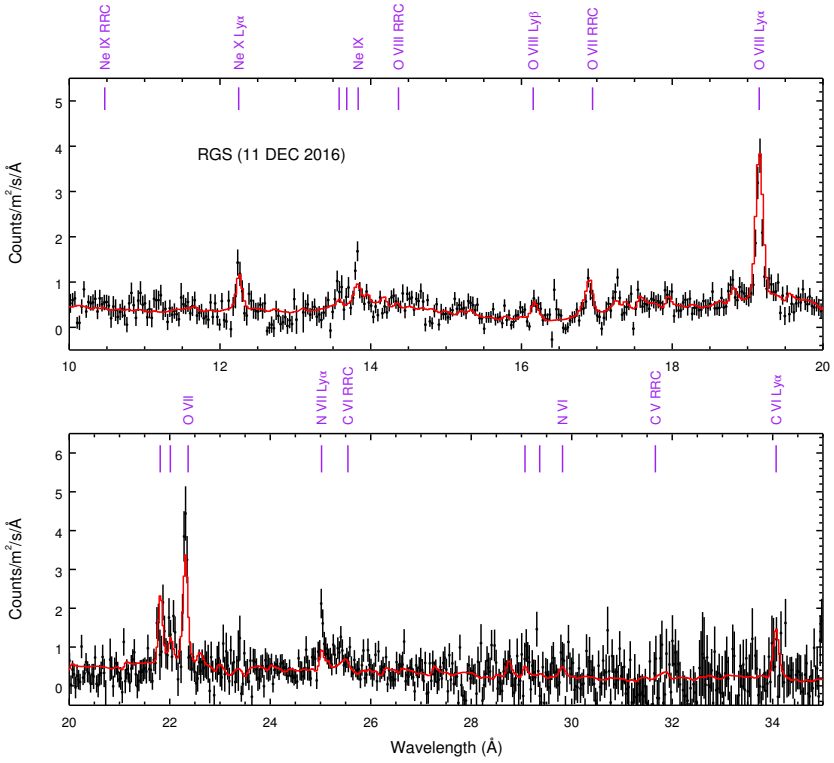

Figure 6.7: The best-fit to the RGS spectrum (in the observed frame) of NGC 3783 on 11 DEC 2016. Most prominent emission features are labeled.

Table 6.4: Best-fit results of the X-ray photoionized emitter in the time-averaged spectra of NGC 3783. The emission measure (E.M.) is calculated based on the best-fit parameters.

Comp.	$N_{\rm H}$ 10^{26} m^{-2}	$\log_{10}(\xi)$ 10^{-9} W m	$v_{\rm mic}$ km s^{-1}	$C_{\rm em}$ %	E.M. 10^{70} m^{-3}
			2000–2001		
1	60 ± 37	2.60 ± 0.07	600 ± 100	0.29 ± 0.12	$0.5^{+0.8}_{-0.4}$
2	$5.2^{+5.4}_{-2.3}$	1.35 ± 0.05	140^{+50}_{-100}	$0.6^{+0.4}_{-0.2}$	$1.5^{+4.1}_{-1.0}$
3	28^{+72}_{-5}	0.82 ± 0.02	100 (f)	$0.3^{+0.1}_{-0.2}$	13^{+53}_{-10}
			11 DEC 2016		
1	25 ± 6	2.58 ± 0.05	590 ± 90	0.98 ± 0.13	$1.0^{+0.6}_{-0.4}$
2	3.0 ± 0.7	1.03 ± 0.05	350 ± 70	7.0 ± 1.3	30^{+19}_{-13}
3	28 (f)	1.00 (f)	100 (f)	0.3 (f)	13 (f)
			21 DEC 2016		
1	35 ± 17	2.58 ± 0.05	460 ± 130	0.7 ± 0.3	$1.6^{+1.6}_{-0.9}$
2	2.3 ± 1.0	1.03 ± 0.05	270 ± 110	7.3 ± 2.4	28^{+32}_{-19}
3	28 (f)	1.06 (f)	100 (f)	0.3 (f)	13 (f)

Notes. Parameters followed by (f) are fixed in the fit. The 2000–2013 MEG ($6 - 17$ Å) data and the 2000–2001 RGS ($7 - 37$ Å) data are fitted simultaneously (Section 6.3.1), but constraints are obtained mainly from the 2000–2001 RGS data since it covers all the emission features from Ne, O, N, and C.

of all *Swift*/XRT spectra in 2008–2017, obscuration events might occur about half of the time (Kaastra et al. 2018), which will affect the photoionization modelling of the X-ray narrow emission features.

Additionally, by comparing the best-fit results of the absorption (Table 6.3) and emission (Table 6.4) components, we find that emission component 1 and absorption component 3 share similar ionization parameter, yet the hydrogen column density, turbulence velocity and outflow velocity are significantly different. The ionization parameter of emission component 2 has no counterpart in absorption components. This is similar to what we find in another Seyfert 1 galaxy NGC 5548 (Mao et al. 2018). It is possible that the X-ray emission and absorption components are not related, although we need distance (thus density) measurement on these components to verify this deduction.

6.4.4. Variability of the X-ray emission features

We check the variability of the most prominent narrow emission lines, the O VIII Lyα line and O VII He-like triplets, in the RGS spectra in 2000–2001 and December 2016. A phenomenological local fit is used in this exercise so that we are not confused by the unknown photoionization continuum effect on the photoionization modeling.

We fix the continuum to the best-fit global continuum corrected for the foreground Galactic absorption, the obscurer, the warm absorber and the broad emission features. Subsequently, the narrow emission lines are accounted for with Gaussian line profiles. The normalization and velocity broadening of the Gaussian profiles are free to vary, except that we limit the velocity broadening to be no larger than $2000\ \mathrm{km\ s^{-1}}$ and couple the broadening of the resonance and intercombination lines of the O VII He-like triplets. The line luminosity and velocity broadening are listed in Table 6.5. The best-fit results of 2000–2001 and 11 December 2016 are plotted in Figs. 6.8 and 6.9.

These emission lines are consistent with each other at a 1σ confidence level between the two observations in December 2016. When compared to 2000–2001, the O VII resonance and forbidden lines remain constant in luminosity at the 1σ confidence level, while the O VIII Lyα line and intercombination line of He-like O VII are marginally brighter in December 2016 at the 2σ confidence level. In addition, the resonance and intercombination lines of O VII appear to be broader in December 2016, although the uncertainty is large.

Since the variability of the X-ray broad emission features cannot be checked directly, we turn to the very broad (FWHM$\gtrsim 10^4\ \mathrm{km\ s^{-1}}$) emission lines in the high-

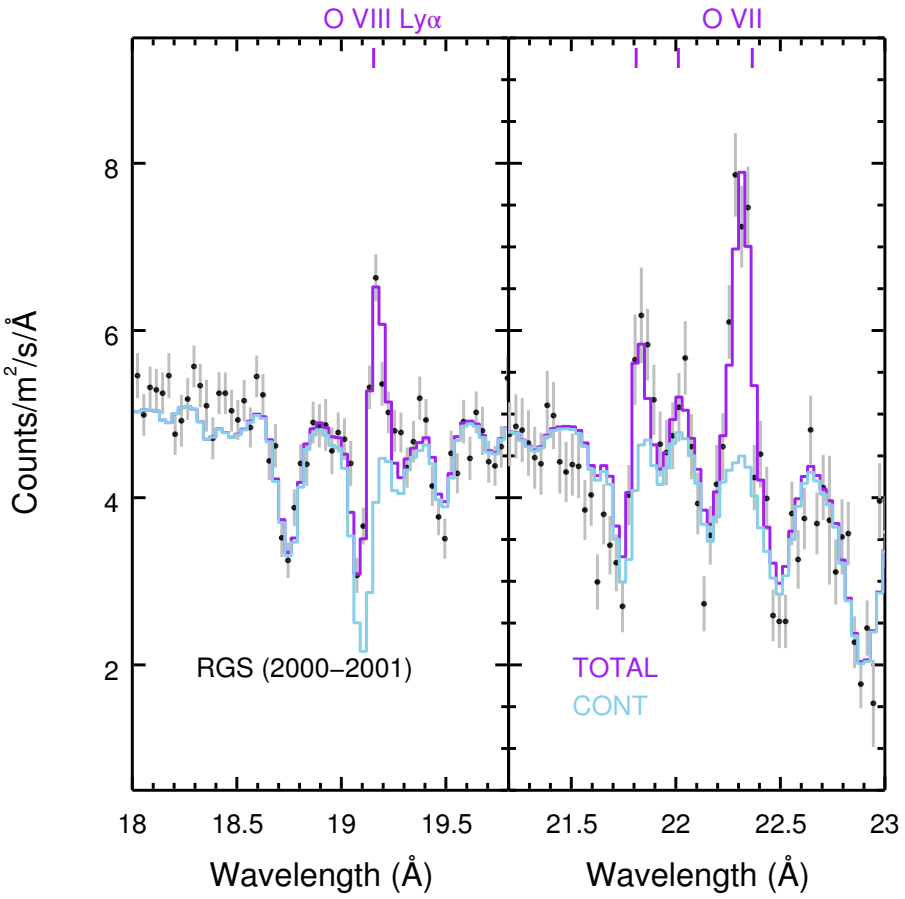

Figure 6.8: Local fit to the O VIII Lyα and O VII He-like triplets in the 2000-2001 time-averaged RGS spectrum of NGC 3783. The continuum is fixed to the best-fit global continuum corrected for the foreground Galactic absorption, the warm absorber and the broad emission features.

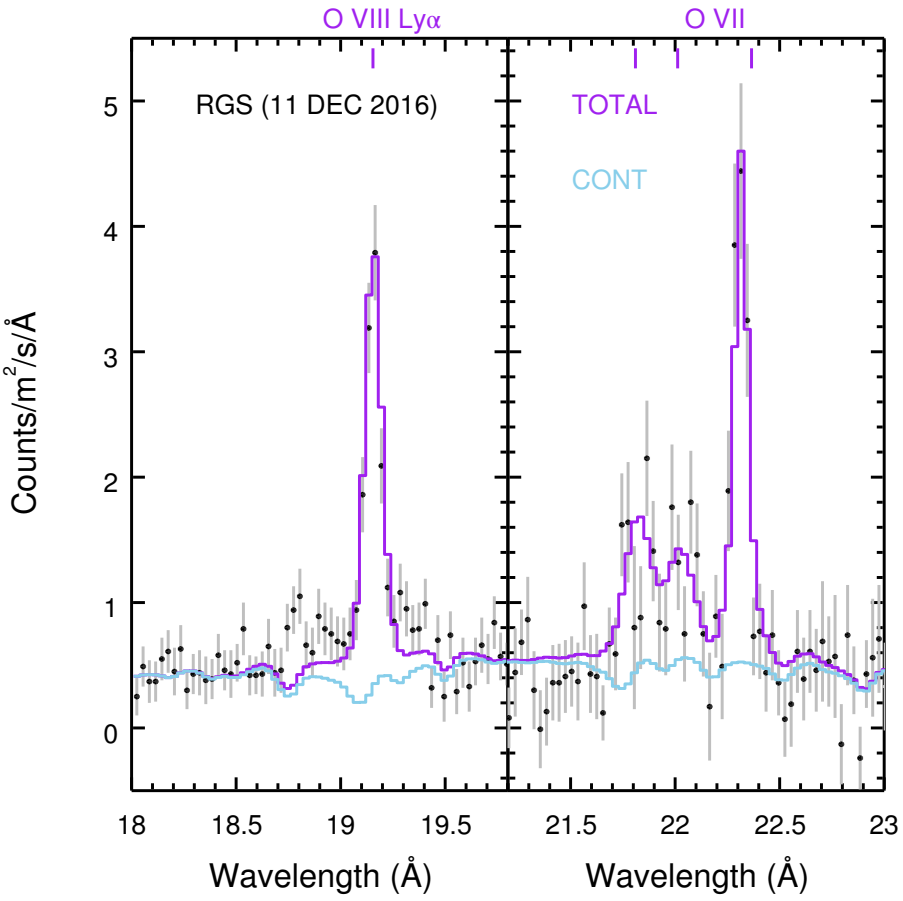

Figure 6.9: Local fit to the O VIII Lyα (left panel) and O VII He-like triplets (right panel) in the RGS spectrum of NGC 3783 from 11 December 2016. The continuum is fixed to the best-fit global continuum corrected for the foreground Galactic absorption, the obscurer, the warm absorber and the broad emission features.

Table 6.5: Best-fit results of the oxygen emission lines from RGS data in 2000–2001 and December 2016.

Ion	Line	2000–2001		11 DEC 2016		21 DEC 2016	
	λ ()	L (10^{32} W)	σ_v (km s^{-1})	L (10^{32} W)	σ_v (km s^{-1})	L (10^{32} W)	σ_v (km s^{-1})
O VIII Lyα	18.97	13.4 ± 0.9	360 ± 130	17.8 ± 1.1	370 ± 100	19.8 ± 1.1	520 ± 130
O VII (r)	21.60	6.6 ± 1.4	< 280	9.2 ± 1.8	740 ± 190	8.4 ± 2.1	< 500
O VII (i)	21.81	1.3 ± 1.3	< 280 (c)	6.0 ± 1.6	740 (c)	5.5 ± 0.6	< 500 (c)
O VII (f)	22.10	18.5 ± 1.7	310 ± 100	17.6 ± 1.9	< 180	17.3 ± 3.1	< 300

Notes. Velocity broadening (σ_v) of the resonance and intercombination lines of O VII are coupled (c) in the fit.

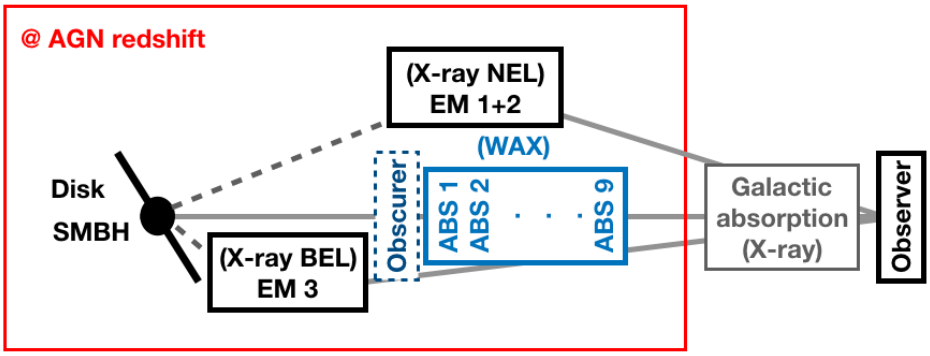

Figure 6.10: Simplified relations of components observed in NGC 3783 in X-rays. Three different light paths are shown here. The obscurer (dashed box) is not always present along the line of sight. Dashed lines indicate that these photons are not directly observable. WAX is short for the warm absorber in X-rays. BEL and NEL refer to the broad and narrow emission line. EM and ABS are short for emission and absorption, respectively.

resolution UV spectra with HST in 2000–2001 and December 2016 (Kriss et al. in prep). No significant variation is found in the line flux of Lyα, Si IV, C IV and He II between the two epochs. Hence, our previous assumption of a non-varying X-ray broad emission component is reasonable.

6.4.5. Summary

We analyzed the X-ray spectra of the Seyfert 1 galaxy NGC 3783 using both archival data in 2000–2013 and newly obtained data in December 2016. The intrinsic SED of the AGN, the obscuration, absorption, emission, and extinction effects are fitted simultaneously. In Figure 6.10 we show a sketch of what we think we are looking at.

Along the line of sight toward the nucleus, prominent absorption line features due to the warm absorber were clearly visible in the 2000–2013 X-ray spectra (e.g., Krongold et al. 2003; Netzer et al. 2003; Scott et al. 2014). Nine X-ray absorption components with different ionization parameters and kinematics are required in our photoionization modeling. On 11 and 21 December 2016, obscuration was seen in NGC 3783 (Mehdipour et al. 2017). The obscurer produces the heavy absorption of the soft X-ray continuum, as well as broad and blueshifted absorption lines in the UV spectra. It is very likely that there are more obscuration events in NGC 3783 (Markowitz et al. 2014, , Kaastra et al. 2018). Moreover, obscuration events have also been discovered in NGC 5548 (Kaastra et al. 2014) and NGC 985 (Ebrero et al.

2016).

The X-ray narrow emission components reprocess photons from the nucleus that are not directly observed (dashed lines in Figure 6.10). Prominent emission features like the O VIII Lyα line and the He-like triplets of O VII are visible whether the soft X-ray continuum is obscured or not. Weak emission features like the O VII RRC are detectable only when the continuum is obscured. Our photoionization modeling requires two components for the X-ray narrow emission features in NGC 3783. The two narrow emission components have different emission measure, ionization parameter, turbulence velocity, and emission covering factor. This is similar to our previous analysis for NGC 5548 (Mao et al. 2018).

Our photoionization modeling (Table 6.4) finds that the ionization parameter of the X-ray narrow emission component 1 remains constant throughout 2000–2016, indicating that either this component has a distance of at least a few light-years or its density is very low. On the other hand, for the X-ray narrow emission component 2, the ionization parameters are consistent between the two observations in December 2016 yet about a factor of two lower when compared to 2000–2001. If the variation is due to the change in the ionizing continuum, this suggests that component 2 is closer than component 1, but its distance should be larger than 10 light-days.

The X-ray broad emission component also reprocesses photons from the nucleus. In this work, we demonstrate that, when the obscurer is present in NGC 3783, it screens photons emitted from the X-ray broad emission component, which leads to the apparent weakening of the X-ray broad emission features in December 2016 (Section 6.4.3). The above interpretation supports the geometry proposed by Mehdipour et al. (2017) that the obscurer is located farther away than the X-ray broad emission component, which is a few light days from the nucleus (Peterson et al. 2004). Our photoionization modeling of the observed X-ray broad emission features is an ad hoc interpretation. There is evidence that the optical, UV, and X-ray broad emission lines originate from the same photoionized plasma (e.g., Costantini et al. 2016). Thus, the broad-line region has a range of densities, ionization parameters, and kinematics. A dedicated analysis with the "locally optimally emitting cloud" approach (e.g., Costantini et al. 2007) or even sophisticated dynamic models (e.g., Pancoast et al. 2011) is required to interpret the optical to X-ray broad emission lines in NGC 3783.

For simplicity, we assume that the X-ray broad and narrow emission components are not further absorbed by the warm absorber (Section 6.3.2), which might not be true. That is to say, the unabsorbed luminosity of the X-ray broad and narrow

emission lines obtained here is only a lower limit. To properly account for the screening effects by the warm absorber, we need to know which warm absorber components are more distant than the X-ray emission regions, and what are the covering factors for these warm absorber components with respect to the X-ray emission regions.

6.5. Conclusions

We focus on the photoionized emission features in the high-resolution X-ray spectra of NGC 3783 obtained in December 2016 when the soft X-ray continuum was heavily obscured. We also analyze the archival time-averaged high-resolution X-ray spectrum in 2000–2001 to compare the photoionized emission features and study the warm absorber. The main results are summarized as follows.

1. Nine photoionization components with different ionization parameters and kinematics are required for the warm absorber.

2. Two photoionization components are required for the X-ray narrow emission features, which are weakly varying over the past 15 years.

3. The presence of a X-ray broad emission component significantly improves the fit to the time-averaged spectrum in 2000–2001.

4. The X-ray broad emission features are much weaker in December 2016. This apparent weakening can be explained by the obscuration effect on the X-ray broad emission component.

6.A. Component relation in fitting the spectra using SPEX

The Comptonized disk component (COMT in SPEX), the power-law component (POW), the neutral reflection component (REFL) are additive components. An exponential cut-off is applied to the high- and low- energy end of the power-law component. This is realized via the ETAU model in SPEX (see also Chapter 7 of the SPEX cookbook), which provides a simple transmission $T(E) = \exp(-\tau_0\ E^a)$, where τ_0 is the optical depth at 1 keV. For the high-energy cut-off, we set $a = 1$ and $\tau_0 = 1/340$, which corresponds to a cut-off energy at 340 keV (De Rosa et al. 2002). For the low-energy cut-off, we set $a = -1$ and $\tau_0 = T_{\rm seed}$, which corre-

sponds to a cut-off at the seed photon temperature ($T_{\rm seed}$) of the Comptonized disk component.

The warm absorber is modeled with nine PION absorption components, which are multiplicative components. The most highly ionized component (index 1) is assumed to be the closest to the nucleus, while the least ionized component (index 9) is assumed to be the furthest. In the absence of the obscurer, the first PION absorption component is directly exposed to the AGN SED. Ionizing photons received by the second PION absorption is the AGN SED screened by the first PION absorption component. The rest is done in the same manner. In the presence of the obscurer, photons from the nucleus are first screened by the obscurer then modified by PION absorption components.

The PION emission components (for the X-ray photoionized emitter) are both multiplicative and additive. This is because they reprocess ionizing photons which are not directly observed (dashed lines in Figure 6.10) and emit photons which are directly observed. Accordingly, the ionizing continuum is first multiplied by the PION emission components (as multiplicative components) then followed by a ETAU component with $\tau_0 = 1000$ and $a = 0$ so that this ionizing continuum is not present in the spectrum. As additive components, the PION emission components are multiplied by the redshift of the AGN and the Galactic absorption in X-rays.

References

Badnell, N. R. 2006, ApJS, 167, 334
Behar, E., Rasmussen, A. P., Blustin, A. J., et al. 2003, ApJ, 598, 232
Bennert, N., Jungwiert, B., Komossa, S., Haas, M., & Chini, R. 2006a, A&A, 459, 55
Bennert, N., Jungwiert, B., Komossa, S., Haas, M., & Chini, R. 2006b, A&A, 456, 953
Bentz, M. C., Denney, K. D., Grier, C. J., et al. 2013, ApJ, 767, 149
Bianchi, S., Guainazzi, M., & Chiaberge, M. 2006, A&A, 448, 499
Blandford, R. D., Netzer, H., Woltjer, L., Courvoisier, T. J.-L., & Mayor, M., eds. 1990, Active Galactic Nuclei, 97
Blustin, A. J., Branduardi-Raymont, G., Behar, E., et al. 2002, A&A, 392, 453
Canizares, C. R., Davis, J. E., Dewey, D., et al. 2005, PASP, 117, 1144
Chelouche, D. & Netzer, H. 2005, ApJ, 625, 95
Costantini, E., Kaastra, J. S., Arav, N., et al. 2007, A&A, 461, 121
Costantini, E., Kriss, G., Kaastra, J. S., et al. 2016, A&A, 595, A106
De Rosa, A., Piro, L., Fiore, F., et al. 2002, A&A, 387, 838
den Herder, J. W., Brinkman, A. C., Kahn, S. M., et al. 2001, A&A, 365, L7
Denney, K. D., De Rosa, G., Croxall, K., et al. 2014, ApJ, 796, 134
Detmers, R. G., Kaastra, J. S., & McHardy, I. M. 2009, A&A, 504, 409
Ebrero, J., Kriss, G. A., Kaastra, J. S., & Ely, J. C. 2016, A&A, 586, A72

Elvis, M., Wilkes, B. J., McDowell, J. C., et al. 1994, ApJS, 95, 1
Fu, X.-D., Zhang, S.-N., Sun, W., Niu, S., & Ji, L. 2017, Research in Astronomy and Astrophysics, 17, 095
Fukumura, K., Kazanas, D., Shrader, C., et al. 2018, ApJ, 853, 40
Goosmann, R. W., Holczer, T., Mouchet, M., et al. 2016, A&A, 589, A76
Green, J. C., Froning, C. S., Osterman, S., et al. 2012, ApJ, 744, 60
Hönig, S. F., Kishimoto, M., Tristram, K. R. W., et al. 2013, ApJ, 771, 87
Kaastra, J. S. 2017, A&A, 605, A51
Kaastra, J. S. & Bleeker, J. A. M. 2016, A&A, 587, A151
Kaastra, J. S., Detmers, R. G., Mehdipour, M., et al. 2012, A&A, 539, A117
Kaastra, J. S., Kriss, G. A., Cappi, M., et al. 2014, Science, 345, 64
Kaastra, J. S., Mewe, R., Liedahl, D. A., Komossa, S., & Brinkman, A. C. 2000, A&A, 354, L83
Kaastra, J. S., Mewe, R., & Nieuwenhuijzen, H. 1996, in UV and X-ray Spectroscopy of Astrophysical and Laboratory Plasmas, ed. K. Yamashita & T. Watanabe, 411–414
Kaspi, S., Brandt, W. N., George, I. M., et al. 2002, ApJ, 574, 643
Kaspi, S., Brandt, W. N., Netzer, H., et al. 2001, ApJ, 554, 216
Kaspi, S., Smith, P. S., Netzer, H., et al. 2000, ApJ, 533, 631
Kraemer, S. B., Crenshaw, D. M., & Gabel, J. R. 2001, ApJ, 557, 30
Krongold, Y., Nicastro, F., Brickhouse, N. S., et al. 2003, ApJ, 597, 832
Landt, H., Ward, M. J., Steenbrugge, K. C., & Ferland, G. J. 2015, MNRAS, 454, 3688
Liedahl, D. A. & Paerels, F. 1996, ApJ, 468, L33
Lodders, K. & Palme, H. 2009, Meteoritics and Planetary Science Supplement, 72, 5154
Magdziarz, P. & Zdziarski, A. A. 1995, MNRAS, 273, 837
Mao, J. & Kaastra, J. 2016, A&A, 587, A84
Mao, J., Kaastra, J., & Badnell, N. R. 2017a, A&A, 599, A10
Mao, J., Kaastra, J. S., Mehdipour, M., et al. 2018, A&A
Mao, J., Kaastra, J. S., Mehdipour, M., et al. 2017b, A&A, 607, A100
Markowitz, A. G., Krumpe, M., & Nikutta, R. 2014, MNRAS, 439, 1403
Mason, K. O., Breeveld, A., Much, R., et al. 2001, A&A, 365, L36
Mehdipour, M., Kaastra, J. S., & Kallman, T. 2016, A&A, 596, A65
Mehdipour, M., Kaastra, J. S., Kriss, G. A., et al. 2017, A&A, 607, A28
Mehdipour, M., Kaastra, J. S., Kriss, G. A., et al. 2015, A&A, 575, A22
Netzer, H., Kaspi, S., Behar, E., et al. 2003, ApJ, 599, 933
Nicastro, F., Fiore, F., Perola, G. C., & Elvis, M. 1999, ApJ, 512, 184
Onken, C. A. & Peterson, B. M. 2002, ApJ, 572, 746
Pancoast, A., Brewer, B. J., & Treu, T. 2011, ApJ, 730, 139
Peterson, B. M., Denney, K. D., De Rosa, G., et al. 2013, ApJ, 779, 109
Peterson, B. M., Ferrarese, L., Gilbert, K. M., et al. 2004, ApJ, 613, 682
Ramírez, J. M., Bautista, M., & Kallman, T. 2005, ApJ, 627, 166
Scott, A. E., Brandt, W. N., Behar, E., et al. 2014, ApJ, 797, 105
Silva, C. V., Uttley, P., & Costantini, E. 2016, A&A, 596, A79
Smith, R. K., Abraham, M. H., Allured, R., et al. 2016, in Proc. SPIE, Vol. 9905, Space Telescopes and Instrumentation 2016: Ultraviolet to Gamma Ray, 99054M
Strüder, L., Briel, U., Dennerl, K., et al. 2001, A&A, 365, L18
Theureau, G., Bottinelli, L., Coudreau-Durand, N., et al. 1998, A&AS, 130, 333

Titarchuk, L. 1994, ApJ, 434, 570
Zycki, P. T., Done, C., & Smith, D. A. 1999, MNRAS, 305, 231

7

Nitrogen abundance in the X-ray halos of clusters and groups of galaxies

Junjie Mao, J. de Plaa, J. S. Kaastra, Ciro Pinto, Liyi Gu, F. Mernier, Hong-Liang Yan, Yu-Ying Zhang and H. Akamatsu

Chemical abundances in the X-ray halos (also known as the intracluster medium, ICM) of clusters and groups of galaxies can be measured via prominent emission line features in their X-ray spectra. Elemental abundances are footprints of time-integrated yields of various stellar populations that have left their specific abundance patterns prior to and during the cluster and group evolution.We aim to constrain nitrogen abundances in the CHEmical Evolution RGS Sample (CHEERS), which contains 44 nearby groups and clusters of galaxies, in order to have a better understanding of their chemical enrichment. We examine the high-resolution spectra of the CHEERS sample carefully and take into account various systematic effects in the spectral modelling. We compare the observed abundance ratios with those in the Galactic stellar populations, as well as predictions from stellar yields (low- and intermediate-mass stars, massive stars and degenerate

This chapter has been submitted to Astronomy & Astrophysics, 2018

stars). The nitrogen abundance can only be well constrained ($\gtrsim 3\sigma$) in one cluster of galaxies and seven groups of galaxies. The [O/Fe] – [Fe/H] relation of the ICM is comparable to that for the Galaxy, while both [N/Fe] and [N/O] ratios of the ICM are higher than in the Galaxy. Future studies on nitrogen radial distributions are required to tell whether the obtained higher [N/Fe] and [N/O] ratios are biased due to the small extraction region ($r/r_{500} \lesssim 0.05$) that we adopt here. Since abundances of odd-Z elements are more sensitive to the initial metallicity of stellar populations, accurate abundance measurements of N, Na and Al are required to better constrain the chemical enrichment in the X-ray halos of clusters and groups of galaxies.

7.1. Introduction

Clusters of galaxies aggregate baryons and dark matter within large-scale structures that have collapsed under their own gravity. A large fraction (∼15−20%) of the total mass of a cluster is in the hot (T∼10^{7-8} K) X-ray halos (also known as the intracluster medium, ICM), while the member galaxies only make up for ∼3−5% of the total mass. The rest is in the form of dark matter. The ICM is an attractive laboratory for the study of nucleosynthesis and chemical enrichment (for a review, see Werner et al. 2008). Due to its deep gravitational potential well, a massive cluster ($M \gtrsim 10^{13}$ $M_\odot$, Renzini & Andreon 2014) can be considered as a "closed-box" (e.g. White et al. 1993), i.e. all the metals synthesized by different stellar populations in the member galaxies are conserved within the cluster. This assumption is based on the consistency (Landry et al. 2013) between the total cluster baryon fraction within a certain radius, say r_{500}[1], and the cosmic baryon fraction. This assumption does not necessarily hold for less massive groups of galaxies, due to the relatively shallow gravitational potential well. Once the metals are released via stellar winds, supernovae, etc., various metal transportation mechanisms working on different locations and time-scales distribute the metals into the X-ray halos. Relevant metal transportation mechanisms include Galactic winds, ram–pressure stripping, AGN–ICM interaction, and galaxy–galaxy interaction (for a review, see Schindler & Diaferio 2008).

Assuming that stellar populations where the metals are synthesized are representative, given stellar yields and observed abundance patterns in the X-ray halos,

[1]The radius within which the plasma mass density is 500 times the critical density of the Universe at the redshift of the groups and clusters of galaxies.

we are able to put constrains on the chemical enrichment to the largest gravitationally bound systems in the Universe (for a review, see Böhringer & Werner 2010). Given that α elements (e.g. O, Ne, Mg) are mainly produced in massive stars via core-collapse supernovae (SNcc), and Fe-peak elements are mainly produced in degenerate stars via Type Ia supernovae (SNIa), the SNIa fraction with respect to the total number of supernovae (SNcc plus SNIa) that enriched the ICM can be obtained by either fitting (e.g. de Plaa et al. 2006; Komiyama et al. 2009; Sanders & Fabian 2006; Sato et al. 2007; Werner et al. 2006b) the best-fit elemental abundances with supernova yields or applying directly supernova yields to immediately predict the X-ray spectrum (Bulbul et al. 2012). The latter assumes that the ICM can be described as a single temperature plasma in collisional ionized equilibrium (CIE). Unlike elements heavier than oxygen, carbon and nitrogen are mainly produced in low- and intermediate-mass stars (for a review, see Nomoto et al. 2013). Thus, the ICM abundances of C and N also provide important information to better understand the chemical enrichment.

Observationally, the abundances of α elements and Fe-peak elements can be measured with both low- and high-resolution grating spectra (e.g., de Plaa et al. 2017; Hitomi Collaboration et al. 2017a; Mernier et al. 2016a). Carbon and nitrogen abundances can only be determined from high-resolution grating spectra, such as those obtained with XMM–*Newton*/RGS (Reflection Grating Spectrometers, den Herder et al. 2001). Xu et al. (2002) first reported the nitrogen abundance in the hot X-ray halo of NGC 4636. Later, the nitrogen abundance was reported in other individual targets (Grange et al. 2011; Sanders et al. 2008, 2010; Tamura et al. 2003; Werner et al. 2006a, 2009) and in the stacked spectra of 62 groups and clusters of galaxies in Sanders et al. (2011).

In this work, we systematically study the nitrogen abundance in the CHEERS sample[2](de Plaa et al. 2017), which contains 44 nearby ($z < 0.1$) X-ray bright cool-core groups and clusters of galaxies. The key sample selection criterion (de Plaa et al. 2017) of the CHEERS sample is that the O VIII Lyα line at ~ 18.97 (rest frame) is detectable ($\gtrsim 5\sigma$) with RGS.

Throughout the paper we use $H_0 = 70$ km s^{-1} Mpc^{-1}, $\Omega_{\rm M} = 0.3$, $\Omega_\Lambda = 0.7$. For the spectral analysis (Section 7.3), we use C-statistics following Kaastra (2017). Unless specified otherwise, all errors correspond to the 68% confidence level for one interesting parameter.

[2]CHEERS is short for CHEmical Evolution Rgs cluster Sample.

7.2. Data reduction

We reduced both RGS and EPIC/MOS data following the same procedures described in Pinto et al. (2015), using XMM-*Newton* Science Analysis System[3] (SAS) v15.0.0. MOS data are reduced since the Reflection Grating Assemblies (RGAs) are aligned with the light path of the MOS cameras. We use MOS data for screening soft-proton flares and deriving the spatial extent of the source along the dispersion direction of RGS.

For each observation, we extract RGS spectra in a ∼3.4-arcmin-wide (along the cross-dispersion direction) region centred on the emission peak. This is done by setting the *xpsfincl* mask to include 99% of the line spread function (LSF) inside the spatial source extraction mask. The extraction region is somewhat different from the circular aperture used for the EPIC data analysis, especially when there is a gradient in temperature structure and/or metal abundances. The spectra and response matrices are converted to SPEX (Kaastra et al. 1996) format through the SPEX task *trafo*. The RGS modelled background spectra are subtracted.

The spatial extent along the dispersion direction of the source dominates the broadening of the emission lines, which can be described as (Tamura et al. 2004)

$$\Delta\lambda = \frac{0.138}{m}\frac{\Delta\theta}{\mathrm{arcmin}}, \tag{7.1}$$

where m is the spectral order, $\Delta\theta$ is the offset angle of the source. The average spatial extent of the ICM that includes half of the maximum line flux is ∼2′, that is to say, the average FWHM of the line profile (Equation 7.1) is ∼0.276 (1st-order) and ∼0.138 (2nd-order), respectively. The bin size that we used in our data processing with *rgsproc* is 0.01 (1st-order) and 0.005 (2nd-order), respectively. Hence we re-binned the RGS spectra by a factor of 10 for both 1st-order (7−28) and 2nd-order data (7−14), which approximately yielded the optimal binning (1/2−1/3 FWHM, Kaastra & Bleeker 2016) for RGS spectra of the ICM.

7.3. Spectral analysis

The high-resolution X-ray spectral analysis package SPEX (v3.03) is used to fit the RGS spectra. For collisional ionized equilibrium (CIE) plasma modelling, a large portion of the out-dated atomic data from the old version of SPEX (v.2.07) has been replaced with the state-of-the-art results published in the last decade, such

[3] http://www.cosmos.esa.int/web/*XMM-Newton*/sas

as level-resolved radiative recombination data (Badnell 2006; Mao & Kaastra 2016) and ionization balance that includes inner-shell ionization data (Urdampilleta et al. 2017). In addition, atomic data including collisional excitation/de-excitation rates, radiative transition probabilities and auto-ionization rates have been consistently calculated using the FAC[4] code (Gu 2008) and are included in the latest version of SPEX code as well. The *Hitomi* Soft X-ray Spectrometer (SXS) spectrum of the Perseus cluster offers an unprecedented benchmark of popular atomic codes, we refer to Hitomi Collaboration et al. (2017b) for more details.

For each cluster or group of galaxies, we fit simultaneously RGS1 and RGS2 spectra of each observation. Unless specified otherwise, the redshifts and Galactic absorption column densities are frozen to the values given in Pinto et al. (2015). We use the collisional ionization equilibrium absorption model (de Plaa et al. 2004; Steenbrugge et al. 2005) with a fixed temperature $T = 0.5$ eV to account for the Galactic neutral absorption. When modelling the thermal component(s) of the ICM, we consider three different differential emission measure (DEM) distributions.

1. The simplest scenario is assuming that the ICM is isothermal so that it can be described as a single temperature CIE model (denoted as 1T).

2. A more complicated scenario is that the ICM consists of a hotter and a cooler CIE component (denoted as 2T). Abundances of the two thermal components are assumed to be the same, while emission measures and temperatures are free to vary.

3. The most sophisticated scenario requires a multi-temperature DEM distribution. We adopted the GDEM model (de Plaa et al. 2006) here, which assumed a Gaussian distribution of the DEM in $\log\ T$,

$$Y(x) = \frac{Y_0}{\sigma\sqrt{2\pi}} \exp\left(-\frac{(x-x_0)^2}{2\sigma^2}\right), \tag{7.2}$$

where $x = \log(T)$ and $x_0 = \log(T_0)$, with T and T_0 (peak temperature of the distribution) in units of keV, and Y_0 is the emission measure. Apparently, when $\sigma = 0$, GDEM is identical to 1T. Again, abundances of the multi-temperature components are assumed to be the same.

The above three DEM distributions are driven by the results of Frank et al. (2013), where the authors measured $\mathrm{DEM} = dY/dT$ (where $Y = \int n_e n_H dV$ is the emission measure) distribution of 62 galaxy clusters in the HIFUGCS sample (Zhang

[4]https://www-amdis.iaea.org/FAC

et al. 2011). By comparing the goodness of the fit, one of the DEM distributions is favored and reported for each cluster or group. Regardless of the choice of the DEM distribution, the abundances of N, O, Ne, Mg, Fe, and Ni are free to vary, while the other elements heavier than He are frozen to 0.3 solar (e.g. Fujita et al. 2008; Werner et al. 2013). All the abundances are normalized to the proto-solar abundances of Lodders & Palme (2009), i.e. $z_{i,\,\mathrm{ICM}}/z_{i,\,\odot}$. The ionization balance described in Urdampilleta et al. (2017) is used. The spatial broadening is taken into account by convolving the thermal plasma model (1T/2T/GDEM) with the spatial broadening model (*lpro*).

The general strategy mentioned above does not necessarily provide an accurate measurement of elemental abundances. Special treatments are required in some cases. When $N_{\mathrm{H\ I}} \gtrsim 7 \times 10^{24}\ \mathrm{m}^{-2}$, the Galactic hydrogen column density (denoted as NH) is allowed to vary (de Plaa et al. 2017). When the ICM thermal emission is contaminated by non-thermal emission, a power law component is added accordingly with parameters fixed to literature values (e.g. for M 87 see Werner et al. 2006a). The derived abundance of a given element is proportional to the equivalent width, i.e. the ratio between the line flux and the continuum flux, given that the abundance is determined mainly from a well resolved emission line. That is to say, any uncertainty in the continuum would also impact the abundance measurement. When fitting the RGS spectra for a broad wavelength range (7–28 in our case), the continuum flux may be slightly over- or under-estimated due to uncertainties in the calibration of the RGS effective area, background subtraction, etc. Consequently, abundance measurement might be significantly biased, compared to the statistical uncertainties in the spectral fit. The same issue has been pointed out by Mernier et al. (2015) for their EPIC spectral analysis. Here we also performed the local fit (± 1 around the line centre) to check whether the global continuum level is correct or not, if not, the local fit results are adopted. Other systematic uncertainties regarding the spatial broadening of the line (Appendix 7.B.2) and RGS background model (Appendix 7.B.3) can be found in the Appendix 7.B.

7.4. Results and comparison with literature values

Nitrogen abundance measurements are best done in plasma with lower temperature (Figure 7.11). Therefore, in the CHEERS sample, we found that the nitrogen abundance can merely be well constrained ($\gtrsim 3\sigma$) in the core ($r/r_{500} \lesssim 0.05$) of one cluster of galaxies (A 3526) and seven groups of galaxies (M 49, M 87, NGC 4636, NGC 4649, NGC 5044, NGC 5813, NGC 5846). For some of the lower temperature

sources (e.g., NGC 3411) in the CHEERS sample, more exposure time is required to better constrain the nitrogen abundance. Spectral fits near the N VII Lyα line for these eight targets are shown in Figure 7.1 and the same (global) fits to the $7-28$ Å wavelength range can be found in Figure 7.10. The abundances and abundance ratios are summarized in Table 7.1.

The O/Fe ratios in the above eight sources (with the extraction region of ~3.4 arcmin) are $\lesssim 1.3$. Some of our results differ from those reported in de Plaa et al. (2017) for the 0.8-arcmin-wide extraction region. This is mainly due to the strong temperature and abundance gradients (Mernier et al. 2017), if present.

The N/Fe ratios reported in Table 7.1 are $\gtrsim 1.4$ with larger scatter. Xu et al. (2002), Werner et al. (2006a, 2009) and Grange et al. (2011) also reported similar N/Fe ratio $\gtrsim 1.4$ with large scatter between individual targets. Tamura et al. (2003) reported a lower N/Fe ratio of $\sim (0.6 \pm 0.2)$ for NGC 5044. The N/Fe ratios for individual targets reported in Sanders et al. (2008, 2010) are (spectral fitting) model dependent, with both higher ($\gtrsim$1) and lower ($\lesssim$1) values.

The N/O ratios reported here are above zero at the $\gtrsim 2.5\sigma$ confidence level. Sanders et al. (2011) reported a N/O ratio of 4.0 ± 0.6 in the stacked spectra of 62 groups and clusters of galaxies. Note that the authors also point out that, among individual targets in their sample, the nitrogen abundances vary considerably.

We caution that the reported abundance ratios in the literature depend on the details of the spectral analysis and/or the adopted extraction region. As discussed in great detail (de Plaa et al. 2017) the O/Fe ratio can be biased up to 30% (in total) due to various kinds of systematic uncertainties, including the effect of spatial line broadening, the choice of the multi-temperature model, the influence of the assumed value of galactic hydrogen column density ($N_{\rm H}$). In addition, the background level around the N VII Lyα neighbourhood is rather high in many cases (Figure 7.1). But the N/Fe ratio is not affected by the uncertainties (a $\lesssim 10\%$ constant bias) in the RGS modelled background (Appendix 7.B.3). As we mentioned in Section 7.4, we perform local fit in some cases (e.g. M 87) to mitigate some systematic uncertainties. In short, the overall systematic uncertainties of the N/Fe ratio is expected to be within 30%.

In addition, Smith et al. (2009) reported $\rm N/Fe \lesssim 3$ after analyzing optical spectra of ~150 red-sequence galaxies over a wide mass range in the Coma cluster and the Shapley Supercluster. Johansson et al. (2012) found $\rm N/Fe \lesssim 3$ for ~4000 early-type galaxies in a narrow redshift bin $z \in (0.05,\ 0.06)$ observed with Sloan Digital Sky Survey (SDSS). In contrast, Greene et al. (2015) measured a remarkably super-

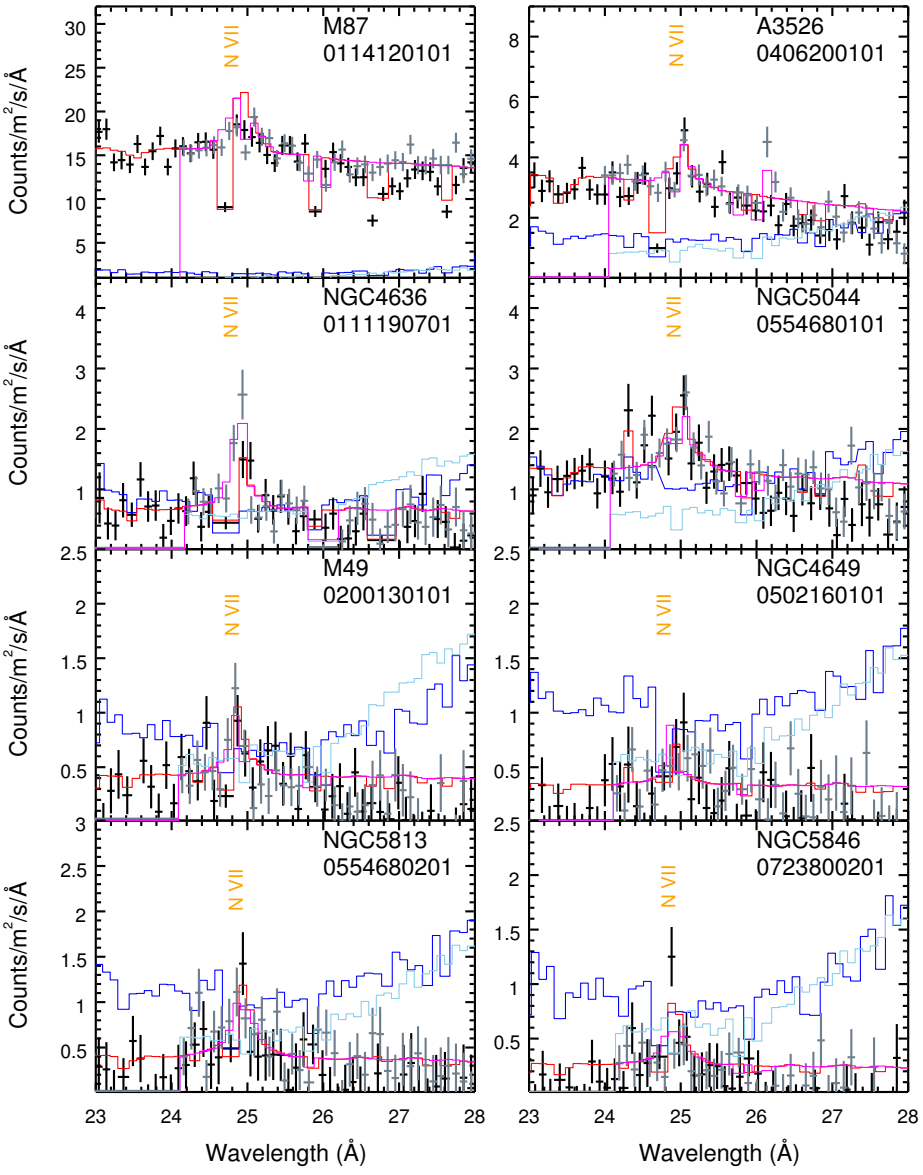

Figure 7.1: The global fits in the 18–28 wavelength range. The data points are shown in black (RGS1) and grey (RGS2), the modelled background spectra are shown in deep blue (RGS1) and light blue (RGS2) histograms, and the model spectra are shown in red (RGS1) and magenta (RGS2) histograms. Vertical dashed lines indicate the O VIII Lyα around 19 Å and N VII Lyα around 25 Å in the observed frame. Spectra from merely one observation per target are shown for clarity. Note that in the global fit to M 87 (the top-left panel), the N abundance is clearly overestimated, thus a local fit is performed (Section 7.4).

Table 7.1: Abundances and abundance ratios within the 3.4-arcmin-wide (along cross dispersion direction) extraction region.

Source	A3526	M49	M87	NGC4636	NGC4649	NGC5044	NGC5813	NGC5846
r/r_{500}	0.026	0.018	0.012	0.022	0.015	0.034	0.031	0.036
kpc	43.2	18.7	17.7	15.6	15.6	37.7	26.9	25.8
Model	NH+2T	GDEM	2T+PL	2T	1T	GDEM	2T	2T
C-stat./d.o.f.	2186/1088	852/544	3954/1111	748/480	1530/1096	1670/1094	2480/1649	1825/1093
$\sigma_{\mathrm{N/Fe}}$	$\sim 7\sigma$	$\sim 3\sigma$	$\sim 9\sigma$	$\sim 4\sigma$	$\sim 3\sigma$	$\sim 5\sigma$	$\sim 5\sigma$	$\sim 3\sigma$
N/O	2.7 ± 0.5	2.7 ± 1.0	2.2 ± 0.3	3.3 ± 1.1	2.9 ± 1.0	2.2 ± 0.5	3.2 ± 0.9	2.7 ± 0.8
N/Fe	1.5 ± 0.2	1.6 ± 0.6	1.8 ± 0.2	1.9 ± 0.5	2.4 ± 0.8	1.4 ± 0.3	1.9 ± 0.4	2.3 ± 0.7
O/Fe	0.54 ± 0.04	0.59 ± 0.10	0.82 ± 0.03	0.59 ± 0.08	0.84 ± 0.11	0.65 ± 0.05	0.58 ± 0.07	0.86 ± 0.12
Ne/Fe	0.57 ± 0.06	0.66 ± 0.17	0.55 ± 0.05	0.64 ± 0.12	1.07 ± 0.19	0.68 ± 0.08	0.53 ± 0.09	0.71 ± 0.14
Mg/Fe	0.66 ± 0.07	0.79 ± 0.19	0.24 ± 0.04	0.64 ± 0.13	1.40 ± 0.23	0.77 ± 0.08	0.83 ± 0.11	0.66 ± 0.14
Fe	1.02 ± 0.03	1.50 ± 0.12	0.55 ± 0.01	0.66 ± 0.04	0.55 ± 0.03	0.78 ± 0.03	0.92 ± 0.04	0.77 ± 0.05
Ni/Fe	1.2 ± 0.1	1.8 ± 0.5	0.65 ± 0.07	2.0 ± 0.4	2.5 ± 0.4	1.5 ± 0.3	$--$	2.0 ± 0.4

Notes. Abundances and abundance ratios are given according to the proto-solar abundance of Lodders & Palme (2009). $\sigma_{\mathrm{N/Fe}}$ is the significance level of nitrogen detection according to the N/Fe ratio (to be greater than zero). The uncertainties shown are 1σ statistical error bars. 1T, 2T and GDEM refer to single-temperature, two-temperature and multi-temperature differential emission measure (DEM) distribution (Section 7.3). For A 3526, "NH" refers to a free Galactic hydrogen column density in the spectral analysis. The Galactic hydrogen column densities for the other seven systems are frozen to literature values. For M 87, we use a power-law (PL) to model the non-thermal component, which is variable between the two observations (Werner et al. 2006a). For NGC 5813, Ni abundance cannot be constrained, and we fix it to solar during the fitting.

solar (at least three times solar) N/Fe abundance within a radius of 15 kpc for ~100 massive early-type galaxies. As pointed out by Greene et al. (2015), their N/Fe ratio would be three times solar if the O/Fe ratio were solar. In their default analysis, Greene et al. assume [O/Fe]=0.5, which leads to even higher N/Fe ratio. This assumed value of [O/Fe] is higher (by 0.2 dex or so) than some chemical enrichment model predicted (Nomoto et al. 2013; Pipino et al. 2009). A full spectral modelling is required to mitigate the impacts of blending and the uncertainties introduced by oxygen (Greene et al. 2015). Anyway, the O/Fe ratio assumed/predicted in the optical analysis is higher than that observed in the X-ray wavelength range. But it is possible that the SNcc products are preferably locked up by stars (Loewenstein 2013). In short, it is not trivial to compare and interpret the abundance ratios measured in the X-ray wavelength range and the optical wavelength range.

Moreover, The Ni/Fe abundance ratios reported in Table 7.1 differ from the solar Ni/Fe ratio found in the Perseus cluster (Hitomi Collaboration et al. 2017a). This might be due to the fact that the present work uses the L-shell lines which have large uncertainties in the current atomic codes.

7.5. Discussion

In the Galactic chemical evolution model (e.g. Kobayashi et al. 2006; Nomoto et al. 2013), nitrogen is mainly enriched via stellar winds of low- and intermediate-mass stars in the asymptotic giant branch (AGB). Therefore, in this section, we include the AGB enrichment channel (Section 7.5.1) for the chemical enrichment theory (e.g. Loewenstein 2013). We then compare the [O/Fe] – [Fe/H][5] and [N/Fe] – [Fe/H] relation between the ICM and different Galactic stellar populations, as well as the [N/O] – [O/Fe] relation between the ICM and supernova yields (Section 7.5.2). These comparisons enable us to discuss whether the nitrogen enrichment in the ICM shares the same origin as that in the Galaxy. Finally, we study elemental abundances in NGC 5044 (Section 7.5.3) to illustrate that by including odd-Z elements like nitrogen, the initial metallicity of the stellar population that enriched the ICM can be better constrained.

7.5.1. ICM Chemical enrichment

To interpret the observed time-integrated chemical abundances, we assume a single population of stars formed at high redshift (say, $z = 2 - 3$, Henriques et al. 2015)

[5] $[\mathrm{A/B}]_{\mathrm{ICM/star}} = \log_{10}\left(\frac{N_\mathrm{A}}{N_\mathrm{B}}\right)_{\mathrm{ICM/star}} - \log_{10}\left(\frac{N_\mathrm{A}}{N_\mathrm{B}}\right)_{\odot} = \log_{10}\left(\frac{Z_\mathrm{A}}{Z_\mathrm{B}}\right)_{\mathrm{ICM/star}}$.

with a common initial mass function (IMF). The ICM elemental abundance (the number of atoms of the ith element relative to that of hydrogen) relative to solar is defined as

$$Z_{i,\ \mathrm{ICM}} = \frac{z_{i,\ \mathrm{ICM}}}{z_{i,\ \odot}} = \frac{N^{\mathrm{li}}_{\mathrm{ICM}} < y^{\mathrm{li}}_{i} > + N^{\mathrm{m}}_{\mathrm{ICM}} < y^{\mathrm{m}}_{i} > + N^{\mathrm{d}}_{\mathrm{ICM}} y^{\mathrm{d}}_{i}}{M_{\mathrm{ICM}} X (A_i/A_H)(n_{i,\ \odot}/n_{\mathrm{H},\ \odot})}\ , \tag{7.3}$$

where $N^{li/m/d}_{\mathrm{ICM}}$ are the total number of low- and intermediate-mass stars (denoted with superscript "li") that enrich the ICM via the AGB channel, massive stars ("m") that explode as SNcc or PISNe (pair-instability supernovae), and single/double degenerate ("d") stars that explode as SNIa to enrich the ICM, $y^{\mathrm{li/m/d}}$ the corresponding stellar yields, M_{ICM} the mass of the ICM, A_i the atomic weight of the ith element, $A_{\mathrm{H}} = 1.0086\ a.m.u.$ the atomic weight of H, $n_{i,\odot}$ the elemental abundance by number in the solar abundance table and X is the mass fraction of H in the present universe.

The first two terms in the numerator of Equation (7.3) include the IMF weighted yields of low- and intermediate-mass or massive stars

$$< y_i >= \frac{\int_{m_{\mathrm{lo}}}^{m_{\mathrm{up}}} \phi(m) y_i(m) dm}{\int_{m_{\mathrm{lo}}}^{m_{\mathrm{up}}} \phi(m) dm}\ , \tag{7.4}$$

where $\phi(m)$ is the IMF, m_{lo} and m_{lo} the lower and upper mass limit (Z_{init} dependent, Table 7.2) of low- and intermediate-mass or massive stars considered.

It is unclear whether a universal IMF is applicable to all the clusters and groups of galaxies, or that the IMF depends on the local star formation rate (SFR) and/or metallicity of the environment (Mollá et al. 2015). For simplicity, other than the standard Salpeter IMF, we consider a top-heavy IMF, which is probably more relevant here, with an arbitrary IMF index (unity here). We caution that changing the IMF has profound consequences (Pols et al. 2012; Romano et al. 2005), including observables other than the chemical abundances that we measured here. For instance, a top-heavy IMF might make the galaxies too red (Saro et al. 2006). The global impacts on other observables introduced by the non-standard IMF are beyond the scope of this paper.

Additionally, the IMF weighted yield for massive stars, y^{m}_{i}, depends on the type(s) of supernovae that are taken into account for massive stars. We consider massive stars with stellar mass between 10 $M_{\odot}$ and 40 $M_{\odot}$ ($Z_{\mathrm{init}} > 0$) or 140 $M_{\odot}$ ($Z_{\mathrm{init}} = 0$) that undergo Fe core collapse at the end of their evolution and become

Table 7.2: The mass ranges (in $M_\odot$) used for calculating the IMF-weighted yields (Equation 7.4). For both low/intermediate-mass stars ("li", progenitors of AGBs) and massive stars ("m", progenitors of SNcc and PISNe), the mass ranges depend on the initial metallicity ($Z_{\rm init}$) of the stellar population.

$Z_{\rm init}$	$(m_{\rm lo},\ m_{\rm up})^{\rm li}$	$(m_{\rm lo},\ m_{\rm up})^{\rm m}$
0	(0.9, 3.5)	(11, 300)
0.001	(0.9, 6.5)	(13, 40)
0.004	(0.9, 6.5)	(13, 40)
0.008	(0.9, 6.5)	(13, 40)
0.02	(0.9, 7.0)	(13, 40)
0.05	(0.9, 7.0)	(13, 40)

Notes. The upper mass limit of intermediate-mass stars, defined as the minimum mass for the off-centre carbon ignition to occur, is smaller for lower metallicity (Gil-Pons et al. 2007; Siess 2007; Umeda & Nomoto 2002). The upper mass limit of massive stars depends on the types of supernovae that are taken into account. Massive stars that explode as core-collapse supernovae (with $m_{\rm up} = 40\ M_\odot$ for $Z \neq 0$ and an explosion energy of 10^{44} J) and pair-instability supernovae (with $m_{\rm up} = 300\ M_\odot$ and an explosion energy greater than 10^{44} J) are considered here.

Type II and Ib/c supernovae (i.e. core-collapse supernovae). Massive stars in the mass range of 25 $M_\odot$ to 40 $M_\odot$ ($Z_{\rm init} > 0$) or 140 $M_\odot$ ($Z_{\rm init} = 0$) can alternatively give rise to hypernovae (HNe) or faint supernovae (FSNe), instead of normal SNcc. Since the ratios among normal SNcc, HNe and FSNe for the relevant mass range are unknown for clusters and groups of galaxies, we do not consider HNe and FSNe enrichment for simplicity. In addition, we also take into account pair-instability supernovae (Umeda & Nomoto 2002) for zero initial metallicity ($Z_{\rm init} = 0$) enrichment, assuming that all the very massive stars, with stellar mass between 140 $M_\odot$ and 300 $M_\odot$, undergo pair-instability supernovae[6] (PISNe). Therefore, our calculation of the predicted abundance (Equation 7.3) is a first-order approximation.

The last term in the numerator of Equation (7.3) include $y_i^{\rm d}$, which is the yield per SNIa, and depends on the SNIa model. SNIa yields from Iwamoto et al. (1999), Badenes et al. (2006) and Maeda et al. (2010) are used for the following analysis.

In Table 7.3, we summarize the 12 sets of IMF weighted yields for non-degenerate stars that enrich the ICM via AGBs, SNcc (and PISNe). In Table 7.4 we summarize the 16 sets of SNIa yields for degenerate stars that enrich the ICM via SNIa.

Since measurement of the elemental abundances relative to hydrogen are limited to various uncertainties in the RGS spectral analysis (Appendix 7.B), the number of stars ($N_{\rm ICM}^{li/m/d}$ in Equation 7.3) in different enrichment channels (AGBs, SNcc and

[6] If very massive stars do not lose much mass, they are completely disrupted without forming a black hole via pair-instability supernovae (Barkat et al. 1967).

Table 7.3: Summary of the underlying model dependency for IMF power-law index and initial metallicity ($Z_{\rm init}$) of the stellar population (Equation 7.4).

Index	(IMF, $Z_{\rm init}$)	Index	(IMF, $Z_{\rm init}$)
1	(2.35, 0.0)	7	(1.0, 0.0)
2	(2.35, 0.001)	8	(1.0, 0.001)
3	(2.35, 0.004)	9	(1.0, 0.004)
4	(2.35, 0.008)	10	(1.0, 0.008)
5	(2.35, 0.02)	11	(1.0, 0.02)
6	(2.35, 0.05)	12	(1.0, 0.05)

Table 7.4: Summary of the underlying model dependency for SNIa enrichment (Equation 7.3).

Index	Model	Index	Model
1	CDD1	2	CDD2
3	W7	4	W70
5	WDD1	6	WDD2
7	WDD3	8	DDTa
9	DDTb	10	DDTc
11	DDTd	12	DDTe
13	DDTf	14	CDEF
15	ODDT	16	CDDT

Notes. [a] The IMF power-law index and the initial metallicity ($Z_{\rm init}$) of the stellar population. [b] SNIa models. The CDD (i.e. index 1 and 2) and WDD (5 to 7) models are delayed-detonation scenario (Iwamoto et al. 1999). The W (3 and 4) models refer to convection deflagration scenario (Iwamoto et al. 1999). The DDT (8 to 12) models are based on observational results from the Tycho supernova remnant (Badenes et al. 2006). The CDEF model refers to 2D deflagration scenario while both ODDT and CDDT models refer to 2D delayed-detonation scenario (Maeda et al. 2010).

SNIa) are not well constrained. Thus, we turn to the abundance ratios (relative to Fe), which can be better constrained. The abundance ratios in the ICM can be characterized by

$$\frac{z_{i,\,\mathrm{ICM}}}{z_{k,\,\mathrm{ICM}}} = \frac{r^{\mathrm{li}}_{\mathrm{ICM}} < y^{\mathrm{li}}_{i} > + < y^{\mathrm{m}}_{i} > + r^{\mathrm{d}}_{\mathrm{ICM}} y^{\mathrm{d}}_{i}}{r^{\mathrm{li}}_{\mathrm{ICM}} < y^{\mathrm{li}}_{k} > + < y^{\mathrm{m}}_{k} > + r^{\mathrm{d}}_{\mathrm{ICM}} y^{\mathrm{d}}_{k}} \frac{A_k\ n_{k,\,\mathrm{ICM}}}{A_i\ n_{i,\,\mathrm{ICM}}}\ , \tag{7.5}$$

where k is the reference atom number (specifically refers to Fe $Z = 26$ hereafter) and $r^{\mathrm{li/d}}_{\mathrm{ICM}} = N^{\mathrm{li/d}}_{\mathrm{ICM}} / N^{\mathrm{m}}_{\mathrm{ICM}}$.

7.5.2. Origin of nitrogen enrichment

We first compare the abundance relations between the ICM and the Galaxy. Figure 7.2 and Figure 7.3 show the [O/Fe] – [Fe/H] and [N/Fe] – [Fe/H] relations, respectively. The corrections for non-local thermodynamic equilibrium (NLTE) and three dimensional (3D) stellar atmosphere models are not taken into account for some N and O abundances in the metal-poor halo stars ([Fe/H]$\lesssim -1$) in Israelian et al. (2004) and Spite et al. (2005). Detailed NLTE and 3D corrections (see e.g. Asplund 2005, for a review), are beyond the scope of this paper and do not alter our interpretation below.

For the [O/Fe] – [Fe/H] relation (Figure 7.2), a gradual decrease of [O/Fe] with increasing [Fe/H] is found in the [Fe/H]$\lesssim -1$ regime. This is due to the fact that the more metal-poor the SNcc progenitor is, the larger the [O/Fe] ratio in the SNcc yields (Romano et al. 2010). The rapid decrease of [O/Fe] in the [Fe/H]$\gtrsim -1$ regime, on the other hand, stems from the Fe enrichment by SNIa. The [O/Fe] ratio of the ICM is slightly smaller compared to disc stars in the Galaxy with the same [Fe/H] ratio. The overall [O/Fe]–[Fe/H] relation of the ICM and the Galaxy still supports the idea that they share the same enrichment channel (SNcc plus SNIa) for O and Fe.

In contrast to the decreasing trend of [O/Fe] with increasing [Fe/H], a relatively flat [N/Fe] ratio with increasing [Fe/H] is found in Figure 7.3, which indicates that N and O are enriched via different channels. In fact, the [N/Fe] – [Fe/H] relation for the disk and halo stars can be explained (see Fig.3 in Romano et al. 2010) with AGB yields from Karakas (2010). The [N/Fe] ratio of the ICM is slightly larger compared to halo stars in the Galaxy with the same [Fe/H] ratio. The overall [N/Fe]–[Fe/H] relation of the ICM and the Galaxy indicates that they share the same enrichment channel (AGB) for N.

Secondly, we compare the [N/O]–[O/Fe] relation of supernova yields (Figure 7.4)

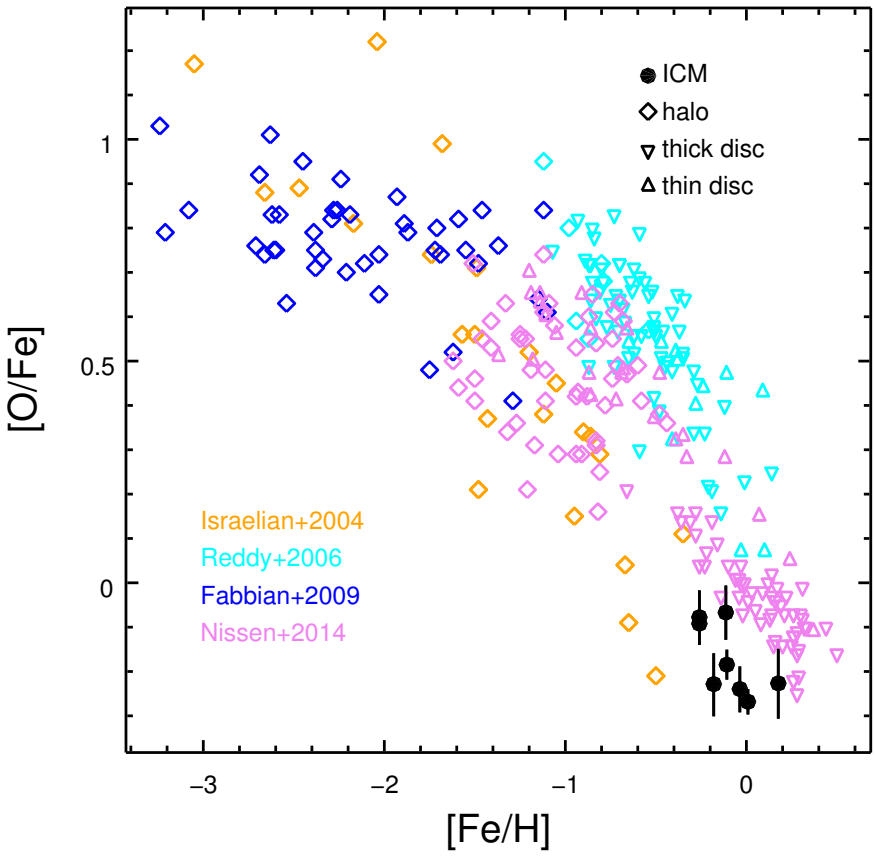

Figure 7.2: The [O/Fe] – [Fe/H] relation for ICM and the Galaxy. The ICM Fe abundances and O/Fe abundance ratios (Table 7.1) are shown as black dots with (statistical) error bars.The Galactic Fe abundances and O/Fe abundance ratios are taken from Israelian et al. (2004) (halo, orange), Reddy et al. (2006) (disc and halo, cyan), Fabbian et al. (2009) (halo, blue) and Nissen et al. (2014) (disc and halo, pink).

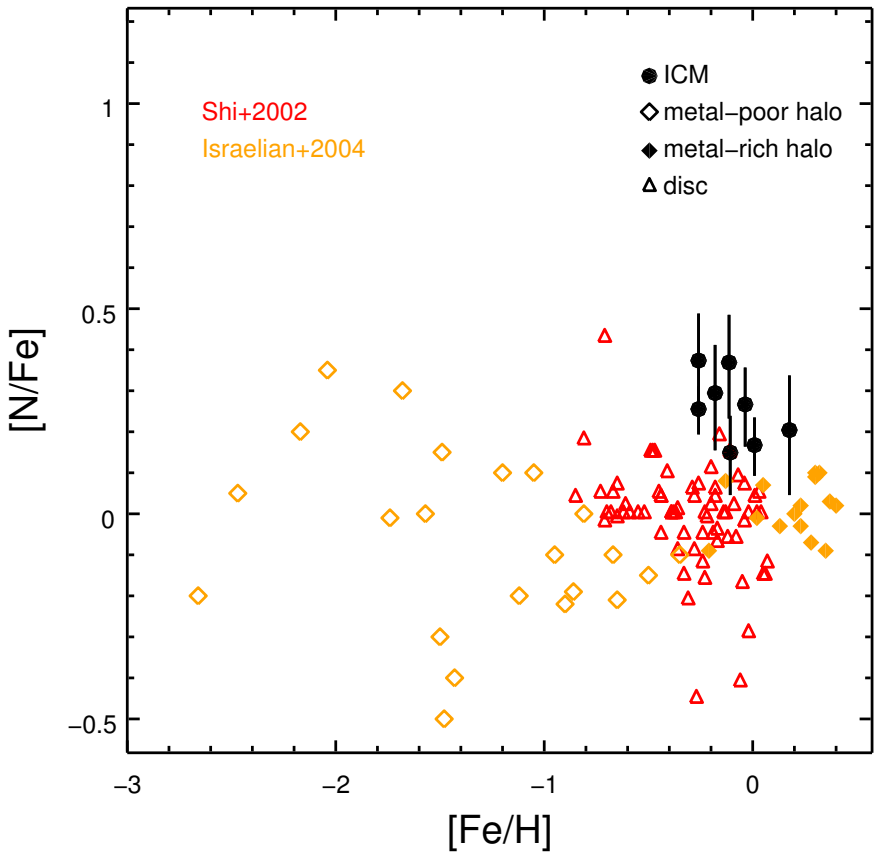

Figure 7.3: Similar to Figure 7.2 but for the [N/Fe] – [Fe/H] relation. The Galactic Fe abundances and N/Fe abundance ratios are taken from Shi et al. (2002) (disc, red triangles) and Israelian et al. (2004) (halo, orange diamonds).

to the observed abundances (Figure 7.5). The [O/Fe] ratio of the ICM is smaller compared to that of halo stars since the ICM is enriched by both SNcc and SNIa, while halo stars are mainly enriched by SNcc. Generally speaking, the [N/O] ratio in the ICM is larger than that of halo stars. Similar results have been reported in Werner et al. (2006a) for M 87.

If the chemical enrichment were completely due to massive stars ($N_{\rm ICM}^{\rm li/d} = 0$ in Equation 7.3), then we would have [O/Fe]$\gtrsim 0.5$ (Figure 7.4), except for $Z_{\rm init} = 0$. For $Z_{\rm init} = 0$, the [O/Fe] ratio can be lower than ~0.5, due to the explosive O-burning by PISNe (Nomoto et al. 2013). In Figure 7.4, we assume all the very massive stars undergo PISNe (Section 7.5.1). In reality, the exact value of [O/Fe] (for $Z_{\rm init} = 0$) might differ, depending on the IMF and the fraction of very massive stars that undergo PISNe. The [O/Fe] ratios in the ICM (Figure 7.5) are in the range of (-0.5, 0.2), suggesting that the enrichment from SNIa is required for the ICM, unless PISNe contributes significantly.

The nitrogen enrichment via SNIa is negligible ([N/O]$\lesssim -1$). Therefore, one would expect [N/O] $\lesssim -0.2$ (Figure 7.4), if the chemical enrichment were completely due to massive stars ($N_{\rm ICM}^{\rm li/d} = 0$ in Equation 7.3). We caution that the [N/O] ratio for $Z_{\rm init} = 0$ in Figure 7.4 is in fact a lower limit, since we do not include enrichment from metal-poor rotating massive stars before they explode as supernovae which is due to the lack of knowledge of corresponding number fraction and yields. Chiappini et al. (2006) have shown that a contribution, as large as [N/Fe]~0.5, from metal-poor ([Fe/H] $\lesssim$-2.5) rotating massive stars is required to solve the primary nitrogen problem (see also Fig.3 in Romano et al. 2010). For a Salpeter IMF, the upper limit of [N/O] is estimated to be zero, given that not all the metal-poor massive stars are rotating (thus [N/Fe] $\lesssim 0.5$) and [O/Fe]$\gtrsim 0.5$ (Figure 7.4), regardless of $Z_{\rm init}$. The same upper limit of [N/O] holds for a top-heavy IMF with $Z_{\rm init} \gtrsim 0.001$. Nonetheless, for a top-heavy IMF with $Z_{\rm init} \lesssim 0.001$, the upper limit of [N/O] might be above zero, since [O/Fe] ratio can be lower than 0.5 as previously discussed.

The [N/O] ratios in the ICM are above zero at the $\gtrsim 2.5\sigma$ confidence level (Table 7.1), indicating that under a Salpeter IMF, the massive stars cannot be the main nitrogen factory. In this case, nitrogen mainly originates from low- and intermediate-mass stars (AGBs). Nevertheless, we cannot rule out that under a top-heavy IMF with a low initial metallicity ($Z_{\rm init} \lesssim 0.001$), massive stars could be an important nitrogen enrichment factory.

Last but not least, we caution that the measured [N/Fe] and [N/O] ratios in Table 7.1 might be biased. Due to the limited field of view (FOV) of RGS, the

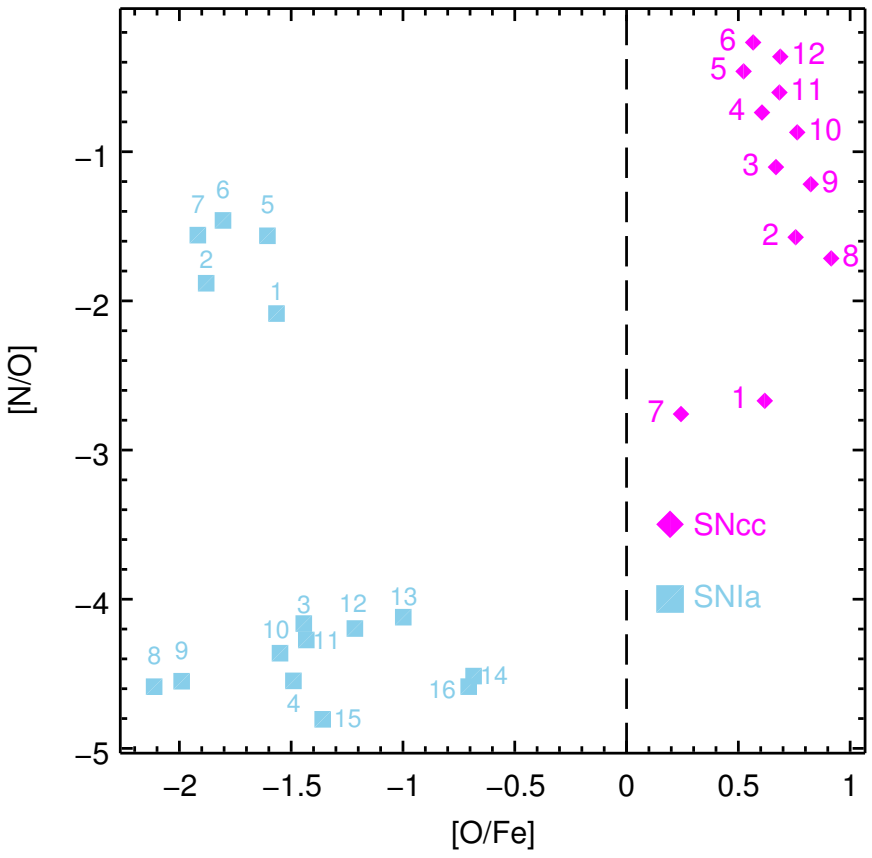

Figure 7.4: The diamonds (magenta) are the IMF-weighted yields of SNcc (and PISNe for $Z_{\rm init} = 0$), while the squares (blue) are SNIa yields. The indices next to the symbols indicate corresponding model dependency (Tabel 7.3 and Tabel 7.4). The yields of all the elements from C to Zn can be found in Figure 7.15 and 7.16.

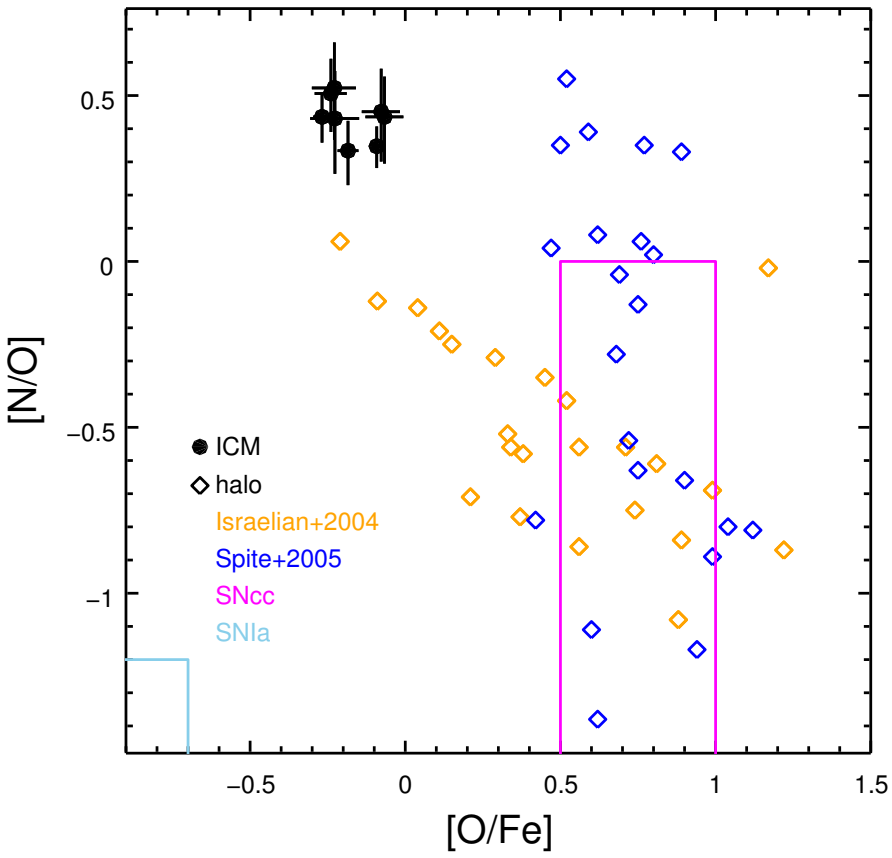

Figure 7.5: Similar to Figure 7.2 but for [N/O] vs. [O/Fe].The results for Galactic stellar populations are taken from Israelian et al. (2004); Spite et al. (2005) (halo, diamonds). The magenta box indicates the region of SNcc yields except for $Z_{\rm init} = 0$, while the blue box indicates the region of SNIa yields (Figure 7.4).

abundance ratios obtained in the rather small ($\lesssim 0.05 r_{500}$) extraction regions do not necessarily represent the abundance patterns within the "closed-box" (Section 7.1). If the elements enriched via different channels were distributed into the ICM in different ways, so that, for instance, N were more centrally peaked than Fe and O, the resulting [N/Fe] and [N/O] ratios in the core region would appear to be larger.

7.5.3. Odd-Z elements

Previous studies on chemical enrichment in the ICM mainly focused on determining the SNIa fraction with respect to the total number of SNe that enriched the ICM (e.g. de Plaa et al. 2006). In terms of elemental abundances, most abundant even-Z elements from oxygen up to and including nickel (except Ti) have been measured. Additionally, one odd-Z Fe-peak element, Mn, is also studied in the stacked spectra of the CHEERS sample (Mernier et al. 2016a). In terms of yields table, in addition to SNcc and SNIa, Pop III stars (de Plaa et al. 2006; Werner et al. 2006b) and Ca-rich gap transients (CaRGT, Mulchaey et al. 2014) have also been taken into account to interpret the observed abundance pattern. In this section, we include the nitrogen abundance and yields from AGBs (Campbell & Lattanzio 2008; Karakas 2010; Nomoto et al. 2013) for the chemical enrichment study of the ICM.

Since the number of abundance ratios derived from the RGS spectra are rather limited, due to the relatively small coverage of the energy range, it is more meaningful when the abundance ratios measured with EPIC are also taken into account. Ideally, one needs to obtain the abundances within $\sim r_{500}$ of the ICM so that the "closed-box" assumption is valid for massive clusters (Section 7.1). In practice, especially for groups of galaxies, the FOV of RGS covers merely a tiny fraction of r_{500}. Moreover, the unknown nitrogen abundance gradients within r_{500}, prevent us from extrapolating the abundances out to r_{500} with the obtained RGS abundances by hand.

We use both the RGS and EPIC results of NGC 5044 (Table 7.5) for the exercise here, given that the measurement uncertainty of the nitrogen abundance is typical (neither too large nor too small), and the extraction regions are comparable ($\sim$0.034 r_{500} for RGS and $\sim$0.05 r_{500} for EPIC). In Table 7.5, the N/Fe, O/Fe, Ne/Fe, Mg/Fe, and Ni/Fe abundance ratios are measured with RGS, while the Si/Fe, S/Fe, Ar/Fe, and Ca/Fe ratios are measured with EPI (see details in Appendix 7.C).

We emphasize that we focus on the comparison among different settings of the ICM enrichment model, i.e. the choice of IMF index and the initial metallicity of the stellar population, the choice of SNIa model, and whether to include enrichment

Table 7.5: The abundance ratios for NGC 5044 within the extraction region (i.e. $\lesssim r/r_{500}$). Abundance ratios measured with EPIC spectra are labeled with †.

X/Fe	Value
N/Fe	1.4 ± 0.3
O/Fe	0.65 ± 0.05
Ne/Fe	0.68 ± 0.08
Mg/Fe	0.77 ± 0.08
Si/Fe†	0.79 ± 0.10
S/Fe†	1.1 ± 0.2
Ar/Fe†	1.0 ± 0.3
Ca/Fe†	1.2 ± 0.2
Fe	0.72 ± 0.02
Ni/Fe	1.5 ± 0.3

from AGBs or not.

It is possible that SNIa from different channels (via single- or double-degenerate, deflagration or detonation, and super- or sub-Chandrasekhar limit) all play a role in the chemical enrichment of the ICM (Finoguenov et al. 2002; Mernier et al. 2016b). We only fit the measured abundance ratios with one set of SNIa yields for simplicity. Including an additional set of Ca-rich gap transients yields improves the statistics negligibly and does not change the above main points.

Since almost all the measured abundance ratios (Table 7.5) are close to solar, we restrict the initial metallicity of stellar populations to be solar and sub-solar (i.e. excluding $Z_{\rm init} = 0.05$). Thus, the observed abundance ratios are fitted to 10 (2 sets of IMF and 5 sets of $Z_{\rm init}$) $\times$16 (for SNIa) combinations of yield tables. The reduced chi-squared ($\chi^2_{\rm red}$) for all the fits are shown in the upper panel of Figure 7.6. The 10×16 combinations of the chemical enrichment models are highly degenerate. We can reject a large number of combinations based on the statistics, say $\chi^2_{\rm red} \gtrsim 3$, i.e. $\log_{10}(\chi^2_{\rm red}) \gtrsim 0.5$, however, the IMF power-law index and SNIa models cannot be exclusively obtained with current abundance measurements.

Typical "best" fits of the abundance ratios in NGC 5044 to stellar yields are shown in Figure 7.7 (without the N/Fe ratio and yields from AGBs) and Figure 7.8 (with the N/Fe ratio and yields from AGBs). Without yields from AGBs (Figure 7.7), we also show the model prediction on the N/Fe ratio (~ 0.2). Compared to the measured N/Fe ratio (1.4 ± 0.3), the predicted N/Fe ratio is lower by $\sim 4\sigma$, indicating that the contribution from SNcc is not enough to explain the observed N/Fe ratio. When we include yields from AGBs (Figure 7.8), the predicted N/Fe ratio is consistent ($\lesssim 1\sigma$) with the observed N/Fe ratio. Additionally, the predicted O/Fe ratio decreases from

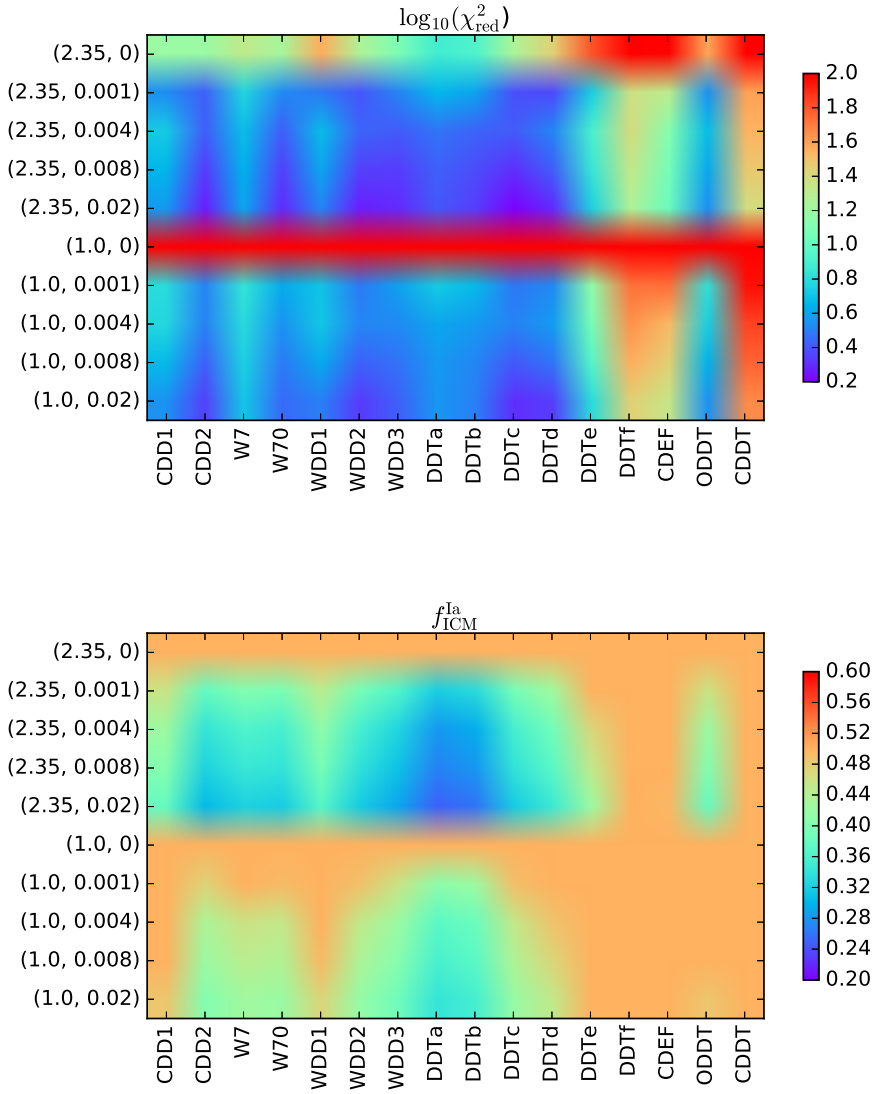

Figure 7.6: Color map of reduced chi-squared (χ^2/d.o.f. in $\log_{10}$-scale, upper panel) and SNIa fraction ($f^{\rm Ia}_{\rm ICM}$, lower panel) for 10×16 combinations of yields we considered to fit the abundance ratios in NGC5044, without N/Fe (d.o.f. = 7). The X-axis labels indicate the SNIa models. The Y-axis labels indicate IMF power-law index and the initial metallicity of the stellar populations.

~0.69 (SNe) to ~0.66 (SNe + AGBs) due to the negative oxygen yields in AGBs.

In most cases, a Salpeter IMF provides better χ^2 statistics (Figure 7.6). When a Salpeter IMF and DDTc SNIa model are adopted, the SNIa fraction ($f_{\rm ICM}^{\rm Ia}$) is consistent with $\sim 32\%$, whether we include N/Fe and AGBs enrichment or not (Figure 7.7 and 7.8). The ratio ($r_{\rm ICM}^{\rm li} = r^{\rm li}/r^{\rm m}$) between the number of low- and intermediate-mass stars and that of massive stars is 180 ± 50. Under a Salpeter IMF, the ratio ($r_{\rm ICM}^{\rm li}$) is expected to be ~ 40, which is lower than the fitted value by $\sim 3\sigma$. Again, the "closed-box" assumption is not fulfilled here, so that if the AGB products were more centrally peaked than the SNcc products (Section 7.5.2), a higher $r_{\rm ICM}^{\rm li}$ obtained here could be explained.

When N/Fe and AGB enrichment are not included in the fit, the "best" fit initial metallicity is 0.02 (solar). This is mainly constrained by the less than unity O/Mg abundance ratio (Figure 7.9). Including N/Fe and AGB enrichment again favours solar initial metallicity. We also notice that, in both cases, a wide range of $Z_{\rm init}$ yields comparable results (Table 7.6), except for $Z_{\rm init} = 0$.

In principle, when odd-Z elemental abundances, like nitrogen, are included in the analysis, the initial metallicity of the stellar population should be better constrained, since yields of odd-Z elements increase significantly with increasing $Z_{\rm init}$ owing to a surplus of neutrons (Nomoto et al. 2013), while those of even-Z and Fe-peak elements are almost constant over a wide range of metallicities. This is shown clearly in Figure 7.9 for massive stars. We emphasize that the denominator of the abundance ratio on the Y-axis is set to Mg instead of Fe in Figure 7.9. This is because Mg enrichment via SNIa and AGBs are negligible, so that the observed abundance ratios of Na/Mg and Al/Mg can be used directly to probe the initial metallicity of the stellar population.

For future work, more accurate abundance measurements of odd-Z elements including N, Na and/or Al are required to better constrain the initial metallicity of the stellar population. Current instruments lack the spectral resolution to resolve the Lyα lines of Na XI and Al XIII. Hopefully, future missions with high spectral resolution and large effective area like *XARM* (X-ray astronomy recovery mission) and *Athena* (Nandra et al. 2013) will address this issues.

7.6. Conclusions

We constrain the N/Fe ratio in the core ($r/r_{500} \lesssim 0.5$) of one cluster (A 3526) and seven groups of galaxies (M 49, M 87, NGC 4636, NGC 4649, NGC 5044, NGC 5813, NGC 5846) in the CHEERS sample with high-resolution RGS spectra. Our main con-

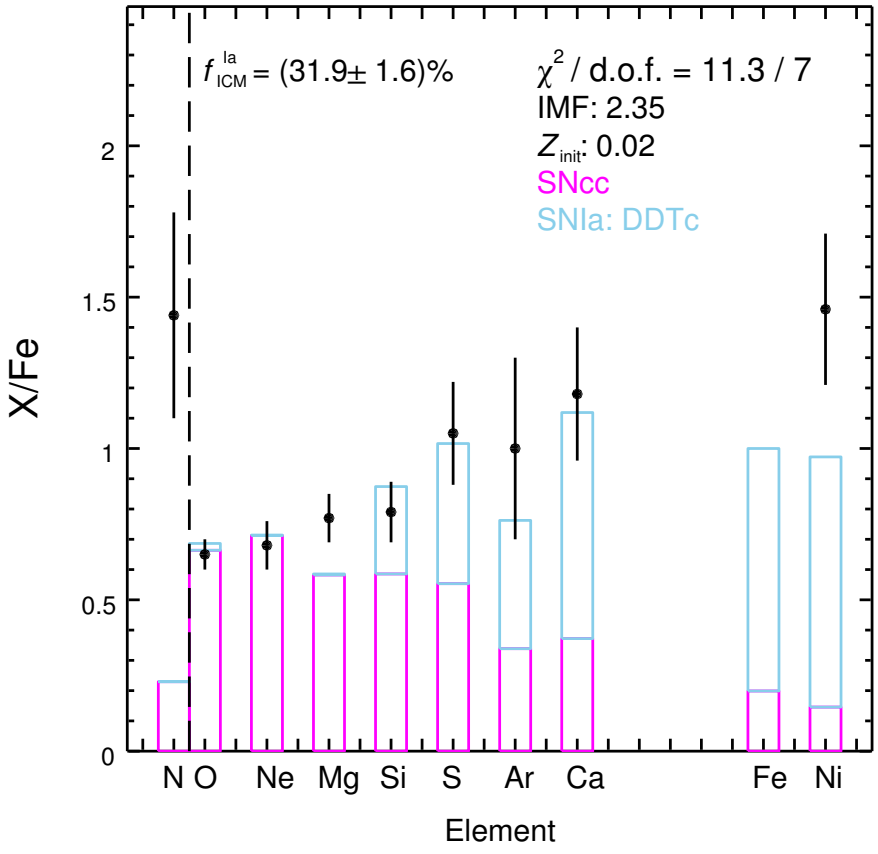

Figure 7.7: One of the acceptable fits of chemical enrichment in NGC 5044. Yields of SNcc (magenta) and SNIa (blue) are used for the fit with Equation (7.5). The adopted IMF power-law index is 2.35 (Salpeter) and the initial metallicity of the stellar population is 0.02 (solar). N/Fe and yields of AGBs are not included in the fit, but shown for comparison. The SNIa fraction $f_{\rm ICM}^{\rm Ia} = r^{\rm d}/(r^{\rm d}+1)$ is $(31.9\pm1.6)\%$.

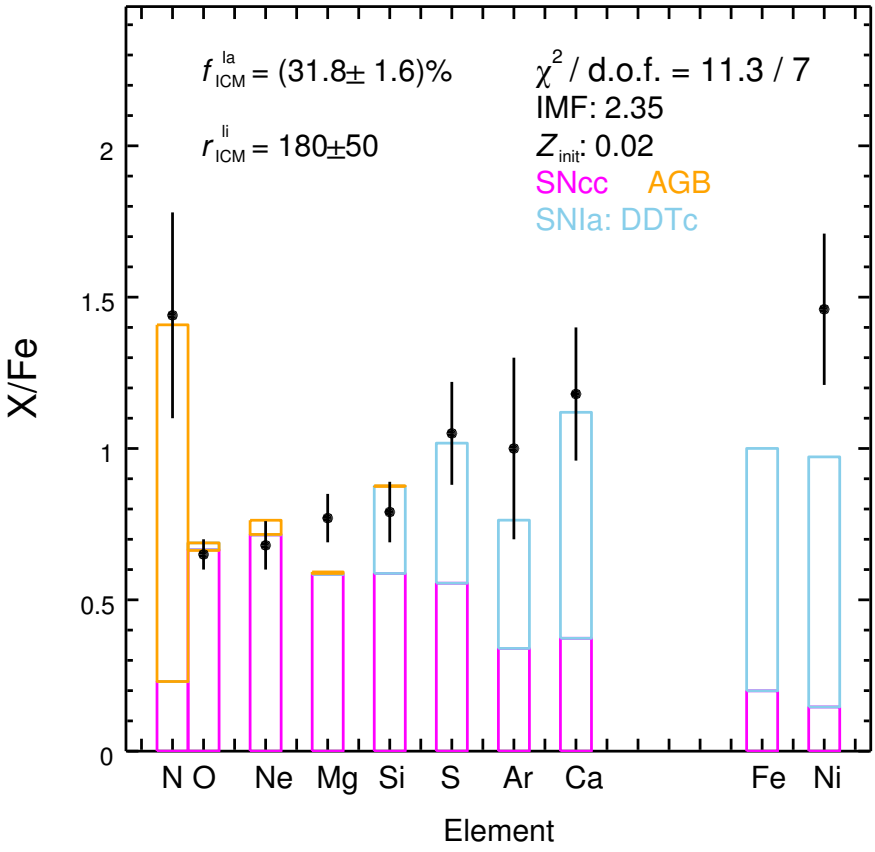

Figure 7.8: Similar to Figure 7.7 but N/Fe and AGB yields (orange) are included during the fit. Again, the favored IMF power-law index is 2.35 (Salpeter) and $Z_{\rm init} = 0.02$. The SNIa fraction is consistent with the previous result. The ratio ($r^{\rm li}_{\rm ICM} = r^{\rm li}/r^{\rm m}$) between the number of low- and intermediate-mass stars and that of massive stars is 180 ± 50.

Table 7.6: The "best" fits (d.o.f. = 7) of chemical enrichment in NGC 5044, given the IMF power-law index and initial metallicity of the stellar population.

IMF[a]	$Z^{b}_{\rm init}$	SNIa	AGB[c]	χ^2
2.35	0.02	DDTc	N	11.3
2.35	0.008	DDTc	N	14.5
2.35	0.004	WDD3	N	18.1
2.35	0.001	DDTd	N	16.5
2.35	0	DDTa	N	53.9
1.0	0.02	DDTc	N	14.2
1.0	0.008	DDTc	N	18.0
1.0	0.004	DDTc	N	22.7
1.0	0.001	DDTc	N	21.5
1.0	0	DDTa	N	>100
2.35	0.02	DDTc	Y	11.3
2.35	0.008	DDTc	Y	13.2
2.35	0.004	DDTc	Y	14.5
2.35	0.001	DDTd	Y	22.5
2.35	0	DDTa	Y	52.5
1.0	0.02	DDTc	Y	13.7
1.0	0.008	DDTc	Y	15.7
1.0	0.004	DDTc	Y	18.7
1.0	0.001	DDTc	Y	18.4
1.0	0	DDTa	Y	>100

Notes. [a] The power-law index of the IMF. [b] The initial metallicity of the stellar populations. [c] Whether the N/Fe ratio and the yields of AGBs are included in the fit.

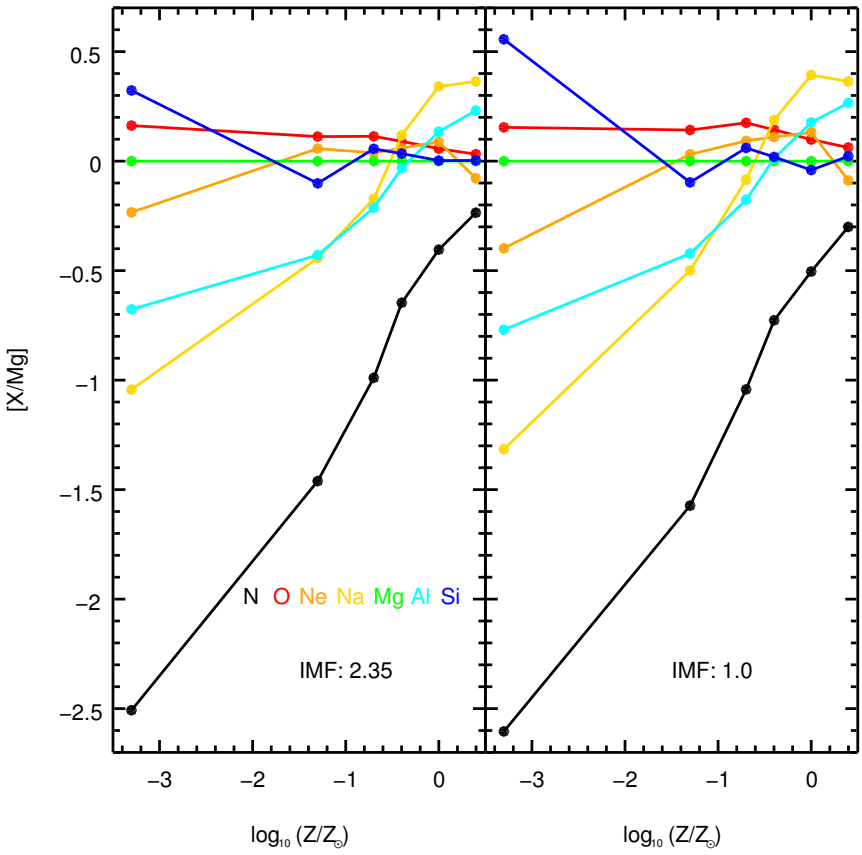

Figure 7.9: The IMF weighted abundance ratios (with respect to Mg) as a function of the initial metallicity of massive stars (the SNcc channel). The results for $Z_{\rm init} = 0$ are plotted at ~ -3.3.

clusions are summarized as follows:

1. The nitrogen abundance is well constrained ($\gtrsim 3\sigma$) in objects with a relatively cool ICM ($kT \lesssim 2$ keV). For some of the systems (e.g. NGC 3411) in the CHEERS sample, more exposure time is required to better constrain the nitrogen abundance. In objects with a hotter ICM ($kT \gtrsim 2-3$ keV), the continuum level is high so that weak emission lines like N VII Lyα cannot be well constrained.

2. Both the [O/Fe]–[Fe/H] and [N/Fe]–[Fe/H] relations observed in the ICM are comparable to those observed in different stellar populations in the Galaxy, indicating that the enrichment channels for N, O and Fe are expected to be the same. One possible explanation for the super solar N/Fe and N/O ratios in the ICM is the bias introduced by our small extraction region ($r < 0.05r_{500}$). This potential bias can be confirmed by radial abundance maps for N, O, and Fe in future work.

3. If the observed ratio [N/O]> 0 (at the $\gtrsim 2.5\sigma$ confidence level) is not biased due to the small extraction region, under a Salpeter IMF, the low- and intermediate-mass stars are found to be the main metal factory for nitrogen. This is in agreement with the Galactic chemical evolution theory and previous studies of M 87. Nitrogen enrichment from massive stars might still be important, especially if the stellar population would have a top-heavy IMF and zero initial metallicity.

4. We find the obtained SNIa fraction is insensitive to the N abundance and AGB yields.

5. We also point out that accurate abundance measurements of odd-Z, such as N, Na, and Al can certainly help to better constrain the initial metallicity of the stellar population that enriched the ICM.

7.A. Global spectral fit

The global fits to the 7–28 wavelength range for each source in Table 7.1 are shown in Figure 7.10. The location (in the observed frame) of characteristic emission lines are labeled, including the Lyα line from H-like N VII, O VIII, Ne X, Mg XII, He-like triplets from O VII, Ne IX, Mg XI and the resonance and forbidden lines of Ne-like Fe XVII.

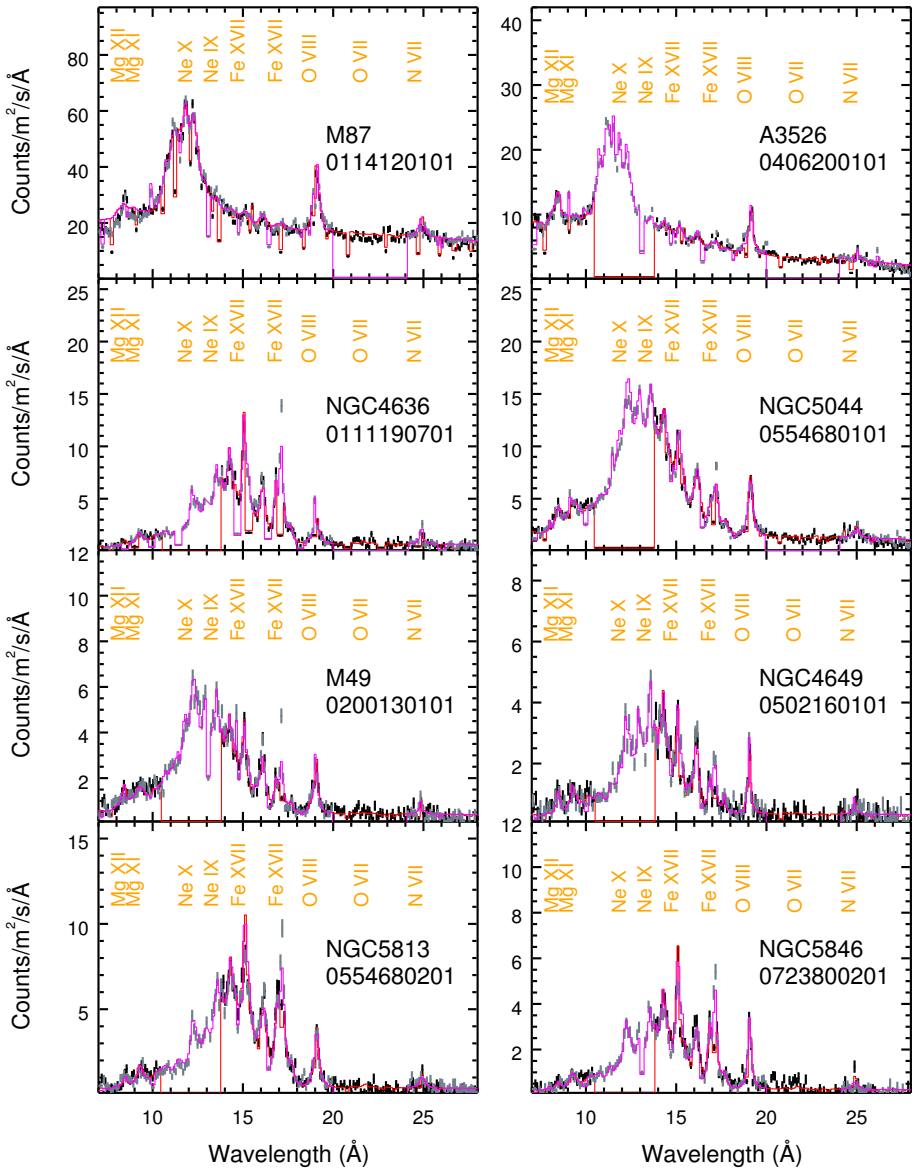

Figure 7.10: The global fits to the 7–28 wavelength range. The data points are shown in black (RGS1) and grey (RGS2) and the model spectra are shown in red (RGS1) and magenta (RGS2) histograms. Spectra from merely one observation per target are shown for clarity.

7.B. Systematic uncertainties in spectral analysis

7.B.1. Differential emission measure distribution

Fitting a multi-temperature plasma with a single temperature (1T) model would often over-estimate the emission measure and under-estimate the abundances (Buote 2000; Buote & Canizares 1994). Alternatively, a two-temperature (2T) or multi-temperature (GDEM) model can measure the nitrogen abundance more accurately.

In a 2T model, if the emission measure of the hotter component is $\gtrsim 5$ times that of the cooler one, the N VII in the hotter CIE component contributes more to the observed N VII Lyα emission in the spectra. Given the same emission measure and nitrogen abundance, the N VII Lyα line flux is proportional to the N VII ion concentration (relative to all the nitrogen atoms and ions in the ICM) times the level occupations of $^2P_{0.5}$ and $^2P_{1.5}$ (the sum of occupations of all the levels are defined as unity). As the level occupations increase gradually as a function of plasma temperature (bottom panel in Figure 7.11), the N VII ion concentration is the leading factor to determine the line emissivity. As mentioned above, we tie the abundances in our 2T model, thus, assuming $kT_{\rm c} \lesssim 0.7$ keV and $kT_{\rm h} \gtrsim 2$ keV, when $Y_{\rm c}/Y_{\rm h} \lesssim 0.2$, the N VII in the hotter component contributes more to the emission line, while for $Y_{\rm c}/Y_{\rm h} \gtrsim 0.2$, the N VII is mainly from the cooler component.

In addition, the line emissivity of N VII Lyα peaks around $T \sim 2\times10^6$ K (Kaastra et al. 2008), implying that nitrogen is preferably found in relatively cooler plasma. As the line emissivity declines rapidly with the increasing temperature of the plasma (top panel in Figure 7.11), we find it is rather difficult to well constrain the nitrogen abundance via the extremely weak N VII Lyα emission line embedded in the relatively high continuum where $kT \gtrsim 2-3$ keV.

7.B.2. Spatial broadening model

The spatial broadening model *lpro* is built based on the spatial broadening profile. The latter is obtained from the MOS1 image, since the MOS1 DETY direction is in parallel to the RGS1 dispersion direction. There are two more free parameters in *lpro*, the scaling factor (s) and the offset parameter. Here we discuss the systematic uncertainties of the spatial broadening model.

For instance, in M 87, due to the presence of the bright non-thermal emission in the second observation (ObsID: 0200920101), not only the spectra are heavily contaminated, but also the spatial broadening model created with the MOS1 image is affected. The brighter the central non-thermal emission, the more centrally peaked

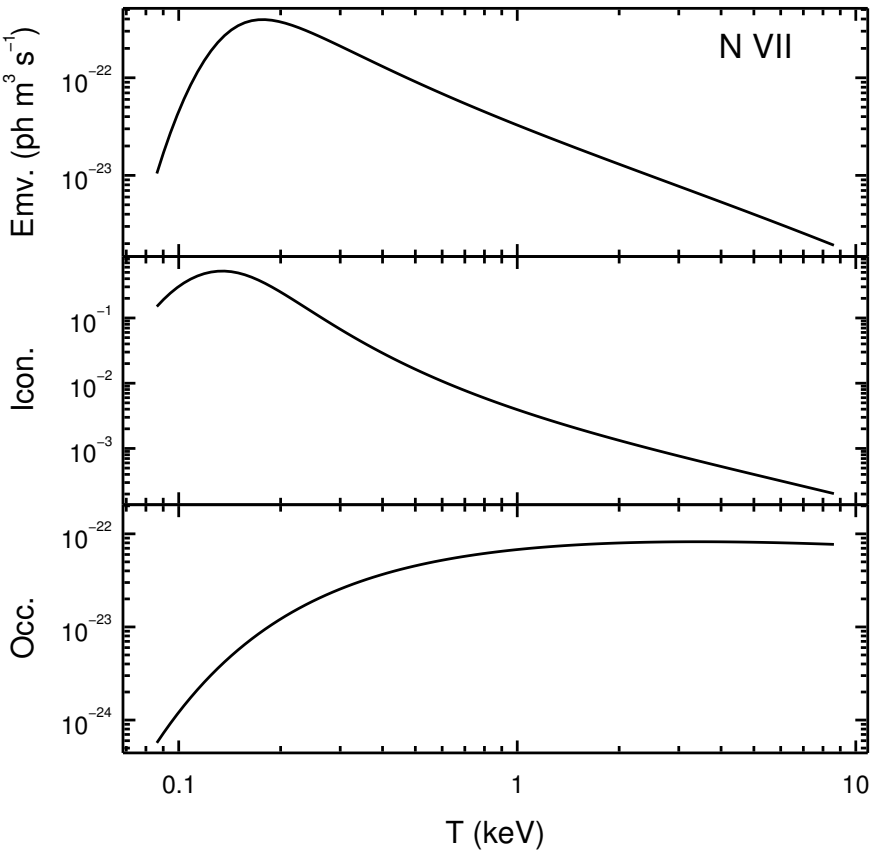

Figure 7.11: The N VII Lyα line emissivity (top), relative ion concentration (middle) and relative level occupation (bottom) of the two upper levels $^2P_{0.5}$ and $^2P_{1.5}$ (in sum, since the fine-structure lines cannot be distinguished). The underlying ionization balance is Urdampilleta et al. (2017) and the proto-solar abundance of Lodders & Palme (2009) is used. In a hot ($kT \gtrsim 0.6$ keV) single-temperature CIE plasma, nitrogen is almost fully ionized in the form of N VIII, i.e. the ion concentration of N VIII is ~ 1. Most of the N VII is in the ground level $^1S_{0.5}$, i.e. the level occupations of $^1S_{0.5}$ is close to unity.

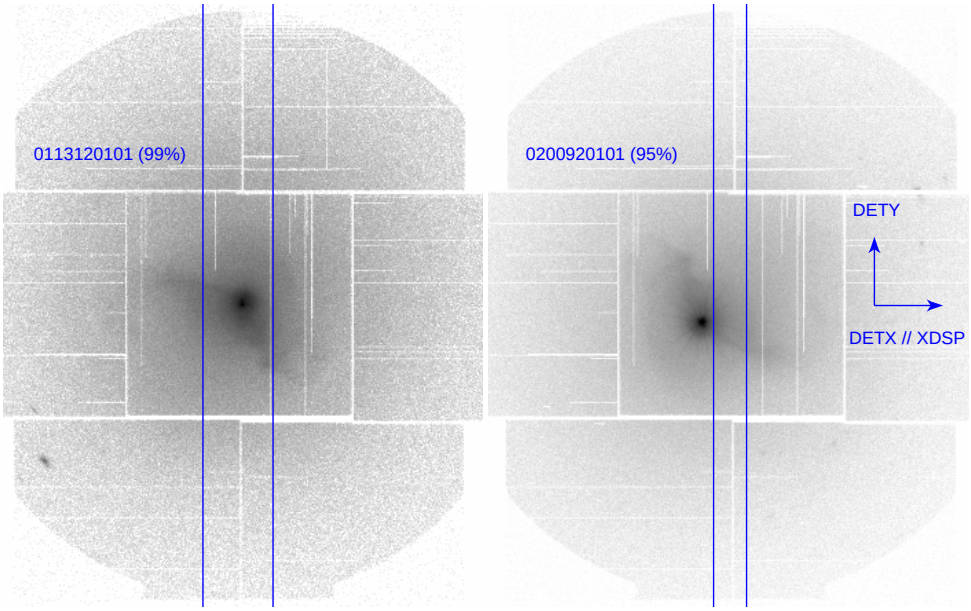

Figure 7.12: The 7–28 energy band MOS1 image in the detector coordinate system for M87. The MOS1 DETX axis is in parallel with the cross dispersion direction (XDSP) of RGS. In the second observation (0200920101), the non-thermal emission is much brighter, offset by ~1.5 arcmin and the image is rotated ~188 degrees clockwise. The (blue) rectangular boxes indicated the extraction regions for *rgsvprof*. For the first observation, a 99%-xpsf (~3.4 arcmin) extraction region, aligned with the RGS source extraction region, is used. For the seconding observation, only the onset 95%-xpsf (~1.6 arcmin) extraction region (to avoid central contamination) is shown for clarity.

the surface brightness profile (seen indirectly in Figure 7.13). Spatial broadening models built on these biased surface brightness profiles reflect no longer the proper spatial extent of the ICM.

We compare the (global) fit results using different line broadening profile of M 87 here. If the non-thermal emission were merely a point source and the ICM were azimuthally symmetric, one might fit the observed 2D image with two Gaussian/Lorentzian profiles with different widths, then subtract the non-thermal emission counterpart to obtain the profile for the ICM only. However, this is not the case for M 87 due to its azimuthal asymmetry (Figure 7.12). Because the emission centre is offset by ~1.5 arcmin in 0200920101, we took advantage of a ~1.6-arcmin-wide extraction region without the non-thermal emission, leading to a better yet still biased (probably flatter) spatial broadening model (Figure 7.13). Whereas, we found the *lpro* scaling factor (free parameter) can account for the bias in the spatial broadening profile.

Other than the accuracy of the spatial broadening profile, the scaling factors

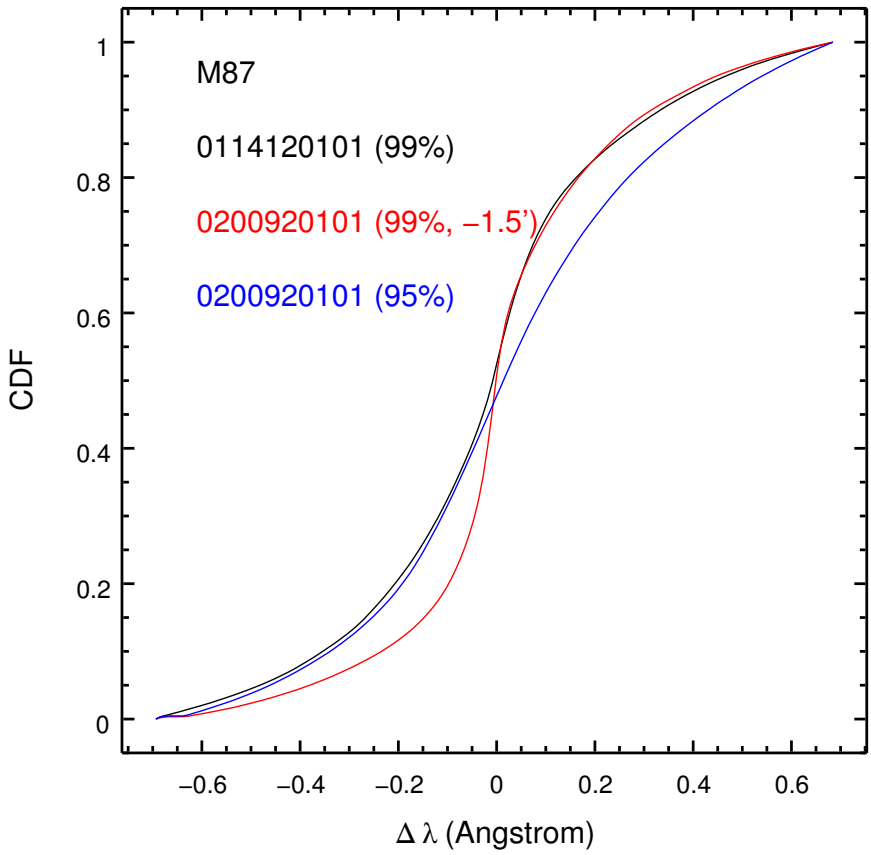

Figure 7.13: The cumulative distribution function (CDF) of the spatial broadening profile of M87. We built the spatial broadening profiles for both two observations (black and red) of the RGS 99%-xpsf source extraction regions. For the second observation (0200920101), a 1.5 arcmin offset is applied so that the extraction region is centred on the peak of the X-ray emission. Moreover, for the second observation, we also built a spatial broadening profile with a narrower 95%-xpsf extraction region (blue) suffering less from central contamination (Figure 7.12).

might be different for different thermal components and/or different ions within the same thermal component. When studying the O VII He-like triplets in the CHEERS sample, Pinto et al. (2016) found the spatial extent of the cooler ICM component is narrower than that of the hotter counterpart, by using two *lpro* model components for the two temperature components. Since in most cases, nitrogen from the hotter component contributes the most to the emission line we observed, thus, applying the same *lpro* model component (mainly determined by the high-temperature lines) to both the hotter and the cooler thermal component should be fine in our case.

7.B.3. RGS background model

In some cases in the CHEERS sample, the modelled background level is even higher than the source continuum level at $\lambda \gtrsim 20$ (Figure 7.1). Thus we check the systematic uncertainties of the modelled background as well. We use A 2029 as an example to compare the observed spectra from an offset observation toward A 2029 with the RGS modelled background.

The outskirts of A 2029 were observed with XMM-*Newton* in 2015. The projected angular distances for the outskirts are ~ 20 arcmin, i.e. at least $\sim 1.3\ r_{500}$. The outskirts of A 2029 were also observed by *Suzaku* and no statistically significant emission is detected beyond 22 arcmin, except for the northern observation (Walker et al. 2012). That is to say, the spectra of the observations toward the outskirts of A 2029 can be considered as background spectra. We used the same data reduction method described in Section 7.2 to screen out the flare time intervals and extracted the RGS spectra in the 99%-xpsf extraction region.

In Figure 7.14, we plot the RGS 1st-order "net" (observed minus modelled background) spectra of the A 2029 southern outskirt (ObsID: 0744411001). If the modelled background spectra is accurate enough, the "net" spectra should be consistent with zero. Above ~26.5 , we see the modelled background spectrum of RGS1 is significantly overestimated. The RGS2 modelled background is more accurate than that of RGS1 above ~26.5 . Therefore, for any source with redshift $z \gtrsim 0.07$, the accuracy of the RGS1 modelled background can be an issue for the N VII Lyα line measurement, if the modelled background level dominates the source continuum level for (redshifted) $\lambda \gtrsim 26.5$.

Last but not least, we take NGC 5846 as an example to show the impact on the abundance measurement if the modelled background were systematically over- or under-estimated. We used the FTOOL task *fcalc* to increase/decrease the values of the entire BACKSCAL column by 10% for the modelled background spectra FITS

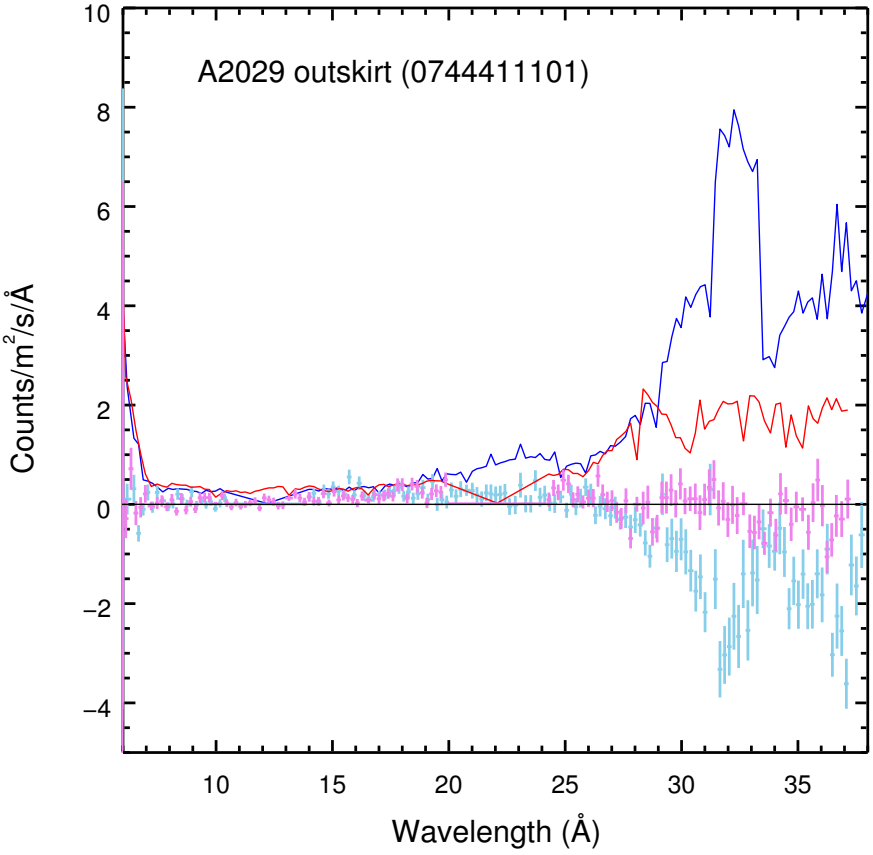

Figure 7.14: The RGS 1st-order spectra of A 2029 outskirt (ObsID: 0744411001). The data with error bars (light blue for RGS1 and violet for RGS2) are the observed background spectra minus the modelled background spectra, which are expected to be around zero, if the modelled background spectra are accurate. The solid lines (deep blue for RGS1 and red for RGS2) are the (subtracted) modelled background spectra obtained with *rgsproc*.

Table 7.7: The best-fit results of the EPIC spectra of NGC 5044 using SPEX v2.06 and v3.03. MOS and pn spectra are fitted simultaneously.

SPEX	v2.05	v3.03	v3.03
SPEXACT	v2.05	v2.05	v3.03
Model	GDEM	3T	3T
C-stat	6502	6210	5635
d.o.f.	1512	1287	1287
Norm.	2.153 ± 0.014	2.218 ± 0.008	2.077 ± 0.023
kT	0.974 ± 0.002	1.043 ± 0.003	0.962 ± 0.004
Si/Fe	0.93 ± 0.14	0.96 ± 0.07	0.79 ± 0.10
S/Fe	1.3 ± 0.3	1.4 ± 0.1	1.1 ± 0.2
Ar/Fe	1.4 ± 0.5	1.3 ± 0.4	1.0 ± 0.3
Ca/Fe	1.5 ± 0.3	1.6 ± 0.3	1.2 ± 0.2

Notes. The normalization in units of 10^{71} m^{-3} refers to the total emission measure. The temperature (in keV) here is where the differential emission measure reaches its maximum.

file. Then we re-analyse the source spectra after subtracting the modified modelled background spectra. Given a 2T model, compared to the results of unmodified modelled background (Table 7.1), the Fe abundance increases/decreases dramatically by $+0.33$ (for 90% BACKSCAL) and -0.15 (for 110% BACKSCAL), respectively. The deviations are significantly larger compared to pure statistical errors. Nevertheless, the abundance ratios of N/Fe and O/Fe are consistent with 3.4 and 1.3, respectively. That is to say, the abundance ratios are robust given a 10% (constant) uncertainty in the modelled background spectra. Similar checks are also performed on other sources with higher modelled background level.

7.C. EPIC spectral analysis of NGC 5044 with SPEX v3.03

The EPIC Si/Fe, S/Fe, Ar/Fe, and Ca/Fe abundance ratios († in Table 7.5) have been reported in Mernier et al. (2016a, their Table D.1). However, an older version of SPEX (v2.05) was used at that time. In the present work, we reanalyze the EPIC spectra with SPEX v3.03. As shown in Table 7.7, the newly obtained abundance ratios are consistent (at a 1σ confidence level) with those reported in Mernier et al. (2016a).

More accurate and complete atomic data (SPEXACT v3.03) are used in SPEX

v3.03 (Section 7.3). The total number of lines has increase by a factor of ~ 400 to reach about 1.8 million in the new version. Consequently, multi-temperature plasma models like GDEM, which has about 20 different normalization/temperature components, is computational expensive for SPEX v3.03. A three temperature (3T) model would be a cheaper alternative for SPEX v3.03. To mimic a Gaussian differential emission measure distribution (GDEM) with a three temperature distribution, we set the temperatures of all three components to be free, the normalization of the main component is also allowed to vary, while the normalization of the low- and high-temperature components are fixed to be half of that of the main component.

MOS and pn spectra are fitted simultaneously. When we use the old atomic database (SPEXACT v2.05), the best-fit C-stat to degree of freedom ratios are 6502/1512 (GDEM in SPEX v2.05) and 6210/1287 (3T in SPEX v3.03), respectively. As expected, the ratio is slightly worse for the 3T model. The degree of freedoms are different mainly due to the fact that the optimal binning algorithm (Kaastra & Bleeker 2016) is different in the two versions of SPEX.

When we use the 3T model and SPEX v3.03, the best-fit C-stat to degree of freedom ratios are 6210/1287 (SPEXACT v2.05) and 5635/1287 (SPEXACT v3.03), respectively. This shows the improvement with the new atomic data.

7.D. IMF weighted SNcc yields and yields of SNIa.

IMF weighted core-collapse supernovae (SNcc) yields are shown in Figure 7.15 with different initial metallicity ($Z_{\rm init}$) and initial mass function (IMF) for the stellar progenitors. Figure 7.16 shows the Type Ia supernovae (SNIa) yields based on theoretical calculations (Iwamoto et al. 1999) and observations of the Tycho supernova remnant (Badenes et al. 2006).

References

Asplund, M. 2005, ARA&A, 43, 481
Badenes, C., Borkowski, K. J., Hughes, J. P., Hwang, U., & Bravo, E. 2006, ApJ, 645, 1373
Badnell, N. R. 2006, ApJS, 167, 334
Barkat, Z., Rakavy, G., & Sack, N. 1967, Physical Review Letters, 18, 379
Böhringer, H. & Werner, N. 2010, A&A Rev., 18, 127
Bulbul, E., Smith, R. K., & Loewenstein, M. 2012, ApJ, 753, 54
Buote, D. A. 2000, MNRAS, 311, 176
Buote, D. A. & Canizares, C. R. 1994, ApJ, 427, 86
Campbell, S. W. & Lattanzio, J. C. 2008, A&A, 490, 769
Chiappini, C., Hirschi, R., Meynet, G., et al. 2006, A&A, 449, L27

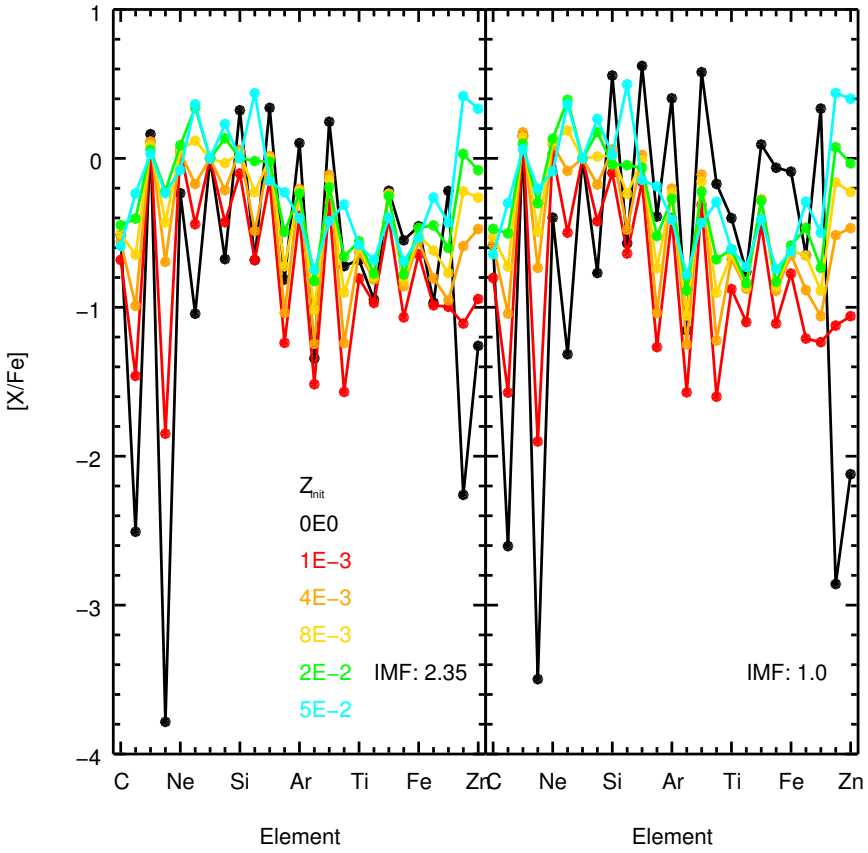

Figure 7.15: IMF weighted SNcc yields, based on the yields table of Nomoto et al. (2013).

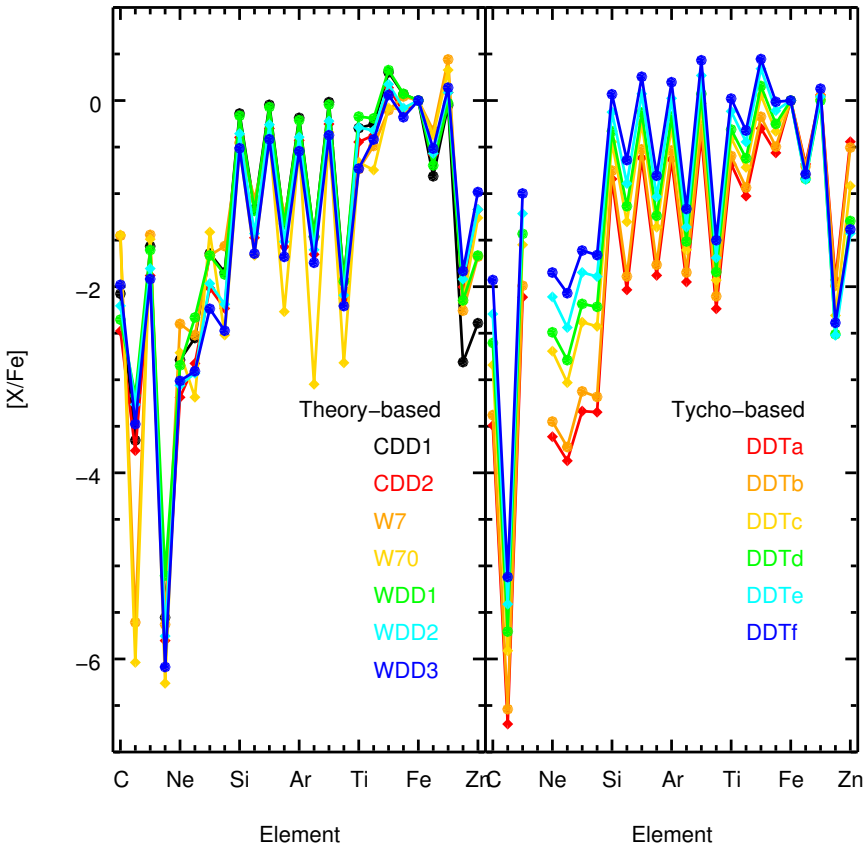

Figure 7.16: Yields from various SNIa models (Badenes et al. 2006; Iwamoto et al. 1999).

de Plaa, J., Kaastra, J. S., Tamura, T., et al. 2004, A&A, 423, 49
de Plaa, J., Kaastra, J. S., Werner, N., et al. 2017, A&A, 607, A98
de Plaa, J., Werner, N., Bykov, A. M., et al. 2006, A&A, 452, 397
den Herder, J. W., Brinkman, A. C., Kahn, S. M., et al. 2001, A&A, 365, L7
Fabbian, D., Nissen, P. E., Asplund, M., Pettini, M., & Akerman, C. 2009, A&A, 500, 1143
Finoguenov, A., Matsushita, K., Böhringer, H., Ikebe, Y., & Arnaud, M. 2002, A&A, 381, 21
Frank, K. A., Peterson, J. R., Andersson, K., Fabian, A. C., & Sanders, J. S. 2013, ApJ, 764, 46
Fujita, Y., Hayashida, K., Nagai, M., et al. 2008, PASJ, 60, 1133
Gil-Pons, P., Gutiérrez, J., & García-Berro, E. 2007, A&A, 464, 667
Grange, Y. G., de Plaa, J., Kaastra, J. S., et al. 2011, A&A, 531, A15
Greene, J. E., Janish, R., Ma, C.-P., et al. 2015, ApJ, 807, 11
Gu, M. F. 2008, Canadian Journal of Physics, 86, 675
Henriques, B. M. B., White, S. D. M., Thomas, P. A., et al. 2015, MNRAS, 451, 2663
Hitomi Collaboration, Aharonian, F., Akamatsu, H., et al. 2017a, Nature, 551, 478
Hitomi Collaboration, Aharonian, F., Akamatsu, H., et al. 2017b, ArXiv e-prints
Israelian, G., Ecuvillon, A., Rebolo, R., et al. 2004, A&A, 421, 649
Iwamoto, K., Brachwitz, F., Nomoto, K., et al. 1999, ApJS, 125, 439
Johansson, J., Thomas, D., & Maraston, C. 2012, MNRAS, 421, 1908
Kaastra, J. S. 2017, Astronomische Nachrichten, 338, 146
Kaastra, J. S. & Bleeker, J. A. M. 2016, A&A, 587, A151
Kaastra, J. S., Mewe, R., & Nieuwenhuijzen, H. 1996, in UV and X-ray Spectroscopy of Astrophysical and Laboratory Plasmas, ed. K. Yamashita & T. Watanabe, 411–414
Kaastra, J. S., Paerels, F. B. S., Durret, F., Schindler, S., & Richter, P. 2008, Space Sci. Rev., 134, 155
Karakas, A. I. 2010, MNRAS, 403, 1413
Kobayashi, C., Umeda, H., Nomoto, K., Tominaga, N., & Ohkubo, T. 2006, ApJ, 653, 1145
Komiyama, M., Sato, K., Nagino, R., Ohashi, T., & Matsushita, K. 2009, PASJ, 61, S337
Landry, D., Bonamente, M., Giles, P., et al. 2013, MNRAS, 433, 2790
Lodders, K. & Palme, H. 2009, Meteoritics and Planetary Science Supplement, 72, 5154
Loewenstein, M. 2013, ApJ, 773, 52
Maeda, K., Röpke, F. K., Fink, M., et al. 2010, ApJ, 712, 624
Mao, J. & Kaastra, J. 2016, A&A, 587, A84
Mernier, F., de Plaa, J., Kaastra, J. S., et al. 2017, A&A, 603, A80
Mernier, F., de Plaa, J., Lovisari, L., et al. 2015, A&A, 575, A37
Mernier, F., de Plaa, J., Pinto, C., et al. 2016a, A&A, 592, A157
Mernier, F., de Plaa, J., Pinto, C., et al. 2016b, A&A, 595, A126
Mollá, M., Cavichia, O., Gavilán, M., & Gibson, B. K. 2015, MNRAS, 451, 3693
Mulchaey, J. S., Kasliwal, M. M., & Kollmeier, J. A. 2014, ApJ, 780, L34
Nandra, K., Barret, D., Barcons, X., et al. 2013, ArXiv e-prints
Nissen, P. E., Chen, Y. Q., Carigi, L., Schuster, W. J., & Zhao, G. 2014, A&A, 568, A25
Nomoto, K., Kobayashi, C., & Tominaga, N. 2013, ARA&A, 51, 457
Pinto, C., Fabian, A. C., Ogorzalek, A., et al. 2016, MNRAS, 461, 2077
Pinto, C., Sanders, J. S., Werner, N., et al. 2015, A&A, 575, A38
Pipino, A., Devriendt, J. E. G., Thomas, D., Silk, J., & Kaviraj, S. 2009, A&A, 505, 1075
Pols, O. R., Izzard, R. G., Stancliffe, R. J., & Glebbeek, E. 2012, A&A, 547, A76

Reddy, B. E., Lambert, D. L., & Allende Prieto, C. 2006, MNRAS, 367, 1329
Renzini, A. & Andreon, S. 2014, MNRAS, 444, 3581
Romano, D., Chiappini, C., Matteucci, F., & Tosi, M. 2005, A&A, 430, 491
Romano, D., Karakas, A. I., Tosi, M., & Matteucci, F. 2010, A&A, 522, A32
Sanders, J. S. & Fabian, A. C. 2006, MNRAS, 371, 1483
Sanders, J. S., Fabian, A. C., Allen, S. W., et al. 2008, MNRAS, 385, 1186
Sanders, J. S., Fabian, A. C., Frank, K. A., Peterson, J. R., & Russell, H. R. 2010, MNRAS, 402, 127
Sanders, J. S., Fabian, A. C., & Smith, R. K. 2011, MNRAS, 410, 1797
Saro, A., Borgani, S., Tornatore, L., et al. 2006, MNRAS, 373, 397
Sato, K., Tokoi, K., Matsushita, K., et al. 2007, ApJ, 667, L41
Schindler, S. & Diaferio, A. 2008, Space Sci. Rev., 134, 363
Shi, J. R., Zhao, G., & Chen, Y. Q. 2002, A&A, 381, 982
Siess, L. 2007, A&A, 476, 893
Smith, R. J., Lucey, J. R., Hudson, M. J., & Bridges, T. J. 2009, MNRAS, 398, 119
Spite, M., Cayrel, R., Plez, B., et al. 2005, A&A, 430, 655
Steenbrugge, K. C., Kaastra, J. S., Crenshaw, D. M., et al. 2005, A&A, 434, 569
Tamura, T., Kaastra, J. S., den Herder, J. W. A., Bleeker, J. A. M., & Peterson, J. R. 2004, A&A, 420, 135
Tamura, T., Kaastra, J. S., Makishima, K., & Takahashi, I. 2003, A&A, 399, 497
Umeda, H. & Nomoto, K. 2002, ApJ, 565, 385
Urdampilleta, I., Kaastra, J. S., & Mehdipour, M. 2017, A&A, 601, A85
Walker, S. A., Fabian, A. C., Sanders, J. S., George, M. R., & Tawara, Y. 2012, MNRAS, 422, 3503
Werner, N., Böhringer, H., Kaastra, J. S., et al. 2006a, A&A, 459, 353
Werner, N., de Plaa, J., Kaastra, J. S., et al. 2006b, A&A, 449, 475
Werner, N., Durret, F., Ohashi, T., Schindler, S., & Wiersma, R. P. C. 2008, Space Sci. Rev., 134, 337
Werner, N., Urban, O., Simionescu, A., & Allen, S. W. 2013, Nature, 502, 656
Werner, N., Zhuravleva, I., Churazov, E., et al. 2009, MNRAS, 398, 23
White, S. D. M., Navarro, J. F., Evrard, A. E., & Frenk, C. S. 1993, Nature, 366, 429
Xu, H., Kahn, S. M., Peterson, J. R., et al. 2002, ApJ, 579, 600
Zhang, Y.-Y., Andernach, H., Caretta, C. A., et al. 2011, A&A, 526, A105

Summary

Hot astrophysical plasma is ubiquitous in the Universe, from comets in our Solar system to the largest scale structures – the cosmic web filaments. These hot plasmas, with temperatures of a few million of degrees, are often observed in the X-ray wavelength range. Spectroscopic diagnostics enable us to probe physical properties like temperature, density, abundance, microscopic turbulence, line of sight velocity, etc. High spectral resolving power is essential to overcome the confusion caused by unresolved spectral features. Thanks to the grating spectrometers aboard *XMM-Newton* and *Chandra*, our knowledge of the hot and energetic Universe is advanced. On the other hand, high quality spectra from current and future generations of X-ray spectrometers also challenge plasma models that are widely used in the community.

Plasma model

To interpret the spectra in a self-consistent way, we need plasma models built on an extensive atomic database. Different plasma models suitable for different astrophysical scenarios are required. For instance, plasmas exposed to a strong external radiation field (e.g. circumnuclear media of active galactic nuclei) require a plasma model in photoionization equilibrium, while low-density high-temperature thermal plasmas (e.g. intracluster media of relaxed galaxy clusters) require a plasma model in collisional ionization equilibrium. In this thesis, we use the SPEX package.

SPEX is a software package optimized for the analysis and interpretation of high-resolution cosmic X-ray spectra. Based on a single atomic database, plasma models provided by SPEX cover a wide range of astrophysical environments. The CIE model is designed for plasmas in collisional ionization equilibrium. The PION model is suitable for plasmas in photoionization equilibrium. The NEIJ model can be applied to the non-equilibrium ionization plasmas. The CX model accounts for charge exchange recombination at the interface between hot and cold plasmas.

Photoionized circumnuclear media

Circumnuclear media of active galactic nuclei can be photoionized by the AGN and they are observed both in absorption and emission in high-resolution spectra. Photoionized outflows are of particular interest since they can influence their nuclear and local galactic environment.

Self-consistent photoionization modeling is the key to properly interpret the intrinsic broad band continuum and all the obscuration, absorption, emission, and extinction effects simultaneously.

Chemical evolution RGS sample

The hot X-ray halos of groups and clusters of galaxies are collisionally ionized. Their line-rich spectra show metal enrichment. The elemental abundances in these collisionally ionized media are footprints of time-integrated yields of various stellar populations. Specific abundance patterns have been left prior to and during the

evolution of groups and clusters of galaxies.

Thanks to the Chemical evolution RGS sample (CHEERS) observed with the Reflection Grating Spectrometer (RGS) aboard *XMM-Newton*, we are able to understand the chemical enrichment of various elements in nearby ellipticals, groups, and clusters of galaxies. Low- and intermediate-massive stars in the asymptotic giant branch are the main metal factories of light elements like nitrogen. Massive stars undergo core collapse at the end of their evolution ejecting a large amount of α-elements (e.g. O, Ne, and Mg). Degenerate stars leading to Type Ia supernovae produce significant amounts of the Fe-peak elements (e.g. Cr, Mn, Fe, and Ni).

This thesis

First, I focus on updating the atomic data for radiative recombination in the SPEX code. Radiative recombination (RR) is a fundamental atomic process. I use the updated collisional ionizied and photoionized plasma models to better understand the physics of circumnuclear media in active galactic nuclei and the nitrogen enrichment in the the hot X-ray halos of ellipticals, groups, and clusters of galaxies.

1. Previously, the RR rate coefficients (i.e., the electron capture rates per ion) in SPEX were approximated with a power law. In **Chapter 2**, I propose a slightly more complicated mathematical function, which matches much better ($\lesssim 5\%$) the state-of-the-art RR rate coefficients.

2. In **Chapter 3**, I update the AUTOSTRUCTURE and ADASRR codes to systematically calculate detailed electron energy loss rates due to radiative recombination. This is the first time the electron energy loss rates due to RR of He-like to Ne-like ions have been calculated.

3. A theoretical study of density diagnostics using absorption lines from metastable levels is presented in **Chapter 4**. With the self-consistent PhotoIONization (PION) model in the SPEX code, we are able to calculate detailed level populations, including the ground and metastable levels. This enables us to determine under what physical conditions the metastable levels are significantly populated. I also reanalyze high-resolution grating spectra of NGC 5548 observed with Chandra in January 2002 using a set of PION components for the photoionized outflow. We derive lower (or upper) limits of plasma density in five out of six PION components based on the presence (or absence) of the metastable absorption lines.

4. The X-ray narrow emission features in the archetypal Seyfert 1 galaxy NGC 5548 are studied in **Chapter 5**. I provide the alternative interpretation that the X-ray narrow emission features in NGC 5548 can be described by a two-phase photoionized plasma with different ionization parameters and kinematics, and no further absorption by the warm absorber components. Moreover, I find that the X-ray and optical narrow emission line regions are most likely the same multi-phase photoionized plasma. The X-ray narrow emission line region is not the counterpart of the UV/X-ray absorber outside the line of sight because their distances and kinematics are not consistent.

5. In **Chapter 6**, I focus on the broad X-ray emission features in another Seyfert 1 galaxy, NGC 3783. I compare the December 2016 RGS spectra to the time-averaged RGS spectrum obtained in 2000–2001. The continuum was obscured in December 2016 but not in 2000–2001. We find a statistically significant broad emission component in the time-averaged RGS spectrum in 2000–2001. This X-ray broad emission component seems to be significantly weaker in December 2016. I demonstrate that the apparent weakening might be due to the extra screening by the obscurer, indicating that the obscurer is located further than the X-ray broad-line region.

6. In **Chapter 7**, I investigate the nitrogen enrichment in the chemical evolution RGS sample. For a standard initial mass function, low- and intermediate-mass stars are the main metal factory of nitrogen in the hot X-ray halos of ellipticals, groups, and clusters of galaxies. I also point out that the abundances of odd-Z elements (e.g. N, Na, Al, and Mn) are sensitive to the initial metallicity of the progenitors but they are not well constrained with current instruments (**Chapter 7**). Nonetheless, future missions like *XARM* with sufficient spectral resolution and photon collection area are required to put tight constraints on the abundances of odd-Z elements so that we can break the degeneracy on initial metallicity of the progenitors.

Samenvatting

Heet astrofysisch plasma is alomtegenwoordig in het universum, van kometen in ons zonnestelsel tot de grootste schaalstructuren - de kosmische webfilamenten. Dit hete plasma, met temperaturen van enkele miljoenen graden, wordt waargenomen met röngenstraling. Met behulp van spectroscopische diagnostiek kunnen we fysische eigenschappen meten, zoals temperatuur, dichtheid, abundantie, microscopische turbulentie, snelheid langs de zichtlijn, enz. Hoog spectraal oplossend vermogen is essentieel om de onzekerheid veroorzaakt door onopgeloste spectraallijnen te verkleinen. Dankzij de traliespectrometers aan boord van *XMM-Newton* en *Chandra* is onze kennis van het hete en energieke universum toegenomen. Aan de andere kant zjin de hoogwaardige spectra van huidige en toekomstige generaties van röntgenspectrometers een uitdaging voor plasmamodellen die veel worden gebruikt in de astrofysische gemeenschap.

Plasmamodel

Om de spectra op een zelfconsistente manier te interpreteren, hebben we plasmamodellen nodig die gebruikmaken van een uitgebreide atomaire database. De verscheidenheid aan astrofysische scenario's vraagt om verschillende plasmamodellen. Bijvoorbeeld plasma's die blootgesteld worden aan een sterk uitwendig stralingsveld (zoals circumnucleaire media van actieve galactische kernen) vereisen een plasmamodel in foto-ionisatie evenwicht, terwijl plasma's met een lage dichtheid en een hoge temperatuur (bijv. intracluster media van ontspannen melkwegclusters) een plasmamodel vereisen in botsings-ionisatie evenwicht. In dit proefschrift gebruiken we de SPEX code.

SPEX is een softwarepakket dat is geoptimaliseerd voor de analyse en interpretatie van kosmische röntgenspectra met hoge resolutie. Gebaseerd op een enkele atomaire database bestrijken plasmamodellen geleverd door SPEX een breed scala van astrofysische omgevingen. Het CIE-model is ontworpen voor plasma's in botsingsionisatie evenwicht. Het PION-model is geschikt voor plasma's in foto-ionisatie evenwicht. Het NEIJ-model kan worden toegepast op de niet evenwicht-ionisatie plasma's. Het CX-model is verantwoordelijk voor recombinatie door ladingsuitwisseling op het raakvlak tussen warme en koude plasma's.

Gefotoioniseerde circumnucleaire media

Circumnucleaire media van actieve galactische kernen kunnen door de AGN worden gefotoioniseerd en ze worden zowel in absorptie als in emissie waargenomen met hoge-resolutiespectra. Gefotoioniseerde uitstromen zijn van bijzonder belang, omdat ze hun nucleaire en lokale galactische omgeving kunnen beïnvloeden.

Zelfconsistente foto-ionisatiemodellering is de oplossing om simultaan het intrinsieke breedbandcontinuüm en alle obscuratie-, absorptie-, emissie- en extinctieeffecten goed te interpreteren.

Chemische evolutie met RGS

De hete röntgenhalo's van groepen en clusters van sterrenstelsels zijn ge ioniseerd door botsingen. De emissielijnen vertonen aanwijzingen voor metaalverrijking. De elementaire abundanties in het gas traceren de tijdgeïntegreerde opbrengsten van verschillende sterpopulaties. Specifieke patronen ontstaan voorafgaand aan en tijdens de evolutie van groepen en clusters van melkwegstelsels.

Dankzij het RGS sample van clusters dat met de Reflectie Tralie Spectrometer (RGS) aan boord van *XMM-Newton* is waargenomen, kunnen we de chemische verrijking van verschillende elementen in nabijgelegen elliptische stelsels, groepen en clusters van sterrenstelsels begrijpen. Lichte en middelzware sterren in de Asymptotic Giant Branch zijn de belangrijkste metaalfabrieken van lichte elementen zoals stikstof. Massieve sterren ondergaan een supernova-explosie aan het einde van hun evolutie en werpen een grote hoeveelheid α-elementen (bijvoorbeeld O, Ne en Mg) uit. Gedegenereerde sterren die leiden tot type Ia supernovae produceren aanzienlijke hoeveelheden van de Fe-piekelementen (bijvoorbeeld Cr, Mn, Fe en Ni).

Dit proefschrift

Eerst richten we ons op het bijwerken van de atomaire gegevens van straling recombinatie in de SPEX-code. Radiatieve recombinatie (RR) is een fundamenteel atoomproces. Vervolgens gebruiken we de bijgewerkte botsings-geïoniseerde en gefotoioniseerde plasmamodellen om de fysica van circumnucleaire media en de stikstofverrijking in de hete röntgenhalo's van elliptische stelsels, groepen en clusters van melkwegstelsels beter te begrijpen.

1. Eerder werden de RR-coëfficiënten (d.w.z. de elektroneninvangsniveaus per ion) in SPEX benaderd met een machtswet. In **Hoofdstuk 2** stel ik een iets gecompliceerdere wiskundige functie voor, die veel beter overeenkomt ($\lesssim 5$ %) met de nieuwste RR-coëfficiënten.

2. In **Hoofdstuk 3** werk ik de codes AUTOSTRUCTURE en ADASRR bij om systematisch gedetailleerde elektronenergieverliessnelheden te berekenen als gevolg van RR. Dit is de eerste keer dat de elektronenergieverliessnelheden als gevolg van RR van He-achtige naar Ne-achtige ionen zijn berekend.

3. Een theoretische studie van dichtheidsdiagnostiek met absorptielijnen van metastabiele niveaus wordt gepresenteerd in **Hoofdstuk 4**. Met het zelfconsistente PhotoIONization (PION)-model in de SPEX-code kunnen we gedetailleerde niveaupopulaties berekenen, inclusief de grond- en metastabiele niveaus. Dit stelt ons in staat te bepalen onder welke fysische omstandigheden de metastabiele niveaus aanzienlijk worden gevuld. In **Hoofdstuk 4** analyseren we ook de hoge-resolutie traliespectra van NGC 5548 geobserveerd door Chandra in januari 2002 met behulp van een set PION-componenten voor de gefotoioniseerde uitstroom. We berekenen lagere (of bovenste) limieten van de plasmadichtheid in vijf van de zes PION-componenten op basis van de aanwezigheid (of afwezigheid) van de metastabiele absorptielijnen.

4. De nauwe emissielijnen van röntgenstraling in het Seyfert 1 sterrenstelsel NGC 5548 worden bestudeerd in **Hoofdstuk 5**. Ik bied een alternatieve interpretatie dat de nauwe emissielijnen van röntgenstraling in NGC 5548 kunnen worden beschreven door een tweefasig, gefotoioniseerd plasma met verschillende ionisatieparameters en kinematica, en geen verdere absorptie door de componenten van het warme plasma in het systeen. Bovendien vinden we dat de röntgenstraling en optische emissielijngebieden hoogstwaarschijnlijk hetzelfde meerfasen-gefotoioniseerde plasma zijn. Dit gebied met nauwe emissielijnen is niet de tegenhanger van de absorberende laag in UV en röntgenstraling buiten de gezichtslijn omdat hun afstanden en kinematica niet consistent zijn.

5. In **Hoofdstuk 6** richt ik me op de röntgenstraling door brede emissielijnen in een ander Seyfert 1-sterrenstelsel (NGC 3783). We vergelijken de RGS-spectra van december 2016 met het tijdgemiddelde RGS-spectrum verkregen in 2000-2001. Het continuüm was zwakker in december 2016, maar niet in 2000-2001. Ik vind een statistisch significante brede emissiecomponent in het tijdgemiddelde RGS-spectrum in 2000-2001. Deze component met brede emissielijnen lijkt aanzienlijk zwakker te zijn in december 2016. Ik toon aan dat de schijnbare verzwakking te wijten kan zijn aan de extra absorptie van het tussenliggende materiaal van de verduisterende laag, wat aangeeft dat die zich bevind verder weg van de kern dan het röntgen breed lijnen gebied.

6. In **Hoofdstuk 7** onderzoeken we de stikstofverrijking in het RGS sample (CHEERS). Onder de aanname van een standaard initiële massafunctie zijn sterren met een lage en gemiddelde massa de belangrijkste metaalfabriek van stikstof in de hete röntgenhalo's van elliptische stelsels, groepen en clusters van melkwegstelsels. Ik wijs er ook op dat de abundanties van elementen met een oneven Z (bijv. N, Na, Al en Mn) gevoelig zijn voor de samenstelling van de ster voordat die explodeert, maar ze zijn niet goed meetbaar met de huidige instrumenten (**Hoofdstuk 7**). Niettemin zijn toekomstige missies zoals *XARM* met voldoende spectrale resolutie en effectief oppervlak nodig om de abundanties van oneven elementen beter te meten, zodat we de samenstelling van de sterpopulatie better kunnen bepalen.

Curriculum Vitæ

I was born on the 5th of September 1988, in Ningbo, an ancient city with its history dating back to the Hemudu culture in 4800 BC. I completed my pre-university education in 2007 in Ningbo High School.

In the summer of 2007, I wanted to study astronomy in Beijing, the capital city of China. But there were merely four top level universities with the department of astronomy throughout the mainland of China, and the competition of the college entrance examination was indisputably fierce. I ended up in Hangzhou, the capital city of the province I was born, which was somehow a quite popular choice among my classmates in that summer. I enrolled to Zhejiang University of Technology with a physics major.

In my final year as a graduate student, I succeeded in the national post-graduate entrance examination and got the opportunity to pursue a Master of Astrophysics hosted by the National Astronomical Observatory, Chinese Academy of Science and University of Chinese Academy of Science, starting from September 2011.

All graduate students spend their first year doing coursework at the University of Chinese Academy of Science. At that time, I was intrigued by one course particularly – gaseous nebulae. The reasons are twofold: I enjoyed reading one of the textbooks *Astrophysics of Gaseous Nebulae and Active Galactic Nuclei* by Osterbrock; I learned a lot from one of the exercises where I reduced the SDSS spectrum of a star burst galaxy from scratch and inferred its physical properties (temperature, density and abundances) using plasma diagnostics.

In the following two years, under the supervision of Prof. Shuang-Nan Zhang (IHEP & NAOC) and Dr. Zhixing Ling (NAOC), I focused on studying small angle X-ray scattering with interstellar dust. I published my very first scientific paper in the Astrophysical Journal early 2014. I obtained my master's degree and got married in the summer of 2014.

My MSc study sparked my interest in high-resolution X-ray spectroscopy. Fortunately, I got a PhD position on this topic under the supervision of prof. dr. J. S. Kaastra (SRON & Leiden) and dr. Jelle de Plaa (SRON). During my PhD, I focused on improving the atomic data in the SPEX code and applying different types of plasma models to various astrophysical environments. I also enjoyed the opportunity to present my work at several international conferences and workshops in Tokyo (Japan), Boston (US), Rome (Italy), and Jekyll Island (US).

In the summer of 2018, I will work on a small project lead by Dr. Matteo Guainazzi (ESTEC) on the first catalogue of ionized emission lines measured by the RGS instrument on board *XMM-Newton*. Then I will move to Glasgow in September to take up a postdoc position with Prof. Nigel Badnell on theoretical and computational studies of atomic process of astrophysical plasmas.

List of publications

20. **Junjie Mao**, M. Mehdipour, J. S. Kaastra, et al. A&A, submitted in 2018
Photoionized emission and absorption features in the high-resolution X-ray spectra of NGC 3783

19. **Junjie Mao**, J. de Plaa, J. S. Kaastra, et al., A&A, submitted in 2017
Nitrogen abundance in the X-ray halos of clusters and groups of galaxies

18. **Junjie Mao**, J. S. Kaastra, M. Mehdipour et al. A&A, 2018, 612, A18
Anatomy of the AGN in NGC 5548 IX. Photoionized emission features in the soft X-ray band

17. **Junjie Mao**, J. S. Kaastra, M. Mehdipour et al., A&A, 2017, 607, A100
Density diagnostics of ionized outflows in active galactic nuclei X-ray and UV absorption lines from metastable levels in Be-like to C-like ions

16. **Junjie Mao**, Jelle Kaastra, N. R. Badnell, A&A, 2017, 599, A10
The energy loss rate of radiative recombination

15. **Junjie Mao**, Jelle Kaastra, 2016, A&A, 2016, 587A, 84M
The level-resolved radiative recombination data for SPEX3

14. **Junjie Mao**, Zhixing Ling, Shuang-Nan Zhang, ApJ, 2014, 785, 23
X-ray scattered halo around IGR J17544-2619

13. Liyi Gu, **Junjie Mao**, Jelle de Plaa et al. A&A, 2018, 611, A26
Charge exchange in galaxy clusters

12. Liyi Gu, **Junjie Mao**, Christopher P. O'Dea, et al., A&A, 2017, 601, A45
Charge exchange in the ultraviolet: implication for interacting clouds in the core of NGC 1275

11. Liyi Gu, **Junjie Mao**, Elisa Costantini, et al., A&A, 2016, 594, A78
Suzaku and XMM-Newton observations of the North Polar Spur: Charge exchange or ISM absorption?

10. F. Mernier, J. de Plaa, J. S. Kaastra et al., MNRAS, submitted in 2018
Mass-invariance of the iron enrichment in the hot haloes of massive ellipticals, groups, and clusters of galaxies

9. J. S. Kaastra, M. Mehdipour, E. Behar, et al. A&A, submitted in 2018
Recurring obscuration in NGC 3783

8. R. Middei, S. Bianchi, M. Cappi, et al., A&A, accepted in 2018
Multi-wavelength campaign on NCG 7469. IV. The broad-band X-ray spectrum

7. M. Mehdipour, J. S. Kaastra, G. A. Kriss, et al. A&A, accepted in 2018
Multi-wavelength campaign on NGC 7469 III. Spectral energy distribution and the AGN wind photoionisation modelling, plus detection of diffuse X-rays from the starburst with Chandra HETGS

6. M. Mehdipour, J. S. Kaastra, G. A. Kriss, et al. A&A, 2017, 607, A28
Chasing obscuration in type-I AGN: discovery of an eclipsing clumpy wind at the outer broad-line region of NGC 3783

5. J. S. Kaastra, L. Gu, J. Mao, et al. JINST, 2017, 12, 08
Science with hot astrophysical plasmas

4. F. Mernier, J. de Plaa, J. Kaastra et al., A&A, 2017, A80, 27
Radial metal abundance profiles in the intra-cluster medium of cool-core galaxy clusters, groups, and ellipticals

3. H. Akamatsu, L. Gu, T. W. Shimwell et al., A&A, 2016, 593, L7
Suzaku and XMM-Newton observations of the newly discovered early-stage cluster merger of 1E2216.0-0401 and 1E2215.7-0404

2. F. Mernier, J. de Plaa, C. Pinto et al., A&A, 2016, 592, A157
Origin of central abundances in the hot intra-cluster medium II. Chemical enrichment and supernova yield models

1. F. Mernier, J. de Plaa, C. Pinto et al., A&A, 2016, 592, A157
Origin of central abundances in the hot intra-cluster medium I. Individual and average abundance ratios from XMM-Newton EPIC

Acknowledgements

I would not have made it this far without the support and help of many people.

I am grateful to those who have helped me to study astrophysics since 2011, including my undergraduate supervisor Prof. Zhongheng Li at ZJUT, former senior graduate students Qin Lin and Jun Xu at NAOC, all my fellow classmates at UCAS, my master supervisor Prof. Shuang-Nan Zhang and Dr. Zhixing Ling, our group members at NAOC and IHEP, and other colleagues and friends at NAOC.

During my search for a PhD position, I deeply thank Prof. Shuang-Nan Zhang, Prof. Weimin Yuan and Dr. Randall Smith for their great support.

I thank my PhD supervisor Prof. dr. Jelle Kaastra. I learned a lot from your useful scientific and non-scientific advises and optimism, especially when *Hitomi* spun out of control. I would also like to thank Dr. Jelle de Plaa for leading the CHEERS project and providing technical support.

I was lucky to work with amazing collaborators on different projects: Liyi, Ton and Nigel (I'm looking forward to starting my postdoc in your group!) on atomic related projects; Liyi, François, Hiroki, Ciro, Yu-Ying, and Hong-Liang on the CHEERS project; Missagh, Elisa, Jon, Graziella, Ehud, Stefano, Jerry, Gabriele, Pop, Laura, Barbara, Ciro, Jacobo, Uria, Riccardo, and Nahum on the AGN related projects.

Many thanks to awesome colleagues and friends in the Netherlands including Igone, Sascha, Catia, Lianghai, Daniele, Kristhell, Ioanna, Ping, Davide, Xiaohu, Maxwell, Dong-Gang, Zujia, Giacomo, Marianne, Laura, Margherita, Zuzanna, Tullio, Francesca, Jean, Cor, Theo, Jan-Willem, Lucien, Wim, Peter, and Jian-Rong. Special thanks to Sascha and Lianghai to be my paranymphs, Google translate and Jelle for the Dutch summary.

I'm also grateful to the staff members in SRON and Leiden, who ensured my stay to be smooth and pleasant, especially the secretaries (Esther, Evelijn, and Marjan), HR (Ilse, Karin, Sandra), and the ICT group (Frank and Eric).

I will never be grateful enough to Randall, Jon, Jean, and Frits for all the efforts and great support during my search for a postdoc position.

Finally, this thesis is dedicated to my wife for her understanding and support along the way.